Biophysical and circuit properties underlying population dynamics in neocortical networks

Yann Zerlaut

THÈSE DE DOCTORAT DE
l'UNIVERSITÉ PIERRE ET MARIE CURIE

Spécialité

Neurosciences

École doctorale Cerveau, Cognition et Comportement

Présentée par

Yann ZERLAUT

Pour obtenir le grade de

DOCTEUR de l'UNIVERSITÉ PIERRE ET MARIE CURIE

Sujet de la thèse :

Biophysical and circuit properties underlying population dynamics in neocortical networks

soutenue le 31 Mai 2016

devant le jury composé de :

Pr. Ad Aersten	Rapporteur
Pr. Stéphane Charpier	Président du Jury
Dr. Frédéric Chavane	Examinateur
Pr. Alain Destexhe	Directeur de thèse
Dr. Jean-Marc Goaillard	Rapporteur
Dr. Gilles Ouanounou	Co-directeur de thèse

Unité de Neurosciences, Information et Complexité
Centre National de la Recherche Scientique, FRE 3693
1 avenue de la terrasse, 91198 Gif sur Yvette

Remerciements

Je voudrais tout d'abord remercier mon directeur de thèse, Alain Destexhe. Il y a 5 ans il m'a chaleuresement ouvert les portes de son équipe et m'a initié avec enthousiasme au domaine des neurosciences computationnelles. Bénéficier de son expertise et avoir son soutien tout au long de cette thèse ont fait de ces années une expérience stimulante et particulièrement enrichissante. Je lui en suis extrêmement reconnaissant.

Ensuite je voudrais remercier Gilles Ouanounou. Il a pris le temps de m'enseigner l'électrophysiologie intracellulaire et travailler à ses côtés fut une très belle expérience scientifique et humaine. Je fais le voeu que, grâce à son exemple, une part de son talent pour l'observation et de sa créativité expérimentale ait réussi à déteindre sur moi.

Bartosz Teleńczuk fut d'une grande aide tout au long de cette thèse : de la *charpenterie logiciel* à l'écriture scientifique, j'ai beaucoup appris grâce à lui. Sa pertinence et sa sagesse ont été de précieux atouts pour façonner une grande partie du contenu de cette thèse.

Je remercie également Charlotte Deleuze et Thierry Bal qui, grâce à leur disponibilité et leur enthousiasme, ont initié la partie expérimentale de ma thèse.

De manière plus ou moins directe, beaucoup de membres du laboratoire on contribué à ce travail, pour n'en citer que quelques uns, merci à Gérard, Guillaume, Kirsty, Aurélie, Manon, Claude, Lyle, Marco, Michelle, Francesca, Sarah, ... Et bien sûr à tous ceux que j'oublie.

Je souhaite remercier le laboratoire, en particulier ses directeurs Yves Frégnac et Daniel Schulz, ils ont créé un endroit particulièrement épanouissant pour l'étudiant curieux que je suis. Venir au laboratoire fut un plaisir et je souhaite le meilleur à tout le monde pour cette nouvelle aventure sur le plateau.

Je voudrais également remercier les collaborateurs extérieurs avec qui nous avons travaillé durant cette thèse, intéragir avec eux fut une réelle source de motivation : Maria-Victoria Sanchez-Vives au début de ma thèse, puis Frédéric Chavane et Sandrine Chemla dans la seconde moitié. Nos échanges furent très stimulants et je pense en avoir retiré beaucoup.

Je remercie Ad Aersten et Jean-Marc Goaillard d'avoir accepté d'être rapporteur de cette thèse, ainsi que Stéphane Charpier et Frédéric Chavane d'avoir accepté d'examiner cette thèse. C'est un grand honneur pour moi qu'ils participent à ce jury.

Cette thèse a été financée successivement par une bourse de l'Initiative d'Excellence Paris-Saclay, puis par une bourse de la Fondation pour la Recherche Médicale, je tiens à leur exprimer ma gratitude.

Pour finir, je ne saurai assez remercier mes parents. Cette thèse est le fruit des opportunités qu'ils m'ont offertes tout au long de ces années, les mots me manquent pour les en remercier. Je remercie également le reste de ma famille pour leur soutien bienveillant et leurs encouragements.

Contents

Summary

The neocortex of awake animals displays an activated state in which cortical activity manifests highly complex, seemingly noisy behavior. At the level of single neurons the activity is characterized by strong subthreshold fluctuations and irregular firing at low rate. At the network level, the activity is weakly synchronized and exhibits a chaotic dynamics. Yet, it is within this regime that information is processed reliably through neural networks. This regime is thus crucial to neural computation. In this thesis, we contribute to its understanding by investigating how the biophysical properties at the cellular level combined with the properties of the network architecture shapes this asynchronous dynamics.

This thesis builds up on the so-called *mean-field* models of network dynamics, a theoretical formalism that describes population dynamics via a self-consistency approach. At the core of this formalism lie the neuronal transfer function: the input-output description of individual neurons. The first part of this thesis focuses on deriving *biologically-realistic* neuronal transfer functions. We first formulate a two step procedure to incorporate biological details (such as an extended dendritic structure and the effect of various ionic channels) into this transfer function based on experimental characterizations.

First, we investigated *in vitro* how layer V pyramidal neocortical neurons respond to membrane potential fluctuations on a cell-by-cell basis. We found that, not only individual neurons strongly differ in terms of their excitability, but also, and unexpectedly, in their sensitivities to fluctuations. In addition, using theoretical modeling, we attempted to reproduce these results. The model predicts that heterogeneous levels of biophysical properties such as sodium inactivation, sharpness of sodium activation and spike frequency adaptation account for the observed diversity of firing rate responses.

Then, we studied theoretically how dendritic integration in branched structures shape the membrane potential fluctuations at the soma. We found that, depending on the type of presynaptic activity, various comodulations of the membrane potential fluctuations could be achieved. We showed that,

when combining this observation with the heterogeneous firing responses found experimentally, individual neurons differentially responded to the different types of presynaptic activities. We thus propose that, because this mechanism offers a way to produce specific activation as a function of the input properties, biophysical heterogeneity might contribute to the encoding of the stimulus properties during sensory processing in neural networks.

The second part of this thesis investigates how circuit properties, such as recurrent connectivity and lateral connectivity, combine with biophysical properties to impact sensory responses through effects mediated by population dynamics.

We first investigated what was the effect of a high level of ongoing dynamics (the Up-state compared to the Down-state) on the scaling of post-synaptic responses. We found that the competition between the recruitment within the active recurrent network (in favor of high responses in the Up-state) and the increased conductance level due to background activity (in favor of reduced responses in the Up-state) predicted a non trivial stimulus-response relationship as a function of the intensity of the stimulation. This prediction was shown to accurately capture measurements of post-synaptic membrane potential responses in response to cortical, thalamic or auditory stimulation in rat auditory cortex *in vivo*.

Finally, by taking advantage of the *mean-field* approach, we constructed a tractable large-scale model of the layer II-III network including the horizontal fiber network. We investigate the spatio-temporal properties of this large-scale model and we compare its predictions with voltage sensitive dye imaging in awake fixating monkey. Notably, we re-construct a typical experimental paradigm of multi-input integration in visual processing: the apparent motion protocol. The model exhibited a similar spatio-temporal pattern of suppression such as the one observed *in vivo*, suggesting that the integrative properties of the network captured by our approach combined with the horizontal fiber network are the key components of this phenomena.

Taken together, those results emphasize the explanatory power of *biologically-realistic* theoretical models of population dynamics. Because they seem to offer a solid theoretical basis to account for the strong effects mediated by population dynamics during neocortical processing, this framework opens the way toward the understanding of the more subtle aspects of neocortical computations.

Résumé

Le néocortex possède un état activé dans lequel l'activité corticale manifeste un comportement complexe. Au niveau cellulaire, l'activité est caractérisée par de fortes fluctuations sous-liminaires du potential membranaire et une décharge irrégulière à basse fréquence. Au niveau du réseau, l'activité est marquée par un faible niveau de synchronie et une dynamique chaotique. Néanmoins, c'est dans ce régime que l'information est traitée de manière fiable par les réseaux neuronaux. Ce régime est donc crucial pour le traitement de l'information par le cortex. Dans cette thèse, nous contribuons à sa compréhension en examinant comment les propriétés biophysiques au niveau cellulaire combinées avec les propriétés d'architecture des réseaux façonnent cette dynamique asynchrone.

Cette thèse repose sur les modèles de dynamique de réseaux appelés modèles de *champ moyen*, un formalisme théorique qui décrit la dynamique de population grâce à une approche auto-consistante. Au coeur de ce formalisme se trouve la *fonction de transfert* neuronale : la fonction entrée-sortie d'un neurone. La première partie de cette thèse s'attache à dériver des fonctions de transfert *biologiquement réalistes* en incorporant des caractérisations expérimentales.

Dans un premier temps, nous avons examiné *in vitro* comment les neurones néocorticaux pyramidaux de la couche V du cortex visuel répondent à des fluctuations du potentiel membranaire. Nous avons observé que les neurones individuels ne diffèrent pas seulement en termes d'excitabilité, mais qu'ils diffèrent aussi par leurs sensibilités aux paramètres des fluctuations. Dans un deuxième temps, nous avons étudié de manière théorique comment l'intégration dendritique dans des structures arborescentes façonne les fluctuations au soma. Nous avons observé que, en fonction des propriétés de l'activité présynaptique, différentes comodulations des paramètres des fluctuations pouvaient être obtenues. En combinant cette observation avec nos mesures expérimentales, nous avons observé que cela induisait des couplages différents entre activité synaptique et décharge neuronale pour

chaque neurone. Nous proposons donc que, puisque ce mécanisme offre un moyen d'activer spécifiquement certains neurones en fonction des propriétés de l'entrée, l'hétérogénéité biophysique pourrait contribuer à l'encodage de propriétés des stimuli dans les traitements de l'information sensorielle.

La deuxième partie de cette thèse examine comment les propriétés d'architecture des réseaux neuronaux se combinent avec les propriétés biophysiques et affectent les réponses sensorielles via des effets de dynamiques de populations.

Nous avons tout d'abord examiné de manière théorique comment un haut niveau d'activité spontanée impactait les réponses post-synaptiques dans le cortex. Nous avons observé que la compétition entre le recrutement dans le réseau cortical activé et les effets de conductances associés prédisaient une relation non-triviale entre l'intensité des stimuli et l'amplitude des réponses. Cette prédiction fut observée dans des enregistrements de réponses post-synaptiques dans le cortex auditif du rat *in vivo* en réponse à des stimuli corticaux, thalamiques et auditifs.

Pour finir, en tirant avantage des approches de champ moyen, nous avons construit un modèle grande échelle du réseau des couches II-III incluant le réseau des fibres horizontales. Nous avons examiné les propriétés intégratives spatio-temporelles du modèle et nous les avons comparées avec des mesures par imagerie optique de l'activité cérébrale chez le singe éveillé. En particulier, nous avons reconstruit une expérience typique du traitement sensoriel: le mouvement apparent. Le modèle prédit un fort signal suppressif dont le profil spatio-temporel correspond quantitativement à celui observé *in vivo*. Cela suggère que la combinaison des propriétés intégratives du réseau capturées par notre approche et du réseau des fibres horizontales sont les ingrédients clefs de ce phénomène.

Dans leur ensemble, ces résultats soulignent le pouvoir explicatif des modèles *biologiquement-réalistes* de dynamique de populations neuronales. Parce que ces modèles semblent offrir un solide socle théorique pour décrire les forts effets de dynamique de populations associée au traitement corticale, ce cadre ouvre la voie à la compréhension des aspects plus subtils du traitement néocortical.

Part I

Introduction

Generalities on neocortical physiology

The nervous system is the part of an animal's body that controls the body's functions (its voluntary and involuntary actions), it coordinates and transmits signals to and from different parts of the body (see the diagram in Figure 1B). The neocortex (Latin for *new bark*) is the superficial sheet of the cerebral cortex, the latter being the upper layer of the cerebral hemisphere (see Figure 2A), it appeared with the evolution of mammals and it is the structure where the most complex cerebral functions (sensory perception, language, generation of motor commands, etc...) are performed. Understanding the physiological mechanisms that render those performances possible is a fundamental question in modern biology.

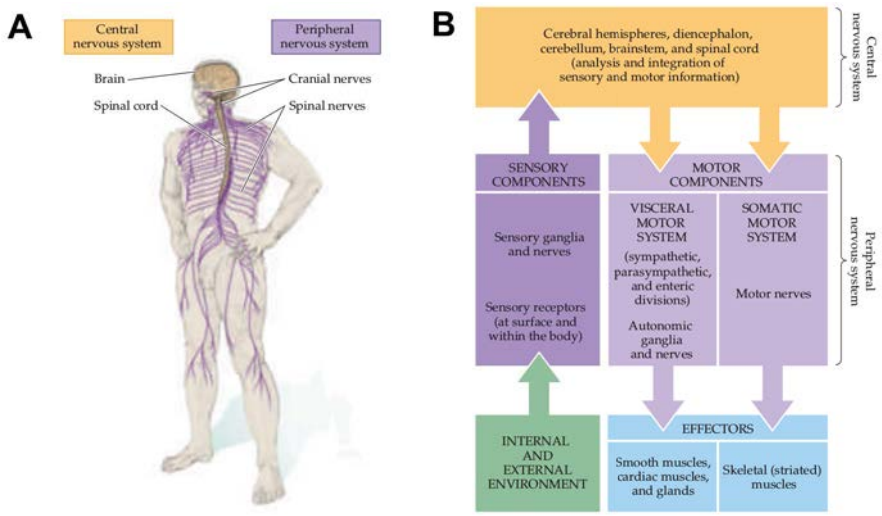

Figure 1: Organization and functions of the human nervous system. **(A)** The nervous system is made of the central nervous system (containing the brain and spinal cord) and the peripherical nervous system (containing the spinal and cranial nerves). **(B)** Diagram of the major components of the central and peripheral nervous systems and their functional relationships. Stimuli from the environment convey information to processing circuits within the brain and spinal cord, which in turn interpret their significance and send signals to peripheral effectors that move the body and adjust the workings of its internal organs. Adapted from Purves D, Augustine GJ, Fitzpatrick D, et al. (2001).

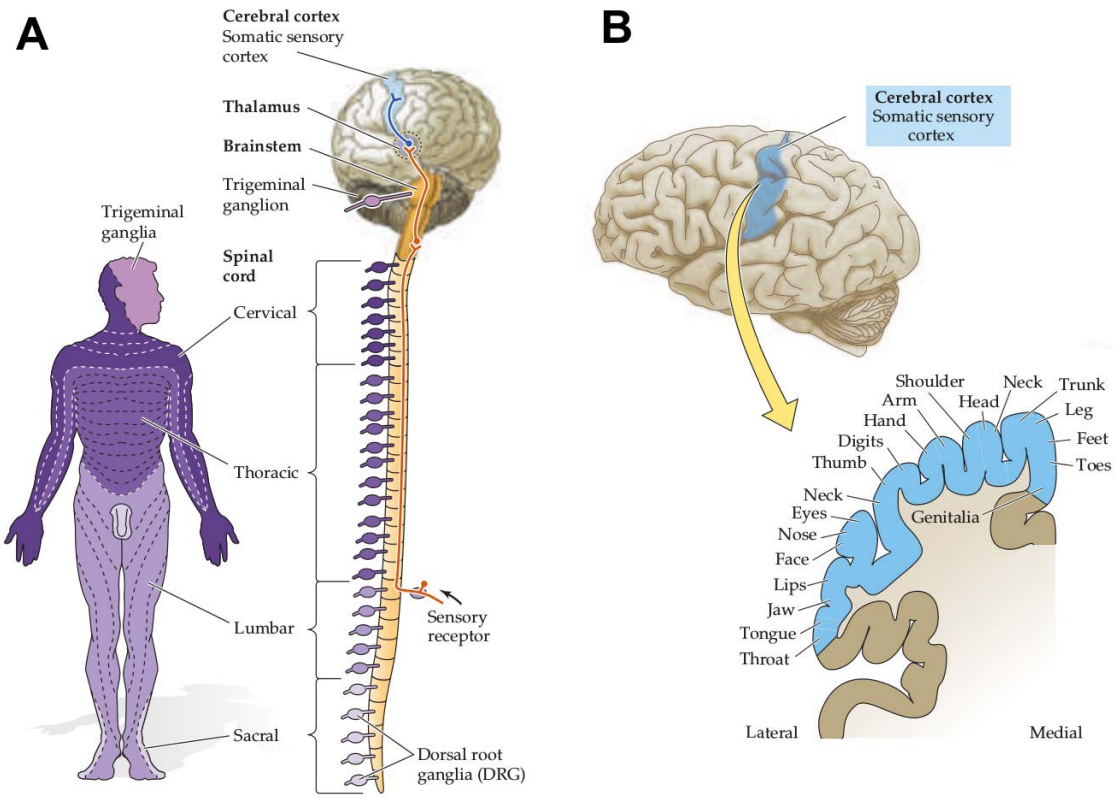

Figure 2: Anatomical and functional organization of a sensory system: example of the human somato-sensory system. **(A)** Somatosensory information from the body surface is mapped onto dorsal root ganglia (DRG), schematically depicted here as attachments to the spinal cord. The various shades of purple indicate correspondence between regions of the body and the DRG that relay information from the body surface to the central nervous system. Somatosensory information travels from this peripheral sensory receptors toward the spinal cord and brainstem, ultimately sending sensory information to the thalamus, from which it is relayed to the somatic sensory cortex in the postcentral gyrus. **(B)** Somatotopic organization of sensory information. (Top) The locations of primary and secondary somatosensory cortical areas on the lateral surface of the brain. (Bottom) Cortical representation of different regions of skin. Reproduced and adapted from Purves D, Augustine GJ, Fitzpatrick D, et al. (2001).

The basic design of the neocortex is conserved across all mammals: 1) it is subdivided into functional areas called cortical areas having a precise cognitive function (see Figure 2B) and 2) the cortical surface corresponds to the juxtaposition of cortical columns comprising about 10000-50000 neurons being each around 500 μm wide. A notable difference between small mammals (e.g. rodents) and larger mammals (e.g. primates, see Figure 2B) is the presence of folds of the neocortical sheet that allow an important increase of the neocortical surface given the limited skull size.

Neocortical tissue is mainly composed of neurons as well as glial cells, the human brain contains about 100 billions neuronal cells and 500 billions

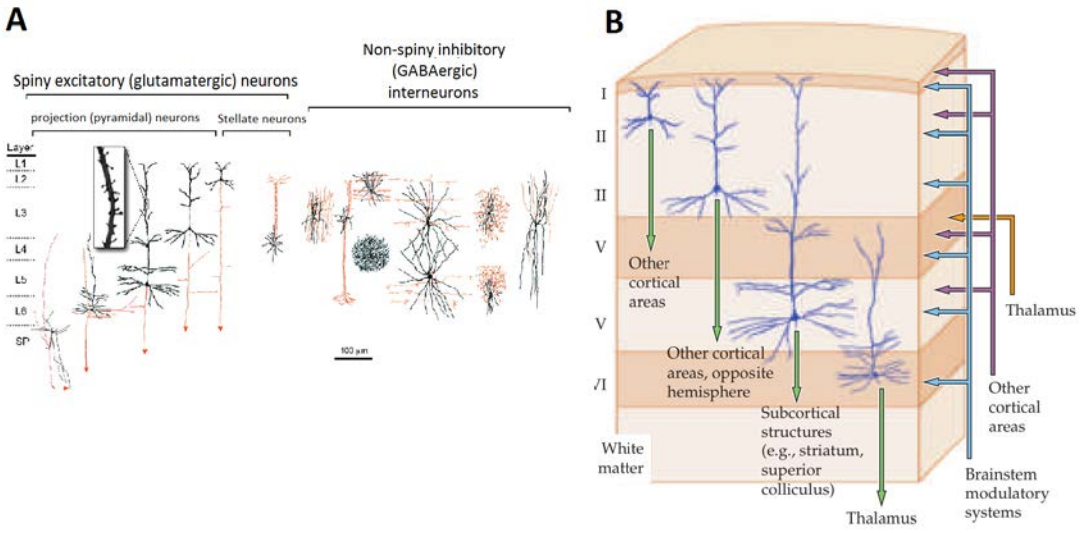

Figure 3: Cellular diversity and laminar organization organization of the neocortex. **(A)** Major neuronal cell types of the adult cerebral cortex. Cortical neurons (shown here for primates) are categorized into two major classes: spiny excitatory (glutamatergic) neurons and non-spiny inhibitory (GABAergic) interneurons. Reproduced from Kwan et al. (2012). **(B)** Canonical neocortical circuitry. Green arrows indicate outputs to the major targets of each of the neocortical layers in humans; orange arrow indicates thalamic input (primarily to layer IV); purple arrows indicate input from other cortical areas; and blue arrows indicate input from the brainstem modulatory systems to each layer. Reproduced from Purves D, Augustine GJ, Fitzpatrick D, et al. (2001).

glial cells. Neuronal cells process information and transmit signals thanks to their electrophysiological and chemical properties. Neurons are highly interconnected via synapses forming recurrent and feedforward networks whose activation corresponds to cognitive processes. Glial cells (from Greek *glue*) are traditionally thought to: 1) surround neurons, hold them in place and insulate one neuron from another 2) supply nutrients and dioxygen to neuronal cells and 3) destroy pathogens and remove dead neurons. Though recent evidences suggest that glial processes might have a more direct role in neocortical function, this potential aspect of neocortical processing will be largely ignored within this thesis, we hypothesize that glial cells only participate to neocortical function by maintaining the *homeostasis* in neuronal assemblies: insuring the stability of neuronal properties and synaptic transmission. We will therefore focus on the neuronal aspect of neocortical processes.

A prominent feature of the neocortex is its laminar organization. It can be divided into six layers according to different types of neuronal cells (see Figure 3A) and different connectivity properties (afferent, recurrent and projecting connections). The functional role of this laminar organization is still largely unresolved, but the layer specific connectivity scheme (see Figure 3B) suggests that supra-granular networks underlie cross-modality communication while infra-granular networks might perform computations related to local cortical features.

In **Work 1** and **Work 2**, we investigate how the biophysical and morphological properties of layer V pyramidal neurons in mice visual cortex shape their functional properties in a regime mimicking active neocortical processing. In **Work 4**, we model a large-scale excitatory-inhibitory Layer II-III network ($\sim$100mm^2) including the horizontal fiber network that interconnects areas responding to different sensory features.

Sensory processing as a model of neocortical computation

Cortical computation can be defined as the operations performed between cortical representations (in a general sense, including brain state, sensory stimuli, etc...). Sensory systems are of particular interest as cortical representations encode information coming from the physical world. The experimentalist can therefore manipulate those physical quantity in a controlled

fashion to establish relationships between sensory stimuli and its neural representation. In particular, in primary sensory areas, the relation with the physical world keeps a relatively simple form. For example, the somatotopic map in the primary somatosensory cortex, see Figure 2C, reflects the fact that neurons respond to a stimulus at a given location on the skin, while higher order area along the somatosensory pathway would be sensitive to more abstract features in the tactile stimulus.

Primary sensory areas therefore provide a good experimental system to investigate the principles of cortical computation. This strategy naturally implies the use of an appropriate recording technique to image the neural representation, such as intracellular recording, extracellular recordings, optical imaging, etc... In **Work 3**, we investigate how the neural representation in the primary auditory cortex of a simple auditory stimulus (a click of white noise) is affected by the level of ongoing activity using intracellular recordings *in vivo*. In **Work 4**, we investigate how two distinct neural representations (encoding a single flash in two distinct visual locations) interacts by using optical imaging *in vivo*.

Neocortical processing and population dynamics

Neuronal assemblies represent and process information through the emission of stereotyped electrophysiological events: the actions potentials. The information encoded by an assembly within a time window is thus contained in its *raster activity*: the set of spike trains across neurons. What are the quantities within this set that are relevant for a *downstream* readout ? This is still an open and very controversial question. As an example, an influential theory (Shadlen and Newsome, 1994), *rate-based* coding states that the information is carried by the temporal variation of the population firing rate (defined over a short time bin). On the other-hand, the more general *spike-based* theory states that the temporal patterns of individual spikes carry the information so that the population rate is a very limited description of the neuronal assembly. I will not review here the arguments in favor of one view or the other, insightful reviews can be found in the classical paper from Shadlen and Newsome (1994) (in favor of the *rate-based* theory) or in Brette (2015) (in favor of the *spike-based* theory). The purpose of this thesis is not

to take position in favor of one or the other theory (also given that a definitive answer is unlikely to hold in the cortex in general, e.g. olfactory system vs. visual system). Nonetheless, we briefly argue here that, whatever the *neural code*, an accurate description of population dynamics in neocortical networks is a necessary prerequisite to the understanding of cortical computation. In a *rate coding* scheme, population dynamics constitute the *neural code*, the increase of the firing of a given cortical sub-population encodes a given sensory feature, the relevance of understanding population dynamics is thus straightforward. In a *temporal coding* scheme, the population activity is not sufficient, it is important to have a very precise description in the spike timings and one should know exactly which neurons are spiking. Nonetheless, in a *temporal coding* scheme (or in a *stochastic temporal coding* scheme, see Rossant et al. (2011)), the robustness of the code relies on the ability of neurons to behave as coincidence detectors (Softky and Koch, 1993) and this feature has been shown to critically rely on the properties of the background activity (Rudolph and Destexhe, 2003; Rossant et al., 2011), i.e. on effects mediated by population dynamics. Finally, several canonical effects are mediated by population dynamics: e.g. the response-dependency on ongoing activity levels (Arieli et al., 1996; Deweese and Zador, 2004; Scholvinck et al., 2015; Lin et al., 2015), or gain modulation of sensory responses putatively mediated by top-down modulation of cortical activity (Zagha et al., 2013; Harris, 2013).

We now give the precise definition of population dynamics adopted in this thesis, as well as its relevance and limitations for the description of neocortical processes. We define population dynamics as the temporal variations of the instantaneous firing rate at the population level. This definition is already problematic as an instantaneous rate can not be defined, a firing rate has to be sampled over a given time window. The question of the time-window thus becomes critical, especially in the *rate* vs. *temporal* coding debate. We take a rather low value: dt $\sim$ 10ms, meaning that we focus on slow dynamics, up to the $\sim$ 100Hz frequency range. For a population of size N, the population firing rate is thus given by $\nu(t) = S(t)/N/dt$, where $S(t)$ is the number of spikes between t and $t+dt$, we give an example of how such a quantity can be determined using extracellular recordings in Figure 4 (the 1ms bins followed by the 12ms Gaussian smoothing approximates our $\sim$ 10ms timescale).

Because we define this firing rate as a firing probability (within each time bin), we assume that neurons fire in an irregular manner where this probabilistic view is relevant (see next section). This also puts constraints on the

range of firing rate values described by population dynamics, values should not exceed 100Hz (probability of 1 in 10ms time bin). All cortical processes that corresponds to instantaneous firing rate larger than 100Hz do not fit in our framework of population dynamics. The precise spiking response seen in various models of sensory processing, e.g. the response to single tones in auditory cortex (Wehr and Zador, 2003) or the response to natural stimuli in primary visual cortex (Baudot et al., 2013) typically represent such processes. For those precise responses, our modeling framework is inefficient and only the precise modeling of the precisely-timed afferent stimulation could capture this type of responses. This thesis thus focuses on describing *slow*

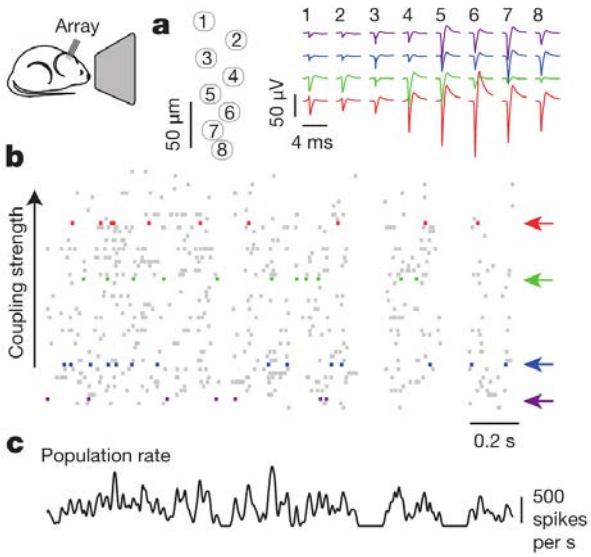

Figure 4: Spontaneous activity in awake mice visual cortex exhibits strong fluctuations of population activity. **(a)** Schematic of a single shank of silicon electrode array, and spike waveforms of four example wide-spiking neighbor neurons measured with the array in deep layers of V1 of an awake mouse. **(b)** Population raster of spontaneous activity in 66 neurons recorded from the whole array. **(c)** Population rate measured by summing all the spikes detected on the entire array (both well-isolated units and multi-unit activity) with 1ms resolution and smoothed with a Gaussian of half-width 12ms (N.B. the smoothing can be seen as a way to reduce the narrow sampling of the population). Reproduced from Okun et al. (2015).

population dynamics and will thus have an explanatory power for all physiological processes mediated by this slow dynamics (stimuli of low frequency content, effects of ongoing activity, top-down modulations, lateral interactions, etc. . .).

In **Work 3**, we investigate how the post-synaptic response to low amplitude stimuli is amplified by a strong level of ongoing recurrent dynamics. In **Work 4**, we show that such a description in terms of population dynamics accurately reproduce the response to brief flashed stimuli in the primary visual cortex of fixating monkey recorded by optical imaging.

Theoretical models of neocortical dynamics

On the theoretical side, much effort has been devoted to design theoretical models reproducing the characteristics of neocortical activity *in vivo*. In particular, the regime characterizing the *awake* state has attracted much attention. In this regime, spontaneous activity is characterized by irregular and weakly synchronized spiking (Softky and Koch, 1993; Shadlen and Newsome, 1994; Ecker et al., 2010; Renart et al., 2010) as well as strong membrane potential fluctuations at the neuronal level (reviewed in Destexhe et al. (2003)).

Such a stochastic-like regime has been successfully achieved in *balanced recurrent networks* (Tsodyks and Sejnowski, 1995; van Vreeswijk and Sompolinsky, 1996; Amit and Brunel, 1997). The mechanism underlying this regime within this architecture can be easily understood. If single neurons have irregular spiking, they will produce fluctuating excitatory and inhibitory input to a single neuron via recurrent connections. Then, provided the network is *balanced*, so that excitation and inhibition cancel each other statistically, neurons will spike irregularly because spiking will result from the fluctuations (a near random walk toward the threshold). We conclude that, if the input of the neuron is irregular, it will produce irregular spiking. This situation therefore enables the existence of an asynchronous state where irregular spiking sustains itself in a recurrent network. The core idea has been initially formulated in networks of binary neurons (van Vreeswijk and Sompolinsky, 1996), since then, theoretical work has increased the biological realism of this picture (Amit and Brunel, 1997; Brunel and Hakim, 1999; Brunel, 2000; Vogels and Abbott, 2005; El Boustani et al., 2007; Kumar et al., 2008).

The balanced network will be used as a theoretical basis all along the thesis, either to reproduce synaptic input (**Work 1** and **Work 2**) or to build networks (**Work 3** and **Work 4**). In **Work 4**, we adapt the classical randomly sparsely connected balanced network model by including an asymmetry in the electrophysiological properties of excitatory and inhibitory cells.

Analytical descriptions of collective dynamics

Thanks to their relative simplicity, those reduced theoretical model of cortical assemblies have a notable advantage: they allow an analytical description of the emergent collective dynamics (via several well-chosen approximations, see Renart et al. (2004) for a review). Indeed, the reasoning of the previous section can be formalized mathematically to obtain equations describing the population dynamics. Those self-consistency approaches describing recurrent dynamics are called *mean-field* approaches (originally, the same kind of self-consistent approach allowed to derive the magnetization in spin glasses, i.e. the mean magnetic field). Similarly to the situation of spin-glasses, they predict the conditions of the regime's stability and they allow to calculate the mean firing rate of the network as a function of its parameters (van Vreeswijk and Sompolinsky, 1996; Amit and Brunel, 1997; Brunel, 2000; Latham et al., 2000; El Boustani and Destexhe, 2009). For example, *mean-field* analysis predicts the conditions leading to run-away activity (similar to epileptic discharge) (Amit and Brunel, 1997; Brunel, 2000) or the emergence of fast oscillations (Brunel and Hakim, 1999; Brunel, 2000; Brunel and Wang, 2003).

Interestingly, they also describe the network response to a given afferent input (van Vreeswijk and Sompolinsky, 1996; Amit and Brunel, 1997; Ledoux and Brunel, 2011) and therefore offer a very interesting possibility to describe neocortical computation.

This last point is the main motivation behind this thesis. **Work 1** and **Work 2** contributes to making those *mean-field* formalism more *biologically-realistic*. In **Work 4**, we also investigate the explanatory power of one of those form of analytical descriptions (a Markovian formalism combined with a semi-analytical approach, see El Boustani and Destexhe (2009)) in a network showing asymmetric electrophysiological properties between excitation and inhibition.

The transfer function of neocortical neurons

At the core of *mean-field* formalisms lies the cellular *transfer function*, i.e. the function that translates the presynaptic release frequencies into a spiking probability (the transfer function is defined within our *population dynamics* framework). Those *transfer functions* account for the cellular computation and, within the *mean-field* picture (that might fail at capturing network dynamics, see e.g. Ostojic (2014)), the network dynamics is solely the recurrent amplification of this cellular computation.

The *transfer function* is thus the key ingredient of network dynamics within this framework. This is also the important insight of the *mean-field* description: having highlighted the crucial features at the cellular level that controls population dynamics. The hypothesis behind this thesis is therefore that by accurately describing the neuronal transfer function, we will accurately predict emergent phenomena at the network level.

Characterizing the transfer functions of neocortical neurons is the focus of **Work 1** and **Work 2**. Neocortical cells are very complex units: they are characterized by a extended dendritic arborization while the spike initiation mechanism lies at the axon initial segment, close to the soma. To deal with this complexity, we formulated an approximation that arbitrarily separate the problem into two distinct problem to make it amenable to analysis. First, dendritic integration of irregular excitatory and inhibitory synaptic input will shape the properties of the membrane potential fluctuations at the soma. We performed this analysis in **Work 2** by using cable theory (Rall, 1962, 1977). Then, we investigate how those membrane potential fluctuations at the soma are translated into spikes. This is the focus of **Work 1**, we performed this analysis *in vitro* on layer V neocortical cells of young mice visual cortex[1].

[1]Why performing experimental cellular biophysics 60 years after the ground-breaking study of Hodgkin and Huxley (1952) ? Since then, the dynamics of ionic-channels have been extensively studied and characterized in isolated preparations. This analysis could thus be done numerically. Nonetheless, cellular biophysics in mammalian neocortical neurons does not easily reduce to ionic-channels dynamics, either because of compartmentalization specificities (McCormick et al., 2007; Kole and Stuart, 2008; Brette, 2013) or exotic channel-gating properties (Naundorf et al., 2006, 2007). As those mammalian-specific properties (for which there is no theoretical consensus) might have a critical impact on the transfer function (Ilin et al., 2013), it requires an experimental determination.

Part II

Research articles

Work 1: Heterogeneous firing response of layer V mice neocortical neurons in the fluctuation-driven regime

Reference: Zerlaut Y, Teleńczuk B, Deleuze C, Bal T , Ouanounou G & Destexhe A. Heterogeneous firing response of layer V mice neocortical neurons in the fluctuation-driven regime, *Journal of Physiology*, in press

French summary

Caractériser les propriétés entrée-sortie des neurones néocorticaux est d'une importance cruciale pour comprendre les propriétés émergentes au niveau du réseau. Dans le régime de décharge irrégulière qui caractérise l'état éveillé, determiner ces propriétés représente un problème théorique et expérimental complexe.

Dans ce travail, nous étudions *in vitro* le taux de décharge de neurones individuels de la couche V du cortex visuel de jeunes souris en réponse à des fluctuations du potentiel membranaire. Nous conduisons cette étude grâce a des enregistrements électrophysiologiques intracellulaires en combinant le *dynamics-clamp* et la technique du patch perforé.

Nous avons observé que les neurones ne diffèrent pas uniquement par leur excitabilité, mais aussi par leurs sensibilités aux propriétés des fluctuations. Nous avons essayé de reproduire ces caractéristiques sur des modèles neuronaux théoriques établis. Le modèle prédit que des niveaux hétérogènes de propriétés biophysiques telles que l'inactivation sodique, la force du courant sodique et le courant d'adaptation reproduisent nos mesures expérimentales.

Parce que la réponse en taux de décharge détermine la dynamique de population dans le régime asynchrone, nos résultats montrent que les assemblées neuronales sont fonctionnellement très inhomogènes dans le cortex de la souris jeune, ce qui devrait avoir des conséquences importantes dans la phase initiale du traitement visuelle.

Heterogeneous firing rate response of mice layer V pyramidal neurons in the *fluctuation-driven* regime

Y. Zerlaut[1,2], B. Telenczuk[1,2], C. Deleuze[1], T. Bal[1], G. Ouanounou[1]* & A. Destexhe[1,2]*

April 5th 2016. Journal of Physiology, *in press*

I Key points summary

- **We recreate *in vitro* the fluctuation-driven regime observed at the soma during asynchronous network activity *in vivo* and we study the firing rate response as a function of the properties of the membrane potential fluctuations.**
- **We provide a simple analytical template that captures the firing response of both pyramidal neurons and various theoretical models.**
- **We found a strong heterogeneity in the firing rate response of layer V pyramidal neurons. In particular, individual neurons do not only differ by their mean excitability level, but also by their sensitivity to fluctuations.**
- **Theoretical modeling suggest that this observed heterogeneity might arise from various expression levels of the following biophysical properties: sodium inactivation, density of sodium channels and spike frequency adaptation.**

II Abstract

Characterizing the input-output properties of neocortical neurons is of crucial importance to understand the properties emerging at the network level. In the regime of low-rate irregular firing (such as in the *awake* state) determining those properties for neocortical cells remains, however, both experimentally and theoretically challenging. Here, we studied this problem using a combination of theoretical modeling and *in vitro* experiments. We first identified, theoretically, three somatic variables that describe the dynamical state at the soma in this *fluctuation-driven* regime: the mean, standard deviation and time constant of the membrane potential fluctuations. Next, we characterized the firing rate response of individual layer V pyramidal cells in this three-dimensional space by means of perforated patch recordings and *dynamic-clamp* in the visual cortex of juvenile mice *in vitro*. We found that, not only, individual neurons strongly differ in terms of their excitability, but also, and unexpectedly, in their sensitivities to fluctuations. Finally, using theoretical modeling, we attempted to reproduce these results. The model predicts that heterogeneous levels of biophysical properties such as sodium inactivation, sharpness of sodium activation and spike frequency adaptation account for the observed diversity of firing rate responses. Because the firing rate response will determine population rate dynamics during asynchronous neocortical activity, our results show that cortical populations are functionally strongly inhomogeneous in young mice visual cortex, which should have important consequences on the strategies of cortical computation at early stages of sensory processing.

III Introduction

The neocortex of awake animals displays an activated state in which cortical activity manifests highly complex, seemingly noisy behavior. At the level of single neurons the activity is characterized by strong subthreshold fluctuations and irregular firing at low rate: this constitutes the fluctuation-driven regime, which is believed to be central to cortical computations (Destexhe and Contreras, 2006). Sensory processing of natural stimuli also evoke sparse response at low population rates, see for example Crochet et al. (2011) in mice somato-sensory cortex or Baudot et al. (2013) in cat visual cortex. Understanding the dynamical and computational properties of this regime at the cellular and network level is a key challenge in systems neuroscience. Because the reliable computation performed during this regime happens on top of strong effects mediated by slow population dynamics (such as variable levels of ongoing activity at time scales T>30-50ms), that in turn, determine the integrative and computational properties at the cellular level (Destexhe and Paré, 1999; Chance et al., 2002; Rudolph and Destexhe, 2003; Rossant et al., 2011; Altwegg-Boussac et al., 2014) , an accurate quantitative description of population dynamics (and its correlate in terms of membrane potential fluctuations) appears to be a necessary prerequisite to the comprehension of this regime.

In the present paper, we investigate the firing rate response as a response to membrane potential fluctuations: a form of neuronal transfer functions that lie at the core of theoretical models of population dynamics , see e.g. Amit and Brunel (1997).

[1] Unité de Neurosciences, Information et Complexité, Centre National de la Recherche Scientifique, FRE 3693, Gif sur Yvette, France

[2] European Institute for Theoretical Neuroscience, 74 Rue du Faubourg Saint-Antoine, 75012 Paris

correspondance : destexhe@unic.cnrs-gif.fr

The sparse firing regime nonetheless constitute a difficulty for experimentalists as responses are of low amplitude and render experimental characterization challenging. In particular, characterizing the firing rate response of single neurons at low rates requires long recording times and stable properties. Here, we propose a characterization of the low rate response of single neurons that was made possible by the combination of the stability offered by the perforated patch technique technique and a simple theoretically-driven fitting procedure for the spiking response.

We identified three somatic variables to investigate single neuron response: the mean, standard deviation and time constant of the membrane potential fluctuations at the soma. In comparison with previous work, reviewed in La Camera et al. (2008), our approach allows 1) to investigate the response to fast membrane potential fluctuations characterizing the high conductance state of cortical networks (Destexhe et al., 2003) and 2) to perform a cell-by-cell comparison because of its formulation in terms of membrane potential variables. This characterization focuses on how these fluctuations are translated into output spikes on top of subthreshold integration effects (Kuhn et al., 2004) and therefore highlights the contribution of active membrane properties . In addition, we also investigated the putative biophysical origin of the measured responses in established theoretical models of single neurons.

IV Material and Methods

This methods section is organized as follows: 1) we present the intracellular recording method used in this study: the perforated-patch technique, 2) we show how analytical calculus combined with the dynamic-clamp technique allowed us to control the membrane potential fluctuations on a cell-by-cell basis, 3) we explain the rationale behind our theoretical estimate of the firing rate response that led to the semi-analytical template used for fitting experimental responses.

IV.1 Experimental preparation

Experiments were performed at the Unité de Neurosciences, Information et Complexité. Experimental procedures with animals were performed following the instructions of the European Council Directive 2010 86/609/EEC and its French transposition (Décret 2013/118). Swiss wild-type mice of either sex, 8–13 days old, were anesthetized with inhaled isoflurane and decapitated, their brain was rapidly removed and immersed in cold "cutting" solution ($\sim 4°C$) containing the following (in mM): 110 Choline Chloride, 2.5 KCl, 1.25 NaH2PO4, 26 NaHCO3, 8 MgCl2, 1 CaCl2, 10 glucose, pH equilibrated to 7.3 with O2/CO2 (95%/5%). Coronal slices (300 μm thick) were prepared with a vibratome (Leica VT1200 S, Leica Microsystems) and stored at room temperature in oxygenated aCSF containing the following (in mM): 126 NaCl, 2.5 KCl, 1.5 NaH2PO4, 26 NaHCO3, 2 MgCl2, 2 CaCl2 and 10 glucose, pH 7.4. The slices were then transferred to the recording chamber (perfused with the same solution) where the temperature was maintained at 34°C. Slices containing primary visual cortex were taken as the first four slices containing brain cortex starting from the most caudal one. The mice visual cortex was chosen as this experimental model is the subject of intense investigation (see e.g. Okun et al. (2015)) and would therefore provide a very interesting system to test the accuracy of the theoretical models of cortical dynamics constrained by the following results.

IV.2 Electrophysiological recordings

We performed intracellular recordings of visually identified pyramidal cells located in the layer V of mice cortex using the perforated patch technique.

Patch electrodes (tip resistance: 1.5–2.5 $M\Omega$) were pulled on a Sutter P-1000 apparatus (Sutter Instruments) and filled in a two step procedure. The pipettes were pre-filled with a solution containing the following (in mM): 130 K-Gluconate, KCl 7, NaCl 1, MgCl2 4, HEPES 10, pH adjusted to 7.3 with KOH (osmolarity 260 mOsm). The pipette was then backfilled with the same solution to which was added Amphotericin-B (Sigma Aldrich) previously dissolved in DMSO, the final concentration of Amphotericin-B was 60 μM. The reason for this two step procedure is to allow a current flow out of the pipette (to preserve the tip from dirt) without pouring the perforant onto the target cell during the pipette approach. The perforation could therefore happen only after diffusion of Amphotericin-B through the "clean" solution, this usually took 5-10 minutes after the pipette filling, thus allowing the cell-attached configuration to form in absence of the perforant molecule.

We recorded from n=30 cells. After perforation, the access resistance R_S was 14.7MΩ ± 6.9. This value was plugged in into the amplifier-build bridge compensation system during the current-clamp recordings. At -75 mV, the recordings exhibited a leak current of -31.9 pA ± 26.8 (minimum observed resting potential: -76 mV), this current value was then set for each neuron as the holding current during the recording. Recorded pyramidal cells had an input resistance R_m of 355.9 MΩ ±184.1 and a membrane time constant at rest of : 31.4ms ±12.0. Recordings lasted 36.7 min ±20.9. In the absence of current injection, cells presented a quiescent activity.

The liquid junction potential was measured to be 6 mV and membrane potential recordings were corrected accordingly. Note that there might be anyway an unknown constant shift in the voltage value because the Amphotericin-B pores are selective channels (so that a non-zero reversal potential could appear if the cellular medium and our pipette medium are different). The absolute values of the membrane potential presented here should therefore be interpreted carefully (but this would only affect the $\langle V_{thre}^{eff} \rangle_{\mathcal{D}}$ quantity reported in this study).

IV.3 Measuring firing rate

We measured the firing rate simply by counting spikes over a fixed time window. Spikes were detected as a upward crossings of -20mV. The first 100ms after fluctuating current onset were removed to avoid transient effects associated to the membrane potential rise. The duration of the stimulation was usually 5s, therefore the minimum (non zero) rate was 0.2 Hz. Also an online analysis was counting spikes and the stimulation was stopped when 20 spikes were reached (see in Figure 4E, the middle episode is shorter than the two other ones), this to avoid spending too much recording time in the high firing rate range.

IV.4 Dynamic-clamp

Our dynamic-clamp system consists of an Intel Quad-Core computer equipped with an acquisition card (NI PCI-6251 ADC/DAC,Mseries, National Instruments) connected to the amplifier operating in current-clamp mode. The dynamic-clamp software is based on a custom ADC/DAC (analog-to-digital/digital-to-analog) program used for data acquisition and analysis [Elphy2, developed at Unité de Neurosciences, Information et Complexité (UNIC) by Gérard Sadoc] and interfaced with the `NEURON` simulator version 6.0 (Hines and Carnevale, 1997). `NEURON` was modified and recompiled to run under the INtime (TenAsys), a Real Time Operating System running alongside Microsoft Windows. The recordings were performed using a Multiclamp 700B amplifier (Molecular Devices). Stimulation protocols were run in real time with the acquisition card at 10 kHz. Acquisition and filter frequencies were set at 10 and 4 kHz, respectively. An unfiltered copy of the membrane potential signal was feeding the dynamic clamp system.

IV.5 Single compartment approximation

Both for the experimentally recorded neurons and for the theoretical models, we will use the single compartment membrane equation. The passive properties of a neuron are therefore described by a leak conductance g_L, a capacitance C_m and a resting potential E_L. With an additional current $I(V,t)$, the membrane potential thus follows:

$$C_m \frac{dV}{dt} = I(V,t) + g_L\,(E_L - V) \tag{1}$$

Passive properties were fitted from the response to a hyperpolarizing current step for the recorded neocortical neurons in the subthreshold domain (around -75 ±5mV).

Though this approximation was found to be satisfactory (Figure 4C), monitoring possible deviations is important in this study as the approximation is used to shape the fluctuations of the membrane potential. We therefore performed a cell-by-cell quantification of the accuracy of the approximation as follows. We take the protocols that were used to determine the membrane properties: prior to each protocol, we recorded and averaged the response to 10 current pulses of $\sim$ 500ms and of $\Delta I \sim$ 15pA amplitude, not the (noisy) continuous monitoring presented in Figure 4. We average over trials the membrane potential response and fit an exponential curve to this mean response $V_{sc}^{fit}(t)$, we get a membrane time τ_m^0 and a membrane resistance R_m^0. For all cells, we calculated the integral of the residual trace with respect to the RC circuit approximation. This allowed us to investigate whether the quality of the approximation had an impact on the excitability and sensitivities presented in the Results, we found no significant correlations between those quantities and the quality of the recordings ($c<0.2$ and $p>0.2$ for all characteristics, Pearson correlations), thus suggesting that the results of our study were not impacted by deviations from the single compartment approximation.

IV.6 Global autocorrelation time

We present here a theoretical estimate for the speed of the membrane potential fluctuations.

In the case of a fluctuating synaptic input with temporal dynamics (e.g. resulting from a shotnoise of *exponential* synapses considered in this study, unlike the *delta* synapses considered in other studies, see Amit and Brunel (1997) for an example), the autocorrelation function is not an exponential function. Consequently, the resulting membrane fluctuations can not be characterised by a single time constant τ_V (see the inset in Figure 1). Nevertheless, the time constant taken from an exponential approximation of the normalized autocorrelation function corresponds to a first order description of the autocorrelation and will be the main contributor to the temporal dynamics of the fluctuations.

As a theoretical prediction for this *global autocorrelation* time, we take the half integral of the normalized autocorrelation correlation function:

$$\tau_V = \frac{1}{2}\int_{\mathbb{R}} d\tau \frac{A(\tau)}{A(0)} \tag{2}$$

where $A(\tau)$ is the autocorrelation function of the V_m fluctuations (see an example of $A(\tau)/A(0)$ in Figure 1). From shotnoise theory (Daley and Vere-Jones, 2007), we will obtain the power spectral density of the V_m fluctuations $P_V(f)$, so we re-express the global autocorrelation time as:

$$\tau_V = \frac{1}{2}\left(\frac{\int_{\mathbb{R}} P_V(f)\,df}{P_V(0)}\right)^{-1} \tag{3}$$

In this study, this formula reduces to a very simple form (see next section). Note that the relations presented in this paper rely on the following convention for the Fourier transform: $\hat{F}(f) = \int_{\mathbb{R}} F(t)\,e^{-2i\pi ft}\,dt$.

IV.7 A stimulation to investigate the dependency on the variables of somatic fluctuations

We aim at reproducing the dynamical state at the soma in the fluctuation-driven regime by reproducing membrane potential fluctuations with the control of the mean μ_V, the standard deviation σ_V of the subthreshold fluctuations as well as a global autocorrelation time τ_V.

Our "input space" is already a response of the neuron, thus we need a stimulation that would reliably produce this response. There exists multiple types of input that would lead to a given set of the $(\mu_V, \sigma_V, \tau_V)$ variables. In the present study, to best characterize the dependency on those precise variables, we wanted a stimulation that would minimize the higher order terms appearing for realistic synaptic inputs, e.g. when injecting excitatory and inhibitory Ornstein-Uhlenbeck conductances (Destexhe et al., 2001; Fernandez et al., 2011). We chose the following stimulation.

The mean membrane potential is achieved through a constant current input:

$$I_{\mu_V} = g_L\,(\mu_V - E_L) \tag{4}$$

Varying the speed of the fluctuations τ_V is achieved by changing the total input conductance at soma μ_G (an increasing conductance reduces the effective membrane time constant of the membrane, events are integrated faster and this renders fluctuations faster). The total conductance μ_G is changed by introducing a current $I_{\mu\,G}$ of static conductance $g_S = \mu_G - g_L$ and of reversal potential μ_V:

$$I_{\mu_G}(V) = g_S\,\big(\mu_V - V\big) \tag{5}$$

We introduce here the effective membrane time constant $\tau_m^{eff} = C_m/(g_S + g_L)$.

An additional noisy current of zero mean creates the fluctuations around μ_V to control the standard deviation σ_V. This current is generated from two independent Poisson processes convolved with an exponential kernel: one excitatory, one inhibitory. They have the same presynaptic rate ν_{in}, the same time constant for the exponential decay τ_S and opposite current increments Q_I and $-Q_I$. This corresponds to the current $I_{fluct}(t)$:

$$\tau_S \frac{dI_{fluct}}{dt} = -I_{fluct} + Q_I\Big(\sum_k \delta(t_e^k - t) - \sum_k \delta(t_i^k - t)\Big) \quad (6)$$

Where $\{t_e^k\}_{k\in\mathbb{N}}$ and $\{t_i^k\}_{k\in\mathbb{N}}$ are two sets of uncorrelated presynaptic events generated by the frequency ν_{in}.

A single excitatory or inhibitory post-synaptic potential event arriving at $t = 0$ will have the following time course:

$$PSP(t) = \pm\frac{Q_I\,\tau_S\,(e^{-\frac{t}{\tau_S}} - e^{-\frac{t}{\tau_m^{eff}}})}{g_L\,(\tau_m^{eff} - \tau_S)}\mathcal{H}(t) \quad (7)$$

where $\mathcal{H}$ is the Heaviside function.

From shotnoise theory (Daley and Vere-Jones, 2007) (see also El Boustani et al. (2009) for an application similar to ours), we can obtain the power spectral density of the V_m fluctuations $P_V(f)$ as a response to the stimulation Equation 6:

$$\begin{aligned} P_V(f) &= \sum_{syn} \nu_{syn}\,\|P\hat{S}P(f)\|^2 \\ &= 2\nu_{in}\,\frac{Q_I^2\,\tau_S^2/\mu_G^2}{\big(1+4\pi^2 f^2\tau_S^2\big)\big(1+4\pi^2 f^2(\tau_m^{eff})^2\big)} \end{aligned} \quad (8)$$

The variance of the membrane potential fluctuations is the integral of the power density spectrum :

$$\big(\sigma_V\big)^2 = \int_{\mathbb{R}} P_V(f)\,df = \frac{\nu_{in}\cdot(Q_I\,\tau_S)^2}{(\mu_G)^2\,(\tau_S+\tau_m^{eff})} \quad (9)$$

And the global autocorrelation time takes the very simple form, see Equation 3 :

$$\tau_V = \frac{1}{2}\Big(\frac{\int_{\mathbb{R}} P_V(f)\,df}{P_V(0)}\Big)^{-1} = \tau_S + \tau_m \quad (10)$$

We rescale this relation with respect to the resting membrane time constant τ_m^0:

$$\tau_V^N = \frac{\tau_V}{\tau_m^0} = \frac{\tau_S}{\tau_m^0} + \frac{g_L}{\mu_G} \quad (11)$$

Because the mean synaptic conductance μ_G should scale with the size of the membrane (because of the constant surfacic density of synapses), as does g_L (because of the constant surfacic density of leak channels), when the presynaptic bombardment increases, it is the rescaled quantity μ_G/g_L that increases. Therefore we investigated a fixed domain of the τ_V/τ_m^0 quantity.

Finally, the time- and voltage-dependent current $I(V,t)$ inserted into the membrane Equation 1 or injected via the dynamic-clamp technique takes the form:

$$\begin{cases} I(V,t) = I_{\mu_V} + g_S\,(\mu_V - V) + I_{fluct}(t) \\ \tau_S \dfrac{dI_{fluct}}{dt} = -I_{fluct} + Q_I\Big(\displaystyle\sum_k \delta(t_e^k - t) - \sum_k \delta(t_i^k - t)\Big) \end{cases} \quad (12)$$

The three variables $(\mu_V, \sigma_V, \tau_V^N)$ are achieved through the five variables of the input $(I_{\mu_V}, g_S, \nu_{in}, \tau_S, Q_I)$. We have two additional degrees of freedom, so 1) to force the input to remain in the *fluctuation-driven* regime (many events of low amplitude) we arbitrarily set the presynaptic frequency to $\nu_{in} = 2kHz$ and 2) we fixed the current time constant to: τ_S/τ_m^0=15% (i.e. τ_S=4.5ms for τ_m^0=30ms).

Thus, when we want to study the firing rate response as a function of $(\mu_V, \sigma_V, \tau_V^N)$, with the membrane parameters (g_L, τ_m^0, E_L), we send an input of the form Equation 12, where (I_{μ_V}, g_S, τ_S, Q_I, ν_{in}) follow:

$$\begin{cases} \tau_S = 0.15\ \tau_m^0 \\ \nu_{in} = 2.10^3 \\ I_{\mu_V} = g_L\,(\mu_V - E_L) \\ g_S = g_L\,\Big((\tau_V^N - \dfrac{\tau_S}{\tau_m^0})^{-1} - 1\Big) \\ Q_I = \dfrac{(g_L+g_S)\,\sigma_V\sqrt{\tau_m^0}\sqrt{\tau_V^N}}{\tau_S\sqrt{\nu_{in}}} \end{cases} \quad (13)$$

IV.8 Monitoring the stability of the cellular properties

Because the stimulation depends on the membrane properties (see the previous section IV.7), it was crucial to insure the stability of those properties during the experiments. We therefore monitored the cellular properties in time in an analogous manner to Köndgen et al. (2008).

In between the episodes, we use the resting period to measure the resting membrane potential E_L and we inject a short current pulse to calculate the membrane resistance. Those quantity over time are then smoothened over a sliding window of 20 points to remove the error introduced by the evaluation over a rather short time window (Figure 4E).

The data kept in the dataset had to keep variations within $\pm$ 3 mV for E_L and below 10 % for R_m.

In addition, we quantified and monitored the stability of the firing rate response. Here, the fitted response was found to be very useful (see Results V.2). When we fit, we do not discriminate between the early and the late measurements, the fitted function $\mathcal{F}$ therefore provides a mean of the response across the measurement. Then we can detect variations around this mean behavior by computing the coefficient of variation of the response:

$$CV_\nu(\vec{x}, t_i) = \frac{\nu_{out}(\vec{x}, t_i) - \mathcal{F}(\vec{x})}{\sqrt{\mathcal{F}(\vec{x})/T_i}} \quad (14)$$

where $\vec{x}$ represents a combination of the input $(\mu_V, \sigma_V, \tau_V^N)$, t_i the time of the measurement and T_i the duration of the measurement. Because of the intrinsic irregularity of the spiking process, we expect strong fluctuations within this curve (see Figure 4D), but the smoothen version of this curve allow to detect changes on a long time scale. For example, a strong *run-down* would correspond to a strongly decreasing CV_ν curve. The criteria to insure stability was to remain close enough from a stationary Poisson process, i.e. the smoothen curve should not cross $\pm$ 1.

Given those criteria, we expect that the effect of the remaining variability in the properties would be canceled by the randomization of the scanned input points and the use of multiple seeds.

IV.9 Theoretical models of neurons

The general model considered in this study is the inactivating Adaptative Exponential and Fire model. It is constructed by combining the theoretical models proposed in Brette and Gerstner (2005) and Platkiewicz and Brette (2011).

$$\begin{cases} C_m \dfrac{dV}{dt} = g_L\,(E_L - V) + I_{syn}(V,t) + k_a e^{\frac{V-\theta}{k_a}} - I_w \\ \tau_w \dfrac{dI_w}{dt} = -I_w + \displaystyle\sum_{t_s\in\{t_{spike}\}} b\ \delta(t - t_s) \\ \tau_i \dfrac{d\theta}{dt} = V_{thre} - \theta + a_i\,(V - V_i)\,\mathcal{H}(V - V_i) \end{cases} \quad (15)$$

where $I_{syn}(V,t)$ is the current emulating synaptic activity that will create the fluctuations, I_w reproduces the I_m current (McCormick et al., 1985) and $\theta(t)$ is a variable threshold whose temporal dynamics and voltage dependence accounts for the fast decrease in sodium channel availability at depolarized levels (Hille, 2001). The spiking mechanism is the following: when $V(t)$ reaches $\theta(t)+5\,k_a$, this triggers a spike $t_s \in \{t_{spike}\}$, this increases the adaptation variable I_w by b, the membrane potential is then clamped at E_L for a duration τ_{refrac}=5ms. Following Platkiewicz and Brette (2011), the steady-state threshold is described by a piecewise linear function ($\mathcal{H}$ is the Heaviside function).

The temporal dynamics of sodium inactivation and spike frequency adaptation were fixed to τ_i=5ms and τ_w = 500ms respectively. Also the threshold of the inactivation curve was fixed relative to the sodium activation threshold as $V_i = V_{thre} - 8mV$.

The leak potential of theoretical models was set to E_L=-70mV. All other parameters are varied along the study (see figure legends).

Finally, because of the variability of membrane time constants in the experimental data (indeed, the data show variations not only in input resistance, also in τ_m^0), the comparison for the firing rate response between data and theoretical models requires a careful treatment. Because when the synaptic bombardment raises, the ratio of input conductance with respect to the leak conductance μ_G/g_L raises, we scanned a fixed range in terms of $\tau_V^N=\tau_V/\tau_m^0$ (see previous section IV.7). But this means that for a given range of $\tau_V^N=\tau_V/\tau_m^0$, there will be different range of τ_V when there is a change in membrane time constant τ_m^0, and consequently a different range of output frequency. The solution that we adopted for a relevant comparison between data and theoretical models is to simulate the models with different membrane time constants τ_m^0 reproducing the variability in experimental data. Only in Figure 2, a single model was numerically simulated with the parameters (g_L = 2.5 nS, C_m = 80pF to get τ_m^0=32ms as the average of the intracellular data). For all other figures (Figures 3, 6 and 7), where the sensitivities are presented, we simulated three models, all with the same leak conductance g_L = 2.5 nS, but with varying capacitance to reach $\tau_m^0 \in$ [20,32,44] ms to reproduce the standard deviation of the data (see previous section IV.2). The presented sensitivities were then the average of the sensitivities of the three models. Note that, even if the scaling of the firing response with the resting membrane time constant is clear in theoretical model ($\nu_{out} \propto 1/\tau_m^0$ for a given τ_V^N space), this effect was not significantly visible in the data (Pearson correlations between mean excitability and membrane time constants, p>0.1) presumably masked by the heterogeneity discussed in this paper.

IV.10 Starting from a simple approximation for the firing rate

The starting approximation for the firing rate given some fluctuation properties is similar to the one introduced in Amit and Brunel (1997). Because our situation is different (our input has a temporal dynamics and includes additional conductance), we justify here the refinement that led to the estimate used in our study.

If a neuron has membrane potential fluctuations described by a mean μ_V, a variance σ_V and a typical autocorrelation time τ_V, then we can divide a time axis of length T (with $T \gg \tau_V$) into N bins of length τ_V. Within each of this bin, we consider that a reorganization of the membrane potential values occurs, then the bins can be considered independently, and in each, we sample randomly from the Gaussian distribution defined by μ_V and σ_V. We remain in the low firing regime ($\nu_{out} \leq$ 30 Hz) , so that we can neglect the repolarization dynamics and saturation effects. Then, if a spike occurs when the membrane potential crosses a threshold V_{thre}^{eff}, the probability to have a spike within a bin is the probability to be above this threshold $Pr(V > V_{thre}^{eff})$. The number of spikes during the time $T = N\tau_V$ is $k = N \cdot Pr(V > V_{thre}^{eff})$. The definition of the stationary firing rate is $\nu_{out} = k/T$, so that we get:

$$\nu_{out} = \frac{Pr(V \geq V_{thre}^{eff})}{\tau_V} \tag{16}$$

i.e. in the case of a Gaussian distribution for the membrane potential:

$$\nu_{out} = \frac{1}{2\,\tau_V} \cdot Erfc\left(\frac{V_{thre}^{eff} - \mu_V}{\sqrt{2}\,\sigma_V}\right) \tag{17}$$

where the subthreshold variables μ_V, σ_V and τ_V can be calculated as a response to the synaptic input as detailed in the previous section IV.7.

IV.11 Fitting

To render the fitting the phenomenological threshold easier, we insured that the linear coefficients of Equation 19 take similar values by normalizing the $(\mu_V, \sigma_V, \tau_V^N)$ space. The normalization factors μ_V^0=-60mV, $\delta\mu_V^0$=10mV, σ_V^0=4mV, $\delta\sigma_V^0$ = 6mV, τ_V^{N0}=0.5, $\delta\tau_V^{N0}$= 1 arbitrarily delimits the *fluctuation-driven* regime (a mean value x^0 and an extent δx, $\forall x \in \{\mu_V, \sigma_V, \tau_V^N\}$). It is kept constant all along the study.

The fitting consisted first in a linear regression in the phenomenological threshold space of Equation 19, followed by a non-linear optimization of Equation 18 on the firing rate response. Both fitting were performed with the `leastsq` method in the `optimize` package of `SciPy`.

IV.12 Numerical simulations

All numerical simulations of single cell dynamics have been performed with custom code written in the numerical library of python : numpy and optimized with the numba library. For the neuronal model, each point (a mean output frequency and its standard deviation across trials) corresponds to numerical simulations running with a time step dt=0.01ms, for a duration of 10s and repeated 4 times with different seeds (one simulation duration: $\sim$ 2s of real time on a Dell Optiplex 9020 desktop computer).

V Results

The paper is organized as follows: we start by we defining the fluctuation-driven regime at the soma and designing a method to reproduce this somatic dynamical state under dynamic-clamp experiments. We also derive a flexible template for the firing rate response, whose accuracy is demonstrated on various theoretical models. Then, we investigate the firing rate response of layer V pyramidal cells in mice juvenile cortex and we analyze the individual features of single neuron responses. Finally, we explore the putative biophysical origin of the observed response in theoretical models of neocortical neurons.

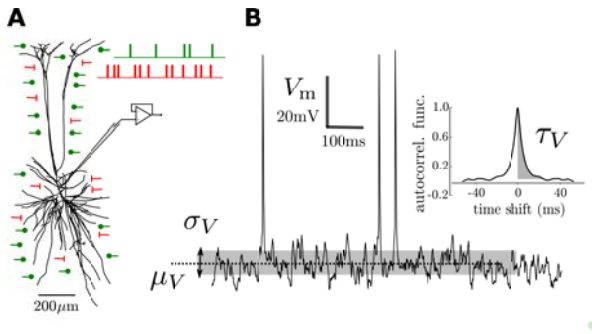

Figure 1: Investigating somatic computation in the fluctuation-driven regime (A) Schematic illustration on a layer V pyramidal cell in cat V1 (Contreras et al., 1997) together with theoretical distribution of inhibitiory (red) and excitatory (green) synaptic inputs. Synaptic and dendritic integration of pre-synaptic spike trains (two sample spike trains in upper right) produce membrane potential fluctuations at the soma as recorded intracellularly in current-clamp. **(B)** A sample trace of membrane potential integrating inputs from all inhibitory and excitatory synapses (black trace). We characterize those fluctuations by a mean μ_V (dashed horizontal line), a standard deviation σ_V of sub-threshold oscillations (gray background) and global autocorrelation time τ_V (determined from the normalized autocorrelation function in the inset, see Methods IV.6). The properties of those fluctuations determine the spiking probability of the neuron (three spikes visible in the membrane-potential trace).

V.1 A three-dimensional description of the dynamical state at the soma in the fictua tion-driven regime

Determining the cellular input-output functions is complex because input of neocortical neurons are mostly in dendrites and output spikes are generated in initial segments of an axon as reviewed in Stuart and Spruston (2015) and Debanne et al. (2011) input will therefore crucially shape their input-output relationship. Various parameters of presynaptic activity can arbitrarily control the properties of the membrane potential fluctuations at the soma. Those properties can be quantified by identifying three somatic variables that provide a reduced description of the dynamical state at the soma in the *fluctuation-driven* regime: the mean μ_V, the standard deviation σ_V of the membrane potential fluctuations and their typical autocorrelation time τ_V (see Methods IV.6). For example, the excitatory/inhibitory balance controls the mean depolarization at the soma μ_V, the mean synaptic bombardment impacts the standard deviation σ_V and the speed of the membrane potential fluctuations τ_V. Other effects such as synchrony in the presynaptic spike trains or ratio between distally and proximally targeting synaptic activity also affect the statistical properties of the fluctuations. The effects of synaptic input and its dendritic integration on somatic variables can be investigated theoretically using cable theory (Tuckwell et al., 2002) and will be the focus of a future communication.

Because the spike initiation site lies electrotonically close to the soma (Debanne et al., 2011), we assume that those three purely somatic variables will define the firing rate uniquely. In this study we investigate the firing response in terms of those somatic variables (illustrated in Figure 1).

We therefore designed a stimulation protocol to reproduce awake-like dynamical state at the soma and investigate the firing rate response in this three dimensional space. We evaluate the parameters of stochastic current and static conductance that would result in a particular configuration of the V_m fluctuations ($\mu_V, \sigma_V and \tau_V$) for passive membrane using a single-compartment approximation (Kuhn et al., 2004). This procedure allows to focus on how active currents convert fluctuations into spikes. Another advantage of this approach is that it naturally rescales the input with respect to the individual cellular properties (R_m, C_m and E_L) and therefore allows a cell-by-cell comparison. In addition, we investigated domains of the dimensionless variable $\tau_V^N = \tau_V \ / \ \tau_m^0$ instead of absolute values for membrane time constant τ_V to account for scaling of the synaptic inputs with membrane area (Equation 11 in Methods IV.7).

V.2 Template for the firing rate response of single neurons

A key challenge for the *in vitro* characterization of input-output relationship is to extract a reliable quantitative estimation of its functional form from a limited number of experimentally sampled points. One approach consists in fitting the response to the formula derived from a specific theoretical model, such as leaky integrate-and-fire neuron (Rauch et al., 2003; Lundstrom et al., 2009). This strategy has three drawbacks: 1) the complexity of the analytical formula requires a careful numerical determination and thus render fitting procedures non trivial, 2) it does not generalize easily to biophysically-realistic synaptic input (e.g. reproducing synaptic dynamics, see Brunel and Sergi (1998)) and 3) the low number of parameters of simple theoretical models (e.g. a single spike threshold for the leaky integrate-and-fire model) imposes that the membrane parameters (e.g. leak conductance and membrane capacitance) are free parameters to have enough degrees of freedom.

We propose here a different strategy: we introduce a flexible analytical template fully determined by membrane parameters, which are experimentally measured, and some free parameters, which can be fitted using a simple two-step minimization procedure.

The basis for the template rely on a simple estimate, analogous to Amit and Brunel (1997), for the firing rate response of the LIF model:

$$\nu_{out} = \frac{\Pr(V > V_{thre})}{\tau_V} = \frac{1}{2\,\tau_V} \cdot Erfc\left(\frac{V_{thre} - \mu_V}{\sqrt{2}\,\sigma_V}\right) \quad (18)$$

It is obtained heuristically by splitting the time axis in bins of length τ_V, the spiking probability is then the probability that the membrane potential is above the threshold V_{thre} (see Methods IV.10). In comparison with earlier approach (Amit and Brunel, 1997), we take here

the global autocorrelation time instead of the membrane time constant. We used this approximation as a baseline trend for the firing rate response and the properties of an individual cell will be described by deviations from this baseline behavior.

We found that those deviations could be accurately accounted for by replacing the hard threshold of the approximation V_{thre} by a linear phenomenological threshold:

$$V_{thre}^{eff}(\mu_V, \sigma_V, \tau_V^N) = P_0 + P_\mu \frac{\mu_V - \mu_V^0}{\delta\mu_V^0} + P_\sigma \frac{\sigma_V - \sigma_V^0}{\delta\sigma_V^0} + P_\tau \frac{\tau_V^N - \tau_V^{N0}}{\delta\tau_V^{N0}} \quad (19)$$

The quantities: $(\mu_V^0, \delta\mu_V, \sigma_V^0, \delta\sigma_V, \tau_V^{N0}, \delta\tau_V^N)$ are constant rescaling factors of the $(\mu_V, \sigma_V, \tau_V^N)$ space, see Methods IV.11.

A practical advantage of the template (Equation 18) is that, given some data $\nu_{out}(\mu_V, \sigma_V, \tau_V^N)$, we can invert the equation to get the phenomenological threshold as a function of the output firing rate:

$$V_{thre}^{eff}(\nu_{out}, \mu_V, \sigma_V, \tau_V^N) = \sqrt{2}\,\sigma_V\, Erfc^{-1}(2\,\tau_V^N\,\tau_m^0\,\nu_{out}) + \mu_V,\ \forall\, \nu_{out} > 0 \quad (20)$$

Where Erfc^{-1} is the inverse of the complementary error function.

We used this property to design the final fitting procedure: given some data $\nu_{out}(\mu_V, \sigma_V, \tau_V^N)$, we calculate the phenomenological threshold data using Equation 20 and fit coefficients $P_0, P_{\mu_V}, P_{\sigma_V}, P_{\tau_V}$ by linear regression. Then starting from those coefficients we perform a non-linear least-square fitting. Those two steps guarantee that the non-linear optimization starts from a good initial guess and ensures that the gradient-descent method converges close to the global minimum.

V.3 Firing rate response of theoretical models

We start by demonstrating the accuracy and flexibility of this phenomenological description on the firing rate response for various theoretical models (Figure 2).

The model considered in this study is the inactivating adaptative exponential and fire (Methods IV.9), which extends the model of Brette and Gerstner (2005) by adding an inactivation mechanism (Platkiewicz and Brette, 2011). Several widespread theoretical models are special cases of this model: the leaky integrate and fire (LIF), the exponential integrate and fire (EIF, Fourcaud et al. (2003)), the inactivating leaky integrate and fire (iLIF, Platkiewicz and Brette (2011)). We also define a LIF model with spike-frequency adaptation only (sfaLIF).

We show on Figure 2 that the template is able to describe the firing rate response of those various theoretical models. The impact on firing of those different biophysical properties of those models could all be accurately captured by differences in the linear phenomenological threshold (Figure 2D).

Table 1: Fitted coefficients of the linear phenomenological threshold for the theoretical models shown in Figure 2

model	P_0(mV)	P_μ(mV)	P_σ(mV)	P_τ(mV)
LIF	-49.74	1.71	0.31	-0.51
EIF	-46.9	1.69	1.47	-3.6
sfaLIF	-49.49	4.29	3.91	0.56
iLIF	-46.11	2.33	-1.06	3.62
iAdExp	-48.78	4.72	5.25	-1.35

We compared the four-parameter description to simpler and more complex models in which the phenomenological threshold is: constant (1 parameter), linear function (4 parameters) or second-order polynomial of μ_V, σ_V and τ_V^N (10 parameters). The goodness to fit of the single-parameter description was 84.6% ± 8.9; it increased to 99.0% ± 0.5 for the four-parameter description; and then to 99.6% ± 0.2 for the quadratic phenomenological threshold with 10 parameters. We conclude that the four-parameter fit is a good compromise between goodness-to-fit and number of parameters.

In absence of active mechanisms, membrane potential fluctuations are statistically identical in all theoretical models (by design, they are the same leaky RC circuit). The active mechanisms may nonetheless have an impact on the membrane potential fluctuations themselves and will, by this mean, impact the firing response. In our description, those effects are captured in the dependency of phenomenological threshold on input variables. For example, the stationary spike-frequency adaptation level induces a net hyperpolarizing current, which, in our description, leads to an increased phenomenological threshold (sfaLIF vs. LIF in Figure 2D).

V.4 Link between the biophysical properties and the characteristics of the firing rate response in theoretical models

To capture the particular features determining the properties of neuronal computation in the fluctuation-driven regime, we now turn to analyzing firing rate responses of the models. We define four simple quantities that provide a reduced description of the response of a single neuron: a mean excitability (mean phenomenological threshold) and average sensitivities to variations of mean μ_V, standard deviation σ_V and speed of the fluctuations τ_V^N. These quantities were average for all combination of the three input variables consistent with awake-like conditions (low-rate, 1 - 15 Hz, fluctuation-driven regime, $\mathcal{D}$ domain in Figure 3).

The LIF model provides a basic picture for the firing rate response (see LIF in Figure 2 and Figure 3A). Spiking in the LIF model increases with mean depolarization and the standard deviation (bottom panels in Figure 3A), while it decreases with the global autocorrelation time (top right panel in Figure 3A). More sophisticated biophysical mechanisms implemented in the considered theoretical models (exponential activation, adaptation, etc.) affect those base-

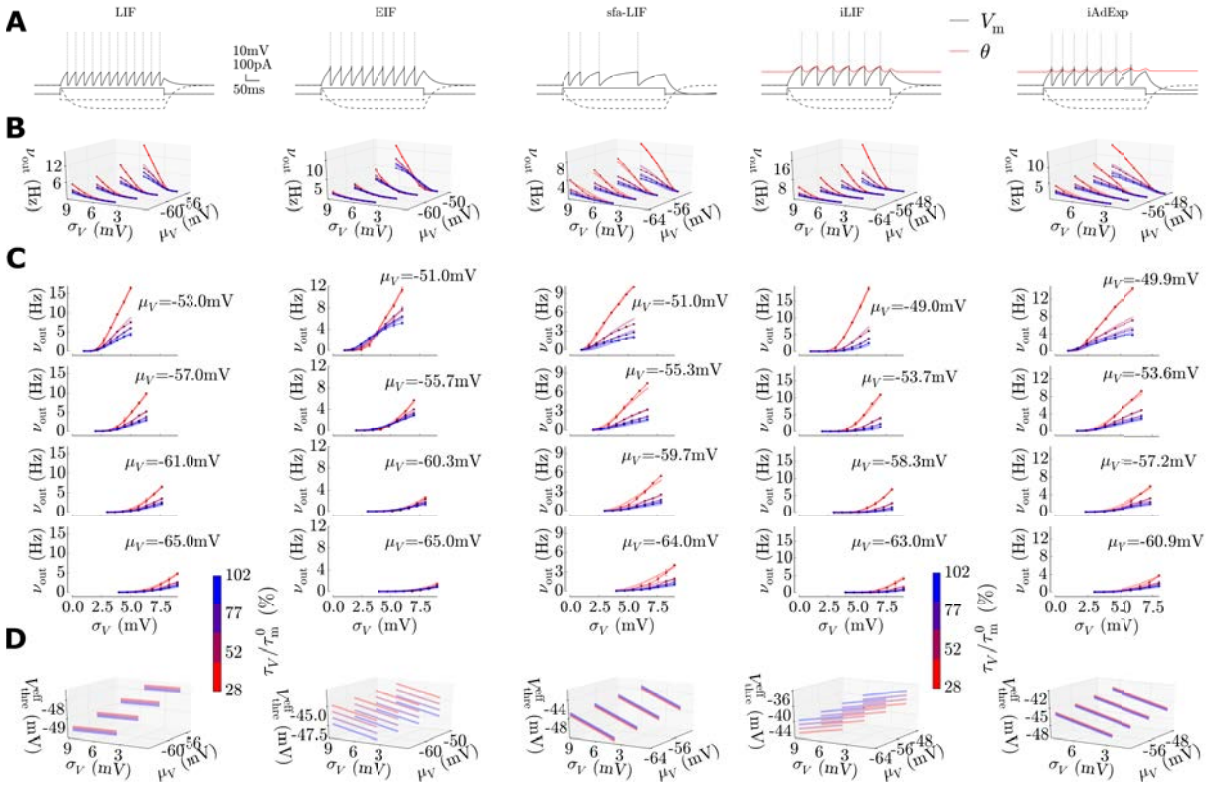

Figure 2: The analytical template (Equations 18 and 19) can capture the firing rate response of various theoretical models. Shown for the Leaky Integrate and Fire model (LIF) with V_{thre}=-47mV (kept for all following models), the EIF with $k_a = 2mV$, the sfaLIF with $b = 20pA$, the iLIF with $a_i = 0.6$ and the iAdExp model that combines all the previously mentioned mechanism with $k_a = 2mV, b = 6pA, a_i = 0.6$. **(A)** Response of the models to a current step. Plain line: response to depolarizing current step, dashed line: response to hyperpolarizing current step. For the iLIF and iAdExp models, we show in red the dynamics of the threshold θ(t). **(B)** Firing rate response in the (μ_V, σ_V) space. Color indexes variation of the global autocorrelation ratio τ_V/τ_m^0. **(C)** Projections along the standard deviation σ_V axis for different mean polarization levels μ_V. Data (points) and fitted analytical template (thick transparent lines). Note the shifts in the scanned μ_V domain to reach a comparable firing range despite a reduced excitability (see main text). **(D)** Phenomenological threshold V_{thre}^{eff} that leads to the fitted firing rate response, the coefficients of the linear functions can be found in Table 1.

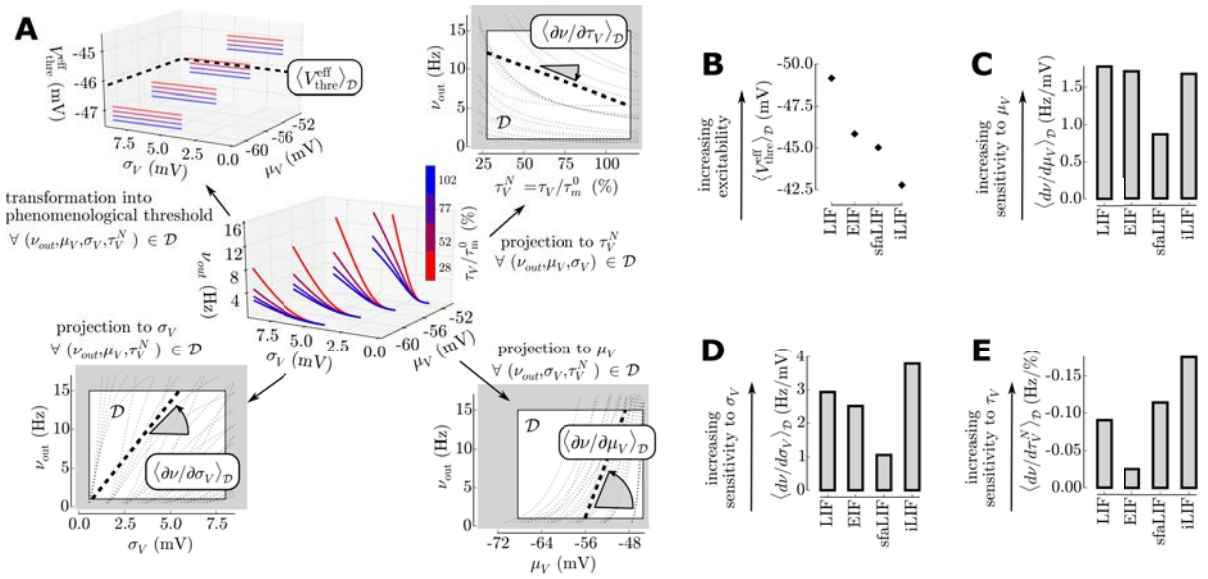

Figure 3: Extracting the mean properties of a single neuron response: excitability and sensitivities to the variables of the *fluctuation-driven* regime. **(A)** Illustration for the LIF model. From the fitting procedure we obtain an analytical description of the firing rate response (center plot). We focus the analysis on the domain $\mathcal{D}$ of the low rate fluctuation-driven regime (see main text V.4), its extent is delimited by the white square in the bottom and top-right insets. The mean phenomenological threshold in the $\mathcal{D}$ domain quantifies the excitability (top left: large dashed line). Then for each variable (top right: τ_V^N, bottom left: σ_V, bottom right: μ_V), we show the projections of the firing response along this dimension for different combinations of the two other variables within the $\mathcal{D}$ domain (dotted lines). The mean derivative (represented by arc angle and large dashed line) with respect to the variable in x-axis over different combinations of the remaining variables quantifies the mean sensitivity to this variable. **(B)** Excitabilities for the LIF, EIF, sfaLIF and iLIF models (parameters as in Figure 2). **(C)** Mean sensitivities to μ_V. **(D)** Mean sensitivities to σ_V. **(E)** Mean sensitivities to τ_V/τ_m^0 for the four models.

line characteristics. First of all, such mechanisms suppress spiking and therefore reduce the mean excitability of all the models (Figure 3B). The effect on average sensitivities is more complex.

The substitution of the hard threshold of LIF with an exponential function in EIF imitates the gradual opening of sodium channels in time. This property has a very strong impact on the dependency on the speed of the fluctuations (Figure 3E). In contrast to LIF, fast fluctuations do not lead to an increase of spiking. This effect, which occurs due to the inability of smooth sodium activation curve to extract fast varying fluctuations (Fourcaud et al., 2003), is well captured by our analysis: the sensitivity to τ_V^N is much reduced for the EIF with respect to the LIF model.

The spike frequency adaptation of sfaLIF reproduces the effect of a calcium-dependent potassium current (Im current) that tend to hyperpolarize neocortical pyramidal neurons at each spike occurrence (McCormick et al., 1985). This is an effect that attenuates firing and because it is proportional to firing itself we expected it would reduce the dependencies to all variables. Indeed the sensitivities to μ_V and σ_V are strongly attenuated with respect to LIF (Figure 3C-D). In contrast, the sensitivity τ_V^N is only mildly affected. The temporal dynamics of the hyperpolarizing current (τ_W=500ms) impedes short inter-spike intervals in the output spike train, consequently slow fluctuations are more strongly dampened than fast fluctuations which restores the sensitivity to τ_V^N (Figure 3E).

The iLIF model reproduce the fast inactivation properties of sodium channels (see Hille (2001) for a review). Close to threshold, sodium channels tend to rapidly inactivate (τ_{inact}=5ms). This mechanism clearly favors fast and high amplitude fluctuations, which allow to trigger a spike before the channels become unavailable. Indeed, the sensitivity to σ_V and τ_V^N is strongly enhanced (see Figure 3D-E).

V.5 Response of juvenile mice layer V pyramidal neurons *in vitro* with the perforated-patch technique

We now use the above analytical tools to determine experimentally firing rate responses *in vitro*.

Scanning the response of neocortical neurons in the fluctuation-driven regime is experimentally challenging because it is characterized by an irregular firing at low rates ($\sim$ 0.1-20 Hz). To obtain a meaningful estimation of the firing rate response we need long and stable recordings (Rauch et al., 2003; Köndgen et al., 2008). Both to obtain this stability and to ensure the integrity of the intracellular medium (in particular to maintain a physiological Ca^{2+} dynamics), we chose the *perforated patch* technique (Rae et al., 1991; Lippiat, 2009), in which electrical access is obtained by inserting a conducting pore (Amphotericin B protein permeant only to monovalent ions) in a patch of membrane (Wendt et al., 1992; Kyrozis and Reichling, 1995). Although the technique may sometimes limit the quality of the electrical access to the cell, we achieved very low ratios between the access resistance and the membrane resistance (4.7 $\pm$ 2.6 %, see also Rae et al. (1991)), thus allowing for reliable use of the *dynamic-clamp* technique (Destexhe and Bal, 2009).

We monitored the stability of recordings by means of three quantities: 1) the resting membrane potential, 2) the membrane resistance and 3) the variations of the firing rate probability and formulated strict criteria for the stability of the recordings (see Figure 4E).

The resulting dataset contains n=30 cells, it totals to 65455 spikes fired at an average frequency of 3.62Hz, i.e. within the low-rate, fluctuation-driven regime defined above (0.2-15 Hz). This relatively large amount of data was necessary to extract the biophysical relations between the fluctuations properties and the stationary firing rate.

We investigated whether the combination of the analytical template (and its fitting procedure) with our experimental recording protocols was able to produce a reliable characterization of the firing rate response of layer V neocortical neurons in juvenile mice visual cortex.

For each of the n=30 cells, we obtained a given scan of the $\mu_V, \sigma_V, \tau_V^N$ space and applied our fitted procedure. We show the data and the fit for four examples in Figure 5. The goodness-to-fit of our template was high (goodness-to-fit of 88.6% $\pm$ 9.4, compared to only 38.4% $\pm$ 35.3 for the constant threshold and 90.6% $\pm$ 9.2 for the quadratic phenomenological threshold), the small divergence is due to intrinsic irregularity of the low-rate spike process (sampled over 5 s per episode, Figure 4E). In spite of this variability, the linear threshold averages the intrinsic firing irregularity and produces a reliable characterization of the firing rate response.

We quantified the robustness of the experimental characterization with cross-validation: we splitted the measurements into two sets and investigated whether the first half of data would give the same phenomenological threshold as the second half. We found a good agreement if the number of scanned configuration of input space $(\mu_V, \sigma_V, \tau_V)$ was $n_p oints \geq 70$ (Pearson correlations, c>0.8 and p<1e-5 for the correlations between first and second half of data, Figure 5B). The high Pearson correlations between the response characteristics in the two subsets indicates that the characterization is robust for $n_p oints \geq 35$ scanned combinations of input parameters. Among the 30 cells used for further analysis, the cell with the minimum number of points had $n_p oints$=42 scanned combinations meeting the above criterion for the robustness.

V.6 Single neurons show strongly heterogeneous firing rate responses

A striking feature in the response of the recorded cells is the differences in their response.

We illustrate this property on the four examples shown in Figure 5A. Cells 1 and 4 show a very strong dependency on speed of the fluctuations τ_V, whereas cells 2 and 3 are almost insensitive to to this parameter (different colors in 5A). The dependency on the standard deviation of fluctuations σ_V is steeper for cell 2 than for 3 and 4. Also the sensitivity to μ_V seems to be variable, a 10 mV depolarization has stronger effect on responses of cell 4 than 3. Finally, the cell excitabilities are also highly variable, so that they reach the 1-15Hz firing range at

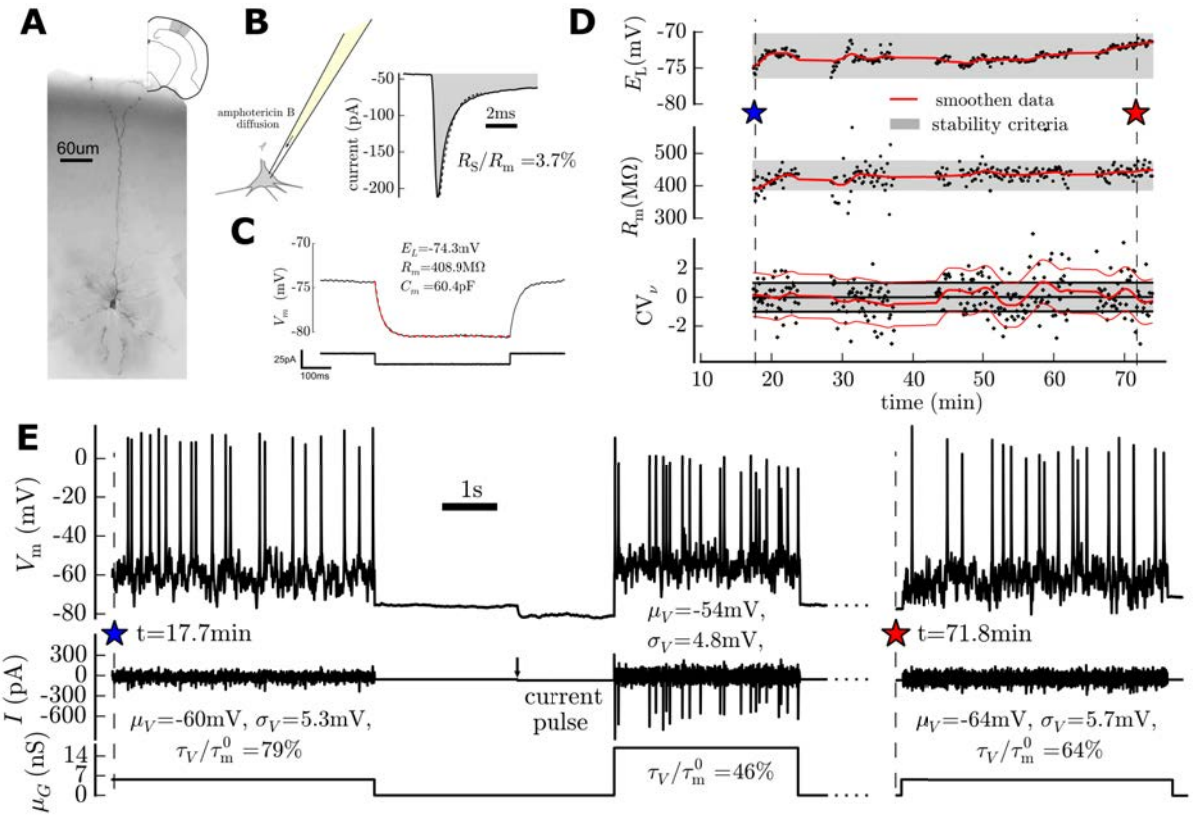

Figure 4: The exploration of a physiologically-relevant space in layer 5 pyramidal neurons of juvenile mice. From **B** to **E**, an example of a single cell. **(A)** A typical layer 5 pyramidal neuron in the primary visual cortex of juvenile mice. Picture from additional experiments: marking with 2% Biocytin (Sigma Aldrich) in whole cell configuration. **(B)** After diffusion of the perforant molecule toward the patch of membrane, a step voltage clamp protocol estimates the quality of the seal and perforation (see details in the Methods IV.2). **(C)** A step current clamp protocol estimate the passive membrane properties. Those properties are used by the stimulation protocols to constrain the V_m fluctuations (see Methods IV.7). **(D)** All along the recording, we monitor the cellular properties: the resting membrane potential E_L, the membrane resistance R_m and the variations of the firing rate with respect to the stationary behavior CV_ν (see details in the main text V.5 and in the Methods IV.8). The smoothened data (red curve) show the global trend, it removes the measurement error due to the short sampling time for R_m and E_L (see **E**), for CV_ν, it removes the intrinsic spiking irregularity. For the CV_ν curve we have added the standard deviation (mean ± std in red) for comparison with a stationary Poisson process (mean ± std in black). **(E)** Sample of the membrane potential V_m, the injected current I and the total conductance μ_G at the beginning of the recording (left,t=17.7min, blue star in **D**) and one hour after (right, t=71.8min, red star in **D**). Within an episode, we scan one combination of the (μ_V, σ_V, τ_V^N) variables. For example, the middle episode corresponds to the most depolarized level μ_V (hence the lower spike amplitude due to Na inactivation) with the fastest fluctuations τ_V^N (i.e. an high input conductance μ_G, also shunting the spikes, see the strong opposite current) and an intermediate variance σ_V. In between the two first episodes, one can see rest period (to monitor E_L) followed by a current pulse (to monitor R_m).

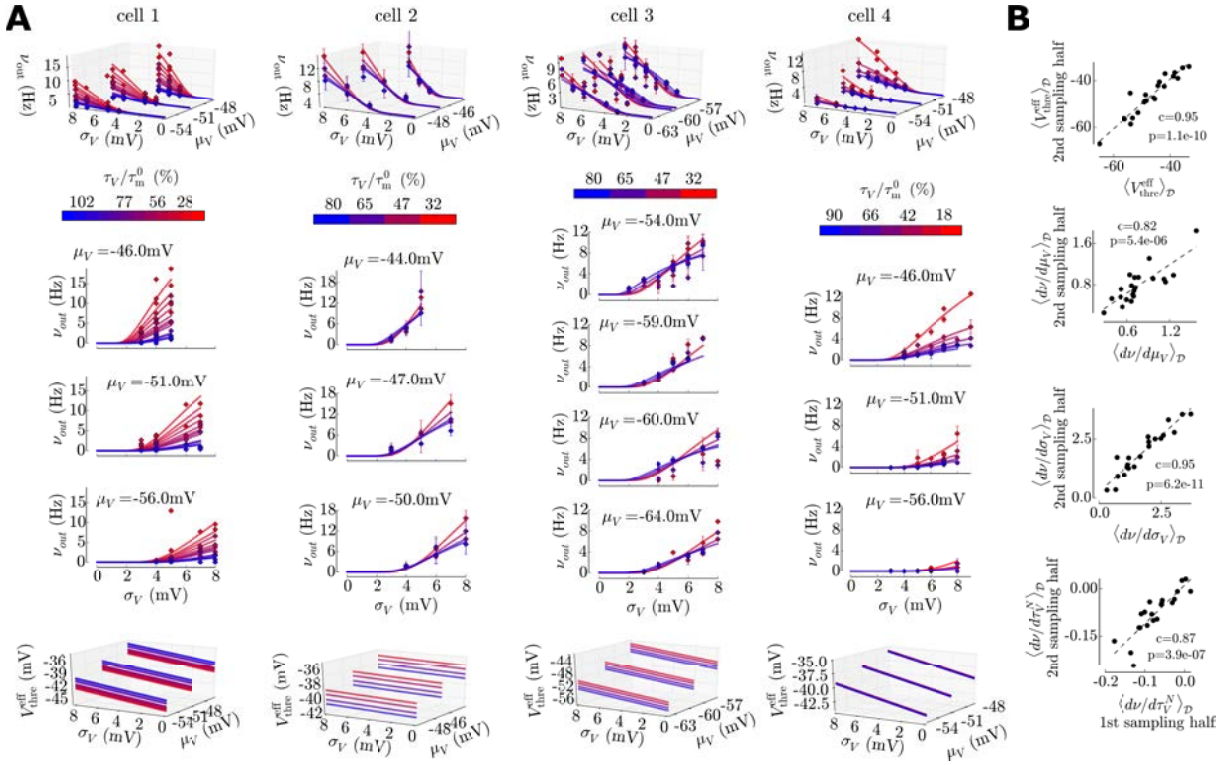

Figure 5: Characterization of the firing rate response of the recorded neocortical pyramidal neurons. **(A)** Four examples of the firing rate response of single neurons, data (diamonds, error bars indicate variability estimated as the standard deviation from responses to multiple trials where available) and fitted template function (plain line), the cells are indexed from 1 to 4 to identify them in the heterogeneity analysis (Figure 6). **(B)** For 21 neurons scanned with at least of 70 different combinations of input statistics, we split the dataset into two and investigate the similarity of the coefficients between the two subsets. The relatively high and significant ($p<0.05$, Pearson correlation) correlation coefficients between characterizations in the first and second datasets indicate a robust characterization of the firing rate response.

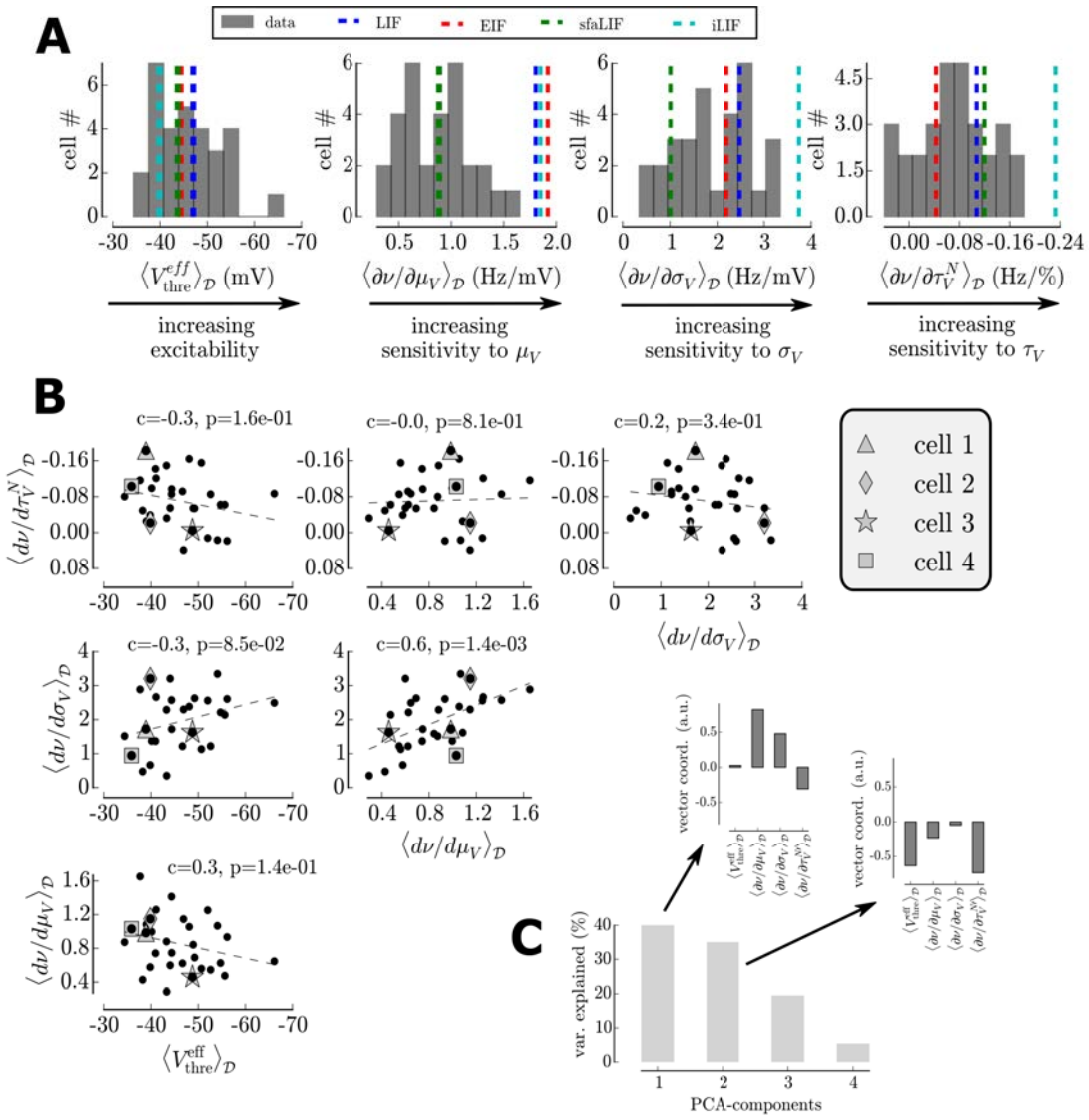

Figure 6: Heterogeneity and underlying structure of the firing response of neocortical cells (A) Histogram over recorded cells of the mean excitabilities and sensitivities to the variables of the fluctuations. The dashed color lines show the values of theoretical models for comparison. **(B)** Scatter plot of the mean excitability and sensitivities to the variables of the fluctuation-driven regime, we highlighted the cells shown in Figure 5 with larger markers. **(C)** Principal component analysis, in the inset, the vector coordinates of the two first components

various depolarization levels (e.g. compare cell 2 and 3). Similar differences are present in all recorded pyramidal cells (Figure 6A).

This strong heterogeneity raises the question whether there is an underlying structure in the variations of the characteristics of the firing rate response and how could it be explained by diverse biophysical mechanisms.

First, when plotted in four-dimensional space of the firing rate response characteristics the data did not seem to distribute into distinct clusters (Figure 6B). Presented on two dimensional projections, the excitability and sensitivities to input variables of different cells co-vary (Pearson correlation, c, Figure 6B). We then looked for the four-dimensional structure of those co-variations in the response characteristics by means of a principal component analysis (Figure 6C). No single co-variation of the sensitivities could explain a strong percentage of the observed heterogeneity, suggesting that the correlation structure is weak.

Nonetheless, two vectors explained 75% of the variations in the data. The first vector corresponds to a co-variation of the sensitivities to mean and amplitude of the fluctuations. This co-variation can be achieved in the sfaLIF model, varying the weight of spike frequency adaptation concomitantly varies the sensitivities to μ_V and σ_V (Figure 7C). The second vector corresponds to a co-variation of a decrease in the excitability and an increase in the sensitivity to the speed of the fluctuations. The variability in excitabilities is quite remarkable, to reproduce it in the LIF model one needs variations of the threshold V_{thre} that spans nearly 15 mV (see Figure 7). The variability in the sensitivity to τ_V covers a wide range of parameters in theoretical models, from an EIF model with a smooth curve (k_a=2mV) to a strongly inactivating iLIF model (a_i=0.7). Increasing the threshold while increasing the impact of sodium inactivation and increasing the sharpness of the sodium activation curve would therefore reproduce the second component of the principal components analysis.

VI Discussion

In this paper, we have provided a study of the spiking responses of mouse cortical neurons, in the *fluctuation-driven* regime, using injection of synthetic synaptic bombardment using dynamic-clamp *in vitro*. In our view, the principal contributions of the present paper are the following: (1) to have identified, theoretically, a set of three somatic variables that characterize the response to fluctuating input; (2) having determined, theoretically, an analytic template for the spike response using these variables, which renders the experiment feasible; (3) to have designed an experimental protocol where these variables could be fully implemented by current and conductance injection to characterize the spiking response; (4) to have performed a full characterization of the spiking response of pyramidal cells in juvenile mouse cortex *in vitro*; (5) to have identified possible biophysical origin for the observed diversity in the firing responses, using computational models. We discuss below the implications of these findings, and how they relate to previous work.

Compared to previous studies (La Camera et al., 2008), we focused on the low rate regime and we extended the domain of somatic *in vivo*-like conditions to cover a broad range of synaptically-induced activity. In particular, we investigated the dependency on the firing rate for high somatic conductance and low autocorrelation time of the membrane potential fluctuations. Scanning the response to low autocorrelation time allowed to highlight the impact of sodium inactivation because this is the regime where the temporal dynamics of this features is likely to play ($\tau_{inact} \sim 5$ms).

We formulated a two-step procedure to circumvent the issue of spatially distributed inputs in neocortical neurons where the intermediate quantities are the properties of the V_m fluctuations at the soma. Other investigators studied the response to the noisy current input properties at the soma and then addressed the problem of how dendritic integration shape the properties of this current (La Camera et al., 2008; Giugliano et al., 2008). Our approach can be seen as a way to include the mean conductance effect due to changes in background synaptic activity. The reason we presented the data as a function of the V_m fluctuations properties and not the quantity that the experimentalist actually controls (the current and the conductance) is that it allows to compare individual cells and that the spiking response is dominated by subthreshold integration effects, e.g. for a same variance of input current, an increasing conductance would decrease the V_m fluctuations amplitude by shunting effects (Kuhn et al., 2004). The effects of the spike-related mechanisms are then difficult to de-intricate from those subthreshold effects. Here, we used calculus to design a stimulation protocol that allows to control the fluctuations and therefore to focus on understanding the single neuron computation on top of the fluctuations properties.

Starting from a simple approximation, we showed that bringing the problem into a phenomenological threshold space was a simple way to describe the firing rate response of neocortical neurons. Other investigators already reported that a shift in the threshold was a convenient way to account for increasing biophysical complexity (Brunel and Sergi, 1998; Platkiewicz and Brette, 2010). Unlike the two mentioned studies, the form of our phenomenological threshold was not derived mathematically (it was arbitrarily taken as linear) but we believe that the descriptive power of this very simple form further confirms the idea that the threshold space is a convenient space to work in.

We showed that this template is able to describe the response of neuronal models of varying complexity. We then used this simple description to design a robust characterization of the firing rate response of single neurons experimentally. This approach, combined with the long and stable recordings provided by the perforated patch technique, was our way to circumvent the experimental and theoretical difficulties of assessing a relevant firing rate response in a low rate irregular firing regime.

We now discuss the biophysical mechanisms relevant for the firing rate response of layer V pyramidal cells in juvenile mice visual cortex.

First, spike frequency adaptation was shown to be an important mechanism to the firing rate response. Notably, all models lacking spike frequency adaptation (LIF, EIF,

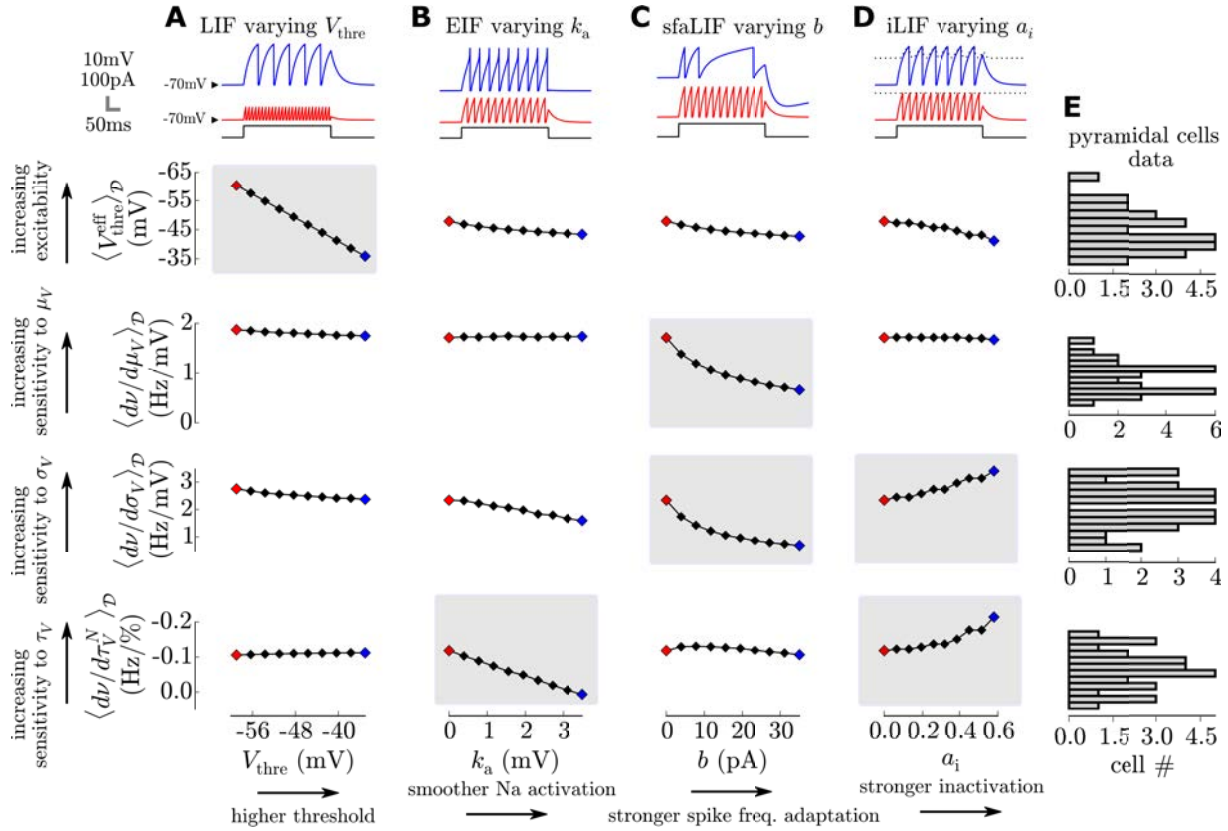

Figure 7: Variations in the expression of biophysical mechanisms explain the observed cellular heterogeneity in their firing rate response. **(A)** Increasing the threshold V_{thre} of the LIF model. Note that this only affects the excitability and negligibly the sensitivities to μ_V, σ_V and τ_V^N. **(B)** Decreasing the sharpness of the sodium activation curve in the EIF model, k_a=0mV corresponds to the LIF model, k_a=3.7mV corresponds to a very smooth activation. Note the strong impact on the sensitivity to τ_V^N. **(C)** Increasing spike frequency adaptation in the sfaLIF model, b=0 mV corresponds to the LIF model, b=35pA corresponds to a strongly adapting model. Note the concomitant variations of the sensitivities to μ_V and σ_V. **(D)** Increasing sodium inactivation in the iLIF model, a_i=0 corresponds to the LIF model, a_i=0.7 corresponds to a strongly inactivating model. Note the strong impact on the increase in sensitivity to sigma$_V$ and τ_V^N. **(E)** Histogram of the data from the n=30 neurons.

iLIF) had a sensitivity to μ_V higher than all recorded cell. This mechanism is therefore crucial to reproduce the attenuated sensitivity to depolarizations of layer V pyramidal cells in mice visual cortex.

Many cells showed a weaker sensitivity to the speed of the fluctuations than the LIF model (n=20 out of 30). This could be reproduced in theoretical models by implementing a smoother activation curve for the sodium channels (EIF models of varying sharpness). This observations contrasts with reports from studies in more mature pyramidal neurons in rat neocortex (Köndgen et al., 2008; Ilin et al., 2013), where it was found that pyramidal cells could have a very sharp activation curve that would enable them to extract very fast input. Nevertheless, even at the soma, the neurons of our recordings show a rather smooth activation curve: $k_a \sim 1.5$ mV (not shown) from the dynamic I-V curve analysis (Badel et al., 2008) rendering this possibility unlikely.

Surprisingly some cells showed a stronger sensitivity to the speed and amplitude of the fluctuations than the LIF model (n=10 out of 30). By penalizing slow and low amplitude fluctuations, sodium inactivation seem to be able to explain this phenomena. Our observation is thus analogous to the phenomena described in Fernandez et al. (2011) for pyramidal cells in rat CA1, where the authors found that a high conductance state (corresponding to fast fluctuations in our study) could evoke more spikes than a low conductance state (slow fluctuations here). Their study provides evidence for the role of fast sodium inactivation in the sensitivity to the speed of the fluctuations and is therefore compatible with our modeling results. Because of its role in promoting large amplitude and/or fast fluctuations, sodium inactivation seems to be a key property in shaping the input-output properties of layer V pyramidal cells in the fluctuation-driven regime.

Finally, we did not discuss the impact of other subthreshold non-linearities usually present in pyramidal cells such as the Ih current. This mechanisms is weakly expressed in the pyramidal cells of our recordings (see response to current steps in Figure 4C). Nevertheless, we investigated its effect on the firing response (not shown). Because of its high pass filtering behavior, it would have an effect very similar to the one of sodium inactivation: penalizing slow fluctuations and therefore increasing the sensitivity to τ_V.

It must be noted that the present analysis was performed on data acquired on immature neurons (P8-P13) during the most rapid phase of electrophysiological maturation (McCormick and Prince, 1987). We investigated whether the firing response properties correlated with the post-natal day of the recording (Pearson correlation). We found no significant correlation for the three sensitivities to fluctuations ($p>0.1$) and a weak correlation ($c=0.4, p=0.02$) for the excitability. Various developmental stages therefore poorly explain the observed variablity, suggesting that the firing response heterogeneity is an intrinsic property of the pyramidal cell population all along the P8-P13 period. A possibility is still that this is a phenomena specific to this post-natal period that would disappear in adult phenotypes. Nonetheless, variability in cellular excitability (as evaluated from action potential threshold) is routinely found in cortical cells in adult mice (Crochet et al., 2011; Okun et al., 2015; Yang et al., 2015), thus suggesting that electrophysiological heterogeneity is, at least partially, preserved in adult cortex and constitutes an important property of cortical assemblies. Its precise extent remains to be evaluated and should be the focus of future studies.

The main perspective for future work is to further explore the variable sensitivities of neurons to fluctuations and their putative functional consequences. We introduced new quantitative measures to quantify the sensitivity of cells to various properties of the fluctuations, which suggest several applications to the present work. First, the present analysis should be combined with a model of dendritic integration to understand how different sensitivities may have an impact on the cellular input-output function. Second, at the network level, previous theoretical work (Mejias and Longtin, 2012) investigated how variability in the excitability level had an impact on network computation, this should be generalized to the variability in the additional quantities introduced in this paper. Our results and measurements should thus be incorporated into mean-field descriptions of cortical dynamics to understand the properties emerging at the population level. Last, our study provided a simple and tractable response function of high empirical accuracy that could be usefull for biologically-inspired algorithmic computation.

In conclusion, the present work shows that the spiking response of cortical neurons is highly inhomogeneous in juvenile mice visual cortex, not only at the level of neuronal excitabilities but also about their sensitivity to fluctuations. This provides quantitative insight on how neuronal diversity may impact population dynamics in the low rate fluctuation-driven regime.

VII Additional information

VII.1 Competing interests

The authors declare no competing financial interests.

VII.2 Author contributions

*G.O. & A.D co-supervised this work, the experimental and theoretical part respectively. A.D. & T.B. initially designed the project, C.D. & Y.Z. performed preliminary whole cell experiments, G.O. designed the perforated patch protocols. Y.Z. designed the dynamic-clamp protocols, performed experiments, numerical simulations and analyzed data. Y.Z., B.T. & A.D. discussed the results and wrote the manuscript. All authors approved the final version of the manuscript and agree to be accountable for all aspects of the present work.

VII.3 Funding

Y.Z was supported by fellowships from the Initiative d'Excellence Paris-Saclay and the Fondation pour la Recherche Médicale (FDT 20150532751). Research funded by the CNRS, the ANR (Complex-V1 project) and the European Community (BrainScales FP7-269921 and the Human Brain Project FP7-604102).

36

VII.4 Acknowledgments

We would like to acknowledge the contribution of Gérard Sadoc in helping us to design the dynamic-clamp protocols. We also thank Guillaume Hucher for the histological work as well as Manon Richard and Aurélie Daret for animal facilities.

VIII References

Altwegg-Boussac T, Chavez M, Mahon S, Charpier S (2014) Excitability and responsiveness of rat barrel cortex neurons in the presence and absence of spontaneous synaptic activity in vivo. *The Journal of physiology* 592:3577–3595.

Amit DJ, Brunel N (1997) Model of global spontaneous activity and local structured activity during delay periods in the cerebral cortex. *Cerebral Cortex* 7:237–252.

Badel L, Lefort S, Berger TK, Petersen CCH, Gerstner W, Richardson MJE (2008) Extracting non-linear integrate-and-fire models from experimental data using dynamic I-V curves. *Biological Cybernetics* 99:361–370.

Baudot P, Levy M, Marre O, Monier C, Pananceau M, Frégnac Y (2013) Animation of natural scene by virtual eye-movements evokes high precision and low noise in V1 neurons. *Frontiers in neural circuits* 7:206.

Brette R, Gerstner W (2005) Adaptive exponential integrate-and-fire model as an effective description of neuronal activity. *Journal of neurophysiology* pp. 3637–3642.

Brunel N, Sergi S (1998) Firing frequency of leaky intergrate-and-fire neurons with synaptic current dynamics. *Journal of theoretical biology* 195:87–95.

Chance FS, Abbott LF, Reyes AD (2002) Gain modulation from background synaptic input. *Neuron* 35:773–782.

Contreras D, Destexhe A, Steriade M (1997) Intracellular and computational characterization of the intracortical inhibitory control of synchronized thalamic inputs in vivo. *Journal of neurophysiology* 78:335–350.

Crochet S, Poulet JFA, Kremer Y, Petersen CCH (2011) Synaptic mechanisms underlying sparse coding of active touch. *Neuron* 69:1160–1175.

Daley DJ, Vere-Jones D (2007) *An introduction to the theory of point processes: volume II: general theory and structure*, Vol. 2 Springer Science & Business Media.

Debanne D, Campanac E, Bialowas A, Carlier E, Alcaraz G (2011) Axon physiology. *Physiological reviews* 91:555–602.

Destexhe A, Rudolph M, Fellous JM, Sejnowski TJ (2001) Fluctuating synaptic conductances recreate in vivo-like activity in neocortical neurons. *Neuroscience* 107:13–24.

Destexhe A, Bal T (2009) Dynamic-Clamp: From Principles to Applications. *From Principles to Applications* 1:443.

Destexhe A, Contreras D (2006) Neuronal computations with stochastic network states. *Science* 989:85–90.

Destexhe A, Paré D (1999) Impact of network activity on the integrative properties of neocortical pyramidal neurons in vivo. *Journal of neurophysiology* 81:1531–1547.

El Boustani S, Marre O, Béhuret S, Baudot P, Yger P, Bal T, Destexhe A, Frégnac Y (2009) Network-state modulation of power-law frequency-scaling in visual cortical neurons. *PLoS computational biology* 5:e1000519.

Fernandez FR, Broicher T, Truong A, White Ja (2011) Membrane voltage fluctuations reduce spike frequency adaptation and preserve output gain in CA1 pyramidal neurons in a high-conductance state. *The Journal of neuroscience : the official journal of the Society for Neuroscience* 31:3880–93.

Fourcaud N, Hansel D, van Vreeswijk C, Brunel N (2003) How spike generation mechanisms determine the neuronal response to fluctuating inputs. *The Journal of neuroscience* 23:11628–11640.

Giugliano M, La Camera G, Fusi S, Senn W (2008) The response of cortical neurons to in vivo-like input current: theory and experiment: II. Time-varying and spatially distributed inputs. *Biological cybernetics* 99:303–18.

Hille B (2001) Ion channels of excitable membranes. *Sunderland, MA: Sinauer* .

Ilin V, Malyshev A, Wolf F, Volgushev M (2013) Fast computations in cortical ensembles require rapid initiation of action potentials. *The Journal of neuroscience : the official journal of the Society for Neuroscience* 33:2281–92.

Köndgen H, Geisler C, Fusi S, Wang XJ, Lüscher HR, Giugliano M (2008) The dynamical response properties of neocortical neurons to temporally modulated noisy inputs in vitro. *Cerebral cortex (New York, N.Y. : 1991)* 18:2086–97.

Kuhn A, Aertsen A, Rotter S (2004) Neuronal integration of synaptic input in the fluctuation-driven regime. *The Journal of neuroscience : the official journal of the Society for Neuroscience* 24:2345–56.

Kyrozis A, Reichling DB (1995) Perforated-patch recording with gramicidin avoids artifactual changes in intracellular chloride concentration. *Journal of Neuroscience methods* 57:27–35.

La Camera G, Giugliano M, Senn W, Fusi S (2008) The response of cortical neurons to in vivo-like input current: theory and experiment : I. Noisy inputs with stationary statistics. *Biological cybernetics* 99:279–301.

Lippiat J (2009) Whole-cell recording using the perforated patch clamp technique In Lippiat J, editor, *Potassium Channels*, Vol. 491 of *methods in Molecular Biology*, pp. 141–149. Humana Press.

Lundstrom BN, Famulare M, Sorensen LB, Spain WJ, Fairhall AL (2009) Sensitivity of firing rate to input fluctuations depends on time scale separation between fast and slow variables in single neurons. *Journal of Computational Neuroscience* 27:277–290.

McCormick DA, Prince DA (1987) Post-natal development of electrophysiological properties of rat cerebral cortical pyramidal neurones. *The Journal of physiology* 393:743–62.

McCormick DA, Connors BW, Lighthall JW, Prince Da (1985) Comparative electrophysiology of pyramidal and sparsely spiny stellate neurons of the neocortex. *Journal of neurophysiology* 54:782–806.

Mejias JF, Longtin A (2012) Optimal heterogeneity for coding in spiking neural networks. *Physical Review Letters* 108:228102.

Okun M, Steinmetz NA, Cossell L, Iacaruso MF, Ko H, Barthó P, Moore T, Hofer SB, Mrsic-Flogel TD, Carandini M et al. (2015) Diverse coupling of neurons to populations in sensory cortex. *Nature* 521:511–515.

Platkiewicz J, Brette R (2010) A threshold equation for action potential initiation. *PLoS computational biology* 6:e1000850.

Platkiewicz J, Brette R (2011) Impact of fast sodium channel inactivation on spike threshold dynamics and synaptic integration. *PLoS computational biology* 7:e1001129.

37

Rae J, Cooper K, Gates P, Watsky M (1991) Low access resistance perforated patch recordings using amphotericin B. *Journal of Neuroscience methods* 37:15–26.

Rauch A, La Camera G, Lüscher HR, Senn W, Fusi S, Luscher HR (2003) Neocortical Pyramidal Cells Respond as Integrate-and-Fire Neurons to In Vivo-Like Input Currents. *J Neurophysiol* 90:1598–1612.

Rossant C, Leijon S, Magnusson aK, Brette R (2011) Sensitivity of Noisy Neurons to Coincident Inputs. *Journal of Neuroscience* 31:17193–17206.

Rudolph M, Destexhe A (2003) Tuning neocortical pyramidal neurons between integrators and coincidence detectors. *Journal of Computational Neuroscience* 14:239–251.

Stuart GJ, Spruston N (2015) Dendritic integration: 60 years of progress. *Nature Neuroscience* 18:1713–1721.

Tuckwell HC, Wan FYM, Rospars JP (2002) A spatial stochastic neuronal model with Ornstein–Uhlenbeck input current. *Biological cybernetics* 86:137–145.

Wendt DJ, Starmer CF, Grant AO (1992) Na channel kinetics remain stable during perforated-patch recordings. *The American journal of physiology* 263:C1234–C1240.

Yang H, Kwon SE, Severson KS, O'Connor DH (2015) Origins of choice-related activity in mouse somatosensory cortex. *Nature neuroscience* 19:127–134.

Work 2: Heterogeneous firing responses induce specific coupling to presynaptic activity properties

French summary

Le traitement néocortical repose sur l'activation spécifique de sous-populations dans les réseaux néocorticaux. Bien que des connectivités spécifiques soient, a priori, le mécanisme principal qui sous-tend ce principe fonctionnel, nous étudions dans ce travail un mécanisme possiblement complémentaire: est-ce que des propriétés biophysiques différentes peuvent donner lieu à des activations différentes.

Dans ce but, nous construisons un modèle simplifié d'arborescence dendritique (que nous calibrons sur des mesures *in vitro*) basé sur la règle de Rall. Nous proposons une dérivation analytique pour calculer les propriétés des fluctuations au soma en fonction des propriétés de la stimulation synaptique dans les dendrites. Cette description mathématique permet d'émuler diverses formes d'activités synaptiques: balancées, non-balancées, purement proximales, purement distales ou synchronisées.

Nous avons en effet observé que, parce qu'ils ont des propriétés biophysiques différentes, différents neurones répondaient différemment à ces types d'activités. Mais l'unique contribution significative est, trivialement, la différence d'excitabilité de ces différents neurones. Une exception intéressante apparaît néanmoins pour l'activité proximale: une augmentation de l'activité proximale peut augmenter l'activité pour certains neurones ou la diminuer pour d'autres quelle que soit leur activité. Cette propriété est expliquée par leur sensibilité à la vitesse des fluctuations que nous avions précedemment reliée au niveau de densité des canaux sodiques et à l'inactivation des canaux sodiques.

Heterogenous firing responses lead to diverse couplings to presynaptic activity

Y. Zerlaut[1] & A. Destexhe[1]

April 11, 2016

I Abstract

Neocortical processing of sensory input rely on the specific activation of subpopulations within the cortical network. Though specific circuitry is thought to be the primary mechanism underlying this functional principle, we investigate here a putative complementary mechanism: whether diverse biophysical features in single neurons contribute to such differential activation.

In a previous study (Zerlaut et al., 2016), we reported that, in young mice visual cortex, individual neurons differ not only in their excitability but also in their sensitivities to the properties of the membrane potential fluctuations. In the present work, we analyze how this heterogeneity is translated into diverse input-ouput properties (i.e. in the relation from presynaptic quantities to spiking probability) in the context of low synchrony population dynamics.

To this purpose, we designed a simplified morphological model of layer V pyramidal neurons with a dendritic tree following Rall's branching rule. We first show that we are able to calibrate this simplified model on *in vitro* measurements of somatic input impedance. We then propose an analytical derivation for the membrane potential fluctuations at the soma as a function of the properties of the synaptic bombardment. This mathematical description allows to easily emulate various forms of presynaptic activities: either balanced, unbalanced, synchronized, purely proximal or purely distal synaptic activity.

We found that those different forms of activity led to various comodulations of the membrane potential fluctuation properties, thus raising the question whether individual neurons might differentially couple to specific forms of activity because of their various firing responses to fluctuations.

We indeed found such an heterogenous response, but trivially, the only significant contribution to the various firing response was the different levels of cellular excitability. A notable exception appeared for proximal activity: increasing proximal activity could either promote firing response in some cells or suppress it in some other cells whatever their individual excitability. This behavior could only be explained by various sensitivities to the speed of the fluctuations, that was previously linked to heterogenous levels of sodium inactivation and sodium channels density.

In addition to giving quantitative insight on the impact of various excitability levels in individual neurons, the present study suggests a new functional impact of biophysical heterogeneity: various levels of density of sodium channels and sodium inactivation will control the response of individual neurons to proximal activity.

II Introduction

Neocortical processing of sensory input rely on the specific activation of subpopulations within the cortical network. The details of how such specific activations happen are key questions in systems neuroscience. As a primary source for specific activation, the neocortex is characterized by some degree of specific circuitry: neurons differ in their afferent connectivity. A classical example can be found in the primary cortex, layer IV simple cells specifically sample their input from ON and OFF cells in the thalamic nucleus (Hubel and Wiesel, 1962; Ferster et al., 1996). Neocortical neurons also vary in their electrophysiological properties: for example, heterogenous levels in the action potential threshold are routinely measured *in vivo* (Crochet et al., 2011; Okun et al., 2015; Yang et al., 2015). Thus, an emerging refinment is that the sensitivity of a neuron to a given feature do not only results from its *circuit specificity* (relative to this feature, e.g. orientation selectivy), but from the combination of its *circuit specificity* and its *biophysical specificity*. The somatosensory cortex studies of Crochet et al. (2011) and Yang et al. (2015) illustrates this point precisely. In Crochet et al. (2011), during active touch, the response probability of a neuron (its sensitivity to whisker touch) follows from the combination of the reached level of synaptically-driven membrane potential deflection (resulting from its *circuit-specificity*) and its threshold for action potential triggering (its *biophysical specificity*). The same result hold for texture recognition in the study of Yang et al. (2015) where only the combination of those two quantities was shown to predict choice-related spiking. Those results therefore suggest that heterogeneity in the electrophysiological or biophysical properties of neocortical neurons might have an impact on their functional role during sensory processing.

In the present work, we further investigate this putative interaction in the light of the variability in the biophysical features reported in our previous communication, namely that single neurons in juvenile mice cortex not only vary in their excitability (linked to the action potential threshold) but also in their sensitivity to the properties of the membrane potential fluctuations. Our previous communication introduced those new dimensions in the *biophysical specificity* and we now aim at understanding their functional impact.

To highlight the impact of the *biophysical specificity*, we

will investigate single neuron responses in a framework where the *circuit specificity* of individual neurons is null, i.e. with the hypothesis that all neurons sample statistically equally their input.

In the context of low synchrony population dynamics (Ecker et al., 2010; Renart et al., 2010), where the neuronal response can be described as a spiking probability and the input can be described by presynaptic firing rates, we implemented various types of presynaptic activity: either unbalanced (to emulate net excitatory input), purely proximal (to emulate local network input (Spruston, 2008)), purely distal (to emulate long-range or thalamic input (Spruston, 2008)) or of increased synchrony (to emulate changes in input statistics (Baudot et al., 2013; El Boustani and Destexhe, 2009)). We found that those various types of activity corrresponds to different variations of the properties of the membrane potential fluctuations (mean depolarization, standard deviation and autocorrelation time). The various firing responses (as a function of the fluctuation properties) for individual neurons found in our previous study then led to diverse coupling to each activity type.

We designed a theoretical model for passive dendritic integration that allows an analytical treatment and thus easily enables the implementation of various types of presynaptic activity. It is based on a symmetrical morphology where branching follows the Rall's 3/2 exponent rule (Rall, 1962), the analytical derivation relies on adapting the equivalent cylinder transformation (Rall, 1962) to the properties of the high conductance state (Destexhe et al., 2003).

We suggested in our previous study that the properties of the fluctuations could follow various comodulations depending on the type of presynaptic activity, what we demonstrate in this study.

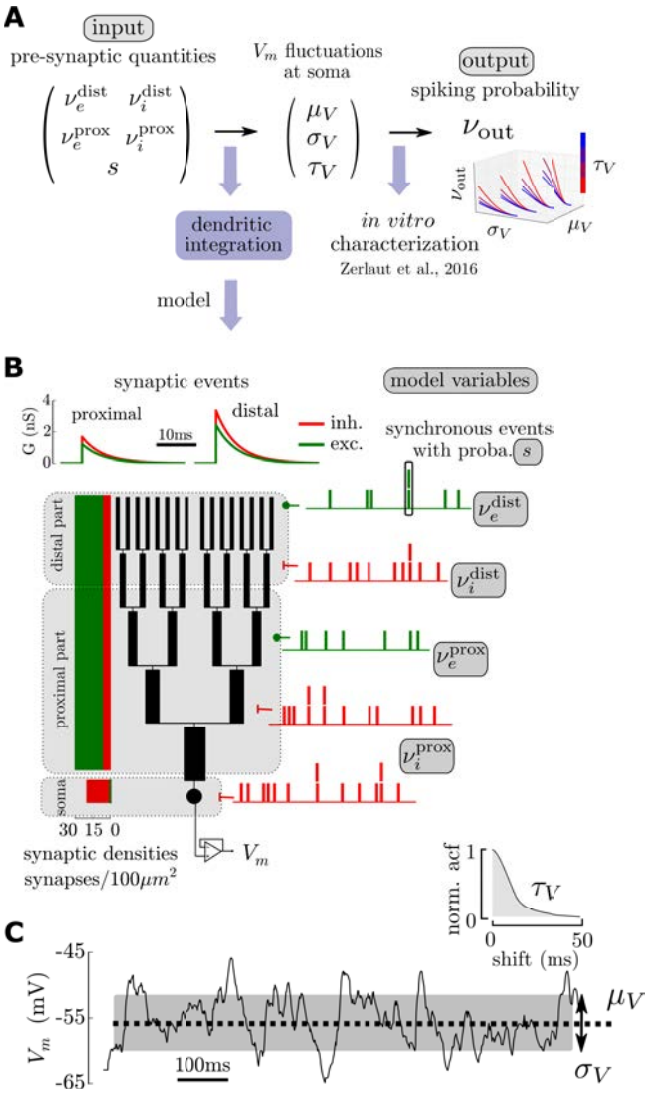

Figure 1: A theoretical framework for single cell computation in the fluctuation-driven regime. (A) Theoretical paradigm: to get the input-output function of a single cell, we split the relation from presynaptic quantities (the input) to the spiking probability (the output) into two steps. 1) passive dendritic integration shape the membrane potential at the soma and 2) how those fluctuations are translated into spikes is captured by a firing response function determined *in vitro* (Zerlaut et al., 2016) **(B)** Theoretical model for dendritic integration. A single cell is made of a lumped impedance somatic compartment and a dendritic tree. The dendritic tree is composed of B branches (here B=5), the branching is symmetric and follow Rall's 3/2 rule for the branch diameters. Synapses are then spread all over the membrane according to physiological synaptic densities. We define 3 domains: a somatic and proximal domain as well as a distal domain, excitatory and inhibitory synaptic input can vary independently in those domains. An additional variable: synaptic synchrony controls the degree of coincidents synaptic inputs. **(C)** A given presynaptic stimulation (here ν_e^p=ν_e^d=0.2Hz, ν_i^p=ν_i^d=1.2Hz and s=0.05) creates membrane potential fluctuations at the soma characterized by their mean μ_V, their amplitude σ_V and their autocorrelation time τ_V.

III Results

The results are organized as follows. We first formulate our theoretical framework for cellular computation which arbitrarily separate the question of dendritic integration and spiking probability. Then we present our simplified model of dendritic morphology which we calibrated on *in vitro* measurements. We derive an analytical approximation for the membrane potential fluctuations at the soma that we compare to numerical simulations using standard compartemental modeling. We implement various types of presynaptic activity we analyze the individual responses of the layer V pyramidal cells characterized in our previous study for those various types of presynaptic activities.

III.1 A theoretical framework for single cell computation in the fluctuation-driven regime

In the fluctuation-driven regime, the cellular input-output function of a neocortical neuron corresponds to the function that maps the presynaptic variables to the spiking probability of the neuron (this is true both in a rate coding paradigm (Shadlen and Newsome, 1994) or in a stochastic

temporal coding paradigm (Rossant et al., 2011)). In addition, because our study focuses on effects resulting from population dynamics, the presynaptic variables will have a simple description: firing rates and a synchrony degree.

III.2 A simplified morphological model for dendritic integration

The morphology of our theoretical model is a lumped impedance somatic compartment in parallel with a dendritic arborization of symmetric branching following Rall's 3/2 branching rule (see Figure 1B and Methods V.1). This morphology is of course a very reductive description of pyramidal cells: it does not discriminate between the distinct apical trunk and the very dense basal arborization. Also, branching in pyramidal cell morphologies have been shown to deviate from Rall's 3/2 branching rule. Nonetheless this simplified model contains the important ingredient for our study: the fact that the transfer impedance to the soma of a synaptic input will strongly depend on its location on the dendritic tree. Indeed, as observed experimentally (Magee, 2000), distal events will be more low-pass filtered than proximal events in this model.

We spread synapses onto this morphology according to physiological densitities (taking lower bounds of DeFelipe et al. (1992)) and describe synaptic events as transient permeability changes of ion-selective channels (see Methods V.2).

We arbitrarily separate the dendritic tree into two domains: a proximal and a distal domain (delimited by theur distance to the soma, see Figure 1B). The main motivation for this separation is to distinguish between two types of projections onto neocortical pyramidal neurons: synaptic inputs from the local network are thought to be more proximal while the distal apical tuft receives input from more distant cortical areas and thalamic locations (Spruston, 2008).

Following experimental evidences (Magee, 2000), we set a higher synaptic efficacy for distal synapses. The synaptic parameters take physiological values (Destexhe et al., 1998) and can be found on Table 1. The passive and morphological parameters will be estimated from *in vitro* measurements.

The model has five variables. Four of them are presynaptic firing rates. To investigate their differential contribution, the proximal and distal parts of the dendritic trees have been separated and each of them has two presynaptic rates corresponding to the excitatory and inhibitory populations (hence four rate variables: ν_e^p, ν_i^p, ν_e^d, ν_i^d). Additionally, a global synchrony variable has been introduced for presynaptic events. This reproduces the effect of pairwise correlations observed in neocortical assemblies (Peyrache et al., 2012) and/or the multi-innervation of a cell by its presynaptic afferent. The synchrony degree in the presynaptic activity has been suggested to vary with stimulus statistics in the primary visual cortex (Baudot et al., 2013; El Boustani and Destexhe, 2009) and justifies its introduction as a variable.

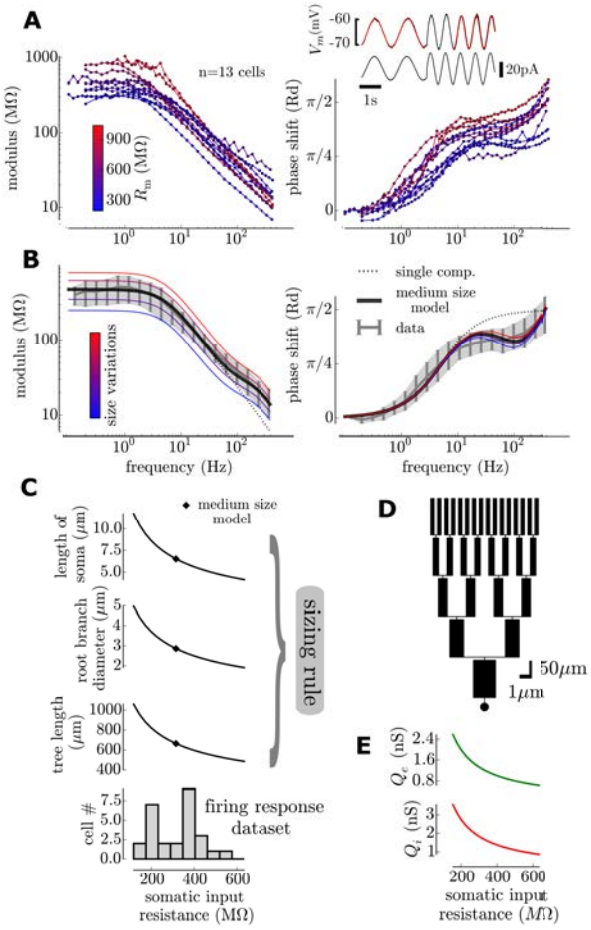

Figure 2: Calibrating the model on *in vitro* measurements: the simplified model and its size variations provides an approximation for the somatic input impedance and its heterogeneity. **(A)** Input impedance (left: modulus and right: phase shift) measured at the soma in intracellular recordings with sine-wave protocols in current-clamp (inset). The color code indicates the input resistance and is likely to result from size variations of individual cells. **(B)** A medium size model accounts for the average data and varying the size of the dendritic tree and soma reproduces the trend in the individual measurements. Large cells (blue) have a lower modulus and a lower phase shift while small cells (red) have both a higher modulus and phase shift. **(C)** We obtain a map between input resistance and size of the morphological model. **(D)** Representation of the medium-size model. **(E)** Additionally the synaptic weights are rescaled with respect to the cell's somatic input resistance. Because the mean transfer resistance to soma is linked to the input resistance, this rescalings insures that the mean synaptic efficacy at soms is the same for all cells.

III.3 Model calibration on *in vitro* measurements

We will use the firing response function of our previous study, we therefore wanted a characterization of the passive and morphological properties on the same experimental system: layer V pyramidal neurons in the primary visual

cortex of young mice. To this purpose, we performed measurements of the input impedance at the soma with intracellular recordings *in vitro* in n=13 cells. The key property on which this characterization relies is the fact that the input impedance at the soma can not be accounted for only by the isopotential somatic compartment (i.e. a RC circuit). The input impedance also shows the contribution of the dendritic tree in parallel to the soma (Rall, 1962). Indeed, both the modulus and the phase of the imput impedance show deviations from the deviations from the RC circuit impedance (see the comparison in Figure 2B): see for example the exponent of the power law scaling of the modulus (-1 for the single compartment and ~ 0.7 for pyramidal cells) or the decreased phase shift at 100Hz.

We first average all data (shown on Figure 2A) to obtain a mean input impedance (shown on Figure 2B) representative of a mean cellular behavior. We then perfomed a minimization procedure to obtain both the passive properties and the morphology corresponding to this average behavior (see Methods V.9). The obtained passive properties were compatible with standard values, e.g. the resulting specific capacitance was 1.05 $\mu F/cm^2$ close to the 1 $\mu F/cm^2$ standard, thus suggesting that the procedure could capture the physiological parameters of pyramidal cells, see Table 1 for the other parameters. Also the obtained morphology seems realistic (B=5 generation of branches, a total tree length of $L_t = 550\mu$m and a root branch diameter of the tree $D_t = 2.25\mu$m) given what can be observed after histological work (Zerlaut et al., 2016). Most importantly, the surface area was physiologically realistic, so that when using synaptic densities, we obtain an accurate number of synapses. A representation of this mean morphology can be seen on Figure 2D.

Pyramidal cells show a great variablity in input impedance, for example their input resistance almost spans one order of magnitude (both in the present n=13 cells, see the low frequency modulus values in Figure 2A, as well as in the firing response dataset, see bottom in Figure 2C). We found that varying the size of the morphological model within a given range around the mean morphological model could partially reproduce the observed variability in the input impedance profiles (see Figure 2B). Size variations corresponds to a linear comodulation of the 1) tree length L_t, 2) the diameter of the root branch D_t and 3) the length of the somatic compartment L_S (see Figure 2C for the range of their variations). On Figure 2A, the cells have been colored as a function of their input resistance while on Figure 2B, we vary the size of the size of the morphological model. Large cells (blue, low input resistance) tend to have a lower input resistance and phase shift than the small cells (red, high input resistance). Note that this very simplistic account of morphological variations only very partially describes the observed behavior in pyramidal cells. In particular, it strongly underestimates the variations of phase shifts at medium and high frequencies (f>20Hz). This discrepancy is likely to be due to the details of dendritic arborescence that are not captured by the strong constraints of our dendritic model (symmetric branching, diameter rules, number of branches, etc...). Despite those discrepancies, size variations in our morphological model constitute a reasonable first approximation to account for cellular variety within the layer V pyramidal cell population.

This characterization, combined with the analytical tractability of the model (see V.8) allow us to construct a map between input resistance at the soma and size of the morphological model (the passive properties are set as identical, the one fitted on the mean impedance behavior). Thus, for each neuron in our previous "firing response dataset", because we have its input resistance at the soma, we can associate a given morphology. The association rule is shown in Figure 2C.

We now check what is the number of synapses obtained from the combination of our fitted morpholgies with the physiological synaptic densities. We found a mean number of synapses: 3953 ± 1748 with a ratio of excitatory to inhibitory numbers of synapses of 4.5 ± 0.1. The fact that those numbers fall within the physiological range offers a validation of our approach.

III.4 An analytical approximation for the properties of the membrane potential fluctuations at the soma

For each cell, we now want to translate the five variables of the model in terms of membrane potential fluctuations properties at the soma (μ_V, σ_V, τ_V) on which we will apply the cell's firing response function. To obtain a final map between the input (the five model variables) and the output (the spiking probability).

Investigating dendritic integration for detailed morphological structures is made difficult by the fact that this has to be done numerically with a relatively high spatial and temporal discretization. In the fluctuation-driven regime, one also needs to sample over long times ($T \gg \tau_V \sim 10$ms) to obtain the statistical properties of the somatic V_m resulting from dendritic integration. In addition, we have n=27 different morphologies in this study and we will explore a five dimensional parameter space (the five variable of our model). Under those conditions, if performed numerically, the computational cost of such a study is clearly prohibitive. We briefly describe here, why, in our simplified model, an analytical treatment is nonetheless possible and thus render this investigation feasible (see details in the Methods V.5 and in the Supplementary Material). The key ingredient is the ability to reduce the dendritic tree to an equivalent cylinder (Rall, 1962), we only adapted this reduction to the changes in membrane permeability associated to the high conductance state (Destexhe et al., 2003). Two approximations underlie our estimation: 1) the driving force during an individual synaptic event is fixed to the level resulting from the mean bombardment (Kuhn et al., 2004) and 2) the effect at the soma of an synaptic event at a distance x in a branch of generation b, corresponds to $1/2^{b-1}$ the post-synaptic response to the stimulation made of synchronous events at distance x in all the 2^{b-1} branches of the generation b. Luckily, the combination of those approximation is a favorable situation. Indeed, hypothesis 1) overestimates the size of

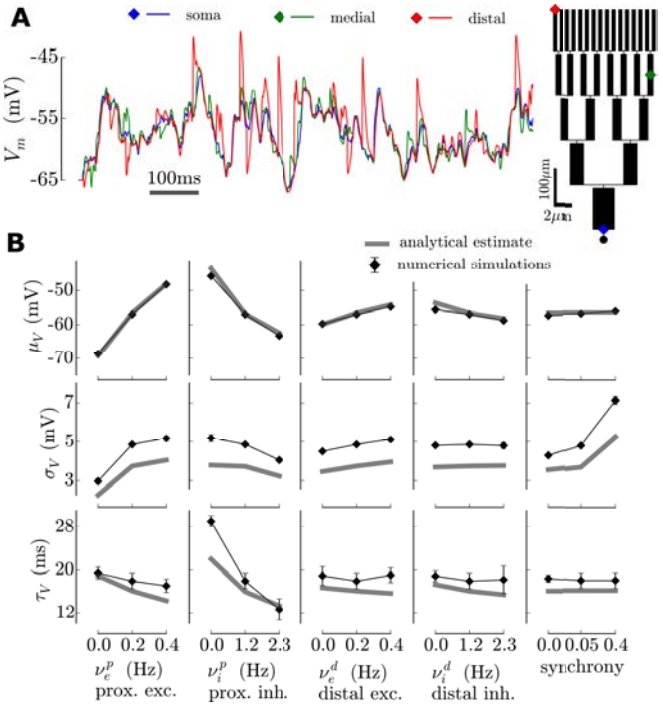

Figure 3: Accuracy of the analytical estimate for the properties of the membrane potential fluctuations at the soma: comparison between numerical simulations and the analytical approximation. Shown for the medium size model of Figure 2D. **(A)** In the numerical simulation, we explicitely simulate the whole dendritic arborization, we show the membrane potential variations for the three locations shown on the left. **(B)** Properties of the membrane potential fluctuations for different configuration of presynaptic activity: analytical predictions and output from numerical simulations in `NEURON`. In each column, one variable is varied while the other variables are fixed to the mean configuration value corresponding to ν_e^p=ν_e^d=0.2Hz, ν_i^p=ν_i^d=1.2Hz and s=0.05.

post-synaptic events (because the driving force is not fixed, it diminishes during the PSP time course) while hypothesis 2) underestimates the size of post-synaptic events (because of the $2^{b-1}-1$ synchronous events in neighboring branches, the membrane conductance is higher than in the case of a single event, consequently neighboring events have a shunting effect that artificially descreases the response). In addition, both of those approximation are likely to hold when single events are of low amplitude compared to the amplitude of the massive synaptic bombardment (see e.g. Kuhn et al. (2004) for the validity of the first hypothesis).

In Figure 3, we compare the analytical approximation to the output of numerical simulations performed with the `NEURON` software (Hines and Carnevale, 1997). We varied the five variables of the model around a mean synaptic bombardment configuration (see next section). Some discrepancies between the approximation and the simulations appeared, in particular one can see a $\sim$ 1mV shift in the standard deviation σ_V of the fluctuation. Because the synchrony controls the amplitude of the fluctuations (Figure 3B and Figure 4B), the analytical estimate could therefore be seen as an accurate estimate, modulo a shift in the synchrony. Nonetheless, the trend in the variations of the fluctuations as a function of the model variables is globally kept between the analytical estimate and the numerical simulations. This relatively good agreement therefore shows that our analytical estimate is a valid tool to study dendritic integration in the fluctuation-driven regime.

III.5 Properties of the fluctuations for different types of presynaptic activity

We now implement various types of presynaptic activity and investigate the properties of the resulting membrane potential fluctuations at the soma. In addition, we represent the variations of the somatic input conductance (relative to the leak input conductance) because, as it is routinely measured in intracellular studies *in vivo*, this quantity allows a comparison between the model and experimentally observed activity levels. On Figure 4, we present those different protocols, on the left one can see how the five variables of the model are comodulated for each protocol (color coded, see bottom legend) and one the left, one can see the resulting properties of the membrane potential fluctuations. We present those results only for the medium-size model, but it was calculated for the morphologies associated to all cells. The variability introduced by the various morphologies is studied in the Supplementary Material and we found that the qualitative behavior discussed in this section was preserved in all cells.

We first introduce a baseline level of presynaptic activity corresponding to a low level of network activity: g_{tot}^{soma}/g_L $\sim$ 1.7, compared to $\sim$ 3-4 in activated states, reviewed in Destexhe et al. (2003). This baseline activity is a mix of proximal and distal activity with a low degree of synchrony (s=0.05). Similarly to (Kuhn et al., 2004), the inhibitory activity is adjusted to obtain a balance of the V_m fluctuations at -55mV. The firing values of this baseline level are very low (ν_e^d=ν_e^p=0.2Hz for the excitation and ν_i^d=ν_i^p=1.2Hz for the inhibition) in accordance with the sparse activity characterizing mammalian neocortical dynamics (Crochet et al., 2011; Peyrache et al., 2012). On top of this non-specific background activity, we will now add a specific stimulation.

We start with unbalanced activity. We define it as a stimulation that brings the mean membrane potential above -55mV corresponding to the previously defined balance. The stimulation corresponds to an increase of the excitatory synaptic activity (still running within a very sparse range of activity, $\nu_e^d = \nu_e^p \in [0.05, 0.5]$Hz) with an increasing inhibitory activity adjusted to linearly disrupt nthe balance between -55mV and -52mV (see Figure 4). The synchrony is kept constant and the activity indifferentially raises in the proximal and distal part. This increase of total activity raises the input conductance ratio close to four. In this moderate range, the variations of the amplitude of the fluctuations σ_V remains a monotonic increase (unlike the non-monotonic variations found in the single-compartment study of Kuhn et al. (2004) and the case of a proximal stimulation, see below), the fluctuations

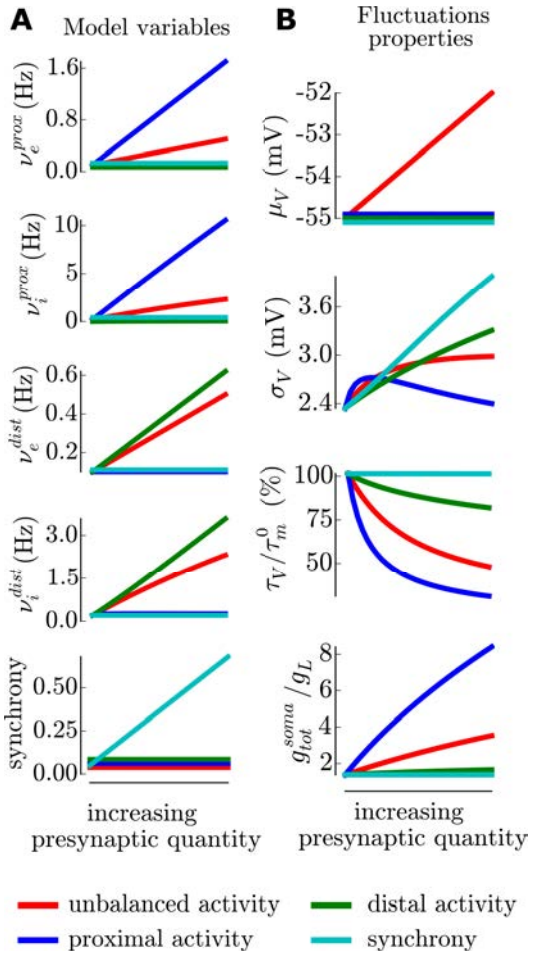

Figure 4: Properties of the membrane potential fluctuations for different types of presynaptic activity: either unbalanced, purely proximal, purely distal, synchronized (color code). A common baseline configuration of low balanced proximal and distal activity gives rise to baseline fluctuations properties, then we increase a given type of activity. **(A)** Model variables to achieve varying levels of those different types of activity. **(B)** Membrane potential fluctuations properties and somatic input conductance at the soma for the different protocols. Shown for the medium-size model, see Supplementary Material for the variability introduced by variations in cell morphologies.

gets approximately twice faster (the normalized autocorrelation time τ_V/τ_m^0 decays from 100% to 50%) and, of course (by design), the mean depolarization has a linear increase of 3mV.

We now emulate purely proximal activity. To this purpose, we fix the distal presynaptic firing frequencies (ν_e^d and ν_i^d) as well as the synchrony to their baseline levels. To remain in a sparse activity level, we increase the proximal excitatory activity from the baseline level to 1.7Hz and we adjust proximal and somatic inhibitory activity to keep the balance at the soma. This would nonethless correspond to large network activity level, as can be seen from the input conductance ratio (that raises up to 8). This situation gives results comparable to the single-compartment study of Kuhn et al. (2004). The amplitude of the fluctuations has a non-monotonic profile and the autocorrelation time strongly decreases. A notable difference is that, even if we investigated high activity levels, the autocorrelation time does not goes to zero and the amplitude of the fluctuations has only a moderate decrease. This discrepancy is due to 1) the choice of non-negligible synaptic time constants compared to the membrane time constants (here τ_{syn}=5ms and $\tau_m^0 \sim$ 25ms, then τ_V/tau$_m^0$ would saturate at τ_{syn}/tau$_m^0$ = 20%) and 2) the fact that the synaptic input is distributed attenuates the strong shunting effects observed in the single compartment case.

For distal activity, we keep the proximal presynaptic frequencies (ν_e^p and ν_i^p) as well as the synchrony to their baseline levels. We increase the distal excitatory activity from the baseline level to a moderate level: 0.7Hz. The distal inhibitory frequency is again adjusted to keep the balance at the soma. Here, we get a different picture than in the proximal case, the increase in activity leads to negligible increase of the somatic input conductance as expected from electrotonically distant input (Koch et al., 1990). Also, the decrease of the speed of the fluctuations is much attenuated, the reason for this is that only the distal part has a high conductance, consequently post-synaptic events are strongly low-pass filtered by the proximal part of the arborization before reaching the soma. Here, the amplitude of the fluctuations strongly increases as a function of the input and do not show the non-monotonic relation found for proximal input. This is explain by the combination of the fact that 1) distal events are of higher amplitude and 2) the shunting of post-synaptic events is much reduced due to the relatively narrow localization of the synaptic conductances.

Finally, we emulate an increase in the presynaptic synchrony. Here, all synaptic frequencies are kept constant with respect to the baseline level and we simply increase the probability of coincident events for each synaptic spike train. Because there is no change in synaptic activity, this stimulation does not affect the input conductance ratio, neither the mean membrane potential or the speed of the fluctuations. However, presynaptic synchrony strongly affects the amplitude of the fluctuations in a near linear manner.

Note, that in addition to the sparse activity constraints or the balance constraints, the criteria for the ranges of the model variables was manually choosen to have the fluctuations in the same domain. For example, we investigated a lower activity range for the distal part than for the proximal part to avoid an explosion of σ_V, the range for the synchrony increase follow the same criteria.

We thus demonstrated here, that, in a theoretical model of dendritic integration, the properties of the fluctuations (μ_V, σ_V, τ_V) can follow various comodulations, depending on the properties of the synaptic stimulation. This behavior is what motivated to fully scan the three dimensional space (μ_V, σ_V, τ_V) in our previous study.

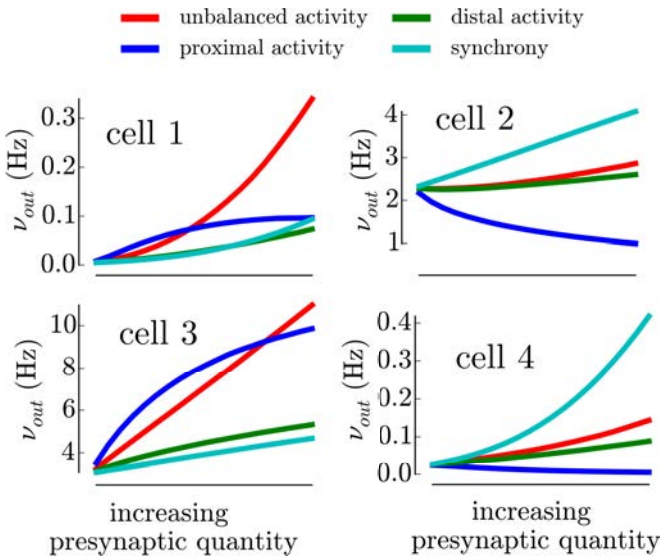

Figure 5: Examples of the firing response of 4 different cells for the different synaptic inputs (color-coded) shown in Figure 4. The abcissa corresponds to the variations of the model variables shown in Figure 4A

III.6 Heterogeneous fi ing responses induce diverse coupling to presynaptic activity

For each one of the n=27 cells of our previous study (Zerlaut et al., 2016), we now have 1) a morphological model and 2) a firing response function $\nu_{out} = \mathcal{F}(\mu_V, \sigma_V, \tau_V)$. Thanks to the analytical approximation, we can translate the five model variables $(\nu_e^p, \nu_i^p, \nu_e^d, \nu_i^d, s)$ into the stationary fluctuations properties $(\mu_V, \sigma_V, \tau_V)$ that, in turn, the firing response trsanslate into a spiking probability. Thus, we finally get the full *input-output* function (within our theoretical framework) as illustrated on Figure 1A.

We show on Figure 5 the response of four cells to the different types of presynaptic activity described in the previous section. The responses show qualitative and quantitative differences, we briefly discuss them here and we perform a more rigorous analysis in the next section.

First, we can see that individual cells have a very different level of response to the baseline level of synaptic activity (initial response in Figure 5). Cell 1 has a baseline at $\sim 10^{-2}$ Hz while Cell2 or Cell3 have response above 1Hz, i.e. two orders of magnitude above.

Importantly, those cells have different preferences for particular types of stimulations. Cell 1 responds more to unbalanced activity whereas Cell 2 and Cell 4 respond more to an increase in synchrony and Cell 3 responds preferentially to proximal activity (within this range). This is what we mean by *preferential coupling*: individual neurons will respond preferentially to a particular type of synaptic activity. An even more pronounced discrepancy appears for proximal activity: the response can be either increased (Cell 1 and Cell 3) or decreased (Cell 2 and Cell 4) with respect to the baseline level.

Given the relative invariance of the fluctuations properties for each cell (see previous section, despite the various morphologies, the same input creates the same fluctuations), those differences are the consequences of the heterogeneity in the firing responses, we conclude that *heterogeneous firing responses induce diverse coupling to presynaptic activity.*

III.7 Biophysical origin of the heterogenous couplings to presynaptic activities

We now make this analysis more quantitative by computing the responses for all n=27 cells. We get their response to the baseline level $\nu_{\rm bsl}$ and their mean response change for each stimulation type (the mean over the range of scanned presynaptic input): $\delta\nu_{\rm ubl}$ for the unbalanced activity, $\delta\nu_{\rm prox}$ for the proximal activity, $\delta\nu_{\rm dist}$ for the distal activity and $\delta\nu_{\rm synch}$ for an increased sychrony. We show the histogram of those values in the left column of Figure 6. We also look for the origin of the individual couplings by correlating them with the characteristics of the neuronal firing responses (Zerlaut et al., 2016).

We first analyze the response to baseline activity $\nu_{\rm bsl}$. When log-scaled (Figure 6A), the distribution is approximately normal and spans 2-3 orders of magnitude. This log-normal distribution of pyramidal cell firing rates during spontaneous activity seems to be a hallmark of mammalian neocortical dynamics (see e.g. (Peyrache et al., 2012) in human neocortex). We investigated what properties of the firing responses could explain this behavior, we therefore looked for correlations between our measures of the firing responses in the fluctuation-driven regime (Zerlaut et al., 2016) and the baseline responses. Not surprisingly, we found a very strong linear correlation between the excitability $\langle V_{\rm thre}^{\rm eff}\rangle_{\rm D}$ and the baseline response level, the other characteristics semt to have no impact (Pearson correlations, see values in Figure 6A). Again, it should be stressed that presynaptic connections are non-specific, those results therefore show that the typical log-normal distribution of firing rates could very naturally emerge as a result of the normal distribution observed in pyramidal cell's excitabilities (Zerlaut et al., 2016), thus suggesting that no specific circuitry is needed to explain this neocortical property.

Despite the important differences in the fluctuations they create (see Figure 4B), the responses over cells to unbalanced activity, distal activity and an increased synchrony share a very similar behavior. Their firing increases show a strong heterogeneity over cells, covering two orders of magnitude (see log y-axis on Figure 6B,D,E). This variability in responses was again highly correlated with the excitability. Surprisingly, the response was not dependent on any other of the characteristics of the firing response. For example, the variability observed during an increase in synchrony could have been linked to the to the sensitivity to the standard deviation $\sigma_{\rm V}$ $\langle\partial\nu/\partial\sigma_V\rangle_{\mathcal{D}}$, but this effect was not significant (p>0.05, Pearson correlation). This analysis therefore revealed that, for those type of synaptic activities, those properties of the firing response have negligible impact compared to the very strong effect of the variability in excitabilities. In the Supplementary Material we also investigated whether, after accounting for

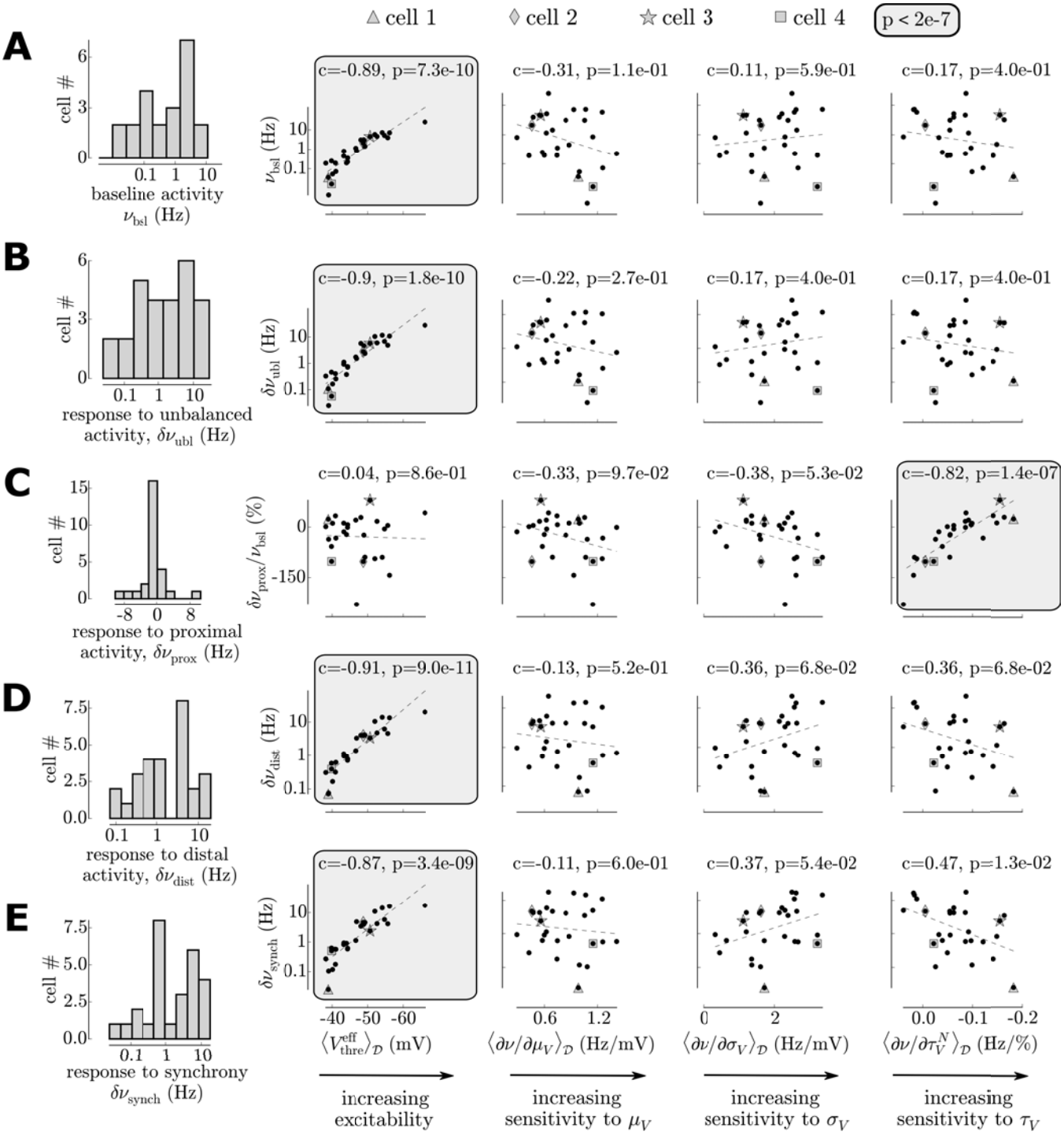

Figure 6: Diverse cellular responses to synaptic stimulation and their link to the chracteristics of their firing response function. Note the logarithmic scale for the firing respones in **B,C,D**. **(A)** Diverse response to baseline stimulation. **(B)** Diverse response to unbalanced activity. **(C)** Diverse response to proximal activity. Note that because the response also show negative changes of firing rate, the data can not be log-scaled. Instead, they have been rescaled by the baseline response. **(D)** Diverse response to distal activity. **(E)** Diverse response to a synchrony increase.

the variability due to the excitability, the residual variability would be explained by the characteristics of the firing response. Again, correlations were not significant, suggesting that those quantities have a very low explanatory power on the firing responses for those types of stimuli.

The response to proximal activity also showed a great variability but with a qualitatively different behavior (Figure 6C). Notably, firing could be suppressed or increased. This variability was independent of the excitability of the cells but was correlated with the sensitivity to the speed of the fluctuations $\langle \partial\nu/\partial\tau_V^N \rangle_{\mathcal{D}}$. Indeed, the proximal stimulation implies a strong variations of the fluctuations speed (i.e. decreasing τ_V, while keeping moderate variations of σ_V and, by design, a constant μ_V) thus rendering the sensitivity to the fluctuation speed the critical quantity for this stimulation type.

IV Discussion

In this paper, by introducing an analytically tractable dendritic model, we presented the final form of our theoretical framework for single cell computation in the fluctuation-driven regime. We used it to investigate how the heterogeneity in firing responses to fluctuating input shape the diverse input-output functions of neocortical pyramidal cells. Focusing on the regime of near asynchronous population dynamics, we emulated various type of presynaptic activity in a theoretical model of dendritic integration. We found that those different types of synaptic stimulation corresponds to various comodulations of the fluctuations properties, and that, because of their different response to the same fluctuations, individual neurons would respond differently to those stimulation.

The proposed theoretical framework for single-cell computation nonetheless suffers from several weaknesses. First the dendritic morphology is not so realistic, deviations from the symmetric branching and Rall's branching rule can have a significant impact on dendritic integration. Most importantly, there is no active mechanisms in dendrites (see London and Häusser (2005) for a review). Future work should try to implement dendritic non-linearities within this framework. Also it only enables to investigate dendritic integration in a context where information is processed through population rate (Shadlen and Newsome, 1994) and where it can be converted into temporal modulations of the membrane potential fluctuations. Future work could also investigate an extension yoward a *temporal coding* scheme. Because the core of the analytical calculus comes from an event-based strategy, this is theoretically feasible.

Despite those weaknesses, we believe that having an analytical model for dendritic integration in the fluctuation-driven regime is a useful tool for many problems in theoretical neuroscience. The main advantage of this model is that you can very naturally plug in physiological parameters (because surface area is physiological as well as transfer resistance to soma) and still it remains analytical (though see deviations of the approximations in Figure 3). In the field of neural network dynamics, the literature is exclusively based on the reduction to the single-compartment. Though being approximative, our framework thus opens the path toward an analysis of recurrent networks (see Renart et al. (2004) for a review) for extended dendritic structures.

Very naturally, a key quantity to explain the various neuronal responses was the cellular excitability. Indeed, the response to unbalanced activity, distal activity or an increase in synchrony was strongly correlated with cellular excitability. Also the sensitivity to the speed of the fluctuations had a crucial impact on the response to proximal activity. The present analysis therefore sheds light on the physiological relevance of the properties that we introduced in our previous study. In all four measures characterizing the cellular properties in the fluctuation-driven regime that we introduced in our previous study, only two of them seems to be physiologically relevant: the excitability and the sensitivity to the speed of the fluctuations (at least for the protocols that we tested). In our previous communication, theoretical modeling suggested that a high sensitivity to the speed of the fluctuations was enable by a high level of sodium inactivation. The present analysis thus proposes a functional role for sodium inactivation: controlling the response level to proximal activity.

In this study, the rescaling rule between input resistance at the soma and the size of the morphological model has led to the invariance in the relation between input (presynaptic variables) and the fluctuation properties. Thus the heterogeneity in morpholgies (here only cell sizes) had very little effects on the heterogeneity of cell responses. The variability in responses could only come from the various firing response functions. This confirms that we achieved a situation where the *circuit specificity* was null and responses varied because of various *biophysical specificities*.

We emphasize here that the introduction of the *biophysical specificity* is a *refinment* to explain the response of individual neurons. In response to a given stimulus, the *circuit specificity* relative to this stimulus will be the main contributor to the response. Taking back the example of the mice somato-sensory study of Crochet et al. (2011), active touch can elicit depolarizations in a *sim* 20mV range (from no depolarization to a 20mV depolarization) while action potential threshold spans a *sim* 5mV range (see Figure 5D in Crochet et al. (2011)). Thus there is a factor about 4 between the *circuit specificity* (how much one neuron will be depolarized in response to active touch) and its *biophysical specificity* (its action potential threshold). Nnote that we employed the term depolarization term to simplify the discussion, this actually corresponds to a reached level of membrane potential V_{rev}, see Crochet et al. (2011).

We now speculate about a putative link between a recent observation and the present findings. The *in vivo* study in mice visual cortex of Okun et al. (2015) reported a strong heterogeneity in the coupling between individual cell's responses and the locally recorded population activity. The authors explained those observations by a variabiliy in the local recurrent connectivity and argued that this diverse coupling did not seem to be explained by biophysical heterogeneity (e.g. the coupling was independent from the action potential threshold, somehow a measure of the

excitability). However, as local connectivity is thought to target more proximal regions (Spruston, 2008), our study proposes a biophysical mechanism that could contribute to their observation. The diverse coupling to proximal activity was explained by the sensitivity to the speed of the fluctuations, and similarly to their results, this coupling was found to be independent on the cellular excitability (see Figure 6). Note that two strong hypothesis underlie the previous reasoning: 1) that local population activity correspond to the proximal activity modeled our study, i.e. the activity should remains balanced, elicits strong changes in the speed of the fluctuations while limiting variations of σ_V and 2) that the biophysical heterogeneity for the sensitivity to τ_V observed in young mice cortex is at least partially preserved in adult animals. Future work could therefore adress this hypothesis by combining recordings of population activity with a more subtle and functionnally-relevant analysis of single cell properties (analogous to that of our previous communication).

V Material and Methods

V.1 Morphological model

The morphology of our theoretical model is the following (depicted in Figure 1B): it is made of an isopotential somatic compartment (i.e. a leaky RC circuit) in parallel with a dendritic structure. The dendritic tree is an arborization of total length L_t containing B generation of branches. For simplicity all branches of a generation $b \in [1, B]$ have a length L_t/B. From one generation to the other, a branch divides into two branches where the diameter of the daughter branches follows Rall's 3/2 branching rule (Rall, 1962): $(d_{b+1})^{\frac{3}{2}} = (d_b)^{\frac{3}{2}}/2$, i.e. $d_b = 2^{-\frac{2}{3}} d_t$ where d_t in the diameter of the root branch of the dendritic tree.

The parameters of the model are presented on Table 1.

V.2 Model equations: synaptic input and passive properties

The cable equation describes the temporal evolution and spatial spread of the membrane potential along the branches of the dendritic tree (Rall, 1962):

$$\frac{1}{r_i}\frac{\partial^2 v}{\partial x^2} = i_m(v,x,t) = c_m\frac{\partial v}{\partial t} + \frac{v - E_L}{r_m} - i_{syn}(v,x,t) \quad (1)$$

the membrane current $i_m(v,x,t)$ is a linear density of current (the presented cable equation already includes the radial symmetry). Though the modeled system has several branches, the equation can be written as a single spatial dependency x because the symmetry of the model across branches imply that the properties of the input are identical at a given distance to the soma.

Synaptic input is modeled by local (infinitely small) and transient changes of membrane permeability to selective ionic channels. Both excitatory (accounting for AMPA synapses) and inhibitory synapses (accounting for GABAa synapses) are considered, their reversal potential is E_e=0mV and E_i=-80mV respectively. Each synaptic event is generated by a shotnoise and its effect on the conductance is a jump followed by an exponential decay. The form of the synaptic current is therefore:

$$\begin{cases} i_{syn}(v,x,t) = g_e(x,t)(E_e - v) + g_i(x,t)(E_i - v) \\ g_e(x,t) = \sum_{\{x_e,\{t_e\}\}} \delta(x - x_e) \sum_{t_e} \mathcal{H}(t - t_e) Q_e(x)\, e^{-\frac{t-t_e}{\tau_e}} \\ g_i(x,t) = \sum_{\{x_i,\{t_i\}\}} \delta(x - x_i) \sum_{t_i} \mathcal{H}(t - t_i) Q_i(x)\, e^{-\frac{t-t_i}{\tau_i}} \end{cases} \quad (2)$$

where g_e and g_i are linear densities of conductances. Each synapse, indexed by s, has a position x_s and a set of presynaptic events $\{t_s\}$, hence the iteration over $\{x_s, \{t_s\}\}$ for the sum over synapses for each synaptic type. $\mathcal{H}$ is the Heaviside step function. The presynaptic events $\{t_s\}$ are generated by point processes at fixed frequencies ν_s with a given degree of synchrony, see details in the next section V.3.

The model distinguishes two domains : a proximal domain with the upper index p and a distal domain with the upper index d (see Figure 1). Then the space-dependent quantities (presynaptic frequencies, synaptic quantal and synaptic decay time constant) can be written as :

$$\begin{cases} \nu_e(x) = \nu_e^P + (\nu_e^d - \nu_e^p)\mathcal{H}(x - l_p) \\ \nu_i(x) = \nu_i^P + (\nu_i^d - \nu_i^p)\mathcal{H}(x - l_p) \\ Q_e(x) = Q_e^P + (Q_e^d - Q_e^p)\mathcal{H}(x - l_p) \\ Q_i(x) = Q_i^P + (Q_i^d - Q_i^p)\mathcal{H}(x - l_p) \end{cases} \quad (3)$$

The continuity of the membrane potential and of the current at the boundaries between the proximal and distal part imply:

$$\begin{cases} v(l_p^-, t) = v(l_p^+, t) \\ \frac{1}{r_i}\frac{\partial v}{\partial x}_{|l_p^-} = \frac{1}{r_i}\frac{\partial v}{\partial x}_{|l_p^+} \end{cases} \quad (4)$$

where the limit with upper index $\pm$ indicate the limit taken from the left or the right respectively.

At the soma, $(x = 0)$, we have a lumped impedance compartment. It has leaky RC circuit properties and also receives synaptic inhibition, the somatic membrane potential therefore follows :

$$\begin{cases} C_M\frac{dV}{dt} + \frac{V - E_L}{R_M} + G_I(t)\,(V - E_i) + I(t) = 0 \\ G_i(t) = \sum_{N_i}\sum_{\{t_i\}} Q_i^p\, e^{-\frac{-(t-t_i)}{\tau_i^p}}\, \mathcal{H}(t - t_i) \end{cases} \quad (5)$$

where $I(t)$ is the time-dependent input current from the soma into the dendrite. R_M and C_M are the RC properties of the lumped compartment (capital letters will indicate the somatic properties throughout the calculus). N_i is the number of somatic synapses, each of them generates a point process $\{t_i\}$ of inhibitory synaptic events. The properties of the somatic synapses (ν_i^S, Q_i^S) are equivalent to the proximal ones.

This equation with the membrane potential continuity will determine the boundary condition at the soma (x=0). We identify $V(t) = v(0,t)$, then $I(t)$ is the current input into the dendritic tree at $x = 0$ so it verifies:

$$\frac{\partial v}{\partial x}_{|x=0} = -r_i\, I(t) \quad (6)$$

So:

$$\frac{\partial v}{\partial x}_{|x=0} = r_i\left(C_M\frac{\partial v}{\partial t}_{|x=0} + \frac{v(0,t) - E_L}{R_m} + G_I(t)\,(v(0,t) - E_i)\right) \quad (7)$$

50

Table 1: Model parameters.

Parameters	Parameter Name	Symbol	Value	Unit
passive				
	leak resistivity density	r_m	325	μS/cm^2
	intracellular resistivity	r_i	30	Ω .cm
	specific capacitance	c_m	1.05	μF/cm^2
	leak reversal potential	$\mathrm{E_L}$	-65	mV
synaptic				
	inhibitory reversal potential	$\mathrm{E_i}$	-80	mV
	excitatory reversal potential	$\mathrm{E_e}$	0	mV
	somatic excitatory density	$\mathcal{D}_e^{soma}$	0	synapses/(100μm^2)
	somatic inhibitory density	$\mathcal{D}_i^{soma}$	20	synapses/(100μm^2)
	tree excitatory density	$\mathcal{D}_e^{tree}$	30	synapses/(100μm^2)
	tree inhibitory density	$\mathcal{D}_i^{tree}$	6	synapses/(100μm^2)
	prox. excitatory weight	$\mathrm{Q_e^{0,p}}$	0.7	nS
	prox. inhibitory weight	$\mathrm{Q_i^{0,p}}$	1.	nS
	distal excitatory weight	$\mathrm{Q_e^{0,d}}$	1.05	nS
	distal inhibitory weight	$\mathrm{Q_i^{0,d}}$	1.5	nS
	excitatory decay	τ_e	5	ms
	inhibitory decay	τ_i	5	ms
Mean morphology				
	soma length	$\mathrm{L_S}$	5.0	μm
	soma diameter	$\mathrm{D_S}$	15.0	μm
	root branch diameter	$\mathrm{D_t}$	2.25	μm
	tree length	$\mathrm{L_t}$	550.0	μm
	branch number	B	5	
	Proximal tree fraction	$\mathrm{f_{prox}}$	7/8	

Finally, the last boundary condition is that all branches terminate with an infinite resistance that impede current flow (sealed-end boundary conditions):

$$\frac{\partial v}{\partial x}_{x=l} = 0 \tag{8}$$

Together with the biased Poisson process for event generation (see the next section V.3), the final set of equations that describes the model, is therefore:

$$\begin{cases} \dfrac{1}{r_i}\dfrac{\partial^2 v}{\partial x^2} = c_m \dfrac{\partial v}{\partial t} + \dfrac{v - E_L}{r_m} - i_{syn}(v,x,t) \\ \dfrac{\partial v}{\partial x}_{|x=0} = r_i \left(C_M \dfrac{\partial v}{\partial t}_{|x=0} + \right. \\ \qquad \left. \dfrac{v(0,t) - E_L}{R_m} + G_I(t)\,(v(0,t) - E_i) \right) \\ v(l_p^-, t) = v(l_p^+, t) \\ \dfrac{\partial v}{\partial x}_{l_p^-} = \dfrac{\partial v}{\partial x}_{l_p^+} \\ \dfrac{\partial v}{\partial x}_{x=l} = 0 \end{cases} \tag{9}$$

V.3 Model of presynaptic activity

Presynaptic activity is modelled as a discrete set of presynaptic events. Because of the apparent random spiking activity in the fluctuation-driven regime, the basis for the generation of those discrete events is the Poisson process. Nonetheless, we want to reproduce the additional degree of presynaptic synchrony found in neocortical asssemblies that result mainly for two phenomena: 1) pairwise correlation between neurons and 2) muti-innervation of a cell by a presynaptic neuron. We therefore introduce a variable s that will bias the event generation of the Poisson process ($s \in [0,1]$). For simplicity in the analytical treatment, synchrony in presynaptic activity is not shared across different synapses. We arbitrarily limit the number of coincident events to four events, therefore for a degree of synchrony s: single events have a probability $1-s$, double events have a probability $s - s^2$, triple events events have a probability $s^2 - s^3$ and quadruple events have a probability s^3. To generate a biased Poisson process of frequency ν with a degree of synchrony s, we therefore generate a Poisson process of frequency:

$$\nu_{synch} = \frac{\nu}{1 + s + s^2 + s^3} \tag{10}$$

and we duplicate (from up to four events) each event according to their probabilities of occurence.

This is a very simplistic and limited model of presynaptic synchrony but it is sufficient for reproducing the impact of synchrony on the quantities investigated in this paper (only the variance of the membrane potential fluctuations).

V.4 Numerical implementation

The full model has been implemented numerically using the `NEURON` software. The branched morhology was created and passive cable properties were introduced (see Table 1). The spatial discretization was `nseg=30` segments per branch. On each segment, one excitatory and one inhibitory synapse were created, the shotnoise

frequency was then scaled according to the segment area and the synaptic density to account for the number of synapses on this segment (using the properties of the Poisson process, N

synapses at frequency ν is a synapse at frequency $N\nu$). Custom event generation was implemented to introduce correlations (instead of classical `NetStim`) and fed `NetCon` objects attached to each synapses (`ExpSyn` synapses). Each simulation had a time step dt=0.01ms and a length of 10s, the simulation was repeated over 4 seeds to yield a mean and a standard deviation in the estimate of the membrane potential fluctuations at the soma (see Figure 3B).

V.5 Analytical derivation of the fluctuation properties: strategy

We present here a derivation that provides an analytical approximation for the properties of the fluctuations of the membrane potential at the soma for our model. Summing up its properties, we get: 1) a morphology with a lumped somatic compartement and a dendritic tree of symmetric branching following Rall's rule 2) conductance-based synapses 3) independent excitatory and inhibitory shotnoise input spread all over the morphology 4) assymetric properties between a proximal part and a distal part and 5) a certain degree of synchrony in the pre-synaptic spikes.

The properties of the membrane potential fluctuations at the soma correspond to three stationary statistical properties of the fluctuations: their mean μ_V, their standard deviation σ_V and their *global* autocorrelation time τ_V. Following Zerlaut et al. (2016), we emphasize that the *global* autocorrelation time is a partial description of the autocorrelation function (as the autocorrelation function is not exponential) but it constitutes the first order description of the temporal dynamics of the fluctuations.

A commonly adopted strategy in the *fluctuation-driven* regime to obtain statistical properties is to use stochastic calculus after having performed the *diffusion approximation*, i.e. approximating the synaptic conductance time course by a stochastic process, see e.g. (Tuckwell et al., 2002)). This approach is nonetheless not easily generalizable to conductance input in an extended structure and render the inclusion of assymetric properties (proximal vs distal) complicated. We rather propose here an approach that combines simplifying assumptions and analytical results from shotnoise theory, it constitutes an extension of the approach proposed in Kuhn et al. (2004).

For each set of synaptic stimulation $\{\nu_p^e, \nu_i^p, \nu_e^d, \nu_i^d, s\}$, the derivation corresponds to the following steps:

- We transform the dendritic structure to its equivalent cylinder. The reduction to the equivalent cylinder is "activity-dependent" and captures the changes in membrane properties that results from the mean synaptic conductance levels.
- We derive a mean membrane potential $\mu_V(x)$ corresponding to the stationary response to constant densities of conductances given by the means of the synaptic stimulation. We use this space-dependent membrane potential $\mu_V(x)$ to fix the driving force all along the membrane for all synapses. The relation between synaptic events and the membrane potential now becomes linear.
- We derive a new cable equation that describes the variations of the membrane potential around this $\mu_V(x)$ solution.
- We calculate the effect of one synaptic event on a branch $b, b \in [1, B]$ at a distance x. We calculate the post-synaptic membrane potential event $\mathrm{PSP}_b(x,t)$ at the soma resulting from b synchronous synaptic events occuring at the distance x from the soma. We approximate the effect of only one event by rescaling the response by the number of input $\mathrm{PSP}_b(x,t)/b$.
- We use shotnoise theory to compute the power spectrum density of the membrane potential fluctuations resulting from all excitatory and inhibitory synaptic events (including the synchrony between events).

The full derivation has been conducted with the help of the python modulus for symbolic computation: `sympy` (deriving homogenous solutions is relatively simple but computing coefficients with the boudaries conditions give rise to complex expressions because of the number of parameters). The resulting expression were then exported to `numpy` functions for numerical evaluation. The `ipython` notebook that presents the full derivation is available on the following link.

V.6 From fluctuation properties to spiking probability

How layer V pyramidal neurons translate membrane potential fluctuations into a firing rate response was the focus of our previous communication, see Zerlaut et al. (2016). We re-use here the same dataset. Note that in the main text, we removed the n=4 cells that had too low or too high excitabilities firing rates, as it is hard to conduct an analysis on 7 orders of magnitudes from $\nu \in [10^{-5}, 10^2]$Hz (especially for data visualization). This reduction reduced the output variations to $\nu \in [10^{-1}, 10^1]$Hz. In the supplementary material, we reintroduce the discarded cells to show that they do not affect the results of the main text.

V.7 Experimental preparation and electrophysiological recordings

Experiments were performed at Unité de Neurosciences, Information et Complexité, Gif sur Yvette, France. Experimental procedures with animals were performed following the instructions of the European Council Directive 2010 86/609/EEC and its French transposition (Décret 2013/118). Experimental methods were identical to those presented in Zerlaut et al. (2016). Very briefly, we performed intracellular recordings in the current-clamp mode using the perforated patch technique on layer V pyramidal neurons of coronal slices of juvenile mice primary visual cortex. For the n=13 cells presented in this study, the access resistance R_S was 13.3MΩ ±5.4, the leak current at -75mV was -25.7pA ±17.3, cells had an input resistance R_m of 387.3MΩ ±197.2 and a membrane time constant at rest of 32.4ms ±23.1.

V.8 Input impedance characterization

To determine the input impedance at the soma, we injected sinusoidal currents in the current-clamp mode of the amplifier (Multiclamp 700B, Molecular Devices), we recorded the membrane potential response to a current input of the form $I(t) = I\ \sin(2\pi\, f\, t)$, we varied the frequencies f and amplitudes $I over 40 episodes per cell. The frequency range scanned was [0.1, 500] Hz. For each cell, we determined manually the current amplitude I_0 that gave a $\sim$ 5mV amplitude in a current step protocol, from this value, the value of I was scaled exponentially between I_0 at 0.1 Hz and $50I_0$ at 500Hz. The reason for varying the current amplitude (and not only the oscillation frequency) in those input impedance protocols is to anticipate for the low pass filtering of the membrane and insure that the

membrane potential response at high frequencies is far above the electronic noise level ($\sim$ 0.1 mV).

After removing the first 3 periods of the oscillations (to avoid transient effects), we fitted the membrane potential response to the form:

$$V(t) = E_L + R\,I\,\sin(2\pi\,f\,t - \phi) \tag{11}$$

where E_L, R and ϕ were fitted with a least-square minimization procedure. The frequency dependent values of R and ϕ give the modulus and phase shift of the input impedance presented in Figure 2A.

V.9 Fitting passive properties and a mean morphology

Because the variables combined discrete (the branch number) and continuous variables, the minimization consisted in taking the minimum over a grid of paramters. The parameter space has 7 dimensions (given here with the considered range): the branch number ($B \in [2, 7]$), the somatic length ($L_S \in [5, 20]\mu$m), the total length of the tree ($L_t \in [300, 800]\mu$m), the diameter of the root branch ($D_t \in [0.5, 4]\mu$m), the leak specific resistance ($r_m \in [100, 1000]\mu S/cm^2$), the intracellular resistivity ($r_i \in [10, 90]\Omega$.cm), the specific capacitance ($c_m \in [0.8, 1.8]\mu F/cm^2$).

Each dimension was discretized in 5 points, the scan of the 7 dimensional space then consisted in finding the least square residual of the product of the modulus and phase of the impedance over this 5^7 points. The resulting parameters are shown on Table 1.

VI Supplementary information

VI.1 Supplementary material

Supplementary material contains the detailed mathematical derivation of the membrane potential fluctuations

VI.2 Acknowledgments

We would like to thank Gilles Ouanounou for his help during electrophysiological recordings and Gérard Sadoc for assistance with the acquisistion software. We also thank Manon Richard and Aurélie Daret for animal facilities.

VI.3 Funding

Y.Z was supported by fellowships from the Initiative d'Excellence Paris-Saclay and the Fondation pour la Recherche Médicale (FDT 20150532751). Research funded by the CNRS and the European Community (BrainScales FP7-269921 and the Human Brain Project FP7-604102 to A.D.). The authors declare no competing financial interests.

VII References

Baudot P, Levy M, Marre O, Monier C, Pananceau M, Frégnac Y (2013) Animation of natural scene by virtual eye-movements evokes high precision and low noise in V1 neurons. *Frontiers in neural circuits* 7:206.

Crochet S, Poulet JFA, Kremer Y, Petersen CCH (2011) Synaptic mechanisms underlying sparse coding of active touch. *Neuron* 69:1160–1175.

DeFelipe J, As IF, Fariñas I (1992) The pyramidal neuron of the cerebral cortex: morphological and chemical characteristics of the synaptic inputs. *Progress in neurobiology* 39:563–607.

Destexhe A, Mainen ZF, Sejnowski TJ (1998) Kinetic Models of Synaptic Transmission.

Destexhe A, Rudolph M, Paré D (2003) The high-conductance state of neocortical neurons in vivo. *Nature reviews. Neuroscience* 4:739–751.

Ecker AS, Berens P, Keliris GA, Bethge M, Logothetis NK, Tolias AS (2010) Decorrelated neuronal firing in cortical microcircuits. *Science (New York, N.Y.)* 327:584–7.

El Boustani S, Destexhe A (2009) A master equation formalism for macroscopic modeling of asynchronous irregular activity states. *Neural computation* 21:46–100.

Ferster D, Chung S, Wheat H (1996) Orientation selectivity of thalamic input to simple cells of cat visual cortex. *Nature* 380:249–252.

Hines ML, Carnevale N (1997) The NEURON simulation environment. *Neural computation* 9:1179–209.

Hubel DH, Wiesel TN (1962) Receptive fields, binocular interaction and functional architecture in the cat's visual cortex. *The Journal of Physiology* 160:106–154.

Koch C, Douglas R, Wehmeier U (1990) Visibility of synaptically induced conductance changes: theory and simulations of anatomically characterized cortical pyramidal cells. *The Journal of neuroscience : the official journal of the Society for Neuroscience* 10:1728–44.

Kuhn A, Aertsen A, Rotter S (2004) Neuronal integration of synaptic input in the fluctuation-driven regime. *The Journal of neuroscience : the official journal of the Society for Neuroscience* 24:2345–56.

London M, Häusser M (2005) Dendritic computation. *Annual review of neuroscience* 28:503–532.

Magee JC (2000) Dendritic integration of excitatory synaptic input. *Nature reviews. Neuroscience* 1:181–190.

Okun M, Steinmetz NA, Cossell L, Iacaruso MF, Ko H, Barthó P, Moore T, Hofer SB, Mrsic-Flogel TD, Carandini M et al. (2015) Diverse coupling of neurons to populations in sensory cortex. *Nature* 521:511–515.

Peyrache A, Dehghani N, Eskandar EN, Madsen JR, Anderson WS, Donoghue Ja, Hochberg LR, Halgren E, Cash SS, Destexhe A (2012) Spatiotemporal dynamics of neocortical excitation and inhibition during human sleep. *Proceedings of the National Academy of Sciences of the United States of America* 109:1731–6.

Rall W (1962) Electrophysiology of a dendritic neuron model. *Biophysical journal* 2:145.

Renart A, Brunel N, Wang XJ (2004) Mean-field theory of irregularly spiking neuronal populations and working memory in recurrent cortical networks. *Computational neuroscience: A comprehensive approach* pp. 431–490.

Renart A, Rocha JD, Bartho P, Hollender L, Parga N, Reyes A, Harris KD, de la Rocha J (2010) The asynchronous state in cortical circuits. *Science (New York, N.Y.)* 327:587–90.

Rossant C, Leijon S, Magnusson aK, Brette R (2011) Sensitivity of Noisy Neurons to Coincident Inputs. *Journal of Neuroscience* 31:17193–17206.

Shadlen MN, Newsome WT (1994) Noise, neural codes and cortical organization. *Current Opinion in Neurobiology* 4:569–579.

53

Spruston N (2008) Pyramidal neurons: dendritic structure and synaptic integration. *Nature reviews. Neuroscience* 9:206–21.

Tuckwell HC, Wan FYM, Rospars JP (2002) A spatial stochastic neuronal model with Ornstein–Uhlenbeck input current. *Biological cybernetics* 86:137–145.

Yang H, Kwon SE, Severson KS, O'Connor DH (2015) Origins of choice-related activity in mouse somatosensory cortex. *Nature neuroscience* 19:127–134.

Zerlaut Y, Telenczuk B, Deleuze C, Bal T, Ouanounou G, Destexhe A (2016) Heterogeneous firing response of mice layer V pyramidal neurons in the fluctuation-driven regime. *The Journal of Physiology* in press.

Supplementary Material

Heterogenous firing responses leads to diverse coupling to presynaptic activity in a simplified morphological model of layer V pyramidal neurons

Y. Zerlaut & A. Destexhe

April 7, 2016

Contents

1 Heterogeneity in the morphologies

We give here a graphical representation of the two extreme morphologies considered in this study.

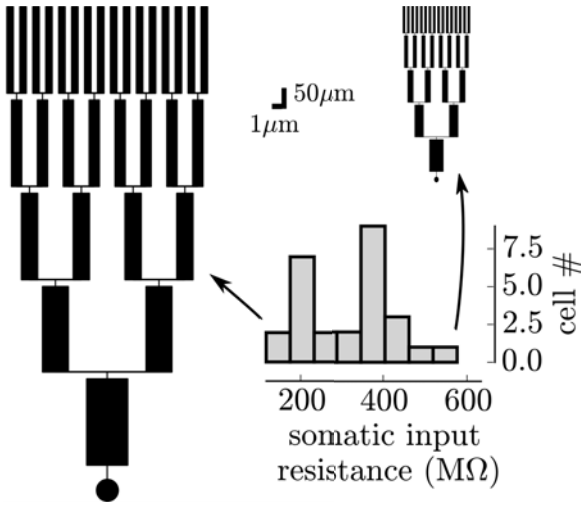

Figure 1: **Representaiton of the biggest and smallest cells.**

2 Reduction to the equivalent cylinder

The key of the derivation relies on having the possibility to reduce the complex morphology to an equivalent cylinder (Rall, 1962). We adapted this procedure to capture the change in integrative properties of the membrane that results from the mean synaptic bombardment during active cortical states, reviewed in Destexhe et al. (2003).

For a set of synaptic stimulation $\{\nu_p^e, \nu_i^p, \nu_e^d, \nu_i^d, s\}$, let's introduce the following stationary densities of conductances:

$$\begin{cases} g_{e0}^p = \pi\, d\, \mathcal{D}_e\, \nu_e^p\, \tau_e^p\, Q_e^p & ; \quad g_{i0}^p = \pi\, d\, \mathcal{D}_i\, \nu_i^p\, \tau_i^p\, Q_i^p \\ g_{e0}^d = \pi\, d\, \mathcal{D}_e\, \nu_e^d\, \tau_e^d\, Q_e^d & ; \quad g_{i0}^d = \pi\, d\, \mathcal{D}_i\, \nu_i^d\, \tau_i^d\, Q_i^d \end{cases} \tag{1}$$

where $\mathcal{D}_e$ and $\mathcal{D}_i$ are the excitatory and inhibitory synaptic densities.

We introduce two activity-dependent electrotonic constants relative to the proximal and distal part respectively:

$$\lambda^p = \sqrt{\frac{r_m}{r_i(1 + r_m g_{e0}^p + r_m g_{i0}^p)}} \quad \lambda^d = \sqrt{\frac{r_m}{r_i(1 + r_m g_{e0}^d + r_m g_{i0}^d)}}$$

(2)

For a dendritic tree of total length l, whose proximal part ends at l_p and with B evenly spaced generations of branches, we define the space-dependent electrotonic constant:

$$\lambda(x) = \big(\lambda^p + \mathcal{H}(x - l_p)(\lambda^d - \lambda^p)\big) 2^{-\frac{1}{3}\lfloor \frac{B\,x}{l} \rfloor} \tag{3}$$

where $\lfloor . \rfloor$ is the floor function. Note that $\lambda(x)$ is constant on a given generation, but it decreases from generation to generation because of the decreasing diameter along the dendritic tree. It also depends on the synaptic activity and therefore has a discontinuity at $x = l_p$.

Following Rall (1962), we now define a dimensionless length X:

$$X(x) = \int_0^x \frac{dx}{\lambda(x)} \tag{4}$$

We define $L = X(l)$ and $L_p = X(l_p)$, the total length and proximal part length respectively (capital letters design rescaled quantities).

3 Mean membrane potential

We derive the mean membrane potential $\mu_V(x)$ corresponding to the stationary response to constant densities of conductances given by the means of the synaptic stimulation. We obtain the stationary equations by removing temporal derivatives in Equation, the set of equation governing this mean membrane potential in all branches is therefore:

$$\begin{cases} \dfrac{1}{r_i}\dfrac{\partial^2 \mu_v}{\partial x^2} = \dfrac{\mu_v(x) - E_L}{r_m} \\ \qquad - g^p_{e0}\left(\mu_v(x) - E_e\right) - g^p_{0i}\left(\mu_v(x) - E_i\right) \quad \forall x \in [0, l_p] \\ \dfrac{1}{r_i}\dfrac{\partial^2 \mu_v}{\partial x^2} = \dfrac{\mu_v(x) - E_L}{r_m} \\ \qquad - g^d_{e0}\left(\mu_v(x) - E_e\right) - g^d_{0i}\left(\mu_v(x) - E_i\right) \quad \forall x \in [l_p, l] \\ \dfrac{\partial \mu_v}{\partial x}_{|x=0} = r_i\left(\dfrac{\mu_v(0) - E_L}{R_m} + G^S_{i0}\left(\mu_v(0) - E_i\right)\right) \\ \mu_v(l_p^-, t) = \mu_v(l_p^+, t) \\ \dfrac{\partial \mu_v}{\partial x}_{l_p^-} = \dfrac{\partial \mu_v}{\partial x}_{l_p^+} \\ \dfrac{\partial \mu_v}{\partial x}_{x=l} = 0 \end{cases} \tag{5}$$

Because the reduction to the equivalent cylinder conserves the membrane area and the previous equation only depends on density of currents, the equation governing $\mu_v(x)$ in all branches can be transformed into an equation on an equivalent cylinder of length L. We rescale x by $\lambda(x)$ (see Equation 4) and we obtain the equation verified by $\mu_V(X)$:

$$\begin{cases} \dfrac{\partial^2 \mu_v}{\partial X^2} = \mu_v(X) - v_0^p \quad \forall X \in [0, L_p] \\ \dfrac{\partial^2 \mu_v}{\partial X^2} = \mu_v(X) - v_0^d \quad \forall X \in [L_p, L] \\ \dfrac{\partial \mu_v}{\partial X}|_{X=0} = \gamma^p \left(\mu_v(0) - V_0\right) \\ \mu_v(L_p^-) = \mu_v(L_p^+) \\ \dfrac{\partial \mu_v}{\partial X}_{L_p^-} = \dfrac{\lambda^p}{\lambda^d} \dfrac{\partial \mu_v}{\partial X}_{L_p^+} \\ \dfrac{\partial \mu_v}{\partial X}_{X=L} = 0 \end{cases} \tag{6}$$

where:

$$\begin{aligned} v_0^p &= \frac{E_L + r_m g_{e0}^p E_e + r_m g_{i0}^p E_i}{1 + r_m g_{e0}^p + r_m g_{i0}^p} \\ v_0^d &= \frac{E_L + r_m g_{e0}^d E_e + r_m g_{i0}^d E_i}{1 + r_m g_{e0}^d + r_m g_{i0}^d} \\ \gamma^p &= \frac{r_i \lambda^p \left(1 + G_i^0 R_m\right)}{R_m} \\ V_0 &= \frac{E_L + G_i^0 R_m E_i}{1 + + G_i^0 R_m} \end{aligned} \tag{7}$$

We write the solution on the form:

$$\begin{cases} \mu_v(X) = v_0^p + A\, \cosh(X) + C\, \sinh(X) \quad \forall\, X \in [0, L_p] \\ \mu_v(X) = v_0^d + B\, \cosh(X - L) + D\, \sinh(X - L) \quad \forall\, X \in [L_p L] \end{cases} \tag{8}$$

- Sealed-end boundary condition at cable end implies $D = 0$
- Somatic boudary condition imply: $C = \gamma^p \left(v_0^p - V_0 + A\right)$
- Then v continuity imply : $v_0^p + A\, \cosh(L_p) + \gamma^p \left(v_0^p - V_0 + A\right) \sinh(L_p) = v_0^d + B\, \cosh(L_p - L)$
- Then current conservation imply: $A\, \sinh(L_p) + \gamma^p \left(v_0^p - V_0 + A\right) \cosh(L_p) = \frac{\lambda^p}{\lambda^d} B\, \sinh(L_p - L)$

We rewrite those condition on a matrix form:

$$\begin{pmatrix} \cosh(L_p) + \gamma^p \sinh(L_p) & -\cosh(L_p - L) \\ \sinh(L_p) + \gamma^p \cosh(L_p) & -\frac{\lambda^p}{\lambda^d} \sinh(L_p - L) \end{pmatrix} \cdot \begin{pmatrix} A \\ B \end{pmatrix} = \begin{pmatrix} v_0^d - v_0^p - \gamma^p \left(v_0^p - V_0\right) \sinh(L_p) \\ -\gamma^p \left(v_0^p - V_0\right) \cosh(L_p) \end{pmatrix} \tag{9}$$

And we solved this equation with the `solve_linear_system_LU` method of `sympy`

The coefficients A and B are given by:

$$A = \frac{\alpha}{\beta} \qquad B = \frac{\gamma}{\delta} \tag{10}$$

where:

$$\begin{aligned}
\alpha &= V_0\gamma^P\lambda^D\cosh(L_p)\cosh(L-L_p) + V_0\gamma^P\lambda^P\sinh(L_p)\sinh(L-L_p) \\
&\quad - \gamma^P\lambda^D v_0^d\cosh(L_p)\cosh(L-L_p) - \gamma^P\lambda^P v_0^d\sinh(L_p)\sinh(L-L_p) \\
&\quad - \lambda^P v_0^d\sinh(L-L_p) + \lambda^P v_0^p\sinh(L-L_p) \\
\beta &= \gamma^P\lambda^D\cosh(L_p)\cosh(L-L_p) + \gamma^P\lambda^P\sinh(L_p)\sinh(L-L_p) + \\
&\quad \lambda^D\sinh(L_p)\cosh(L-L_p) + \lambda^P\sinh(L-L_p)\cosh(L_p) \\
\gamma &= \lambda^D\big(V_0\gamma^P + \gamma^P v_0^d\cosh(L_p) - \gamma^P v_0^d \\
&\quad - \gamma^P v_0^p\cosh(L_p) + v_0^d\sinh(L_p) - v_0^p\sinh(L_p)\big) \\
\delta &= \gamma^P\lambda^D\cosh(L_p)\cosh(L-L_p) + \gamma^P\lambda^P\sinh(L_p)\sinh(L-L_p) \\
&\quad + \lambda^D\sinh(L_p)\cosh(L-L_p) + \lambda^P\sinh(L-L_p)\cosh(L_p)
\end{aligned} \tag{11}$$

4 Membrane potential response to a synaptic event

We now look for the response to $n_{src} = \lfloor \frac{B\,x_{src}}{l} \rfloor$ synaptic events at position x_{src} on all branches of the generation of x_src, those events have a conductance $g(t)/n_{src}$ and reversal potential E_{rev}. We make the hypothesis that the initial condition correspond to the stationary mean membrane potential $\mu_V(x)$. This potential will also be used to fix the driving force at the synapse to $\mu_v(x_{src}) - E_{rev}$, this linearizes the equation and will allow an analytical treatment. To derive the equation for the response around the mean $\mu_v(x)$, we rewrite Equation 9 in main text with $v(x,t) = \delta v(x,t) + \mu_v(x)$, we obtain the equation for $\delta v(x,t)$:

$$
\begin{cases}
\dfrac{1}{r_i}\dfrac{\partial^2 \delta v}{\partial x^2} = c_m \dfrac{\partial \delta v}{\partial t} + \dfrac{\delta v}{r_m}(1 + r_m\, g^p_{e0} + r_m\, g^p_{i0}) \\
\qquad\qquad - \delta(x - x_{src})\left(\mu_v(x_{src}) - E_{rev}\right)\dfrac{g(t)}{n_{src}}, \quad \forall x \in [0, l_p] \\
\dfrac{1}{r_i}\dfrac{\partial^2 \delta v}{\partial x^2} = c_m \dfrac{\partial \delta v}{\partial t} + \dfrac{\delta v}{r_m}(1 + r_m\, g^d_{e0} + r_m\, g^d_{i0}) \\
\qquad\qquad - \delta(x - x_{src})\left(\mu_v(x_{src}) - E_{rev}\right)\dfrac{g(t)}{n_{src}}, \quad \forall x \in [l_p, l] \\
\dfrac{1}{r_i}\dfrac{\partial \delta v}{\partial x}_{|x=0} = C_M \dfrac{\partial \delta v}{\partial t}_{|x=0} + \dfrac{\delta v(0,t)}{R_m}(1 + R_m G^S_{i0}) \\
\delta v(l_p^-, t) = \delta v(l_p^+, t) \\
\dfrac{\partial \delta v}{\partial x}_{l_p^-} = \dfrac{\partial \delta v}{\partial x}_{l_p^+} \\
\dfrac{\partial \delta v}{\partial x}_{x=l} = 0
\end{cases}
\tag{12}
$$

Because this synaptic event is concomitant in all branches at distance x_{src}, we can use again the reduction to the equivalent cylinder (note that the event has now a weight multiplied by n_{src} so that its conductance becomes $g(t)$), we obtain:

$$
\begin{cases}
\dfrac{\partial^2 \delta v}{\partial X^2} = \left(\tau^p_m + (\tau^d_m - \tau^p_m)\mathcal{H}(X - L_p)\right)\dfrac{\partial \delta v}{\partial t} + \delta v \\
\qquad\qquad - \left(\mu_v(X_{src}) - E_{rev}\right)\delta(X - X_{src})\times \\
\qquad\qquad\quad \dfrac{g(t)}{c_m}\left(\dfrac{\tau^p_m}{\lambda^p} + (\dfrac{\tau^d_m}{\lambda^d} - \dfrac{\tau^p_m}{\lambda^p})\mathcal{H}(X_{src} - L_p)\right) \\
\dfrac{\partial \delta v}{\partial X}_{|X=0} = \gamma^p\left(\tau^S_m \dfrac{\partial \delta v}{\partial t}_{|X=0} + \delta v(0,t)\right) \\
\delta v(L_p^-, t) = \delta v(L_p^+, t) \\
\dfrac{\partial \delta v}{\partial X}_{L_p^-} = \dfrac{\lambda^p}{\lambda^d}\dfrac{\partial \delta v}{\partial X}_{L_p^+} \\
\dfrac{\partial \delta v}{\partial X}_{X=L} = 0
\end{cases}
\tag{13}
$$

where we have introduced the following time constants:

$$
\begin{aligned}
\tau^D_m &= \frac{r_m\, c_m}{1 + r_m\, g^d_{e0} + r_m\, g^d_{i0}} \\
\tau^P_m &= \frac{r_m\, c_m}{1 + r_m\, g^p_{e0} + r_m\, g^p_{i0}} \\
\tau^S_m &= \frac{R_m\, C_m}{1 + R_m\, G^S_{i0}}
\end{aligned}
\tag{14}
$$

Now used distribution theory (see Appel (2008) for a comprehensive textbook) to translate the synaptic input into boundary conditions at X_{src}, physically this corresponds to: 1) the continuity of the membrane potential and 2) the discontinuity of the current resulting from the synaptic input.

$$\begin{cases} \delta v(X_{src}^-, f) = \delta v(X_{src}^+, f) \\ \dfrac{\partial \delta v}{\partial X}_{X_{src}^+} - \dfrac{\partial \delta v}{\partial X}_{X_{src}^-} = -\big(\mu_v(X_{src}) - E_{rev}\big)\times \\ \qquad\qquad \Big(\dfrac{\tau_m^p}{\lambda^p} + (\dfrac{\tau_m^d}{\lambda^d} - \dfrac{\tau_m^p}{\lambda^p})\mathcal{H}(X_{src} - L_p)\Big)\,\dfrac{g(t)}{c_m} \end{cases} \tag{15}$$

We will solve Equation 13 by using Fourier analysis. We take the following convention for the Fourier transform:

$$\hat{F}(f) = \int_{\mathbb{R}} F(t)\, e^{-2i\pi f t}\, dt \tag{16}$$

We Fourier transform the set of Equations 13, we obtain:

$$\begin{cases} \dfrac{\partial^2 \hat{\delta v}}{\partial X^2} = \big(\alpha_f^p + (\alpha_f^d - \alpha_f^p)\mathcal{H}(X - L_p)\big)^2\, \hat{\delta v} \\ \dfrac{\partial \hat{\delta v}}{\partial X}_{|X=0} = \gamma_f^p\, \hat{\delta v}(0, f) \\ \hat{\delta v}(X_{src}^-, f) = \hat{\delta v}(X_{src}^+, f) \\ \dfrac{\partial \hat{\delta v}}{\partial X}_{X_{src}^-} = \dfrac{\partial \hat{\delta v}}{\partial X}_{X_{src}^+} - \big(\mu_v(X_{src}) - E_{rev}\big)\times \\ \qquad\qquad \big(r_f^p + (r_f^d - r_f^p)\mathcal{H}(X_{src} - L_p)\big)\, \hat{g(f)} \\ \hat{\delta v}(L_p^-, f) = \hat{\delta v}(L_p^+, f) \\ \dfrac{\partial \hat{\delta v}}{\partial X}_{L_p^-} = \dfrac{\lambda^p}{\lambda^d}\, \dfrac{\partial \hat{\delta v}}{\partial X}_{L_p^+} \\ \dfrac{\partial \hat{\delta v}}{\partial X}_{X=L} = 0 \end{cases} \tag{17}$$

where

$$\begin{aligned} \alpha_f^p &= \sqrt{1 + 2i\pi f \tau_m^p} \qquad r_f^p = \frac{\tau_m^p}{c_m\, \lambda^p} \\ \alpha_f^d &= \sqrt{1 + 2i\pi f \tau_m^d} \qquad r_f^d = \frac{\tau_m^d}{c_m\, \lambda^d} \\ \gamma_f^p &= \gamma^p\, (1 + 2i\pi f \tau_m^S) \end{aligned} \tag{18}$$

To obtain the solution, we need to split the solution into two cases:

1. $X_{src} \leq L_p$

Let's write the solution to this equation as the form (already including the boundary conditions at $X = 0$ and $X = L$):

$$\hat{\delta v}(X, X_{src}, f) =$$
$$\begin{cases} A_f(X_{src}) \left(\cosh(\alpha_f^p \, X) + \gamma^p \, \sinh(\alpha_f^p \, X) \right) \\ \qquad \text{if :} 0 \leq X \leq X_{src} \leq L_p \leq L \\ B_f(X_{src}) \, \cosh(\alpha_f^p \, (X - L_p)) + C_f(X_{src}) \, \sinh(\alpha_f^p \, (X - L_p)) \\ \qquad \text{if :} 0 \leq X_{src} \leq X \leq L_p \leq L \\ D_f(X_{src}) \, \cosh(\alpha_f^d \, (X - L)) \\ \qquad \text{if :} 0 \leq X_{src} \leq L_p \leq X \leq L \end{cases} \tag{19}$$

We write the 4 conditions correspondingto the conditions in X_{src} and L_p to get A_f, B_f, C_f, D_f. On a matrix form, this gives:

$$M = \begin{pmatrix} \cosh(\alpha_f^p \, X_{src}) + \gamma_f^p \sinh(\alpha_f^p \, X_{src}) & -\cosh(\alpha_f^p \, (X_{src} - L_p)) & -\sinh(\alpha_f^p \, (X_{src} - L_p)) & 0 \\ \alpha_f^p \big(\sinh(\alpha_f^p \, X_{src}) + \gamma_f^p \cosh(\alpha_f^p \, X_{src}) \big) & -\alpha_f^p \sinh(\alpha_f^p \, (X_{src} - L_p)) & -\alpha_f^p \cosh(\alpha_f^p \, (X_{src} - L_p)) & 0 \\ 0 & 1 & 0 & -\cosh(\alpha_f^d \, (L_p - L)) \\ 0 & 0 & \alpha_f^p & -\alpha_f^d \frac{\lambda^p}{\lambda^d} \, \sinh(\alpha_f^d \, (L_p - L)) \end{pmatrix} \tag{20}$$

$$M \cdot \begin{pmatrix} A_f \\ B_f \\ C_f \\ D_f \end{pmatrix} = \begin{pmatrix} 0 \\ -r_f^p I_f \\ 0 \\ 0 \end{pmatrix} \tag{21}$$

And we will solve it with the `solve_linear_system_LU` method of `sympy`. For the $A_f(X_{src})$ coefficient, we obtain:

$$A_f(X_{src}) = \frac{a_f^1(X_{src})}{a_f^2(X_{src})} \tag{22}$$

with:

$$
\begin{aligned}
a_f^1(X_{src}) = I_f r_f^P \big(&-\alpha_f^D \lambda^P \cosh\left(L\alpha_f^D - L_p\alpha_f^D - L_p\alpha_f^P + X_s\alpha_f^P\right) \\
&+ \alpha_f^D \lambda^P \cosh\left(L\alpha_f^D - L_p\alpha_f^D + L_p\alpha_f^P - X_s\alpha_f^P\right) \\
&+ \alpha_f^P \lambda^D \cosh\left(L\alpha_f^D - L_p\alpha_f^D - L_p\alpha_f^P + X_s\alpha_f^P\right) \\
&+ \alpha_f^P \lambda^D \cosh\left(L\alpha_f^D - L_p\alpha_f^D + L_p\alpha_f^P - X_s\alpha_f^P\right) \\
a_f^2(X_{src}) = \alpha_f^P \big(&-\alpha_f^D \gamma_f^P \lambda^P \cosh\left(-L\alpha_f^D + L_p\alpha_f^D + L_p\alpha_f^P\right) \\
&+ \alpha_f^D \gamma_f^P \lambda^P \cosh\left(L\alpha_f^D - L_p\alpha_f^D + L_p\alpha_f^P\right) - \\
&\alpha_f^D \lambda^P \sinh\left(-L\alpha_f^D + L_p\alpha_f^D + L_p\alpha_f^P\right) \\
&+ \alpha_f^D \lambda^P \sinh\left(L\alpha_f^D - L_p\alpha_f^D + L_p\alpha_f^P\right) \\
&+ \alpha_f^P \gamma_f^P \lambda^D \cosh\left(-L\alpha_f^D + L_p\alpha_f^D + L_p\alpha_f^P\right) \\
&+ \alpha_f^P \gamma_f^P \lambda^D \cosh\left(L\alpha_f^D - L_p\alpha_f^D + L_p\alpha_f^P\right) \\
&+ \alpha_f^P \lambda^D \sinh\left(-L\alpha_f^D + L_p\alpha_f^D + L_p\alpha_f^P\right) \\
&+ \alpha_f^P \lambda^D \sinh\left(L\alpha_f^D - L_p\alpha_f^D + L_p\alpha_f^P\right)
\end{aligned}
\tag{23}
$$

2. $ $ \mathrm{L_p} \leq \mathrm{X_{src}} $ $

   Let's write the solution to this equation as the form (already including the boundary conditions at $X = 0$ and $X = L$:

$$
\hat{\delta v}(X, X_{src}, f) =
\begin{cases}
E_f(X_{src}) \left(\cosh(\alpha_f^p\, X) + \gamma^p\, \sinh(\alpha_f^p\, X)\right) \\
\qquad \text{if } :0 \leq X \leq L_p \leq X_{src} \leq L \\
F_f(X_{src})\, \cosh(\alpha_f^d\, (X - L_p)) + G_f(X_{src})\, \sinh(\alpha_f^d\, (X - L_p)) \\
\qquad \text{if } :0 \leq L_p \leq X \leq X_{src} \leq L \\
H_f(X_{src})\, \cosh(\alpha_f^d\, (X - L)) \\
\qquad \text{if } :0 \leq L_p \leq X_{src} \leq X \leq L
\end{cases}
\tag{24}
$$

   We write the 4 conditions correspondingto the conditions in X_{src} and L_p to get A_f, B_f, C_f, D_f. On a matrix form, this gives:

   We rewrite this condition on a matrix form:

$$
M_2 = \begin{pmatrix}
\cosh(\alpha_f^p\, L_p) + \gamma_f^p \sinh(\alpha_f^p\, L_p) & -1 & 0 & 0 & 0 \\
\alpha_f^p \big(\sinh(\alpha_f^p\, L_p) + \gamma_f^p \cosh(\alpha_f^p\, L_p)\big) & 0 & -\alpha_f^d \frac{\lambda^p}{\lambda^d} & 0 & \\
0 & \cosh(\alpha_f^d\, (X_{src} - L_p)) & \sinh(\alpha_f^d\, (X_{src} - L_p)) & -\cosh(\alpha_f^d\, (X_{src} - L)) & \\
0 & \alpha_f^d\, \sinh(\alpha_f^d\, (X_{src} - L_p)) & \alpha_f^d\, \cosh(\alpha_f^d\, (X_{src} - L_p)) & -\alpha_f^d\, \sinh(\alpha_f^d\, (X_{src} - L)) &
\end{pmatrix}
\tag{25}
$$

$$M \cdot \begin{pmatrix} E_f \\ F_f \\ G_f \\ H_f \end{pmatrix} = \begin{pmatrix} 0 \\ 0 \\ 0 \\ -r_f^d I_f \end{pmatrix} \tag{26}$$

And we will solve it with the `solve_linear_system_LU` method of `sympy`. For the $E_f(X_{src})$ coefficient, we obtain:

$$E_f(X_{src}) = \frac{e_f^1(X_{src})}{e_f^2(X_{src})} \tag{27}$$

with:

$$\begin{aligned}
e_f^1(X_{src}) &= 2 I_f \lambda^P r_f^D \cosh\left(\alpha_f^D \left(L - X_s\right)\right) \\
e_f^2(X_{src}) &= -\alpha_f^D \gamma_f^P \lambda^P \cosh\left(-L\alpha_f^D + L_p\alpha_f^D + L_p\alpha_f^P\right) \\
&\quad + \alpha_f^D \gamma_f^P \lambda^P \cosh\left(L\alpha_f^D - L_p\alpha_f^D + L_p\alpha_f^P\right) \\
&\quad - \alpha_f^D \lambda^P \sinh\left(-L\alpha_f^D + L_p\alpha_f^D + L_p\alpha_f^P\right) \\
&\quad + \alpha_f^D \lambda^P \sinh\left(L\alpha_f^D - L_p\alpha_f^D + L_p\alpha_f^P\right) \\
&\quad + \alpha_f^P \gamma_f^P \lambda^D \cosh\left(-L\alpha_f^D + L_p\alpha_f^D + L_p\alpha_f^P\right) \\
&\quad + \alpha_f^P \gamma_f^P \lambda^D \cosh\left(L\alpha_f^D - L_p\alpha_f^D + L_p\alpha_f^P\right) \\
&\quad + \alpha_f^P \lambda^D \sinh\left(-L\alpha_f^D + L_p\alpha_f^D + L_p\alpha_f^P\right) \\
&\quad + \alpha_f^P \lambda^D \sinh\left(L\alpha_f^D - L_p\alpha_f^D + L_p\alpha_f^P\right)
\end{aligned} \tag{28}$$

3. PSP at the soma

   The main text writes a solution for the PSP at soma of the form:

$$\hat{\delta v}(X = 0, X_{src}, f) = K_f(X_{src}) \left(\mu_v(X_{src}) - E_{rev}\right) \hat{g(f)} \tag{29}$$

   The correspondance with the previous calculus is to take a unitary current $I_f = 1$ and $K_f(X_{src})$ given by:

$$K_f(X_{src}) = \begin{cases} A_f(X_{src}) \forall X_{src} \in [0, L_p] \\ E_f(X_{src}) \forall X_{src} \in [L_p, L] \end{cases} \tag{30}$$

5 Variability in the fluctuations properties introduced by the different morphologies

In Figure 2, we investigate what is the variability introduced by the different morphologies for the implemented protocols. We fix ($\nu_{\mathrm{e}}^{\mathrm{p}}$, $\nu_{\mathrm{e}}^{\mathrm{p}}$, s) and μ_{V}, the

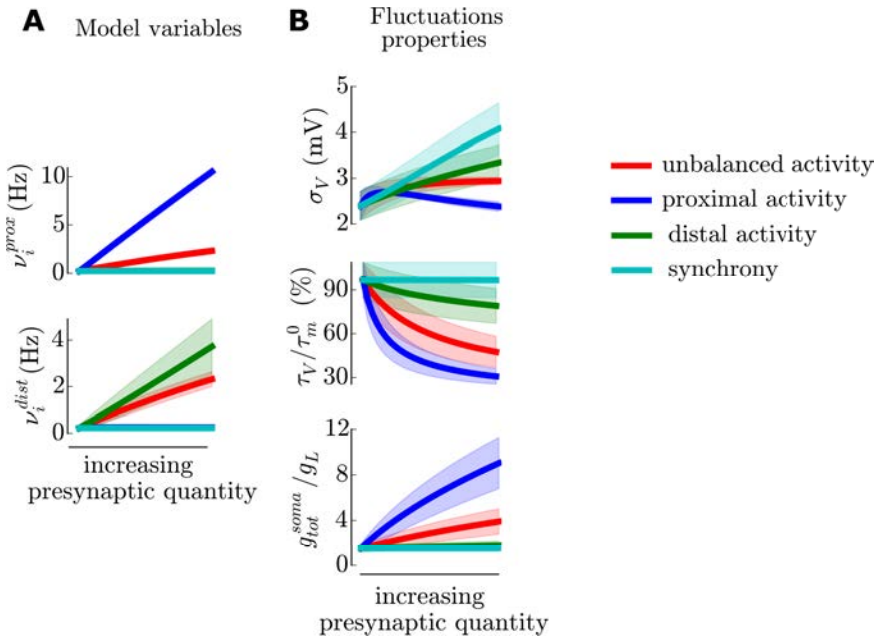

Figure 2: **Variability in the fluctuations properties introduced by the different morphologies.** Showing only the quantities that vary across cells, all other variables (ν_e^p, ν_e^p, s) or μ_V are fixed across cells. **(A)** Model variables. The balance μ_V is adjusted for each cells and the cells have different surfaces, so different number of synapses (and especially different ratio of excitatory to inhibitory numbers) so the inihibitory activity is adjusted differently for each cell. **(B)** Fluctuations properties.

inhibitory frequencies are adjusted adjusted depending on the morphology and the fluctuations properties also depend on the morphology.

We conclude that the impact of the different morphology is weak for those protocols.

6 Residual correlations after accounting for the excitability effects

7 Including cells of very low excitability in the analysis

In this section, we re-include the n=3 cells of very low excitabilities that have been discarded in the analysis presented in the main text.

The global trend is conserved but their very low values of the firing rate render data visualization poorly informative.

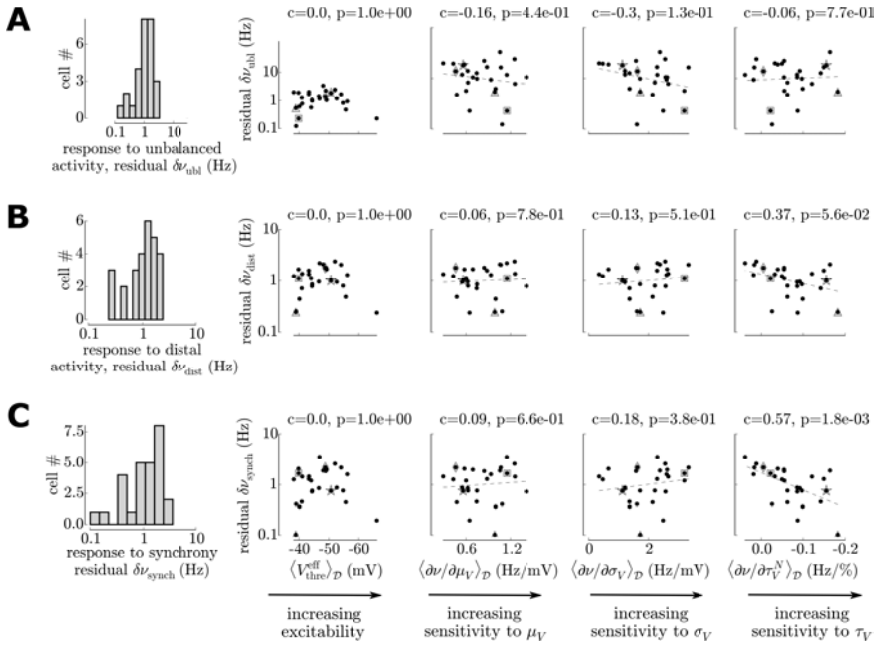

Figure 3: **Residual correaltions after removing the dependency on the excitability (see null correlation with excitability).**

8 References

Appel W (2008) *Mathématiques pour la physique et les physiciens* H. et K. Editions.

Destexhe A, Rudolph M, Paré D (2003) The high-conductance state of neocortical neurons in vivo. *Nature reviews. Neuroscience* 4:739–751.

Rall W (1962) Electrophysiology of a dendritic neuron model. *Biophysical journal* 2:145.

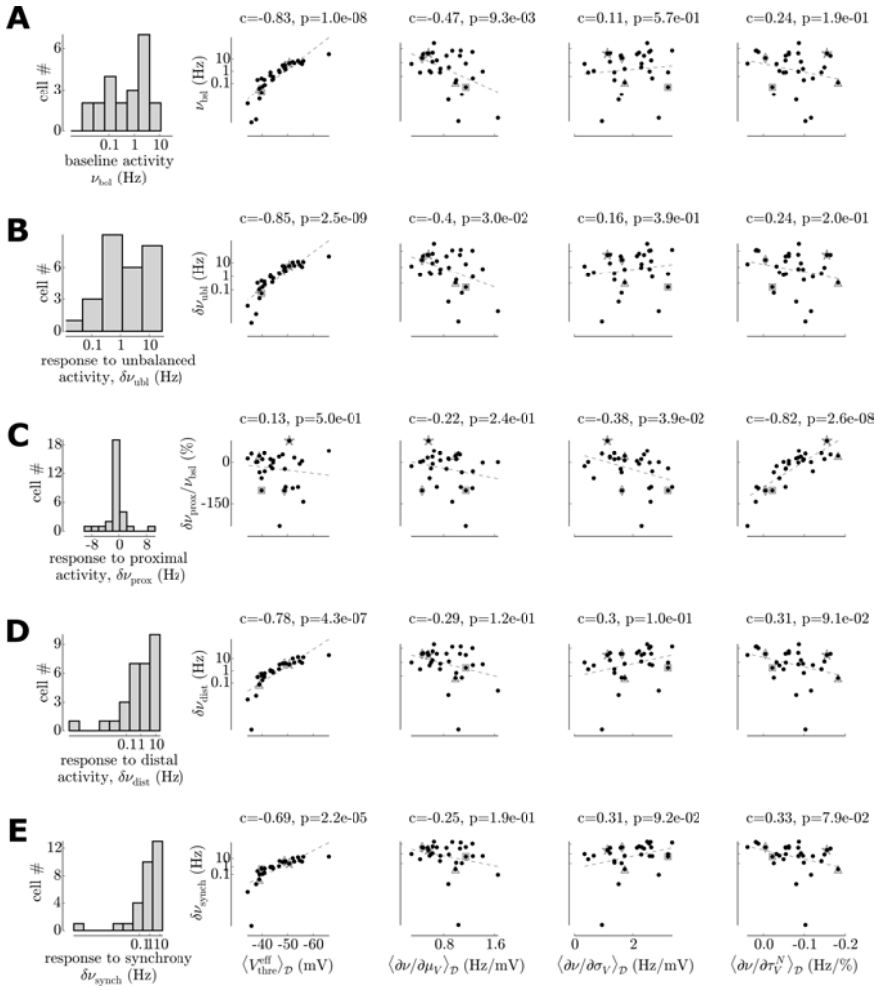

Figure 4: **Including all cells in the correlating responses with biophysical features.** (i.e. the very low firing rates: $\nu<10^{-4}$)

Work 3: Gain Modulation of Synaptic Inputs by Network State in Auditory Cortex In Vivo

Reference: Reig, R., Zerlaut, Y., Vergara, R., Destexhe, A., & Sanchez-Vives, M. V. (2015). Gain modulation of synaptic inputs by network state in auditory cortex in vivo. The Journal of Neuroscience : The Official Journal of the Society for Neuroscience, 35(6), 2689–702. 10.1523/JNEUROSCI.2004-14.2015

French summary

Les circuits récurrents corticaux génèrent de l'activité spontanée qui oscille entre état activé et état quiescent dans le sommeil à ondes lentes ou sous anésthésie. Ces différents états d'activation modulent le gain de la transmmission synaptique. Cependant la modulation imposée par les états activés est disparate dans la littérature, on reporte dans certains cas une augmentation du gain et une diminution dans d'autres cas. Dans ce travail, nous testons l'hypothèse que ces différentes observations dépendent de l'intensité de la stimulation. Nous avons comparé les potentiels post-synaptiques dans les états activés et quiescents en réponse à de stimulations corticales, thalamiques et auditives dans le cortex auditif du rat. Dans les états activés, les faibles réponses étaient potentiées par l'état activé alors que pour des fortes intensités, elles étaient atténuées par rapport à l'état quiescent. Nous avons examiné de manière théorique comment un haut niveau d'activité spontanée impactait les réponses post-synaptiques dans le cortex. Nous avons observé que la compétition entre le recrutement dans le réseau cortical activé et les effets de conductances prédisait une relation non-triviale entre l'intensité des stimuli et l'amplitude des réponses. Ce scénario explique quantitativement et qualitativement les observations expérimentales.

Systems/Circuits

Gain Modulation of Synaptic Inputs by Network State in Auditory Cortex *In Vivo*

Ramon Reig,[1] Yann Zerlaut,[2] Ramiro Vergara,[1] Alain Destexhe,[2] and Maria V. Sanchez-Vives[1,3]

[1]Institut d'Investigacions Biomèdiques August Pi i Sunyer, 08036 Barcelona, Spain, [2]Unité de Neurosciences, Information et Complexité, CNRS, 91198 Gif sur Yvette, France, and [3]Institució Catalana de Recerca i Estudis Avançats, 08010 Barcelona, Spain

The cortical network recurrent circuitry generates spontaneous activity organized into Up (active) and Down (quiescent) states during slow-wave sleep or anesthesia. These different states of cortical activation gain modulate synaptic transmission. However, the reported modulation that Up states impose on synaptic inputs is disparate in the literature, including both increases and decreases of responsiveness. Here, we tested the hypothesis that such disparate observations may depend on the intensity of the stimulation. By means of intracellular recordings, we studied synaptic transmission during Up and Down states in rat auditory cortex *in vivo*. Synaptic potentials were evoked either by auditory or electrical (thalamocortical, intracortical) stimulation while randomly varying the intensity of the stimulus. Synaptic potentials evoked by the same stimulus intensity were compared in Up/Down states. Up states had a scaling effect on the stimulus-evoked synaptic responses: the amplitude of weaker responses was potentiated whereas that of larger responses was maintained or decreased with respect to the amplitude during Down states. We used a computational model to explore the potential mechanisms explaining this nontrivial stimulus–response relationship. During Up/Down states, there is different excitability in the network and the neuronal conductance varies. We demonstrate that the competition between presynaptic recruitment and the changing conductance might be the central mechanism explaining the experimentally observed stimulus–response relationships. We conclude that the effect that cortical network activation has on synaptic transmission is not constant but contingent on the strength of the stimulation, with a larger modulation for stimuli involving both thalamic and cortical networks.

Key words: **cerebral cortex; computational model; oscillations; synaptic inputs; thalamocortical; Up states**

Introduction

Cortical spontaneous activity varies with the brain's functional state. During slow-wave sleep and anesthesia, this activity is organized in slow oscillations (Steriade et al., 1993) generated through the recurrent connectivity between cortical neurons (Lorente de Nó, 1938). These slow oscillations are characterized by active periods of high synaptic activity, depolarized membrane potential, and neuronal firing (Up states) interspersed with silent periods of low synaptic activity and hyperpolarized membrane potential or Down states (Metherate and Ashe, 1993; Steriade et al., 1993; Cowan and Wilson, 1994; Sanchez-Vives and McCormick, 2000; Petersen et al., 2003). Network activity has an impact on different properties of the network itself, including intrinsic (Paré et al., 1998; Steriade, 2001) and circuit properties (Boudreau and Ferster, 2005; Crochet et al., 2005; Crochet et al., 2006; Reig et al., 2006; Haider et al., 2007; Reig and Sanchez-Vives, 2007). One of these network properties is synaptic responsiveness. Different studies have analyzed how cortical states affect synaptic responsiveness (Timofeev et al., 1996) and sensory transmission (Azouz and Gray, 1999; Petersen et al., 2003; Sachdev et al., 2004; Crochet et al., 2005; Crochet et al., 2006; Haider et al., 2007; Hasenstaub et al., 2007; Reig and Sanchez-Vives, 2007; Rigas and Castro-Alamancos, 2009), yielding diverse and sometimes contradictory results. Depending on the cortical areas and on the protocols used, Up states have been reported either to decrease (Petersen et al., 2003; Sachdev et al., 2004; Crochet et al., 2006; Hasenstaub et al., 2007; Rigas and Castro-Alamancos, 2009) or to increase (Azouz and Gray, 1999; Haider et al., 2007; Reig and Sanchez-Vives, 2007) cortical responsiveness with respect to Down states.

Understanding gain modulation during Up states is also important because cortical dynamics during wakefulness shares properties with Up states (Steriade et al., 2001; Destexhe et al., 2007; Constantinople and Bruno, 2011). Computational models suggest that several features of Up states may provide interesting computational properties such as making neurons probabilistic and thus controlling their gain and transfer function (Hô and Destexhe, 2000; Destexhe and Contreras, 2006). It is therefore of primary importance to understand such interactions.

Received May 17, 2014; revised Dec. 4, 2014; accepted Dec. 10, 2014.

Author contributions: R.R. and M.V.S.-V. designed research; R.R., Y.Z., R.V., and A.D. performed research; R.R., Y.Z., A.D., and M.V.S.-V. analyzed data; R.R., Y.Z., A.D., and M.V.S.-V. wrote the paper.

This work was supported by Ministerio de Economía y Competitividad, Spain (Grant BFU2011-27094), the European Union (Project CORTICONIC Contract 600806 to M.V.S.-V.), BrainScales (Grant FP7-269921 to A.D.), and the Human Brain Project. We thank Anders Ledberg, Maurizio Mattia, and Idan Segev for comments on different stages of the manuscript and Lorena Pérez Méndez for her contribution to data analysis.

The authors declare no competing financial interests.

Correspondence should be addressed to Maria V. Sanchez-Vives, IDIBAPS, Roselló 149-153, 08036 Barcelona. E-mail: msanche3@clinic.ub.es.

R. Reig's present address: Department of Neuroscience, Karolinska Institute, Stockholm 17177, Sweden.

R. Vergara's present address: Laboratorio de Acústica y Percepción Sonora, Universidad Nacional de Quilmes, B1876BXD Buenos Aires, Argentina.

DOI:10.1523/JNEUROSCI.2004-14.2015

 0270-6474/15/352689-14$15.00/0

To understand quantitatively the neuronal transfer function during Up states, we recorded intracellularly from A1 (auditory cortex) neurons *in vivo* synaptic potentials evoked by either auditory or electrical stimulation (intracortical or thalamocortical) over a wide range of intensities. The activation of cortical neuronal populations by auditory stimuli and during spontaneous activity under anesthesia has been described previously (Luczak et al., 2009; Sakata and Harris, 2009). However, the extent to which cortical activation imposes a modulation of synaptic inputs depending on the intensity of the stimulus has not been reported. We find that Up states can gain-modulate synaptic responses by either enhancing or decreasing synaptic potentials contingent on the intensity of stimulation. The result is a global scaling of the evoked responses. To understand the network mechanisms mediating this stimulus–response relationship, we modeled different ensembles of the full recurrent and feedforward sensory pathway to account for the auditory, intracortical, and thalamocortical stimulation. We provide a quantitative mechanism that produces the gain modulation of synaptic responses during Up states.

Materials and Methods

Ethics approval

The experiments described here have been approved by the Animal Ethics Committee of the University of Barcelona under the supervision of the Autonomous Government of Catalonia and following the guidelines of the European Communities Council (86/609/EEC).

Intracellular recordings from rat auditory cortex

Adult male Wistar rats (200–340 g; $n = 29$) were used for recordings in auditory cortex (A1). Anesthesia was induced by injection of ketamine (80 mg/kg) and xylazine (8 mg/kg). Anesthesia levels were monitored by the heart rate (240–300 bpm), blood O_2 concentration (95%), the recording of low-frequency electroencephalogram, and the absence of reflexes. The animals were not paralyzed. The maintenance dose of ketamine was 30–50 mg/kg/h and xylazine 1–2 mg/kg/h. Intraperitoneal maintenance doses of anesthesia were given with intervals of 30–70 min and an overdose was given at the end of the experiment. Rectal temperature was maintained at 37°C during the experiment. Once in the stereotaxic apparatus, a craniotomy (2 × 2 mm) was made at coordinates AP −4.30 from bregma, L 7 mm (Paxinos and Watson, 2005). After opening the dura, intracellular recordings were obtained with borosilicate glass capillaries 1 mm outer diameter × 0.5 inner diameter (Harvard Apparatus). For stability and to avoid desiccation agar (4%) was used to cover the area.

Sharp intracellular recording electrodes were formed on a Sutter Instruments P-97 micropipette puller from medium-walled glass and beveled to final resistances of 50–100 MΩ. Micropipettes were filled with 2 M potassium acetate. Only very stable recordings were included (average duration 58 min) and they all had overshooting action potentials and a stable input resistance. Recordings were digitized, acquired, and analyzed using a data acquisition interface and software from Cambridge Electronic Design and its commercial software Spike 2. Further details of the procedure can be found in Reig and Sanchez-Vives (2007).

Conductance measurement

By means of intracellular injection of DC current, the membrane potential of auditory neurons was current clamped at different membrane potentials as in Compte et al. (2009). The bridge was carefully balanced at each DC level to compensate for the electrode resistance. The distribution of subthreshold membrane potential values was obtained for each membrane potential level, yielding a bimodal distribution corresponding to Up and Down states (Fig. 1*D*). An *I–V* relationship between the Up and Down state peak values of the bimodal distribution and the value of the DC-injected current was built, the inverse of the slope being the conductance.

Electrical stimulation

Electrical stimulation (0.2 ms, 10–300 μA) was delivered by means of a WPI A-360 stimulus isolation unit that prevents electrode polarization. Thalamocortical (TC) or intracortical (IC) fibers were stimulated with bipolar electrodes made of sharpened tungsten wires. The stimulation electrode was placed in the medial geniculate nucleus of the thalamus (−5.6 mm AP, −3.4 mm L, 5.2–6.2 mm D). To ensure that the location was correct, first, the electrode was used to record thalamic responses to auditory stimulation and then it was switched to the stimulation mode. Thalamocortical electrical stimulation evoked onset postsynaptic potentials with latencies ranging between 2.3 and 5 ms. Intracortical electrical stimulation was delivered by means of a bipolar electrode in the vicinity of the intracellularly recorded neuron (0.5–1.5 mm as in Reig et al., 2006). This stimulation evoked postsynaptic potentials with latencies ranging between 1.7 and 3.5 ms.

In the series of electrical stimulation, for each one of the intensities, a minimum of 100 shocks were given at 0.2–0.33 Hz. The stimulation could randomly occur during Up or Down states and were sorted out during the offline analysis.

Auditory stimulation

A click of white noise of 5 ms of duration was used to stimulate. White noise was generated by a MATLAB sequencer and recorded with the data acquisition system. Stimuli onset and duration were controlled by a computer. The stereotaxic frame had hollow ear bars and the loudspeakers were placed inside them (Sanchez-Vives et al., 2006). Therefore, stimuli were delivered binaurally through a closed acoustic system based on Sony MDR E-868 earphones housed in a metal enclosure and surrounded by damping material that fit into the Perspex specula (Rees et al., 1997). The output of the system for each stimulus was calibrated to be between 55 and 85 dB_{SPL}. We used a series of 90–100 clicks at 0.2–0.33 Hz for each intensity value, the stimulus occurring on different phases of the oscillatory cycle. The analysis was done offline and the synaptic responses were sorted for different periods of the cycle (Up states, Down states, etc).

Detection of Up and Down states

Up and Down states were detected using an algorithm described in Seamari et al. (2007). This algorithm calculates the two exponential moving averages of the membrane potential, a slow and a fast one. The size of the windows for averaging are calculated for each particular signal and the system uses the information of the previous dynamics of the system to predict the future transitions. The crossing of the slow and fast moving averages provides a good estimation of the Up/Down states transitions. A more precise method is also integrated to better determine the moment of Up/Down transition based on the momentum. These two combined methods are reliable and work better than other detection methods even in noisy conditions (Seamari et al., 2007). The classification of responses was done following Reig and Sanchez-Vives (2007) into those occurring during Up and during Down states. This classification of responses was checked on a single response basis by hand.

Analysis

The amplitude of the postsynaptic potentials (PSPs) was measured at the peak, which had latencies between 4 and 10 ms. PSP slope and amplitude were highly correlated (Reig et al., 2006). When normalization was necessary to compare synaptic potentials evoked in Up versus Down states, it was done with respect to the amplitude of the PSPs during Down states. Next, the normalized values for individual neurons were averaged to provide population data; these values were depicted in the scatter diagrams in the different figures. Absolute values are also provided. Data are given in the text as mean ± SD. Error bars in the figures correspond to the SEM.

Model

In this section, we propose a quantitative description of how the cell and network properties during Up and Down states shape the postsynaptic response to a given stimulation. Two cases are considered, intracortical and thalamocortical stimulation. We performed this study using analytical approximations of the different processes.

The general strategy that we adopt is related to the probabilistic theoretical framework that was described previously (Hô and Destexhe, 2000; Destexhe and Contreras, 2006).

The information needed to derive the effect of the stimulus on a network is as follows. At the cellular level, we need to know the relationship

Table 1. Parameters of the model

Name	Symbol	Value
Cellular properties		
Leak conductance	g_L	10 nS
Membrane capacitance	C_m	200 pF
Leak reversal potential	E_L	−65 mV
Threshold potential	V_{thre}	−50 mV
Refractory period	τ_{ref}	5 ms
Synapses		
Excitatory cortical weight	$Q_{e,cort}$	0.4 nS
Inhibitory cortical weight	$Q_{i,cort}$	1.2 nS
Excitatory thalamic weight	$Q_{e,thal}$	2 nS
Excitatory time constant	τ_e	7.3 ms
Inhibitory time constant	τ_i	5 ms
Excitatory reversal potential	E_e	0 mV
Inhibitory reversal potential	E_i	−80 mV
Background activity: cortical network		
Mean excitatory conductance: Up state	$\bar{g}_e^{Up}$	7 nS
Mean inhibitory conductance: Up state	$\bar{g}_i^{Up}$	20 nS
Standard deviation excitatory conductance: Up state	σ_e^{Up}	3 nS
Standard deviation inhibitory conductance: Up state	σ_i^{Up}	8 nS
Mean excitatory conductance: Down state	$\bar{g}_e^{Down}$	1 nS
Mean inhibitory conductance: Down state	$\bar{g}_i^{Down}$	2 nS
Standard deviation excitatory conductance: Down state	σ_e^{Down}	0.1 nS
Standard deviation inhibitory conductance: Down state	σ_i^{Down}	0.5 nS
Background activity: thalamic network		
Mean membrane potential: Up state	$\mu_{V,thal}^{Up}$	−61 mV
Standard deviation membrane potential: Up state	$\sigma_{V,thal}^{Up}$	5 mV
Mean membrane potential: Down state	$\mu_{V,thal}^{Down}$	−64 mV
Standard deviation membrane potential: Down state	$\sigma_{V,thal}^{Down}$	4 mV
Network architecture		
Cortical recurrent connectivity probability	ε_{cort}	2%
Thalamocortical afference probability	ε_{thal}	2%
Number of cells: cortical network	N_{cort}	10000
Percentage of cortical inhibitory neurons	g	25%
Number of excitatory cells: thalamic network	N_{thal}	2000
Electrical stimulation model		
Cortical maximal radius	$r_{\max,cort}$	1 mm
Cortical minimal radius	$r_{0,cort}$	300 μm
Depolarization relation: cortical stimulation	$\Delta V_{cort}(I, r)$	$0.6 \cdot \frac{I}{1+\left(\frac{r}{r_{0,cort}}\right)^2} - 1$
Thalamic maximal radius	$r_{\max,thal}$	200 μm
Thalamic minimal radius	$r_{0,thal}$	60 μm
Depolarization relation: thalamic stimulation	$\Delta V_{thal}(I, r)$	$0.056 \cdot \frac{I+316.2}{1+\left(\frac{r}{r_{0,thal}}\right)^2} - 315.3$

between the input intensity and the firing probability, this is the "activation function." A given stimulus has a differential effect over cells within the network (e.g., in the case of an electrical stimulation, the distance to the electrode or in the case of an afferent network the wiring realizations to the different cells), so we will compute the histogram over cells of the effect of this stimulus. We will finally apply the "activation function" on the histogram of the stimulus effect to get the number of spiking cells and then derive the postsynaptic response.

Cell properties. We use the Leaky Integrate and Fire model (later adapted from Lapicque (1907)) to describe the neurons. For simplicity, the three populations considered here (excitatory cortical neurons, inhibitory cortical neurons, and thalamocortical neurons) have identical properties and the parameters can be found in Table 1.

The subthreshold dynamics results from passive and synaptic currents. The passive properties are described by a simple RC circuit, the capacitive current is characterized by a membrane capacitance C_m, the leak current is set by a conductance g_L and a reversal potential E_L. The membrane equation below threshold is therefore:

$$C_m \frac{dV}{dt} = g_L (E_L - V) + I_{syn}(V, t) \quad (1)$$

The synaptic currents $I_{syn}(V, t)$ integrate excitatory and inhibitory input with reversal potentials E_e and E_i. Their respective conductances, G_e and G_i, will be determined by the sum of the background and stimulus-evoked activity. The synaptic current is given by:

$$I_{syn}(V, t) = G_e(t) \cdot (E_e - V) + G_i(t) \cdot (E_i - V) \quad (2)$$

The spiking mechanism is described by a simple threshold crossing: we consider that a spike is emitted when $V(t)$ reaches the threshold membrane potential value V_{thre} and from that moment the neuron is at rest during a period τ_{ref} before the subthreshold dynamics can restart.

Architecture of the network models. The cortical network is modeled as a random recurrent network of $N_{cort} = 10000$ cells, where $g = 25\%$ are inhibitory neurons and with a probability of connection $\varepsilon_{cort} = 2\%$. In the thalamic network, we consider only the $N_{thal} = 2000$ excitatory thalamocortical cells that project onto the cortical network with a connection probability $\varepsilon_{thal} = 2\%$.

Background cortical activity. The cortical network activity is made of excitatory and inhibitory recurrent input and we describe this background input as Ornstein-Uhlenbeck processes. So, in general:

$$dG_{syn}^{bg} = (\overline{g_{syn}} - G_{syn}^{bg}) \cdot \frac{dt}{\tau_{syn}} + \sqrt{2\tau_{syn}}\sigma_{syn} \cdot dW \quad (3)$$

where dW is a Wiener process and $syn \in \{e, i\}$ is the index for the excitation and the inhibition, respectively.

This input varies considerably between Up and Down states. The Up state is characterized by a very high synaptic bombardment, whereas the synaptic activity is almost null in the Down state. This can be seen in the values of Table 1. The autocorrelation time τ_{syn} is taken as the same as the synaptic decay time in the explicit model of synaptic conductance time course.

The membrane potential fluctuations resulting from this input have been studied analytically (Richardson, 2004; Rudolph and Destexhe, 2005) and we use the Gaussian approximation formulated in Rudolph et al. (2004) for the stationary membrane potential distribution $\rho^S(V)$ as follows:

$$\rho^S(V) = \frac{1}{\sigma_V^S\sqrt{2\pi}} e^{\frac{-(V-\mu_V^S)^2}{\sqrt{2\sigma_V^S}}} \quad (4)$$

With the mean μ_V^S, standard deviation σ_V^S, and effective membrane time constant τ_m^S given by the following:

$$\begin{cases} \mu_V^S = \dfrac{\bar{g}_e^S E_e + \bar{g}_i^S E_i + g_L E_L}{\bar{g}_e^S + \bar{g}_i^S + g_L} \\ \tau_m^S = \dfrac{C_m}{\bar{g}_e^S + \bar{g}_i^S + g_L} \\ (\sigma_V^S)^2 = \left(\dfrac{\sigma_e^S \tau_m^S}{C_m}\right)^2 \dfrac{\tau_e}{\tau_m^S + \tau_e}(\mu_V^S - E_e)^2 + \left(\dfrac{\sigma_i^S \tau_m^S}{C_m}\right)^2 \dfrac{\tau_i}{\tau_m^S + \tau_i}(\mu_V^S - E_i)^2 \end{cases} \quad (5)$$

Here, S indexes the dependency of the network state, either Up or Down.

Background thalamic activity. We do not consider the effect of input within the thalamic network, so we do not explicitly describe the conductance state. The effect of the network state (Up or Down) will be described by a change of the Gaussian membrane potential distribution (Table 1); the mean and variance of the membrane potential are slightly increased in the Up state with respect to the Down state (Contreras et al., 1996).

Effect of the electrical stimulation. Our goal is to translate the electrical current injected through the bipolar stimulation into an histogram of depolarization across the considered network (cortical or thalamic). Modeling the complexity of such a phenomenon is not straightforward (Ranck, 1975), so we adopt an heuristic approach and derive simple expressions based on qualitative features. The parameters of those expressions are manually adjusted to bring the output of the model to approximate to the experimentally observed response in the Down state.

Our area of interest is the local network around the electrode, a network that is delimited by a crown of minimal radius (r_0) and maximal radius (r_{max}) of 0.3 and 1 mm, respectively, for the cortical network and 60 and 200 μm, respectively, for the thalamic network. The neuronal depolarization is linked to the intensity of the extracellular electric field (Ranck, 1975). Given the bipolar nature of the stimulation and the approximately isotropic resistive nature of gray matter (Logothetis et al., 2007), the electric field at $\vec{r}$ in the extracellular medium follows:

$$\vec{E}(\vec{r}) = \frac{I}{4\pi\sigma}((\vec{r} - \vec{r}_0)/\|\vec{r} - \vec{r}_0\|^3 - (\vec{r} + \vec{r}_0)/\|\vec{r} + \vec{r}_0\|^3) \quad (6)$$

Where σ is the extracellular conductivity, I is the injected current, $\vec{r}$ is the position in spherical coordinates, and the two electrodes are located in $\vec{r}_0$ and $-\vec{r}_0$.

This is a rather complicated expression and the final depolarization also depends on many factors, such as cellular orientation, myelination, and stimulus duration (Ranck, 1975). We do not need this level of detail—we only want to model the decaying impact of the stimulus within the local network of interest.

Therefore, from the previous expression, we will only keep the approximate quadratic decay of the modulus with distance (valid because we remain in a domain close enough from the stimulation electrode, between r_0 and r_{max}).

To this extracellular field, we associate a maximum depolarization value via an affine relation (the parameters of which are adjusted manually; Table 1). Our heuristic expression for the depolarization as a function of the injected current and distance from the electrode is then:

$$\Delta V(I, r) = \alpha \cdot \frac{I - \beta}{1 + (r/r_0)^2} - \gamma \quad (7)$$

To get the histogram of depolarization over the network, we need the radial density of neurons. Because of the laminar organization of the cells, we make the hypothesis of an homogenous surface density $D = \dfrac{N}{\pi \cdot (r_{max}^2 - r_0^2)}$, where N is the number of neurons within the network, we get a radial density:

$$N(r) = 2\pi \cdot r \cdot D \quad (8)$$

For a given current stimulation value, the depolarization–distance relation is monotonic (Equation 7) so we can easily apply the law of conservation of probability $dr \cdot N(r) = N_I(\Delta V) \cdot d\Delta V$ to calculate the histogram of depolarization $N_I(\Delta V)$ for an injected current I as follows:

$$N_I(\Delta V) = \frac{N \cdot r_0^2}{(r_{\max}{}^2 - r_0)^2} \cdot \alpha \cdot \frac{I - \beta}{(\Delta V + \gamma)^2} \quad (9)$$

The quantity $N_I(\Delta V) \cdot d\Delta V$ represents the number of neurons in which the depolarization level lies between ΔV and $\Delta V + d\Delta V$ for a current input I. The few closest neurons will be maximally depolarized by $\Delta V(I, r_0)$ whereas the more numerous neurons at r_{max} will be depolarized by a much smaller quantity: $\Delta V(I, r_{max})$. Increasing the current level I shifts the histogram toward high depolarization. Examples for the shape of $N_I(\Delta V)$ can be seen in Figure 5*B*.

Recruitment of a stimulation within the neural network. Given a histogram of depolarization over the neural network (as provided by Equation 9), we wanted to estimate what fraction of the cells will fire as a response to this stimulus-evoked depolarization.

We consider a time bin of ~5 ms around the mean time of maximum depolarization induced by the stimulus. Within this time bin (as it is equal to the refractory period), the neurons can fire only once and we will split them between spiking and nonspiking. This temporal window is also lower than the membrane time constant (approximately 20 ms in the Down state and 5 ms in the Up state) so that the membrane potential fluctuations are weak within this window and we can classify the neurons according to their stationary membrane potential distribution $\rho^S(V)$ (as given by Equation 4 and 5). According to this classification, in the absence of stimulus, a fraction of neurons is firing due to background activity and the rest are silent. We then divide those silent neurons into two groups: the ones that the stimulus brings to fire and the ones that remain silent. The number of neurons that have a membrane potential above threshold (in the Up state in particular) is: $N_{bg} = N \cdot \int_{V_{thre}}^{\infty} \rho^S(V)dV = N_{tot}\left(1 - Erf\left(\dfrac{V_{thre} - \mu_V^S}{\sqrt{2} \cdot \sigma_V^S}\right)\right)\Big/2$, where N_{bg} corresponds to neurons that participate in the baseline firing rate and will induce the background (bg) conductance level in the next time bin. For those neurons, the stimulation will not affect their behavior within this time bin. We are interested in the evoked response that is due to the remaining neurons, those that would all be silent in the absence of stim-

ulation. In the absence of stimulation, their membrane potential follows the distribution:

$$\rho'^{S}(V) = \frac{\sqrt{2}}{\sqrt{\pi} \cdot \sigma_{V^S} \cdot \left(1 + Erf\left(\frac{V_{thre} - \mu_V^S}{\sqrt{2} \cdot \sigma_V^S}\right)\right)} \cdot e^{-\left(\frac{V - \mu_V^S}{\sqrt{2} \cdot \sigma_V^S}\right)^2} \quad (10)$$

Within a time bin, they would take a random value from this distribution. So their probability to get above threshold in response to an evoked depolarization ΔV is given by:

$$f(\Delta V) = \int_{V_{thre} - \Delta V}^{V_{thre}} \rho'^{S}(V) \cdot dV = \frac{Erf\left(\frac{V_{thre} - \mu_V^S}{\sqrt{2} \cdot \sigma_V^S}\right) - Erf\left(\frac{V_{thre} - \mu_V^S - \Delta V}{\sqrt{2} \cdot \sigma_V^S}\right)}{1 + Erf\left(\frac{V_{thre} - \mu_V^S}{\sqrt{2} \cdot \sigma_V^S}\right)} \quad (11)$$

We call this function the "activation function" of the network and it is an analytical analogous of the quantity introduced in the numerical study of Hô and Destexhe (2000). We use this quantity to calculate the number of activated neurons N_{act} as a result of a stimulation (synaptic or electrical) that produces the histogram of depolarization $N(\Delta V)$. This number is given by the following convolution:

$$N_{act} = \int_{\Delta V_{min}}^{\Delta V_{max}} f(\Delta V) \cdot N(\Delta V) \cdot d\Delta V \quad (12)$$

Where ΔV_{min} and ΔV_{max} are the minimum and maximum values of the stimulation, respectively.

Calculus of the PSP induced by the stimulus-evoked synaptic activity. On top of the stochastic background input, the cortical cells will be stimulated by the synaptic input resulting from the activity induced by the stimulation. We analyze how a deterministic synaptic input triggers a PSP response (as typically recorded in our experiments) depending on the network state. A synaptic event is modeled as a transient conductance change: an instantaneous jump of value Q_{syn} followed by an exponential decay of time constant τ_{syn} (the so-called "exponential synapse" model); $syn \in \{e, i\}$ is the index for the excitation and the inhibition, respectively.

For this calculation, we use the approximation presented in Kuhn et al. (2004), namely that the driving force is not modified within the time course of the response to the synaptic event. We consider that synaptic driving forces are constant $(E_{syn} - V(t)) \sim (E_{syn} - \mu_V^S)$ because they are fixed by the mean membrane potential μ_V^S. Therefore, we can rewrite Equation 1 as follows:

$$\tau_m^S \frac{dV}{dt} = \mu_V^S - V(t) + \frac{\tau_m^S}{C_m} \sum_{syn} \delta G_{syn}(t) \cdot (E_{syn} - \mu_V^S) \quad (13)$$

With this approximation, the effect of different synaptic events do not interact within each other (via the variation of the driving force) so that they sum independently. Therefore, we calculate the effect of one event and then sum linearly.

For one event starting at $t = 0$, the synaptic conductance variations will be $\delta G_{syn}(t) = Q_{syn} e^{-t/\tau_{syn}} H(t)$, so for $t \in [0, \infty]$, we get the membrane equation:

$$\tau_m^S \frac{dV}{dt} = \mu_V^S - V(t) + \frac{\tau_m^S}{C_m} \cdot (E_{syn} - \mu_V^S) \cdot Q_{syn} \cdot e^{-t/\tau_{syn}} \quad (14)$$

That has the following solution (given $V(0) = \mu_V^S$ and $\tau_m^S \neq \tau_{syn}$):

$$\begin{cases} V(t) = \mu_V^S + A_{syn} \cdot (e^{-t/\tau_m^S} - e^{-t/\tau_{syn}}) \\ A_{syn} = \frac{\tau_m^S \cdot Q_{syn} \cdot \tau_{syn}}{C_m \cdot (\tau_m^S - \tau_{syn})} \cdot (E_{syn} - \mu_V^S) \end{cases} \quad (15)$$

We next calculate the postsynaptic response in case of N_e and N_i excitatory and inhibitory events, respectively. For simplicity, all events arrive at the same time. The total membrane potential response is as follows:

$$V(t) = \mu_V^S + N_e \cdot A_e \cdot \left(e^{-t/\tau_m^S} - e^{-t/\tau_e}\right) + N_i \cdot A_i \cdot \left(e^{-t/\tau_m^S} - e^{-t/\tau_i}\right) \quad (16)$$

From this, we obtain that the time of maximum amplitude $t_{\max}$ is the solution of:

$$-\frac{(N_e \cdot A_e + N_i \cdot A_i) \cdot e^{-t_{\max}/\tau_m^S}}{\tau_m^S} + \frac{N_e \cdot A_e \cdot e^{-t_{\max}/\tau_e}}{\tau_e} + \frac{N_i \cdot A_i \cdot e^{-t_{\max}/\tau_i}}{\tau_i} = 0 \quad (17)$$

In practice, we will solve this using a Newton method and then compute the maximum amplitude response by evaluating $V(t_{max})$.

Results

Twenty-four intracellular recordings from primary auditory cortex in the ketamine/xylazine-anesthetized rat were included in the analysis (Fig. 1*A*). Neurons were classified into electrophysiological types following the method of Nowak et al. (2003). We identified 21 regular spiking (six of them "thin regular spiking"), one intrinsic bursting, and two fast-spiking neurons. The average input resistance was 28.7 ± 11.3 MΩ. Spontaneous and periodic Up states were interspersed with Down states generating an oscillatory rhythm (Fig. 1*A*,*B*), the intracellular potential showing the classical bimodal distribution (Fig. 1*C*; Steriade et al., 1993; Cowan and Wilson, 1994). The average duration of Up states was 0.43 ± 0.04 s and that of Down states 0.28 ± 0.02 s, resulting in an oscillatory frequency of 1.39 ± 0.11 Hz.

The conductance of six regular spiking neurons was estimated for both Up and Down states for different membrane potentials held by DC current injection (Paré et al., 1998; Waters and Helmchen, 2006). The bimodal distribution of membrane potential values at these different depolarization levels (Fig. 1*D*) was used to obtain the membrane potential values for Up and Down states and to construct the *I–V* relationships. In this way we estimated that the conductance (G) values were higher for Up than for Down states, with $G_{\mathrm{Up}}/G_{\mathrm{Down}}$ of 2.5, 3.3, 2.7, 1.3, 2.2, and 2.6. Four of these examples are illustrated in Figure 1*E*.

The objective of the study was to determine how the occurrence of Up and Down states influenced the amplitude of synaptic potentials evoked by different intensities of stimulation—in other words, how the activity (Up states) or quiescence (Down states) in the cortical network influence synaptic transmission. With the purpose of analyzing the respective contributions to this modulation of the different blocks of the sensory pathway, synaptic potentials were evoked in three different ways: auditory stimulation (Fig. 2), electrical stimulation of intracortical connections (Fig. 3), and electrical stimulation of thalamocortical connections (Fig. 4).

Auditory stimulation

Auditory synaptic potentials were evoked by 5 ms clicks (see Materials and Methods) that were given every 3–5 s. The evoked

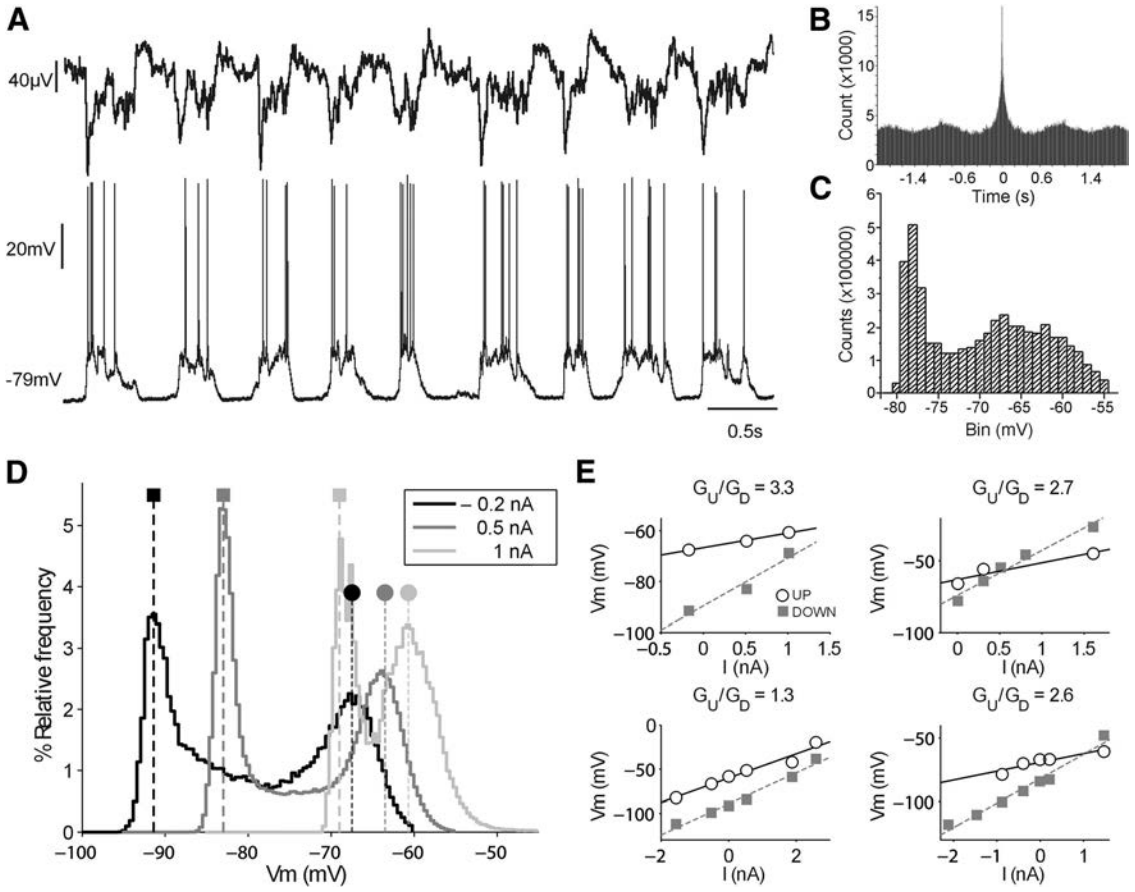

Figure 1. Slow oscillations in auditory cortex and auditory membrane conductances. ***A***, Simultaneous LFP (top) and intracellular recording (bottom) of slow oscillations in A1. Note the neuronal firing during Up state and the decreased activity during Down state. ***B***, Autocorrelogram of the neuronal firing illustrating the rhythmicity of the slow oscillations. ***C***, Distribution of the membrane potential values resulting in the classical bimodal distribution that corresponds to Up (depolarized) and Down (hyperpolarized) states. Bin size = 1 mV. ***D***, Distribution of the membrane potential values in one neuron for three different levels of DC current injection (grayscale for current). Notice that Up states (circles) had a larger overall conductance compared with Down states (squares). ***E***, *I–V* plots for four different regular spiking neurons in A1. The inverse of the slope corresponds to the conductance (*G*) and G_{Up}/G_{Down} is indicated for each case on top of the *I–V*. Notice that, in all cases, the conductance is larger in the Up states.

auditory synaptic responses had an onset latency of 11.6 ± 2.2 ms and a peak latency of 21.8 ± 3.4 ms ($n = 9$ cells). Stimulus-evoked synaptic potentials occurred during Down or during Up states. Synaptic potentials occurring during Down states could also recruit the cortical network and thus evoke a new Up state. In those cases, the amplitude of the evoked synaptic potential is difficult to measure because the recruitment of the local network induces a further depolarization (Fig. 6*C–E* in Reig and Sanchez-Vives, 2007). For that reason, the stimulus-evoked synaptic potentials were sorted offline into those occurring during Down states and not evoking an Up state and those occurring during Up states (Fig. 1*D*,*E*). Auditory responses were evoked by seven different intensities (55, 61, 67, 72, 77, 82, and 85 dB), that were given at random (90–100 stimuli per intensity). At least 10 sound-evoked synaptic potentials were averaged for each of the intensities and part of the cycle (Up or Down state). Those cases in which a synaptic potential during the Down state induced an Up state (Reig and Sanchez-Vives, 2007) have not been illustrated here and were excluded from the analysis given that the amplitude of the evoked synaptic potential cannot be disentangled from the network recruitment. Figure 2*A* illustrates raw traces of four different intensities with PSPs occurring during either Up or Down states, the average PSP for each intensity being averaged in Figure 2*B*. The average PSP's amplitude for each intensity for Down and Up states are represented for this particular neuron in Figure 2*C*.

For sound stimuli of intensities ranging between 55 and 85 dB, the average amplitudes of the evoked PSPs during Down states for the population ranged between 1 and 9 mV, the amplitude increasing with the stimulus intensity. However, those evoked by the same stimulus intensities during Up states varied within a narrower range of amplitudes: 4.3–6.5 mV. The stimulus–response relationship was thus attenuated during Up states with respect to Down states. Figure 2*D* shows a reduced stimulus–response relationship during Up states with respect to Down states. This is a representative example of the global scaling that takes place during Up states: for auditory stimuli and within these range of intensities, scaling occurs mostly as potentiation of small responses. The stimulus–response relationship, however, is maintained (Fig. 2*C* for an example of a single case), although reduced.

For lower intensities of stimulation (55 and 61 dB), the synaptic potentials evoked during Up states were significantly larger than those evoked during Down states ($p < 0.02$ for 55 dB and $p < 0.05$ for 61 dB; Fig. 2*E*). For louder stimuli (≥67 dB), the difference between the amplitudes of synaptic potentials evoked in the Up and Down states disappeared. In some cases, for louder stimuli, we observed the inverted phenomenon; namely larger PSPs in Down than in Up states. This was the case, for example, in

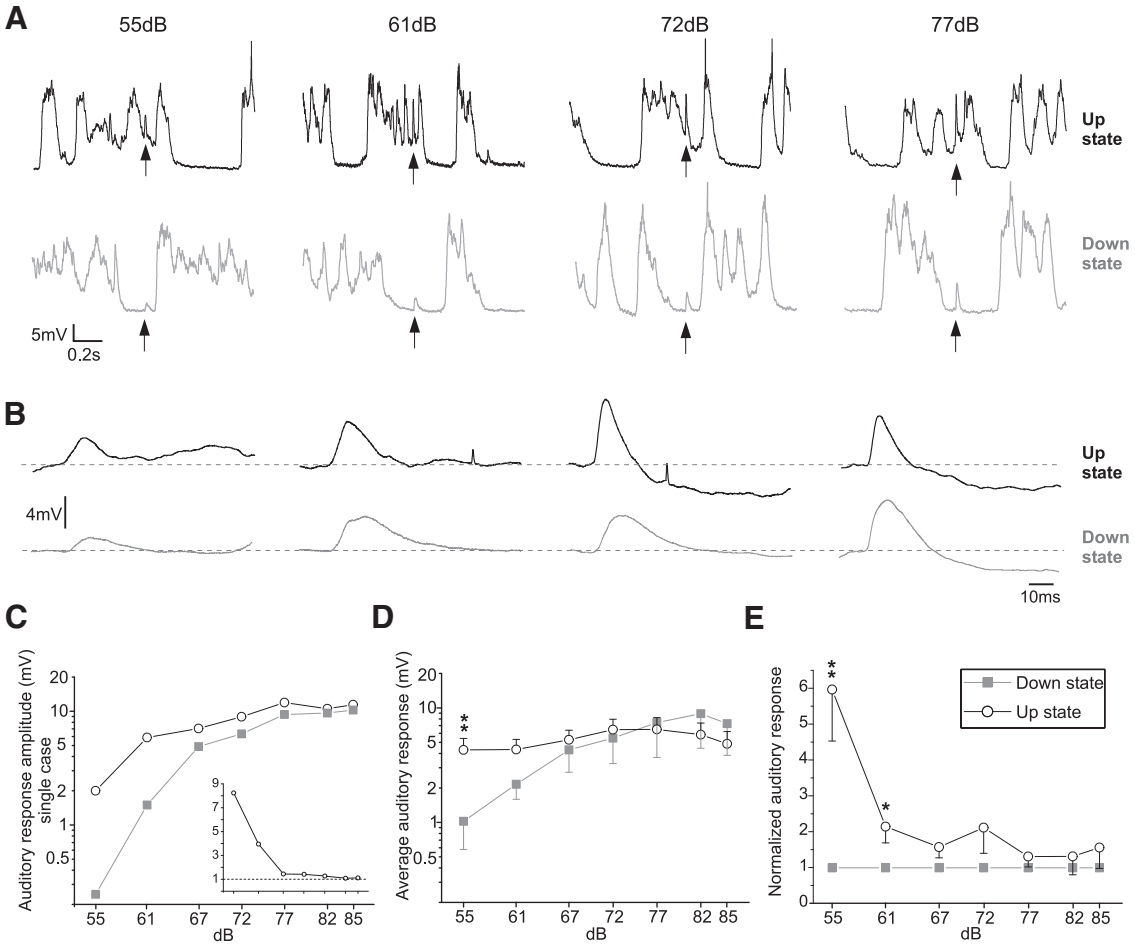

Figure 2. Synaptic potentials evoked by auditory stimulation during Up and Down states. ***A***, Raw traces of intracellular recordings displaying synaptic responses in one neuron. Responses to different intensities of auditory stimulation (55, 61, 72, and 77 dB) during Up and Down states (top and bottom, respectively). The black arrows indicate the time of occurrence of the auditory stimuli. ***B***, Waveform average of the synaptic potential evoked by the corresponding intensity (in ***A***) during Up (top traces) and Down states (bottom traces). ***C***, Amplitudes of the sound-evoked synaptic responses during Up and Down states against intensity of stimulation in the neuron illustrated in ***A*** and ***B***. Inset shows the normalized values with respect to the Down state for this neuron. ***D***, Average amplitude of auditory synaptic responses during Down and Up states for different stimulation intensities ($n = 9$ cells). ***E***, Average of the cell-by-cell normalization of the PSP amplitudes with respect to the ones in the Down state. *t* test $^{*}p < 0.05$; $^{**}p < 0.02$; $^{***}p < 0.01$.

the average in Figure 2*B* response to 77 dB. That trend is also apparent in the population average (Fig. 2*D*, 82–85 dB), although the difference was not significant.

In conclusion, cortical synaptic potentials evoked by auditory stimulation had larger amplitudes in Up than in Down states for low-intensity stimulations (<61 dB). For louder stimuli, no difference between the evoked potentials was found between the Up and Down states. Interestingly, the average intensity/response relationship observed during Down states was diminished during Up states, where a scaling of the auditory responses occurred.

Intracortical activation

Intracortical electrical stimulation of the intracellularly recorded neurons evoked synaptic potentials with an average onset latency of 2.89 ± 1.16 ms and a latency to the peak of 7.75 ± 2.54 ms ($n = 9$). The rank of amplitudes of the synaptic potentials evoked by different stimulus intensities (30–90 μA) in these connections was larger than for the sound-evoked and thalamocortical ones: 0.3–29 mV. We also observed larger excitatory amplitudes evoked by intracortical than by either sensory or thalamocortical activation. One reason could be that sensory and thalamocortical activations recruit larger feedforward inhibition than intracortical synapses (Gil and Amitai, 1996).

The experimental design was similar to the one used for auditory stimulation: at least six different intensities were used (30, 40, 50, 60, 70, and 90 μA) in different time periods of the oscillatory cycle. The amplitude of synaptic potentials evoked with stimuli of lower intensities (Fig. 3*B–E*; 30–40 μA) was significantly larger when occurring during Up than during Down states. For intensities between 50 and 70 μA, there was no significant difference between those occurring in Down versus Up states. However, when intensities were increased further, in this case to 90 μA, the relative amplitude of the normalized evoked potential during the Up state was significantly smaller than that during the Down state, thus inverting the trend (Fig. 3*E*).

As observed for auditory stimulation, intracortical synaptic potentials evoked during Up states showed a weaker dependence on the intensity of stimulation (ranging on average between 1.5 and 12.3 mV) than those evoked during Down states (ranging on average between 0.7 and 17.5 mV; Fig. 3*D*). For weak stimulation, the evoked potentials were 2.1 times larger in the Up than in the Down states, but for more intense stimuli, amplitudes were larger during Down states (1.4 times). This is again largely suggestive of the scaling effect that the active cortical network imposes over inputs.

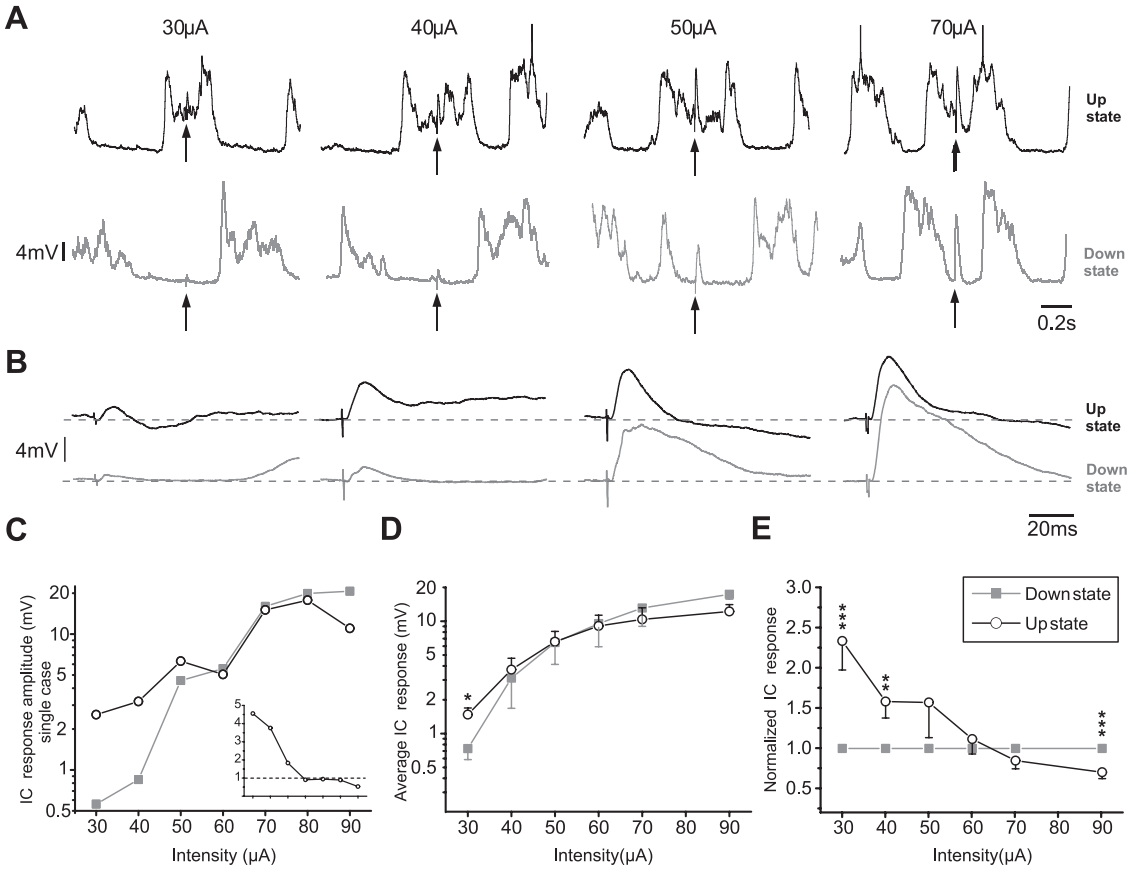

Figure 3. Synaptic potentials evoked by intracortical electrical stimulation during Up and Down states. ***A***, Raw traces of intracellular recordings displaying synaptic responses in one neuron. Responses to different intensities of intracortical stimulation (30, 40, 50, 70 μA) during Up and Down states (top and bottom, respectively). The black arrows indicate the time of occurrence of the electrical stimuli. ***B***, Waveform average of the synaptic potential evoked by the corresponding intensity (in ***A***) during Up (top traces) and Down states (bottom traces). ***C***, Amplitudes of the intracortically evoked synaptic responses during Up and Down states against intensity of stimulation in the neuron illustrated in ***A*** and ***B***. In the inset, the normalized values with respect to the Down state for this neuron. ***D***, Average amplitude of intracortical synaptic responses during Down and Up states for different stimulation intensities ($n = 9$ cells). ***E***, Average of the cell-by-cell normalization of the PSP amplitudes with respect to the ones in the Down state. *t* test $^*p < 0.05$; $^{**}p < 0.02$; $^{***}p < 0.01$.

Thalamocortical activation

In this part of the study, postsynaptic potentials were evoked by means of electrical stimulation of the auditory thalamus ($n = 10$), their average onset latency being 3.85 ± 1.32 ms and a peak latency of 9.24 ± 1.58 ms. Four different stimulation intensities were tested (90, 120, 150, and 200 μA). Synaptic potentials evoked during both the Up and Down states had a significant stimulus–response relationship, their amplitudes increasing for larger intensities (Fig. 4*A*,*B*). A thalamic stimulus intensity of 90 μA evoked an average synaptic response of 1 mV during the Down state and 3.8 mV during the Up state. In general, for the three lower intensities (90, 120, and 150 μA), the synaptic potentials evoked during the Up states had in all cases significantly larger amplitudes than those occurring during Down states. However, synaptic potentials evoked by larger intensities (200 μA) were not significantly different in amplitude when evoked during Up versus during Down states (Fig. 4*D*,*E*). Similar to what we have described for sound-evoked potentials, the gain of synaptic potentials varied in the Up versus Down states and was stimulus dependent: weaker stimuli invariably evoked synaptic responses that were larger during Up states than those during Down states, the difference disappearing for stronger stimuli.

Modeling synaptic transmission during Up and Down states

Based on an idea introduced previously (Hô and Destexhe, 2000), we considered that the experimentally observed gain modulation could be understood as a result of the interaction between the Up/Down variations in network excitability and input impedance. To test this possibility, we used the tools presented in the Model section of Materials and Methods to investigate the modulation predicted by artificial neural networks displaying either the Up state or the Down state activity. We illustrate this modulation on the effect of electrical stimulation of the cortical and the thalamic network consecutively. We derive the relationship between the current intensity value and the postsynaptic response in those two stimulation paradigms. The different steps that construct this relationship are detailed next.

Gain modulation in a cortical model: postsynaptic response to intracortical stimulation

We started by modeling the effect of the electrical stimulation. The bipolar stimulation in Figure 5*A* spreads over the local cortical network (the 1 mm circumference around the stimulation electrode where the recorded cell also lies). Each neuron within this network will be depolarized by the local extracellular current according to Equation 7. The extracellular field decays as stated by Equation 6 because of resistive dissipation, whereas the number of neurons reached raises with distance from the electrode (Equation 8). Those two factors lead to the histogram of induced depolarization across the cortical network (Equation 9) such that many distant neurons are weakly depolarized, whereas the few neurons close from the electrode are strongly depolarized. The histograms of activated neurons for three

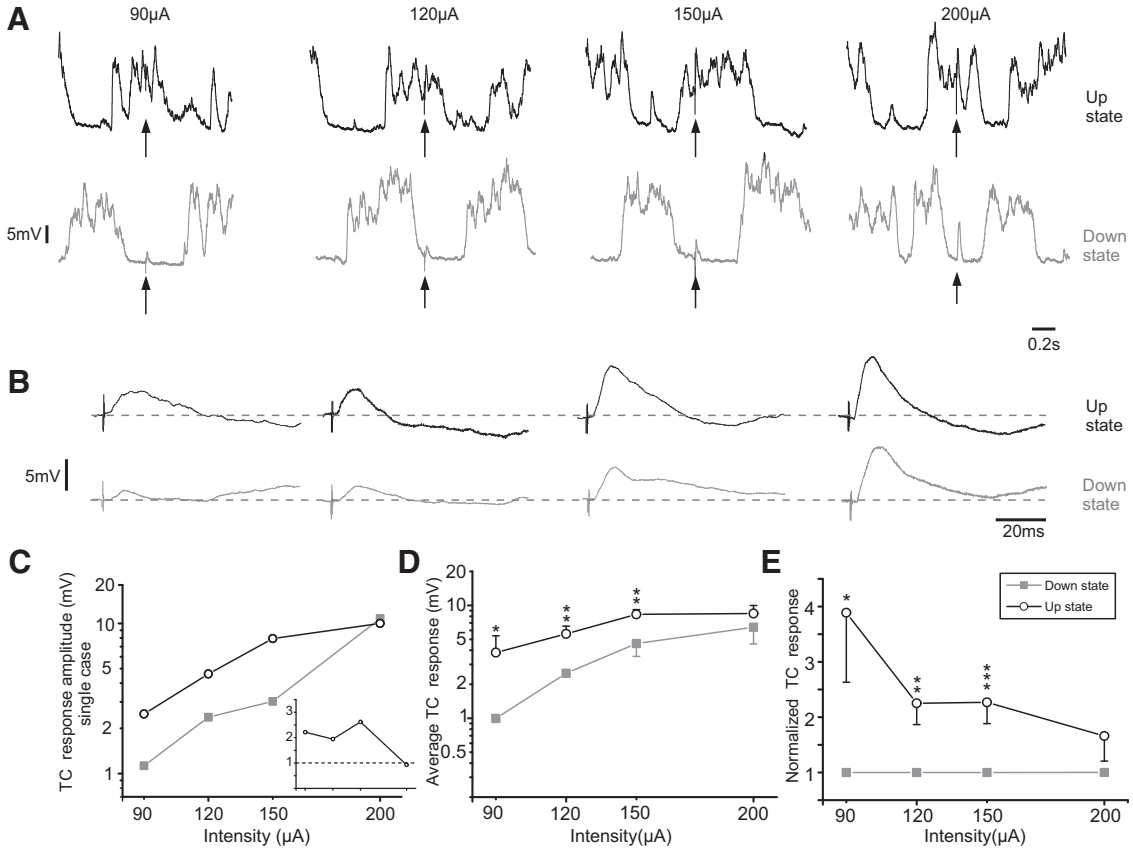

Figure 4. Synaptic potentials evoked by thalamocortical electrical stimulation during Up and Down states. ***A***, Raw traces of intracellular recordings displaying synaptic responses in one neuron. Responses to different intensities of thalamocortical stimulation (90, 120, 150, 200 μA) during Up and Down states (top and bottom, respectively). The black arrows indicate the time of occurrence of the electrical stimuli. ***B***, Waveform average of the synaptic potential evoked by the corresponding intensity (in ***A***) during Up (top traces) and Down states (bottom traces). ***C***, Amplitudes of the thalamocortically evoked synaptic responses during Up and Down states against intensity of stimulation in the neuron illustrated in ***A*** and ***B***. In the inset, the normalized values with respect to the Down state for this neuron. ***D***, Average amplitude of thalamocortical synaptic responses during Down and Up states for different stimulation intensities ($n = 10$ cells). ***E***, Average of the cell-by-cell normalization of the PSP amplitudes with respect to the ones in the Down state. *t* test $*p < 0.05$; $**p < 0.02$; $***p < 0.01$.

different levels of injected current I are represented in Figure 5*B*.

The cortical network translates this stimulation into different firing intensities for the two different network states. In the Up state, the background activity amplifies the effect of the stimulation. The evoked depolarization brings many neurons to suprathreshold levels and evokes firing because of membrane potential fluctuations and initial depolarization (Nowak et al., 1997). This is not the case in the Down state, where only the few neurons depolarized above threshold by the stimulus reach the threshold and fire. Following the method of Hô and Destexhe (2000), we introduce the "activation function" of the network that translates the stimulus value into the probability to evoke a spike. This can be calculated explicitly from the fluctuations of the membrane potential and a basic threshold mechanism for spiking (Equation 11). The comparison of the functions between Up and Down states is illustrated in Figure 5*C*. The activation function is convoluted with the histogram of depolarization to obtain the number of activated neurons (Equation 12). Note that in the Up state, this "activation function" should be applied only to the neurons that would be silent in the absence of stimulation. To calculate the number of cells responding to the evoked input, we first discard the fraction of the network that participates in the baseline firing rate and therefore to the baseline conductance and depolarization levels (see Materials and Methods). An example of this procedure is presented in Figure 5*D* for a stimulus current of 60 μA. We show the distribution of "available" neurons, (those that do not participate in the baseline rate), and we convolute this distribution with the activation function, to get the number of activated neurons (the shaded parts of the histogram). We repeat this procedure for all stimulation levels and count the total number of activated neurons within the cortical network, leading to the plot in Figure 5*E*. Therefore, for every stimulation level I, we have a number of activated neurons $N_{act}(I)$. To obtain the postsynaptic response, we first calculated the number of afferent activated neurons onto the recorded cell. Given a random recurrent connectivity $\varepsilon_{cort} = 2\%$ (the connectivity of the network is considered homogenous within the defined local cortical network) and a fraction of inhibitory neurons $g = 25\%$, the recorded neuron will have $N_e = N_{act}(I) \cdot (1 - g)$ and $N_i = N_{act}(I) \cdot g$ excitatory and inhibitory active synapses, respectively. The maximum depolarization value induced by this stimulation is then given by calculating the time of maximum amplitude (Equation 17) and evaluating the membrane potential time course (Equation 16) at that time. The synaptic and membrane parameters used in this calculation can be found in Table 1. The whole procedure results in Figure 5, *F* and *G*, where the postsynaptic response and the modulation factor for evoked intracortical postsynaptic potentials in Up versus Down states are represented. The gain modulation imposed by the Up and Down states results in a scaling of the responses, potentiating the smaller responses and dampening

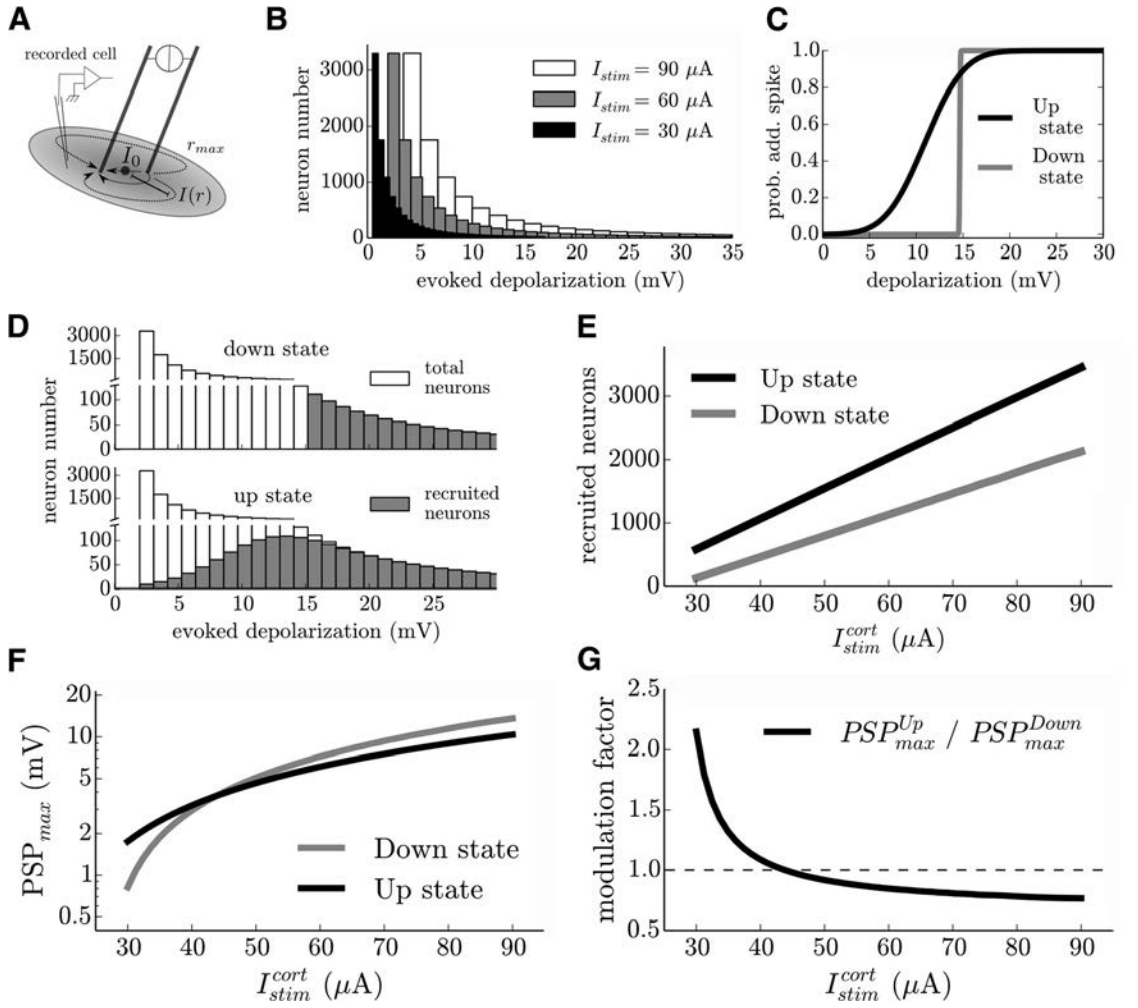

Figure 5. Modeling the effect of intracortical electrical stimulation on cortical postsynaptic potentials. ***A***, We define a local cortical network that is sensitive to the stimulation; the recorded cell is part of it and receives recurrent input from this network. ***B***, Recruitment of neurons for different stimulation intensities. Stimulation $N_I(\Delta V)$ (Equation 16) of the local cortical network given the decaying stimulus intensity $I(r)$ and the increasing cell density $N(r)$. ***C***, The activation function represents the excitability of the cortical network. It estimates the probability to elicit a spike as a response to the stimulation (for the cell's fraction that does not participate in the background activity level in the considered time bin, see Materials and Methods) ***D***, The number of recruited neurons by the IC stimulation is the convolution of the depolarization histogram with the activation function. We show for $I = 80$ μA how the recruitment differs between Up and Down states. ***E***, Repeating the procedure of ***D*** for all intensity levels provides the number of activated neurons within the network as a function of the current stimulation. ***F***, For given network parameters, we can estimate the network input to the recorded cell and deduce the maximum postsynaptic potential to be compared with the experimental results of Figure 2*C*. ***G***, Modulation factor (amplitude of PSP in Up state divided by amplitude of PSP in Down state) as a function of the stimulus intensity.

the larger ones in a similar way to the experimental intracortical stimulation (Figs. 3*E*, 7).

Gain modulation in a thalamocortical model: cortical postsynaptic response to thalamic stimulation

We investigated the impact of the thalamic processing of the input on the gain modulation. To that end, we included the change of the excitability properties of the thalamic network between Up and Down states. Indeed, the *in vivo* intracellular study of (Contreras et al., 1996) shows that the Up state has an impact in the thalamic neurons (membrane depolarization and conductance increase). Therefore, the recruitment effect that we described for the intracortical stimulation case (see above) applies not only for the cortical, but also for the thalamic network. We implemented this idea in a model, simplifying the thalamocortical model presented in Destexhe (2009) to adapt it to our situation (see Materials and Methods). To construct the current-depolarization relationship, we first model the TC stimulation that recruits thalamic neurons in a state-dependent manner (Fig. 6*B*, shown for $I^{thal} = 145$ μA) following their different activation function (Fig. 6*A*). This results in a mean number of activated TC neurons $N_{act}^{thal}(I^{thal})$ as a function of the injected current. We hypothesize a random projection between the thalamic network of size $N_{tot}^{thal} = 2000$ and the cortical network of size $N_{tot}^{cort} = 10000$ with a probability $\varepsilon^{thal} = 2\%$. The number of activated synapses onto cortical neurons will result from the sampling of $N_{act}^{cort}(I^{thal})$ neurons with a connection probability ε^{thal}, which means that the number of activated synapses over the cortical network will follow a binomial distribution (Fig. 6*C*, shown for $I^{thal} = 145$ μA). With the parameters of the thalamocortical synapse (Table 1), we translate a number of activated excitatory synapses into a maximum depolarization using Equation 17 (expression for the time of maximum amplitude) and Equation 16 (time course of the membrane potential variations). In this way, we generate a histogram of depolarization over the available neurons on which we can apply the activation function (Fig. 6*D*, shown for $I^{thal} = 145$ μA) to get the number of activated neurons in the cortical network $N_{act}^{cort}(I^{thal})$. In Figure 6*E*, we show the number of activated TC neurons (inset) and cortical neurons

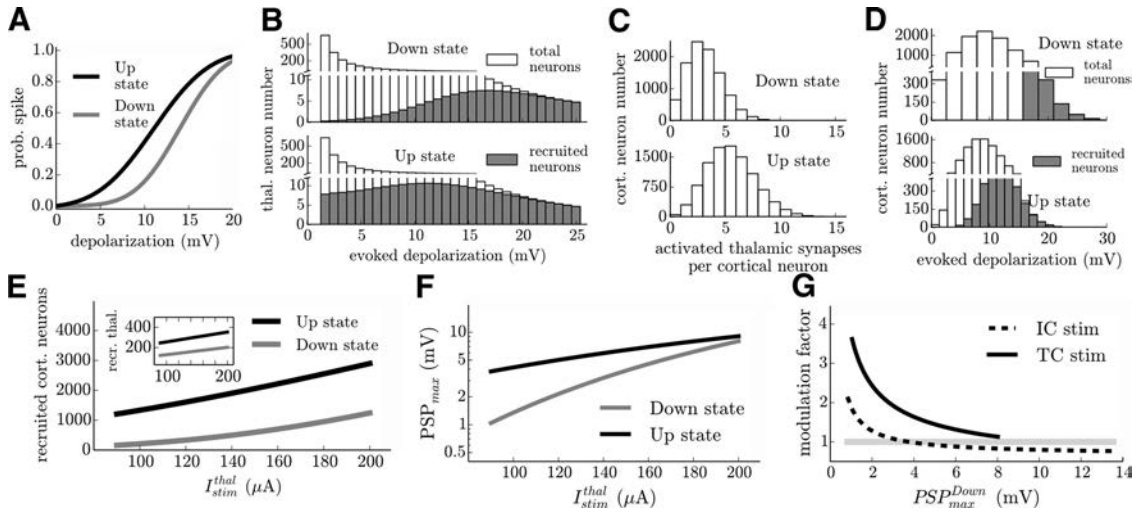

Figure 6. Modeling the effect of thalamocortical electrical stimulation on cortical postsynaptic potentials. ***A***, Activation functions of the thalamic cells that represent the difference of excitability of the thalamic network in the Up and Down states, respectively. ***B***, The recruitment within the cortical network is done as in the cortical case (see Fig. 4). The procedure allows to have a number of activated thalamic cells in the Up and Down states, shown for $I_{stim}^{thal} = 145\ \mu A$. ***C***, Histogram over the cortical network (binomial distribution) of the number of activated afferent TC synapses per cortical neuron, shown for the same level of stimulation. ***D***, Each number of activated synapses can be translated into a depolarization level. This provides the histogram of the depolarization over the cortical network. The number of activated cortical neurons is calculated (as in the IC stimulation case) by convolution of the depolarization histogram with the activation function. ***E***, We repeat this procedure for all levels of the TC stimulation levels and get the number of activated TC cells (inset) and the number of activated cortical cells as a function of the stimulation level in the Up and Down states, respectively. ***F***, Amplitude of PSP as a function of the current stimulation level. ***G***, Modulation factor as a function of the PSP amplitude in the Down state. Shown is a comparison between the model of IC stimulation and TC stimulation. The gain modulation between Up and Down state is greatly increased with respect to the cortical case as a consequence of the cumulative effect of the increased excitability of the cortical and thalamic networks.

(main plot) for all values of stimulation intensities. Finally, as in the previous section, we calculate the mean postsynaptic response resulting from the activation of those $N_{act}^{cort}(I^{thal})$. This is shown in Figure 6*F* for a whole range of stimulus intensities.

Comparing the modulation in the different stimulation types

In the models, we get an equal postsynaptic response of 2 mV in the Down state for $I^{thal} = 116.9\ \mu$A and for $I^{cort} = 36.1\ \mu$A. In the Up state, this stimulation intensity corresponds to two different postsynaptic responses: 2.6 and 4.9 mV for the IC and TC stimulation, respectively. Because the cortical network has the same activation function in the two situations, the origin of this potentiation in the TC case comes from the enhanced excitability of the thalamic network in the Up state (as can be seen in the activation function; Fig. 6*A*). Indeed, in this model, only two phenomena can lead to a difference between the IC and TC stimulation cases: the enhanced excitability of the thalamic network and the scaling of the thalamocortical postsynaptic effect on cortical cells because of the conductance state of the cortical cells. The first one potentiates the Up state response and the second one attenuates it. We found that, for our parameters, the combination of those two effects is in favor of the Up state potentiated response. We plot in Figure 6*G* the modulation as a function of the Down state response in the IC and TC cases. The deviation between the two curves is the trace of the modulation that happens in the thalamic nucleus.

To compare with the experimental data in Figure 7, we represented the modulation factor of postsynaptic responses as a function of the Down state for both IC and TC stimulation. As predicted by the model (Fig. 6*G*), the increase in the modulation in the TC case with respect to the IC is evident, as is the scaling of the postsynaptic responses. The introduced model provides a feasible mechanistic explanation for this experimental observation.

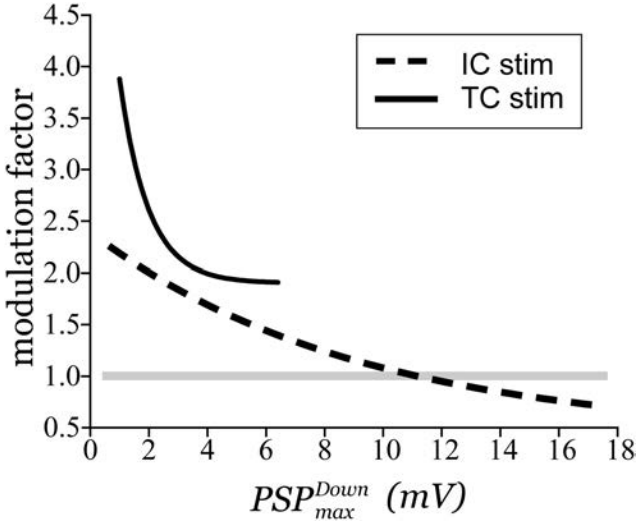

Figure 7. Experimental modulation factor for TC and IC synaptic inputs. Comparison of the input modulation factor as a function of the Down state response for TC and IC stimuli. The TC stimulation paradigm displayed a larger modulation than the IC stimulation. Auditory and TC stimulation involve the thalamocortical pathway while the IC stimulation only involves the recurrent cortical network. A mechanism such as the one discussed in the text and illustrated in Figure 5 could explain this increased modulation by taking into account the impact of both the thalamic and cortical network excitability in the Up state.

Discussion

Cortical dynamics during Up states are similar in various aspects to those during cortical activated states or wakefulness (for a review, see Destexhe et al., 2007). That is one reason why the study of synaptic responsiveness during Up and Down states is relevant for understanding information transmission and processing in different brain states, in particular during wakefulness. In this study, we have recorded Up and Down states in the auditory cortex. In different cortical areas, the transition from anes-

thesia or deep sleep to awake has been described as an elongation or persistence of the Up states (Steriade et al., 2001; Constantinople and Bruno, 2011). Even when slow oscillatory activity has been also studied by others in the auditory cortex under anesthesia (Sakata and Harris, 2009), Hromádka et al. (2013) reported that Up states are rare in the awake auditory cortex. The possibility exists that auditory cortex would be a special case on this regard. However, it is known that the dynamics of the network slow oscillatory activity are very sensitive to the brain state. In a study by Deco et al. (2009), the emergent activity in both deep and light anesthesia is described in auditory cortex. There, when in light anesthesia, the silent state is more depolarized and the dynamics of Down/Up transitions are radically different from those in deep anesthesia, the membrane potential remaining for longer periods in depolarized values. Furthermore, the content of high frequencies during silent states is larger in light than in deep anesthesia. In Figure 5 of Hromádka et al. (2013), the silent state also shows both more depolarized values and larger high-frequency activity in the awake than under anesthesia. Based on this, one could argue that in the awake auditory cortex the silent state does not exactly correspond to a "classical" Down state.

The influence that Up states have on sensory or synaptic transmission has been studied in different systems (see Introduction). However, there is no consensus as to whether synaptic transmission during cortical Up states is increased or decreased with respect to Down states (see below). In the study that we present here, we have evoked synaptic potentials in primary auditory cortex *in vivo* by three means: auditory stimulation and intracortical and thalamocortical electrical stimulation with stimuli of different intensities. Synaptic potentials evoked during Up states were compared with those evoked during Down states with the same stimulus intensity. For all types of stimulation, we found that the relative synaptic transmission in Up versus Down states is critically dependent on the intensity of stimulation. Our results show that, during Up states, there is gain modulation of synaptic responses such that the transmission of small inputs is potentiated and very strong inputs are attenuated, resulting in a scaling of the responses. This was the case for all forms of stimulation and it was especially evident for intracortical stimulation.

Synaptic transmission in Up versus Down states: increased or decreased?

The issue of how Up states and therefore network activity affects synaptic inputs has been discussed by different investigators. Studies in the visual cortex generally found increased responses during Up states, both suprathreshold and subthreshold (Arieli et al., 1996; Azouz and Gray, 1999; Haider et al., 2007; Reig and Sanchez-Vives, 2007). However, several studies in barrel cortex reported that, during Up states, responsiveness was decreased with respect to that during Down states (Castro-Alamancos and Oldford, 2002; Sachdev et al., 2004; Crochet et al., 2006; Hasenstaub et al., 2007; Rigas and Castro-Alamancos, 2009).

An increase in responsiveness during Up states is quite straightforward to explain: during these periods, the excitability of the thalamocortical network is increased and thus any stimulus recruits more presynaptic inputs. Postsynaptically, neurons are depolarized and are thus closer to threshold during Up states and are therefore more responsive to inputs. These arguments have been used to explain increased responsiveness in visual cortex (Arieli et al., 1996; Azouz and Gray, 1999; Haider et al., 2007; Reig and Sanchez-Vives, 2007).

Different mechanisms can also be invoked to explain the opposite, why synaptic responses may decrease during Up versus Down states. That both thalamocortical and intracortical synaptic responses depress with activity has been used as an argument supporting why synaptic transmission is attenuated during Up states (Castro-Alamancos and Oldford, 2002). A smaller driving force for glutamatergic transmission during Up states (Castro-Alamancos, 2002; Petersen et al., 2003; Sachdev et al., 2004), increased membrane conductance (Hasenstaub et al., 2007), an increase in the action potential threshold (Sachdev et al., 2004), or low calcium during Up states (Crochet et al., 2005), are among the other possible mechanisms that might override the increased excitability during Up states.

Differences in intrinsic properties across cortical areas could contribute to differences across areas. For example, the apparent input resistance in Up states appears to be very low in cat association cortex (Paré et al., 1998) but high in rat barrel cortex (Zou et al., 2005; Waters and Helmchen, 2006). Our conductance measurements in auditory cortical neurons reported above find a 1.3–3.3 times larger conductance in Up than in Down states in regular spiking neurons, probably due to the accumulation of excitatory and inhibitory synaptic events described in A1 during Up states (Compte et al., 2009). Such differences in input resistance may also contribute to the observed differences of responsiveness, which further emphasizes the need to precisely measure the conductance state in Up/Down states.

Despite the different mechanisms just mentioned, we propose here two possible explanations supporting the disparate results reported so far in the literature about cortical activation and its effects on responsiveness. One is the relevance of the stimulation intensity because we find that, in the same system (auditory, in the present study), one can observe both increases and decreases of the synaptic response depending on the stimulus intensity. Therefore, different intensities of stimulation used by different groups could generate different results.

Another critical element is the degree of network recruitment integrated in the synaptic response evoked during Down states that is taken as a reference. Given that synaptic responses during Up states are evaluated against those during Down states, the measurements of synaptic responses during Down states is crucial. Synaptic potentials occurring during Down states can trigger or not a new Up state. The probability to induce an Up state is larger for larger-intensity stimuli. When a synaptic response is large enough to recruit the local network and activate an Up state, the evoked synaptic amplitude includes the postsynaptic potential plus the reverberation of activity in the network (Fig. 6 in Reig and Sanchez-Vives, 2007). To correctly compare synaptic responses in Down versus Up states, it is critical to include only synaptic responses in Down states, and not the evoked synaptic reverberation. When the intensity of stimulation is large but not maximum, the synaptic potential occurring during the Down state is immediately followed by an Up state (Reig and Sanchez-Vives, 2007). In these cases, the amplitude of the synaptic potential is still well segregated in time from that of the Up state and can be measured separately. For still larger intensities, the network recruitment by the stimulus is immediate and therefore the network activation cannot be separated from the synaptic potential. In some of the studies discussed above, the stimulation was such that the responses during Down states always included the network response. This can result in a mistaken detection of a large synaptic response during Down states such that the one during Up states appears decreased in comparison.

In the present study, we only included stimulus intensities that did not trigger an Up state. This limits the use of high-intensity stimuli. This was the case for auditory and thalamocortical stim-

ulation, whereas intracortical stimuli could be of large amplitudes without recruiting Up states. This is probably why intracortical stimuli was the one where an actual decrease of the synaptic potential amplitudes during Up states was more obvious for high-intensity stimuli. When the intensity of stimulation is low, this problem does not arise because Up states are not recruited by the stimulation. For low-intensity stimulation, the responses during Up states were invariably increased with respect to those during Down states (Figs. 2, 3, 4). This increment was independent of how the synaptic potential was evoked (auditory, intracortical, or thalamocortical stimulation).

Scaling of synaptic inputs during Up states

The effect of network state that we have described here results in gain modulation of the incoming inputs, enhancing small inputs and attenuating very large ones while still maintaining the intensity–response relationship. This change in the input/output slope during activated states of the cortex could have a function expanding the range of inputs that can be processed, improving detectability of weak inputs.

The model that we introduce here provides a possible mechanism to explain the experimentally observed properties. We find that Up and Down states represent different modes of treatment of the synaptic input: the first uses the depolarization and the fluctuations to amplify the input at the network level and the latter makes use of a low conductance state to generate strong postsynaptic responses.

To explain the results of thalamocortical inputs, we had to consider a double gain modulation in both thalamic cells (Wolfart et al., 2005) and cortical recipient cells. Our model shows that the combined action of synaptic noise on these two interconnected networks can lead to a duplication of the gain modulation effects on synaptic responsiveness. The feedforward arrangement of excitable neural networks is a powerful mechanism to enhance the propagation of the Up state response compared with the Down state response. It also suggests that such combined effects may need to be taken into account for interpreting responses in areas downstream to A1, which should be investigated in future studies. Furthermore, our model results suggest the need of precise measurements of synaptic noise in different areas to correctly reconstruct the combined effect of integrating information from different networks.

References

Arieli A, Sterkin A, Grinvald A, Aertsen A (1996) Dynamics of ongoing activity: explanation of the large variability in evoked cortical responses. Science 273:1868–1871. CrossRef Medline

Azouz R, Gray CM (1999) Cellular mechanisms contributing to response variability of cortical neurons in vivo. J Neurosci 19:2209–2223. Medline

Boudreau CE, Ferster D (2005) Short-term depression in thalamocortical synapses of cat primary visual cortex. J Neurosci 25:7179–7190. CrossRef Medline

Castro-Alamancos MA (2002) Different temporal processing of sensory inputs in the rat thalamus during quiescent and information processing states in vivo. J Physiol 539:567–578. CrossRef Medline

Castro-Alamancos MA, Oldford E (2002) Cortical sensory suppression during arousal is due to the activity-dependent depression of thalamocortical synapses. J Physiol 541:319–331. CrossRef Medline

Compte A, Reig R, Sanchez-Vives M (2009) Timing excitation and inhibition in the cortical network. In: Coherent behavior in neuronal networks (Josic K, Rubin J, Matias M, Romo R, eds), pp 17–46. New York: Springer.

Constantinople CM, Bruno RM (2011) Effects and mechanisms of wakefulness on local cortical networks. Neuron 69:1061–1068. CrossRef Medline

Contreras D, Timofeev I, Steriade M (1996) Mechanisms of long-lasting hyperpolarizations underlying slow sleep oscillations in cat corticothalamic networks. J Physiol 494:251–264. CrossRef Medline

Cowan RL, Wilson CJ (1994) Spontaneous firing patterns and axonal projections of single corticostriatal neurons in the rat medial agranular cortex. J Neurophysiol 71:17–32. Medline

Crochet S, Chauvette S, Boucetta S, Timofeev I (2005) Modulation of synaptic transmission in neocortex by network activities. Eur J Neurosci 21:1030–1044. CrossRef Medline

Crochet S, Fuentealba P, Cissé Y, Timofeev I, Steriade M (2006) Synaptic plasticity in local cortical network in vivo and its modulation by the level of neuronal activity. Cereb Cortex 16:618–631. Medline

Deco G, Martí D, Ledberg A, Reig R, Vives MVS (2009) Effective reduced diffusion-models: a data driven approach to the analysis of neuronal dynamics. PLoS Comput Biol 5:e1000587. CrossRef Medline

Destexhe A (2009) Self-sustained asynchronous irregular states and Up-Down states in thalamic, cortical and thalamocortical networks of nonlinear integrate-and-fire neurons. J Comput Neurosci 27:493–506. CrossRef Medline

Destexhe A, Contreras D (2006) Neuronal computations with stochastic network states. Science 314:85–90. CrossRef Medline

Destexhe A, Hughes SW, Rudolph M, Crunelli V (2007) Are corticothalamic 'up' states fragments of wakefulness? Trends Neurosci 30:334–342. CrossRef Medline

Gil Z, Amitai Y (1996) Properties of convergent thalamocortical and intracortical synaptic potentials in single neurons of neocortex. J Neurosci 16:6567–6578. Medline

Haider B, Duque A, Hasenstaub AR, Yu Y, McCormick DA (2007) Enhancement of visual responsiveness by spontaneous local network activity in vivo. J Neurophysiol 97:4186–4202. CrossRef Medline

Hasenstaub A, Sachdev RN, McCormick DA (2007) State changes rapidly modulate cortical neuronal responsiveness. J Neurosci 27:9607–9622. CrossRef Medline

Hô N, Destexhe A (2000) Synaptic background activity enhances the responsiveness of neocortical pyramidal neurons. J Neurophysiol 84:1488–1496. Medline

Hromádka T, Zador AM, DeWeese MR (2013) Up states are rare in awake auditory cortex. J Neurophysiol 109:1989–1995. CrossRef Medline

Kuhn A, Aertsen A, Rotter S (2004) Neuronal integration of synaptic input in the fluctuation-driven regime. J Neurosci 24:2345–2356. Medline

Lapicque L (1907) Recherches quantitatives sur l'excitation électrique des nerfs traitée comme une polarisation. J Physiol Pathol Gen 9:620–635.

Logothetis NK, Kayser C, Oeltermann A (2007) In vivo measurement of cortical impedance spectrum in monkeys: implications for signal propagation. Neuron 55:809–823. CrossRef Medline

Lorente de No R (1938) Analysis of the activity of the chains of internuncial neurons. J Neurophysiol 1:207–244.

Luczak A, Barthó P, Harris KD (2009) Spontaneous events outline the realm of possible sensory responses in neocortical populations. Neuron 62:413–425. CrossRef Medline

Metherate R, Ashe JH (1993) Ionic flux contributions to neocortical slow waves and nucleus basalis-mediated activation: whole-cell recordings in vivo. J Neurosci 13:5312–5323. Medline

Nowak LG, Sanchez-Vives MV, McCormick DA (1997) Influence of low and high frequency inputs on spike timing in visual cortical neurons. Cereb Cortex 7:487–501. CrossRef Medline

Nowak LG, Azouz R, Sanchez-Vives MV, Gray CM, McCormick DA (2003) Electrophysiological classes of cat primary visual cortical neurons in vivo as revealed by quantitative analyses. J Neurophysiol 89:1541–1566. Medline

Paré D, Shink E, Gaudreau H, Destexhe A, Lang EJ (1998) Impact of spontaneous synaptic activity on the resting properties of cat neocortical pyramidal neurons in vivo. J Neurophysiol 79:1450–1460. Medline

Paxinos G, Watson C (2005) The rat brain in stereotaxic coordinates, ed 5. Amsterdam: Elsevier Academic.

Petersen CC, Hahn TT, Mehta M, Grinvald A, Sakmann B (2003) Interaction of sensory responses with spontaneous depolarization in layer 2/3 barrel cortex. Proc Natl Acad Sci U S A 100:13638–13643. CrossRef Medline

Ranck JB Jr (1975) Which elements are excited in electrical stimulation of mammalian central nervous system: a review. Brain Res 98:417–440. CrossRef Medline

Rees A, Sarbaz A, Malmierca MS, Le Beau FE (1997) Regularity of firing of neurons in the inferior colliculus. J Neurophysiol 77:2945–2965. Medline

Reig R, Sanchez-Vives MV (2007) Synaptic transmission and plasticity in an active cortical network. PLoS One 2:e670. CrossRef Medline

Reig R, Gallego R, Nowak LG, Sanchez-Vives MV (2006) Impact of cortical network activity on short-term synaptic depression. Cereb Cortex 16: 688–695. CrossRef Medline

Richardson MJ (2004) Effects of synaptic conductance on the voltage distribution and firing rate of spiking neurons. Phys Rev E Stat Nonlin Soft Matter Phys 69:051918. CrossRef Medline

Rigas P, Castro-Alamancos MA (2009) Impact of persistent cortical activity (up States) on intracortical and thalamocortical synaptic inputs. J Neurophysiol 102:119–131. CrossRef Medline

Rudolph M, Piwkowska Z, Badoual M, Bal T, Destexhe A (2004) A method to estimate synaptic conductances from membrane potential fluctuations. J Neurophysiol 91:2884–2896. CrossRef Medline

Sachdev RN, Ebner FF, Wilson CJ (2004) Effect of subthreshold up and down states on the whisker-evoked response in somatosensory cortex. J Neurophysiol 92:3511–3521. CrossRef Medline

Sakata S, Harris KD (2009) Laminar structure of spontaneous and sensory-evoked population activity in auditory cortex. Neuron 64:404–418. CrossRef Medline

Sanchez-Vives MV, McCormick DA (2000) Cellular and network mechanisms of rhythmic recurrent activity in neocortex. Nat Neurosci 3:1027–1034. CrossRef Medline

Sanchez-Vives MV, Nowak LG, Descalzo VF, Garcia-Velasco JV, Gallego R, Berbel P (2006) Crossmodal audio-visual interactions in the primary visual cortex of the visually deprived cat: a physiological and anatomical study. Prog Brain Res 155:287–311. CrossRef Medline

Seamari Y, Narváez JA, Vico FJ, Lobo D, Sanchez-Vives MV (2007) Robust off- and online separation of intracellularly recorded up and down cortical states. PLoS One 2:e888. CrossRef Medline

Steriade M (2001) Impact of network activities on neuronal properties in corticothalamic systems. J Neurophysiol 86:1–39. Medline

Steriade M, Nuñez A, Amzica F (1993) A novel slow (<1 Hz) oscillation of neocortical neurons in vivo: depolarizing and hyperpolarizing components. J Neurosci 13:3252–3265. Medline

Steriade M, Timofeev I, Grenier F (2001) Natural waking and sleep states: a view from inside neocortical neurons. J Neurophysiol 85:1969–1985. Medline

Timofeev I, Contreras D, Steriade M (1996) Synaptic responsiveness of cortical and thalamic neurones during various phases of slow sleep oscillation in cat. J Physiol 494:265–278. CrossRef Medline

Waters J, Helmchen F (2006) Background synaptic activity is sparse in neocortex. J Neurosci 26:8267–8277. CrossRef Medline

Wolfart J, Debay D, Le Masson G, Destexhe A, Bal T (2005) Synaptic background activity controls spike transfer from thalamus to cortex. Nat Neurosci 8:1760–1767. CrossRef Medline

Zou Q, Rudolph M, Roy N, Sanchez-Vives M, Contreras D, Destexhe A (2005) Reconstructing synaptic background activity from conductance measurements in vivo. Neurocomputing 65:673–678. CrossRef

Work 4: Spatio-temporal dynamics of multi-input integration in primary visual cortex: comparison between a *mean-field* model and optical imaging of population activity *in vivo*

French summary

L'imagerie VSD s'est révélée un outil majeur pour explorer comment la dynamique de populations neuronales façonne les fonctions corticales. Néanmoins, à notre connaissance, il n'existe pas de modèle théorique qui offre une explication du lien entre les sources de signaux imagés et la dynamique neuronale pour les échelles spatiales associées à l'imagerie optique. Dans ce travail, nous tirons parti du travail théorique effectué à l'échelle mésoscopique (les approches *mean-field*) pour construire un modèle large-échelle de la dynamique de population tout en gardant un correlat en terme de dynamique cellulaire (en particulier en terme de potentiel membranaire) pour pouvoir générer des prédictions pour le signal imagé par la technique VSD.

La première partie de ce travail étudie la validité et les faiblesses du formalisme théorique pour décrire l'activité d'une colonne corticale. Nous avons construit un modèle grande échelle du réseau des couches corticales II-III incluant le réseau des fibres horizontales. Nous avons examiné les propriétés intégratives spatio-temporelles du modèle et nous les avons comparées avec des mesures par imageries optiques de l'activité cérébrale chez le singe éveillé. En particulier, nous avons reconstruit une expérience typique du traitement visuel: le mouvement apparent. Le modèle prédit un fort signal suppressif dont le profil spatio-temporel correspond quantitativement à celui observé *in vivo*. Ce qui suggère que la combinaison des propriétés intégratives du réseau capturées par notre approche et du réseau des fibres horizontales sont les ingrédients clefs de ce phénomène.

A Markovian model for spatio-temporal population dynamics in neocortex

Collab.: S. Chemla[1] & F. Chavane[1] (*in vivo* VSD imaging)

Y. Zerlaut[2] & A. Destexhe[2]

Abstract

While voltage sensitive dye imaging (VSDi) has been shown to be a decisive tool in the exploration of how neural population dynamics shape cortical function, to our knowledge, no theoretical model offers a detailed account of the link between neural dynamics and the source signal at the large spatial scale imaged by optical imaging ($\sim$ 100mm^2).

In this communication, we take advantage of the extensive theoretical work performed at the mesoscopic scale ($\sim$ 10000 neurons, 0.25mm^2) to analytically describe population dynamics in terms of few variables (the so-called *mean-field* approach to network dynamics) to build a large scale model of population dynamics but still with a correlate in terms of single-cell dynamics (in particular membrane potential dynamics) so that the model can directly generate predictions for the signal imaged by the VSDi technique.

The first part establishes the validity and weaknesses of the mesoscopic description of network dynamics used to model the activity of a single cortical column. By comparing its prediction with numerical simulations of artificial neural networks, we investigate whether the markovian formalism proposed in El Boustani and Destexhe (2009) allows to describe the dynamics of a network of excitatory and inhibitory neurons with different electrophysiological properties. In particular, we investigate whether this formalism generalizes to the description of network dynamics in the presence of time-dependent inputs.

We next analyze the integrative properties of the model: how does it responds to increasing stimuli strength or how is it modulated by an increase in external background activity. We found that, while the firing response scales linearly the response in terms of membrane potential variations over the population exhibits a strong suppression. We then embed this local network description in a ring geometry to describe the spatial integration across the neocortical sheet. We first show that this simple model accurately predicts the emergence of propagating waves in response to simple stimuli (Muller et al., 2014).

Finally we re-construct a typical experimental paradigm of multi-input integration in visual processing: the apparent motion protocol. We compare the model's response to optical imaging of spatio-temporal dynamics in the primary visual cortex of fixating monkey (Chemla & Chavane, unpublished observations). The model exhibited a similar spatio-temporal pattern of suppression such as the one observed *in vivo*, our study therefore proposes that the horizontal fib re network combined with the strongly sublinear relation between membrane potential deflection and activity in the local network appears as a putative sufficient explanation for the observation found in VSDi recordings during an apparent motion stimulus in fixating monkeys.

[1] Team InVibe, Institut de Neurosciences de la Timone, UMR 7289, CNRS and Aix-Marseille Université, Marseille, France

[2] Unité de Neurosciences, Information et Complexité, Centre National de la Recherche Scientifique, FRE 3693, Gif sur Yvette, France

Introduction

Recent advances in imaging technique, in particular voltage-sensitive dye imaging (VSDi), have revealed fundamental properties of neocortical processing (Arieli et al., 1996; Contreras and Llinas, 2001; Petersen and Sakmann, 2001; Ferezou et al., 2006; Civillico and Contreras, 2012): subthreshold responses to sensory inputs are locally homogeneous in primary sensory areas, depolarizations tend to spread across spatially neighboring regions and responses to sensory stimuli are strongly affected by the level of ongoing activity. It also appears as great tools to unveil how the spatio-temporal dynamics in the neocortex shape canonical cortical operations such as normalization (Reynaud et al., 2012).

On the other hand, the literature lacks, to the best of our knowledge, theoretical models that provides a detailed account of those phenomena with a clear relation between how this signal is generated and those physiological phenomena at that spatial scale (i.e. at the millimeters or centimeters scale). Detailed model of a neocortical column (i.e. $\sim$0.5mm^2 scale) have been recently proposed, see Chemla and Chavane (2010) for the link with the VSDi signal or more generally Markram et al. (2015), but their computational cost impedes the generalization to higher spatial scale. The aim of the present communication is thus to design a theoretical model of neocortical dynamics with the following properties: 1) it should operate at the temporal and spatial scales of optical imaging and 2) it should have a correlate in terms of single-cell dynamics (in particular membrane potential dynamics), so that the model can directly generate predictions for the signal imaged by the VSDi technique (Berger et al., 2007).

More specifically, our study focuses on network dynamics in *activated* cortical states, thus the desired model should

describe neocortical computation in the asynchronous regime, where cortical activity is characterized by irregular firing and strong subthreshold fluctuations at the neuronal level (Steriade et al., 2001; Destexhe et al., 2003). The strategy behind the present model is to take advantage of the *mean-field* descriptions of network dynamics in this regime. Via self-consistent approaches, those descriptions allow to capture the dynamical properties of population activity in recurrent networks (Amit and Brunel, 1997; Brunel and Hakim, 1999; Brunel, 2000; Latham et al., 2000; El Boustani and Destexhe, 2009). The present model thus relies on the following scheme: 1) we consider the randomly connected network of 10000 neurons as a unit to describe a cortical column and 2) we embedded the analytical description of this cortical column model into a ring geometry with physiological local connectivity profiles to model spatio-temporal integration on the neocortical sheet.

A prerequisite was therefore to establish the accuracy of the analytical description of the cortical column model. This is the focus of the first part of this paper: by comparing analytical prediction of the model with numerical simulations, we can precisely evaluate the accuracy and/or weaknesses of the analytical description to evaluate its potential impact on the modeling of the network.

The second part of the paper investigates the integrative properties of the model, i.e. the relation between the network response and the properties of the input. Finally we compare the model prediction with VSDi recordings in awake behaving monkey in a stereotypical paradigm of visual processing: the apparent-motion protocol.

Material and Methods

We describe the equations and parameters used for the neuronal, synaptic and network modeling. We present our *heuristic* treatment of the neuronal *transfer functions*: the quantity that accounts for the cellular computation in *mean-field* models of population activity. Then, we present the specific markovian model of population activity used in this study. Finally, we embed this description of local population dynamics in a ring model to describe spatio-temporal integration on the neocortical sheet.

Single neuron models

The neuronal model used in this study is the adaptative exponential and fire (AdExp) model (Brette and Gerstner, 2005). The equation for the membrane potential and the adaptation current therefore reads:

$$\begin{cases} C_m \dfrac{dV}{dt} = g_L\,(E_L - V) + I_{syn}(V,t) + k_a e^{\frac{V-V_{thre}}{k_a}} - I_w \\ \tau_w \dfrac{dI_w}{dt} = -I_w + \displaystyle\sum_{t_s \in \{t_{spike}\}} b\;\delta(t-t_s) \end{cases} \quad (1)$$

where $I_{syn}(V,t)$ is the current emulating synaptic activity that will create the fluctuations, I_w reproduces the I_m current (McCormick et al., 1985). The spiking mechanism is the following: when $V(t)$ reaches $V_{thre} + 5\,k_a$, this triggers a spike $t_s \in \{t_{spike}\}$, this increases the adaptation variable I_w by b, the membrane potential is then clamped at E_L for a duration τ_{refrac}=5ms. We consider two versions of this model: a regular spiking neuron for the excitatory cells and a fast spiking neuron for the inhibitory cells (see Figure 2). The parameters of those two models can be found on Table 1.

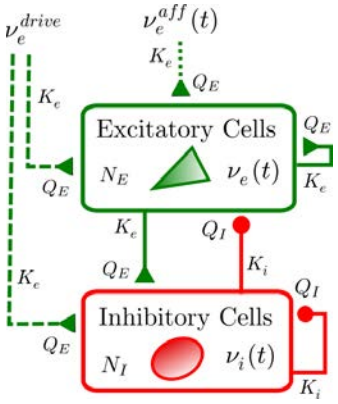

Figure 1: Schematic of the local network architecture. The network is made of $N_e = (1-g)\,N_{tot}$ excitatory and $N_i = g\,N_{tot}$ inhibitory neurons. All excitatory connections (afferent and recurrent) onto a neuron corresponds to $K_e = \epsilon\,(1-g)\,N_{tot}$ synapses of weight Q_e. All inhibitory connections (afferent and recurrent) onto a neuron corresponds to $K_i = \epsilon\,g\,N_{tot}$ synapses of weight Q_i

Synaptic model

The time- and voltage-dependent current that stimulate the neuron is made of the sum of an excitatory and inhibitory currents (indexed by $s \in \{e,i\}$ and having a reversal potential E_s):

$$I_{syn}(V,t) = \sum_{s\in\{e,i\}} \sum_{t_s\in\{t_s\}} Q_s\, e^{-\frac{t}{\tau_s}}\,(E_s - V)\,\mathcal{H}(t-t_s) \quad (2)$$

where $\mathcal{H}$ is the Heaviside function.

This synaptic model is referred to as the *conductance-based exponential* synapse. The set of events $\{t_e\}$ and $\{t_i\}$ are the set of excitatory and inhibitory events arriving to the neuron. In numerical simulations of single neurons, it will be generated by stationary Poisson processes. In numerical simulations of network dynamics it will correspond to the set of spike times of the neurons connecting to the target neurons, both via recurrent and feedforward connectivity.

Numerical network model

All simulations of numerical network were performed with the `brian2` simulator (Goodman and Brette, 2009), see `http://brian2.readthedocs.org`. For all simulations, the network was composed of N_{tot}=10000 neurons, separated in two populations, one excitatory and one inhibitory with a ratio of g=20% inhibitory cells. Those two populations we recurrently connected (internally and mutually) with a connectivity probability ϵ=5%.

Because this network did not display self-sustained activity (see Figure 3, in contrast to Vogels and Abbott (2005)), an excitatory population exerted an *external drive* to bring the network out of the quiescent state. This population targeted both the excitatory and inhibitory neurons. Note that the firing rate of this population was linearly increased to avoid

Table 1: Model parameters.

Parameters	Parameter Name	Symbol	Value	Unit
cellular properties				
	leak conductance	g_L	10	nS
	leak reversal potential	E_L	-65	mV
	membrane capacitance	C_m	150	pF
	leak reversal potential	E_L	-65	mV
	AP threshold	V_{thre}	-50	mV
	refractory period	τ_{refrec}	5	ms
	adaptation time constant	τ_w	500	ms
excitatory cell				
	sodium sharpness	k_a	2	mV
	adaptation current increment	b	20	pA
	adaptation conductance	a	4	nS
inhibitory cell				
	sodium sharpness	k_a	0.5	mV
	adaptation current increment	b	0	pA
	adaptation conductance	a	0	nS
synaptic properties				
	excitatory reversal potential	E_e	0	mV
	inhibitory reversal potential	E_i	-80	mV
	excitatory quantal conductance	Q_e	1	nS
	inhibitory quantal conductance	Q_i	5	nS
	excitatory decay	τ_e	5	ms
	inhibitory decay	τ_i	5	ms
numerical network				
	cell number	N_{tot}	10000	
	connectivity probability	ϵ	5%	
	fraction of inhibitory cells	g	20%	
	external drive	ν_e^{drive}	4	Hz
ring model				
	total extent	L_{tot}	40	mm
	excitatory connectivity extent	l_{exc}	5	mm
	inhibitory connectivity extent	l_{inh}	1	mm
	propagation delay	v_c	300	mm/s

a too strong initial synchronization (see Figure 4). Finally, an excitatory population of time varying firing rate could was added to evoke activity transients in the population dynamics. This last stimulation targeted only the excitatory population. The number of neurons in those two excitatory populations was taken as identical to the number of excitatory neurons (i.e. $(1-g)\,N_{tot}$) and created synapses onto the recurrent network with the same probability ϵ. After temporal discretization, the firing rates of those afferent populations were converted into spikes by using the properties of a Poisson process (i.e. eliciting a spike at t with a probability $\nu(t)\,dt$). All simulations were performed with a time-step dt=0.1ms.

Estimating the transfer functions of single neurons

The transfer function $\mathcal{F}$ of a single neuron is defined here as the function that maps the value of the stationary excitatory and inhibitory presynaptic release frequencies to the output stationary firing rate response, i.e. $\nu_{out} = \mathcal{F}(\nu_e, \nu_i)$. Note the stationary hypothesis in the definition of the transfer function (see discussion in main text).

Because an analytical solution of this function for the single neuron models considered in our study is a very challenging mathematical problem, we adopted a semi-analytical approach. We performed numerical simulations of single cell dynamics at various excitatory and inhibitory presynaptic frequencies (ν_e and ν_i respectively) (see the output in Figure 2) on which we fitted the coefficients of an analytical template to capture the single cell model's response.

The procedure relied on fitting a *phenomenological threshold* V_{thre}^{eff} that accounts for the single neuron non-linearities (spiking and reset mechanism, adaptation mechanisms) on top of the subthreshold integration effects (Zerlaut et al., 2016). This phenomenological threshold is then plugged-in into the following formula (analogous to Amit and Brunel (1997)) to become our firing response estimate:

$$\nu_{out} = \frac{1}{2\,\tau_V} \cdot Erfc\left(\frac{V_{thre}^{eff} - \mu_V}{\sqrt{2}\,\sigma_V}\right) \tag{3}$$

Where $(\mu_V, \sigma_V, \tau_V)$ are the mean, standard deviation and autocorrelation time constant of the membrane potential fluctuations. How to calculate those quantities as a response to a stationary stimulation is the focus of the next section.

The phenomenological threshold was taken as a second order polynomial in the three dimensional space $(\mu_V, \sigma_V, \tau_V)$:

87

$$V_{thre}^{eff}(\mu_V,\sigma_V,\tau_V^N) = P_0 + \sum_{x\in\{\mu_V,\sigma_V,\tau_V^N\}} P_x\cdot\left(\frac{x-x^0}{\delta x^0}\right) + \sum_{x,y\in\{\mu_V,\sigma_V,\tau_V^N\}^2} P_{xy}\cdot\left(\frac{x-x^0}{\delta x^0}\right)\left(\frac{y-y^0}{\delta y^0}\right) \quad (4)$$

Where the normalization factors μ_V^0=-60mV, $\delta\mu_V^0$=10mV, σ_V^0=4mV, $\delta\sigma_V^0$ = 6mV, τ_V^{N0}=0.5 and $\delta\tau_V^{N0}$= 1 arbitrarily delimits the *fluctuation-driven* regime (a mean value x and an extent δx, $\forall x \in \{\mu_V,\sigma_V,\tau_V^N\}$). They render the fitting of the phenomenological threshold easier, as they insure that the coefficients take similar values. It is kept constant all along the study. The phenomenological threshold was taken as a second order polynomial and not as a linear threshold, for two reasons: 1) unlike in an experimental study (Zerlaut et al., 2016), we are not limited by the number of sampling points, the number of fitted coefficients can thus be higher as the probability of overfitting becomes negligible 2) it gives more flexibility to the template, indeed the linear threshold was found a good approximation in the *fluctuation-driven* regime, i.e. when the diffusion approximation holds, however, for low values of the presynaptic frequencies, we can be far from this approximation, the additional coefficients are used to capture the firing response in those domains.

The fitting procedure was identical to Zerlaut et al. (2016), it consisted first in a linear regression in the phenomenological threshold space of Equation 4, followed by a non-linear optimization of Equation 3 on the firing rate response. Both fitting were performed with the `leastsq` method in the `optimize` package of `SciPy`.

Calculus of the subthreshold membrane potential fluctuations

Here, we detail the analytical calculus that translate the input to the neuron into the properties of the membrane potential fluctuations. The input is made of two Poisson shotnoise: one excitatory and one inhibitory that are both convoluted with an exponential waveform to produce the synaptic conductances time courses.

Conductances fluctuations

From Campbell's theorem (Papoulis, 1991), we first get the mean (μ_{Ge},μ_{Gi}) and standard deviation $(\sigma_{Ge},\sigma_{Gi})$ of the excitatory and inhibitory conductance fluctuations:

$$\begin{aligned}\mu_{Ge}(\nu_e,\nu_i) &= \nu_e\,K_e\,\tau_e\,Q_e\\ \sigma_{Ge}(\nu_e,\nu_i) &= \sqrt{\frac{\nu_e\,K_e\,\tau_e}{2}}\,Q_e\\ \mu_{Gi}(\nu_e,\nu_i) &= \nu_i\,K_i\,\tau_i\,Q_i\\ \sigma_{Gi}(\nu_e,\nu_i) &= \sqrt{\frac{\nu_i\,K_i\,\tau_i}{2}}\,Q_i\end{aligned} \quad (5)$$

The mean conductances will control the input conductance of the neuron μ_G and therefore its effective membrane time constant τ_m:

$$\begin{aligned}\mu_G(\nu_e,\nu_i) &= \mu_{Ge}+\mu_{Gi}+g_L\\ \tau_m(\nu_e,\nu_i) &= \frac{C_m}{\mu_G}\end{aligned} \quad (6)$$

Mean membrane potential

Following Kuhn et al. (2004), the mean membrane potential is obtained by taking the stationary solution to static conductances given by the mean synaptic bombardment (for the passive version of Equation 1, i.e. removing the adaptation and spiking mechanisms). We obtain:

$$\mu_V(\nu_e,\nu_i) = \frac{\mu_{Ge}\,E_e+\mu_{Gi}\,E_i+g_L\,E_L}{\mu_G} \quad (7)$$

We will now approximate the driving force $E_s - V(t)$ of synaptic events by the level resulting from the mean conductance bombardment: $E_s-\mu_V$. This will enable an analytical solution for the standard deviation σ_V and the autocorrelation time σ_V of the fluctuations.

Power spectrum of the membrane potential fluctuations

Obtaining σ_V and τ_V is achieved by computing the power spectrum density of the fluctuations. In the case of Poisson processes, the power spectrum density of the fluctuations resulting from the sum of events $PSP_s(t)$ at frequency $K_s\,\nu_s$ can be obtained from shotnoise theory (Daley and Vere-Jones, 2007):

$$P_V(f) = \sum_{s\in\{e,i\}} K_s\,\nu_s\,\|\hat{\mathrm{PSP}}_s(f)\|^2 \quad (8)$$

where $\hat{\mathrm{PSP}}_s(f)$ is the Fourier transform of the time-varying function $\mathrm{PSP}(t)$. Note that the relations presented in this paper rely on the following convention for the Fourier transform: $\hat{F}(f) = \int_{\mathbb{R}} F(t)\,e^{-2i\pi ft}\,dt$.

After fixing the driving force to $E_s-\mu_V$, the equation for a post-synaptic membrane potential event s around μ_V is

$$\tau_m\frac{d\,\mathrm{PSP}_s}{dt} + \mathrm{PSP}_s = U_s\,\mathcal{H}(t)\,e^{\frac{-t}{\tau_s}} \quad (9)$$

where $U_s = \frac{Q_s}{\mu_G}(E_s-\mu_V)$ and $\mathcal{H}(t)$ is the Heaviside function. Its solution is:

$$\mathrm{PSP}_s(t) = U_s\,\frac{\tau_s}{\tau_m-\tau_s}\left(e^{\frac{-t}{\tau_m}} - e^{\frac{-t}{\tau_s}}\right)\mathcal{H}(t) \quad (10)$$

We take the Fourier transform:

$$\hat{\mathrm{PSP}}_s(f) = U_s\,\frac{\tau_s}{\tau_m-\tau_s}\left(\frac{\tau_m}{2\,i\,\pi\,f\,\tau_m+1} - \frac{\tau_s}{2\,i\,\pi\,f\,\tau_s+1}\right) \quad (11)$$

We will need the value of the square modulus at $f=0$:

$$\|\hat{\mathrm{PSP}}(0)\|^2 = (U_s\cdot\tau_s)^2 \quad (12)$$

As well as the integral of the square modulus:

$$\int_{\mathbb{R}} df\,\|\hat{\mathrm{PSP}}(f)\|^2 = \frac{(U_s\cdot\tau_s)^2}{2\,(\tau_{\mathrm{m}}^{\mathrm{eff}}+\tau_s)} \quad (13)$$

Standard deviation of the fluctuations

The standard deviation follows:

$$(\sigma_V)^2 = \int_{\mathbb{R}} df\,P_V(f) \quad (14)$$

Using Equation 13, we find the final expression for σ_V:

$$\sigma_V(\nu_e,\nu_i) = \sqrt{\sum_s K_s\,\nu_s\,\frac{(U_s\cdot\tau_s)^2}{2\,(\tau_{\mathrm{m}}^{\mathrm{eff}}+\tau_s)}} \quad (15)$$

88

Autocorrelation-time of the fluctuations

We defined the global autocorrelation time as (Zerlaut et al., 2016):

$$\tau_V = \frac{1}{2}\left(\frac{\int_{\mathbb{R}} P_V(f)\,df}{P_V(0)}\right)^{-1} \tag{16}$$

Using Equations 13 and 12, we find the final expression for τ_V:

$$\tau_V(\nu_e,\nu_i) = \left(\frac{\sum_s \left(K_s\,\nu_s\,(U_s\cdot\tau_s)^2\right)}{\sum_s \left(K_s\,\nu_s\,(U_s\cdot\tau_s)^2/(\tau_m^{\text{eff}}+\tau_s)\right)}\right) \tag{17}$$

Therefore the set of Equations 7, 15 and 17 translate the presynaptic frequencies into membrane fluctuations properties μ_V, σ_V, τ_V.

The previous methodological section allowed to translate the fluctuations properties μ_V, σ_V, τ_V into a spiking probability thanks to a minimization procedure. The combination of the present analytical calculus and the previous fitting procedure (on numerical simulations data) constitute our semi-analytical approach to determine the transfer function of a single cell model: $\nu_{out} = \mathcal{F}(\nu_e,\nu_i)$.

Master equation for local population dynamics

An analytical description of the cellular transfer function is the core of theoretical descriptions of asynchronous dynamics in sparsely connected random networks (Amit and Brunel, 1997; Brunel, 2000; Renart et al., 2004).

Because we will investigate relatively slow dynamics (τ>25-50ms) (and because of the stationary formulation of our transfer function), we will use the Markovian description developed in El Boustani and Destexhe (2009), it describes network activity at a time scale T, for which the network dynamics should be Markovian. The choice of the time-scale T is quite crucial in this formalism, it should be large enough so that activity can be considered as memoryless (e.g. it can not be much smaller than the refractory period, that would introduce memory effects) and small enough so that each neuron can fire statistically only once per time interval T. Following El Boustani and Destexhe (2009), we will arbitrarily take T=5ms all along the study as it offers a good compromise between those two constraints.

The formalism describes the first and second moments of the population activity for each populations. We consider here two populations: one excitatory and one inhibitory, the formalism thus describes the evolution of five quantities: the two means $\nu_e(t)$ and $\nu_i(t)$ of the excitatory and inhibitory population activity respectively (the instantaneous population firing rate, i.e. after binning in bins of T=5ms, see discussion in El Boustani and Destexhe (2009)), the two variances $c_{ee}(t)$ and $c_{ii}(t)$ of the the excitatory and inhibitory population activity respectively and the covariance $c_{ei}(t)$ between the excitatory and inhibitory population activities. The set of differential equations followed by those quantities reads (El Boustani and Destexhe, 2009):

$$\begin{cases} T\,\dfrac{\partial \nu_\mu}{\partial t} = (\mathcal{F}_\mu - \nu_\mu) + \dfrac{1}{2}\,c_{\lambda\eta}\,\dfrac{\partial^2 \mathcal{F}_\mu}{\partial\nu_\lambda \partial\nu_\eta} \\ T\,\dfrac{\partial c_{\lambda\eta}}{\partial t} = A_{\lambda\eta} + (\mathcal{F}_\lambda - \nu_\lambda)\,(\mathcal{F}_\eta - \nu_\eta) + \\ \qquad c_{\lambda\mu}\,\dfrac{\partial \mathcal{F}_\mu}{\partial \nu_\lambda} + c_{\mu\eta}\,\dfrac{\partial \mathcal{F}_\mu}{\partial \nu_\eta} - 2c_{\lambda\eta} \end{cases} \tag{18}$$

with:

$$A_{\lambda\eta} = \begin{cases} \dfrac{\mathcal{F}_\lambda\,(1/T - \mathcal{F}_\lambda)}{N_\lambda} & \text{if } \lambda = \eta \\ 0 & \text{otherwise} \end{cases} \tag{19}$$

Note that, for the concision of the expressions, we used Einstein's index summation convention: if an index is repeated in a product, a summation over the whole range of value is implied (e.g. we sum over $\lambda \in \{e,i\}$ in the first equation, note that, consequently, λ does not appear in the left side of the equation). Also the dependency of the firing rate response to the excitatory and inhibitory activities has been omitted: yielding $\mathcal{F}_\mu$ instead of $\mathcal{F}_\mu(\nu_e,\nu_i)$, $\forall \mu \in \{e,i\}$.

We will also use the reduction to first order of this system (for the phase-space analysis, see Results). This yields:

$$T\,\frac{\partial \nu_\mu}{\partial t} = \mathcal{F}_\mu - \nu_\mu \tag{20}$$

Ring model

We now embed the previous markovian description of population dynamics in a ring geometry to model spatio-temporal integration on the neocortical sheet. The ring geometry corresponds to a one dimensional spatial description with an invariance by translation, i.e. for all quantities f, $f(x) = f(x+L)$(also termed one dimensional periodic boundary conditions), where L is the length of the ring model. For simplicity, we consider here only the first moments of the second-order description: i.e. the means of the excitatory and inhibitory population activities: $\nu_e(t)$ and $\nu_i(t)$ respectively.

We introduce the Gaussian connectivity profiles (see Figure 10) that defines the connectivity across cortical columns (i.e. local networks described in the previous section):

$$\mathcal{N}_e(x) = \frac{1}{\sqrt{2\pi}l_{exc}}e^{-(\frac{x}{\sqrt{2}l_{exc}})^2} \quad ; \quad \mathcal{N}_i(x) = \frac{1}{\sqrt{2\pi}l_{inh}}e^{-(\frac{x}{\sqrt{2}l_{inh}})^2} \tag{21}$$

where l_{exc} and l_{inh} are the excitatory and inhibitory extent of the connectivity profiles respectively.

We also introduce the effect of a finite axonal conduction speed v_c, this will introduce delays for the propagation of activity across cortical columns: for a network at a distance x, the afferent activity will arrive delayed by x/v_c.

Finally, the equations that govern the activity in space and time are given by:

$$\begin{cases} \nu_e^{input}(x,t) = \nu_e^{drive} + \displaystyle\int_{\mathbb{R}} dy\,\mathcal{N}_e(x-y)\,\nu_e(y,t-\|y-x\|/v_c) \\ \nu_i^{input}(x,t) = \displaystyle\int_{\mathbb{R}} dy\,\mathcal{N}_i(x-y)\,\nu_i(y,t-\|y-x\|/v_c) \\ T\dfrac{\partial \nu_e(x,t)}{\partial t} = -\nu_e(x,t) + \\ \qquad \mathcal{F}_e(\nu_e^{aff}(x,t) + \nu_e^{input}(x,t), \nu_i^{input}(x,t)) \\ T\dfrac{\partial \nu_i(x,t)}{\partial t} = -\nu_i(x,t) + \mathcal{F}_i(\nu_e^{input}(x,t), \nu_i^{input}(x,t)) \end{cases} \tag{22}$$

where ν_e^{drive} is the external drive and $\nu_e^{aff}(x,t)$ is the afferent (thalamic) stimulation.

The local correlate in terms of mean membrane potential $\mu_V(x,t)$ is given by Equation 7.

89

Afferent stimulation

In the case of the local population model, the afferent input was chosen as a piecewise double Gaussian waveform:

$$\nu_e^{aff}(t) = A\left(e^{-(\frac{t-t_0}{\sqrt{2}\tau_1})^2}\mathcal{H}(t_0-t) + e^{-(\frac{t-t_0}{\sqrt{2}\tau_2})^2}\mathcal{H}(t-t_0)\right) \quad (23)$$

Thus, we independently control: 1) the maximum amplitude A of the stimulation, its rising time constant τ_1 and its decay time constant τ_2.

In the case of the ring model, this temporal waveform was multiplied by a Gaussian profile in space of extent l_{stim} to yield the waveform:

$$\nu_e^{aff}(x,t)) = A\, e^{-(\frac{x-x_0}{\sqrt{2}l_{stim}})^2}\left(e^{-(\frac{t-t_0}{\sqrt{2}\tau_1})^2}\mathcal{H}(t_0-t)+e^{-(\frac{t-t_0}{\sqrt{2}\tau_2})^2}\mathcal{H}(t-t_0)\right) \quad (24)$$

Results

The results are organized as follows. We first construct the analytical model that will describe the dynamics of a single cortical column. In particular, we describe the semi-analytical workflow that enables the derivation of the cellular transfer function: the core of the population model. Next, we investigate whether the analytical description accurately describe population dynamics by comparing its prediction to numerical simulations. Then, we investigate the integrative properties of the network model. Finally we embed the cortical column model into a ring model and we compare its predictions to VSDi recordings in the visual cortex of awake behaving monkey.

Modeling a single cortical column

Because optical imaging presumably sample most of its signals from superficial layers, we model here the layer II/III network: it is characterized by a strong recurrent connectivity and an important cellular diversity, in particular one finds many types of interneurons (Markram et al., 2004; Ascoli et al., 2008). We adopt here a very simplistic description of this network, it is made of two neuronal population: one excitatory and one inhibitory comprising 8000 and 2000 neurons respectively. All neurons within the two population synaptically interconnect randomly to each other with a connectivity probability of 5%. The excitatory and inhibitory cells have the same passive properties. We nonetheless include an asymmetry between the excitatory and inhibitory populations: because the inhibitory population includes Fast-Spiking cells that can exhibit very high firing frequencies (Markram et al., 2004), we set its spiking mechanism sharper (more precisely its sodium activation activation curve is steeper, see Methods) than that of excitatory cells, additionally we add a strong spike-frequency adaptation current in excitatory cells that is absent in inhibitory cells. Those two effects render the inhibitory neurons more excitable (see the different responses to the same current step in Figure 2). All parameters of the cortical column can be found in Table 1.

A Markovian model to describe population dynamics

We now want to have an analytical description of the collective dynamics of this local network. We adopted the formalism presented in El Boustani and Destexhe (2009). Two reasons motivated this choice: 1) because 10000 neurons is still far from the large network limit, finite-size effects could have a significant impact on the dynamics and 2) because of the relative complexity of the cellular models, an analytic treatment of the type Amit and Brunel (1997) is, to our knowledge, not accessible and would be extremely challenging to derive. The Markovian framework proposed in El Boustani and Destexhe (2009) positively respond to those two constraints: it is a second-order description of population activity that describes fluctuations emerging from finite-size effects and it is applicable to any neuron model as long as its transfer function can be characterized. In a companion study (Zerlaut et al., 2016), we developed a semi-analytical approach to characterize those transfer functions (see next section), we will therefore incorporate this description into the formalism.

Nonetheless, the study of El Boustani and Destexhe (2009) only investigated the ability of the formalism to describe 1) the stationary point of the network activity and 2) in a situation where the neuronal models models had an analytic estimate for the transfer function (current-based integrate-and-fire model). Investigating whether this description generalizes to transient dynamics and transfer functions estimated with a semi-analytical approach is investigated in the next sections.

Transfer functions of excitatory and inhibitory cells

We briefly describe here the semi-analytical approach used to characterize the transfer function (see details in the Methods).

The transfer function $\mathcal{F}$ of a single neuron is defined here as the function that maps the value of the stationary excitatory and inhibitory presynaptic release frequencies to the output stationary firing rate response, i.e. $\nu_{out} = \mathcal{F}(\nu_e, \nu_i)$. This kind of input-output functions lie at the core of *mean-field* models of population dynamics, reviewed in Renart et al. (2004) and is consequently the main ingredient of the formalism adopted here (El Boustani and Destexhe, 2009). Note here that the formulation of the transfer function imply a stationary hypothesis: both for the input (stationary Poisson processes) and the output firing (a stationary firing rate). We will study in the following what are the limitations introduced by this stationary hypothesis in the description of the temporal dynamics of network activity.

In a previous communication (Zerlaut et al., 2016), we found that the firing rate response of several models (including the adaptative exponential integrate and fire considered in this study) would be captured by a *fluctuations-dependent* threshold in a simple approximation of the firing probability (see Methods).

The semi-analytical approach thus consisted in making numerical simulations of single-cell dynamics for various presynaptic activity levels (i.e. scanning various ν_e, ν_i con-

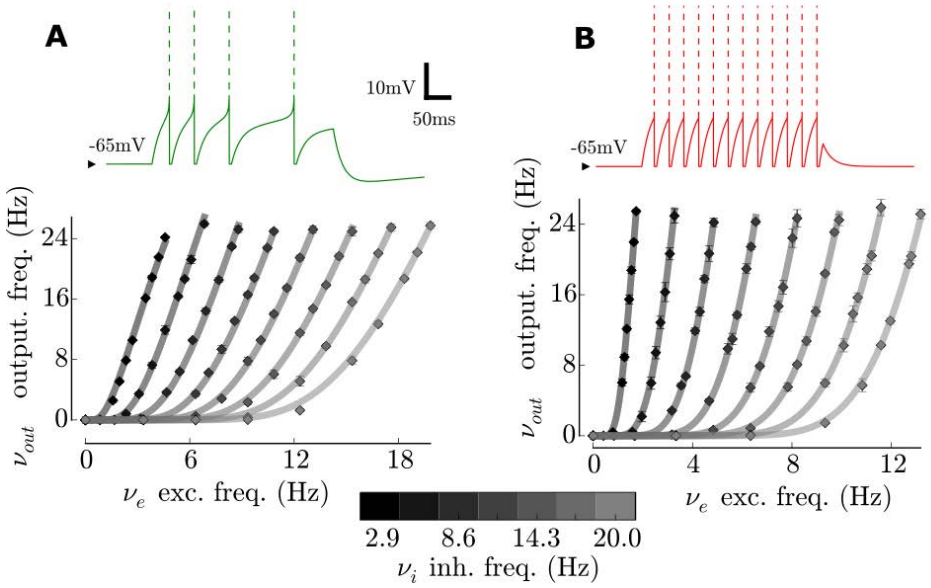

Figure 2: Single cell models of the excitatory and inhibitory populations. Top: response to a current step of 200pA lasting 300ms. Bottom: *transfer function* of the single cell, i.e. output firing rate as a function of the excitatory (x-axis) and inhibitory (color-coded) presynaptic release frequencies. Note that the range of the excitatory and frequencies assumes numbers of synapses (K_e=40 and K_i=10 for the excitation and inhibition respectively). **(A)** Excitatory cells. Note the presence of spike-frequency adaptation and subthreshold adaptation. **(B)** Inhibitory cells. Note the very narrow spike initiation dynamics (k_a=0.5mV). Also, note the steepest relation to excitation (with respect to the excitatory cell) at various inhibitory levels as a result of the increased excitability as a result of the increased excitability of the inhibitory cell (with respect to the excitatory cell).

figurations) and measuring the output firing rate ν_{out}. All those configurations corresponded to analytical estimates of $(\mu_V, \sigma_V, \tau_V)$, we then fitted the *fluctuations-dependent* threshold that bring the analytical estimate to the measured firing response. This procedure resulted in the analytical estimates shown in Figure 2 and compared with the results of numerical simulations.

Spontaneous activity in the cortical column

The combination of the transfer function and the markovian formalism (Equation 18 in the Methods) yields our analytical description of the layer II-III population dynamics in a single cortical column.

We first use this analytical description to look for a physiological configuration of spontaneous activity. There exists two qualitatively different types of spontaneous asynchronous activity (Vogels and Abbott, 2005; Kumar et al., 2008): either the network is dominated by inhibition and the network needs an asynchronous external excitatory drive to exhibit spontaneous activity (Amit and Brunel, 1997; Brunel, 2000) or the network exhibits an asynchronous self-sustained activity state and just needs an initial "kick" to exit from the quiescent state (Vogels and Abbott, 2005; Kumar et al., 2008; El Boustani and Destexhe, 2009). In the latter case, the network is globally dominated by excitation and strong *shunting* conductance effects prevents the network from an excitatory runaway (Kuhn et al., 2004; Kumar et al., 2008). Those two behaviors are thus determined by the membrane, synaptic and connectivity parameters. We therefore investigate how the chosen network parameters in this study would determine the qualitative nature of the spontaneous activity state.

In the case of a single electrophysiological type (e.g. excitatory and inhibitory neurons taken as the same integrate-and-fire model), it was shown that a simple *mean-field* analysis allow to predict in which situation the network parameters corresponds (Brunel, 2000; Kumar et al., 2008), here we generalized this approach to the two populations considered in this study and we investigate the behavior of our network model given the parameters of Table 1. To this purpose, we simplified the dynamical system describing population activity (Equation 18) to its first order so that we get a two dimensional system describing the population spiking activity $\nu_e(t)$ and $\nu_i(t)$. We then plotted the vector field of the time evolution operator in the phase space of the dynamical system direction and launched some trajectories with different initial conditions (see Figure 3). The result of this analysis is that, in absence of external input (ν_e^{drive}=0Hz), the only fixed point of the system is the quiescent state (see Figure 3A). This prediction of the mean-field analysis was indeed confirmed by numerical simulations, whatever the initial external "kick", the activity rapidly decayed (T<50ms) to the quiescent state.

We conclude that, given the parameters of Table 1, our network model does not have the ability to self-sustain activity and will need an external excitatory drive to exhibit

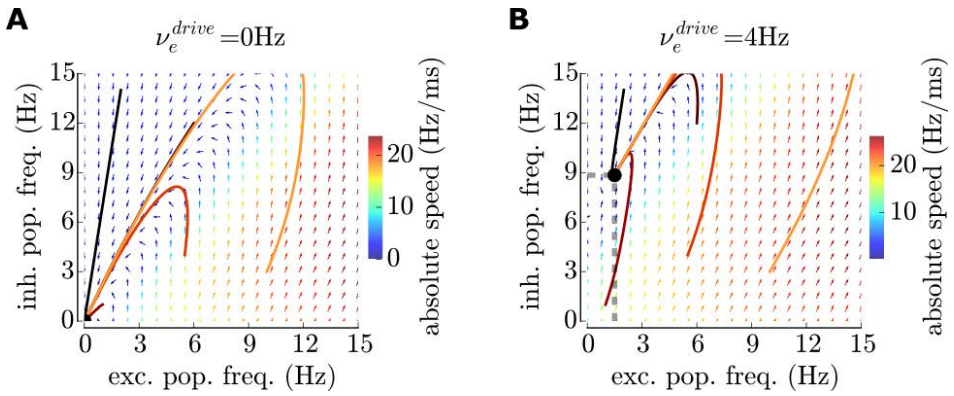

Figure 3: Using the analytical description to look for a stable configuration of spontaneous network activity. Phase space of the dynamical system resulting from the first order of the markovian description, shown for two levels of external excitatory drive ν_e^{drive}. The lines represents trajectories resulting from different initial conditions. The vector field correspond to the time-evolution operator (the arrows represent the direction in the two-dimensional space and the color codes for the norm of the vector). **(A)** Phase space in the absence of an external drive ν_e^{drive}=0Hz, the stable fixed point of the dynamics correspond to the quiescent network state $\nu_e = \nu_i$=0Hz. **(A)** Phase space with an external drive ν_e^{drive}=4Hz, the stable fixed point of the dynamics correspond now corresponds to an active state with asymmetric activity levels: ν_e=1.6Hz and ν_i=8.9Hz (round marker).

spontaneous activity (note that this is also consistently with recent *in vivo* observations in mice visual cortex, see Reinhold et al. (2015)). Indeed, when raising the external drive, a non-quiescent fixed point appears (see Figure 3B for ν_e^{drive}=4Hz). Numerical simulations confirmed the existence of such a fixed point at those levels of activity (see Figure 4).

The particularity of this stationary fixed-point is its asymmetry in terms of population activity, it corresponds to ν_e=1.6Hz and ν_i=8.9Hz (i.e. corresponding to a factor 5-6 between the their respective firing rates). The origin of this asymmetry is very naturally the asymmetry in electrophysiological properties as the excitatory and inhibitory neurons sample statistically the same recurrent and external input. This phenomena has been observed in extracellular recordings in human cortex (Peyrache et al., 2012), cells categorized as Fast-Spiking (such as our inhibitory cells) were shown to fire 6-7 times more than cells categorized as Regular-Spiking (such as our excitatory cells), an asymmetry in excitabilities thus naturally provides a putative explanation for this phenomena (rather than specific circuitry).

Accuracy of the description of the spontaneous activity state

We compare more closely the numerical simulation (Figure 4) to the prediction of the Markovian description.

First, we see that there is a transient period of $\sim$ 400ms resulting from the onset of the external drive (see Figure 4B-D), we will therefore evaluate stationary properties after discarding the first 500ms of the simulation.

After this initial transient, the population activities (ν_e and ν_i) fluctuates around the stationary levels (see Figure 4). The Markovian description predicts this phenomena as it contains the impact of finite size effects (the network comprises 10000 neurons). In Figure 5A, we can see that the distributions of the excitatory and inhibitory population activities are rather well predicted by the formalism (it slightly overestimates the means of the population activities).

We also investigated whether the average neuronal and synaptic quantities were well predicted by the Markovian formalism. Indeed, we found a very good match for all quantities (see Figure 5B,C, mean and variance of membrane potential and synaptic conductances). Only the standard deviation of the membrane potential fluctuations was underestimated (Figure 5C), presumably because of residual synchrony in the dynamics whereas the Markovian formalism assumes a purely asynchronous regime.

Description of the response to time-varying input

We now examine whether the formalism captures the response to time-varying input. Here again, we set the input and examine the response after 500ms of initial simulation to discard transient effects.

We first choose an afferent input of relatively low frequency content ($\sim$ [5-20]Hz, τ_1=60ms and τ_2=100ms in Equation 23). The afferent input waveform, formulated in terms of firing rate, was translated into individual afferent spikes targeting the excitatory population. The response of the network to this input is shown in Figure 6 in comparison with the prediction of the Markovian formalism. The excitatory population activity raises and immediately entrains a raise of the inhibitory population. The analytical description captures well the order of magnitude of the deflection, it only slightly underestimates the peak value (Figure 6B). But the numerical simulations also show a marked hyperpolarization after the stimulation, the return to the baseline level happens only $\sim$ 200-300 ms after the end of the stimulus, and not immediately as predicted by the Markovian framework. Here this strong hyperpolarization is the result of the strong spike-frequency adaptation current that remains as a consequence of the high activ-

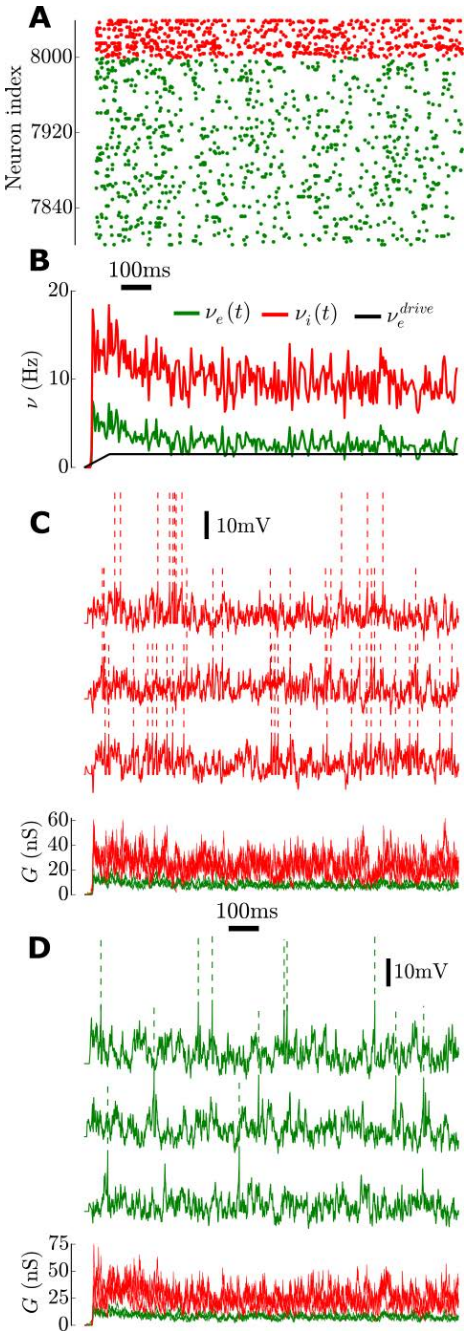

Figure 4: Numerical simulations of the dynamics of a recurrent network of 10000 neurons (see parameters in Table 1). Note that all plots have the same x-axis: time. **(A)** Sample of the spiking activity of 500 neurons (green, 400 excitatory and red, 100 inhibitory). **(B)** Population activity (i.e. spiking activity sampled in 5ms time bins across the population) of the excitatory (green) and inhibitory (red) sub-populations. We also show the applied external drive ($\nu_e^{drive}(t)$, black line), note the slow linear increase to reach ν_e^{drive}=4Hz and try to reduce the initial synchronization that would result from an abrupt onset. **(C)** Membrane potential (top) and conductances (bottom, excitatory in green and inhibitory in red) time courses of three randomly chosen inhibitory neurons. **(D)** Membrane potential and conductances time courses of three randomly chosen excitatory neurons.

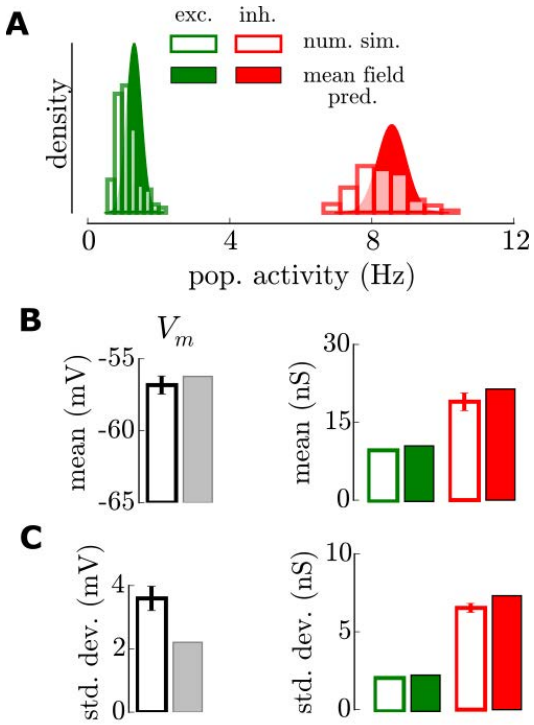

Figure 5: Mean field prediction of the stationary activity. Those quantities are evaluated after discarding the initial 500ms transient. **(A)** Gaussian predictions of the population activities (filled curve) compared to those observed in numerical simulations (empty bars). **(B)** Mean of the membrane potential and conductances time courses. Evaluated over 3 cells for the numerical simulations (empty bars, mean and standard deviation). **(C)** Standard deviation of membrane potential and conductances time courses.

ity evoked by the stimulus. In the Markovian there is no memory of the previous activity and therefore this phenomena can not be accounted for. This typically illustrates a limitation of the analytical description provided here. Note that this is not a fundamental limitation of the Markovian formalism, it is a limitation of this version of the formalism, that contains only variables related to the instantaneous activity (see Discussion).

To study more precisely the temporal validity of the formalism, we modulated the network activity by sinusoidal input and compared the response predicted by the analytical description.

The numerical simulations showed a marked resonance at ∼50Hz. Given the relatively high strength (compared to the external input) of the excitatory-inhibitory loop, the network is close to a bifurcation toward oscillations that are typically in the gamma range (Brunel and Wang, 2003). A sinusoidal input therefore amplifies those frequencies (Ledoux and Brunel, 2011). Because the individual excitatory and inhibitory post-synaptic currents approximately match each other, the theoretical study of Brunel and Wang (2003) would predict oscillations at 50-60Hz (the bifurcation would be achieved by reducing τ_e), thus compatible with the present observation.

More importantly, the main insight of this analysis

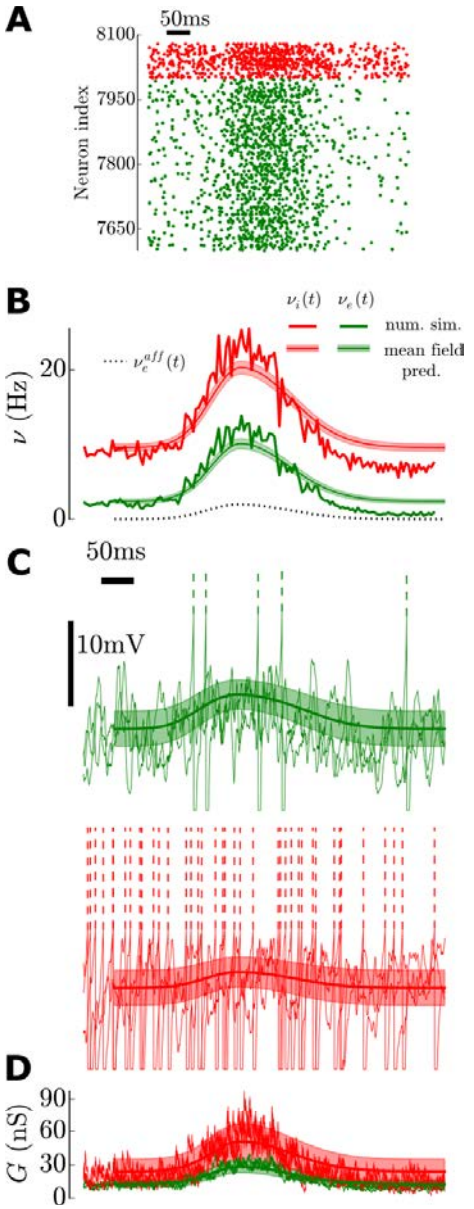

Figure 6: Network response to a time-varying input and associated prediction of the Markovian formalism. For all plots, the x-axis corresponds to time. Shown after 500ms of initial stimulation. **(A)** Sample of the spiking activity of 500 neurons (green, 400 excitatory and red, 100 inhibitory). **(B)** Population activity (in 5ms bins) of the excitatory (green) and inhibitory (red) sub-populations. Superimposed is the mean and standard deviation over time predicted by the Markovian formalism. We also show the applied external stimulation ($\nu_e^{aff}(t)$, dotted line). **(C)** Membrane potential time courses of three excitatory cells (green, top) and three inhibitory cells (red, bottom) with the prediction of the mean and standard deviation in time. **(D)** Conductance time courses of the six cells in **C** with the predictions of the fluctuations superimposed.

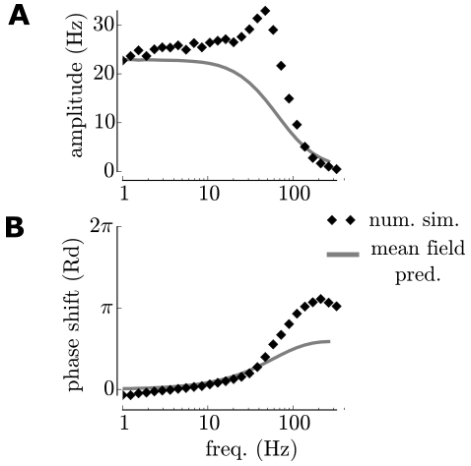

Figure 7: Limitations of the Markovian description in the frequency domain. Response of the network (numerical simulation and analytical description) to sinusoidal stimulation of the form $\nu_e^{aff} = 5\text{Hz}\left(1 - \cos(2\pi f(t - t_0))\right)/2$. The stimulation was set on at t_0=500ms. The response was fitted by a function of the form $\nu(t) = A\left(1 - \cos(2\pi f(t - t_0) - \phi)\right)/2$. **(A)** Amplitude of the sinusoidal response (A in the fitted response) for various frequencies. **(B)** Phase shift of the sinusoidal response (ϕ in the fitted response) for various frequencies.

is to show that the network can track very fast temporal variations in the input, even at time scales smaller than the integration time constant of the single neurons (van Vreeswijk and Sompolinsky, 1996). Recurrent neural networks globally behave as low-pass filters (though see (Ledoux and Brunel, 2011) for a detailed treatment of the appearance of resonances), but with a high cutoff frequency compared to the frequency content of thalamic input for classical artificial stimuli (e.g. in the visual system: drifting gratings, supra-10ms flashes, etc. . .).

Leaving apart the failure of capturing the network resonance (that is linked to this special configuration of synaptic parameters), we conclude that in the frequency range that will be used in the following (f<50-100Hz) the description of the formalism gives a relatively accurate description of the network response in the sense that it accurately predicts that there should not be a frequency filtering within this range. Again, *in vivo* experiments in awake mice suggested that V1 cortical networks had a cut-off frequency above this range (∼100Hz in Reinhold et al. (2015)).

This section concludes the comparison between numerical simulations of network dynamics and the Markovian formalism. We showed that, despite some discrepancies, this analytical framework describes both the spontaneous activity and the response in the [0,100]Hz range of a sparsely connected recurrent network of distinct excitatory and inhibitory cells.

Integrative properties of the network

As the computational cost of the analytical description is negligible, we can now perform a detailed analysis of the network model. We want to investigate the *integrative properties* of the network, i.e. the relation between the network response and the stimulus properties. We analyzed two quantities in the network response: 1) the population activity $\nu(t) = (1 - g)\nu_e(t) + g\nu_i(t)$, i.e. the firing rates weighted by the fraction of neurons in each population,

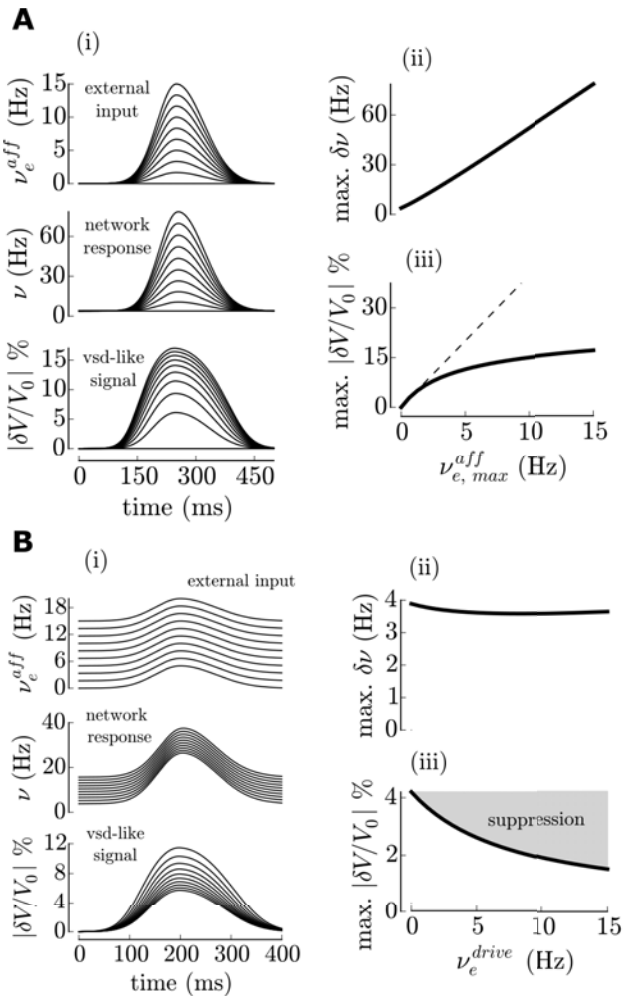

Figure 8: Integrative properties of the network model. For all stimuli the waveform (Equation 23) keeps the temporal characteristics: τ_1=60ms and τ_2=100ms. For both **A** and **B**: (i) Time courses of the stimulus, the network response and the normalized membrane potential (see main text) (ii) Maximum of the population rate responses as a function of the amplitude. (iii) Maximum of the normalized membrane potential deflection as a function of the amplitude. **(A)** Stimulus-response relationship. We increase the amplitude of the stimulus from 0 to 15Hz. In (iii), we show the linear prediction (dashed line) for comparison. **(B)** Modulation of the response to a stimulus by various levels of background activity (external drive varied from 0 to 15Hz).

this is the kind of signals sampled by multi-unit recordings, and 2) the normalized membrane potential over the population $\delta V(t)/V_0 = (1-g)\,(V_m^{exc}(t) - V_{m,}^{stat})/V_m^{stat} + g(V_m^{inh}(t) - V_{m,}^{stat})/V_m^{stat}$ where $V_m^{exc}(t)$ and $V_m^{inh}(t)$ are the time courses of the excitatory and inhibitory membrane potential respectively and V_m^{stat} is the stationary membrane potenial value before stimulus onset. This quantity provides a first approximation of the signal recorded by voltage-sensitive dye imaging (Berger et al., 2007), see Chemla and Chavane (2010) for a more detailed treatment of the relation between neural activity and VSDi signals in a cortical column.

First, we investigated the relation between stimulus

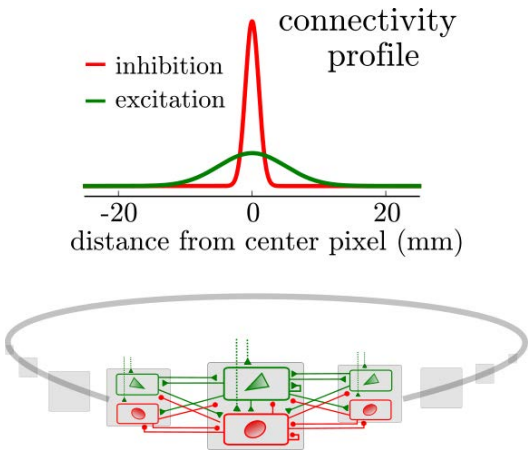

Figure 9: A spatial model of the cortical sheet. The balanced network units are embedded in a ring geometry. The lateral connectivity follows two Gaussian profile of extent l_{exc}=5mm and l_{inh}=1mm for the excitation and inhibition respectively.

intensity and network response, see 8A. On top of the external drive, we added a time-varying stimulus with various amplitudes, see Figure 8A(i). We found that the population activity scaled linearly with the strength on the input. Therefore despite the highly nonlinear dynamics of single neurons (see Figure 2), the network exhibits a linear response (van Vreeswijk and Sompolinsky, 1996). On the other hand, the normalized membrane potential deflection (the "vsd-like signal" in Figure 8A(i,iii)) behave non linearly, it exhibits a strong sublinear behavior (see the distance to the linear prediction, dashed line in Figure 8A(iii)). This behavior follows from the non-linear relation that associate the mean membrane potential to the excitatory and inhibitory activities (Equation 7): the mean membrane potential is not a linear combination of the excitatory and inhibitory contribution it is strongly *shunted* by the total activity.

Another important *integrative property* is how a given input will be modulated by changes in local ongoing activity (that could either come from local spontaneous fluctuations or from afferent activity). The response in terms of population activity was found to be unaffected by the level of background activity, again, in accordance with the characteristics of a linear system. On the other hand the membrane potential response exhibited a strong suppression (up to 60% of the response in absence of additional drive). This phenomena also naturally follows from the previously described non-linear relationship between population activity and mean membrane potential.

Embedding the model in a ring model to describe spatial integration

We now embed this local population dynamics description into a spatial model to investigate the emergence of spatio-temporal integrative properties.

The ring model (see e.g. (Hansel and Sompolinsky, 1996)) offers a simple framework to implement such interactions. The local balanced network units are intercon-

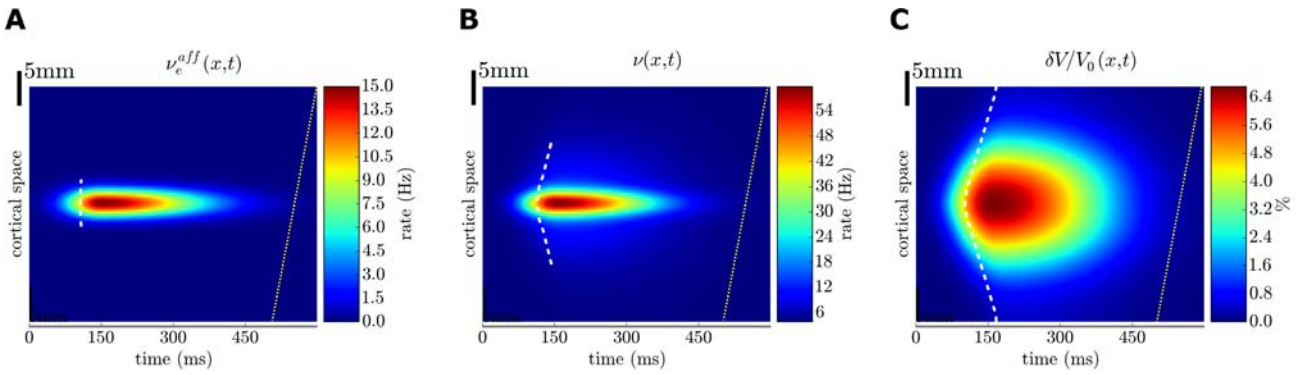

Figure 10: Model response to a local stimulus. An *early response line* (see main text) indicates whether the signal exhibits propagation over space (vertical meaning no propagation), the line stops when the response is below 1% of the maximum signal over space. The yellow dotted line on the right of each plot represents to conduction velocity (300mm/s) for comparison. **(A)** Afferent stimulation: an input of the form Equation 24 with the parameters A=10Hz, τ_1=50ms, τ_2=150ms and l_{exc}=1.5mm. **(B)** Population response in terms of population firing rate ($\sim$ multiunit signal). **(C)** Population response in terms of normalized membrane potential deflection ($\sim$ VSDi signal).

nected to each other via two Gaussian connectivity profiles (see Figure 9 and Methods) according to anatomical connectivity estimates (Buzás et al., 2006). Importantly, we integrate distance-dependent propagation delays due to the finite velocity of axonal conduction of action potentials (see Methods), we took here an axonal conduction velocity of 300mm/s.

We stimulated this large-scale model with an external input mimicking thalamic stimulation. We took a separable spatio-temporal waveform as an input (see Equation 24). In space, the profile was a Gaussian curve, in time, it was a piecewise double Gaussian function. Despite its various amplitude over space, it should be emphasized that this input does not propagate: e.g. its maximum is achieved at all position at the same time. To highlight this feature, we implemented a simple analysis of propagation: we normalize the responses with respect to their local amplitude and we look for a specific crossing of the normalized amplitude. To focus on early responses, we highlight the initial crossing of the fourth of the normalized amplitude over space, we call it the *early response line* (drawn with a white dashed-line, see Figure 10). In Figure 10A, the horizontal *early response line* indeed show that the input does not propagate, the fourth of the maximum of the normalized response is achieved everywhere at the same time.

The response of the model in terms of population dynamics showed a marked propagation (see the V-shape of the *early response line* in Figure 10B). This is naturally the result of the local connectivity profiles implemented in the model (see Figure 9 and Table 1), the excitation has a broad spatial extent, it can depolarizes neighboring locations and evoke spiking (both of excitatory and inhibitory populations). This propagated activity nonetheless exhibits a very strong attenuation over space, this is due to the strong non-linear relationship between depolarizations and firing response (see previous sections). Confirming this picture, the normalized membrane potential responses indeed exhibits the same propagation profile but with a much weaker attenuation over space. Naturally, the propagation dynamics in the model is led by the conduction velocity, see its representation (yellow dotted line) in Figure 10B,C. A strong prediction of the model is therefore that the detectability of responses in multiunit recordings have a lower spatial extent than for VSDi responses (see the lower range of the *early response line* that stops when the maximum local response is below 1% of the maximum response).

The propagating wave in the model are thus very similar to those detected in primary visual cortex of awake monkey, either in spontaneous activity or following visual stimulation, as recently shown by a phase-based analysis applied at single-trial level (Muller et al., 2014). Note that, to highlight this qualitative similarity between model and *in vivo* VSDi recordings, the spatio-temporal parameters of the input (τ_1=50ms, τ_2=150ms, l_{exc}=1.5mm) have been manually calibrated to reproduce the properties of the response observed as a response to a single Gaussian blob in the visual space of 0.5^o spatial extent.

Deintricating the cortical operation underlying the response to an apparent motion stimulus

The presence of traveling waves detected in the VSDi signal in response to simple stimuli (Muller et al., 2014) raises the question of a putative physiological role during the integration of complex stimuli. Indeed, such transient depolarization of excitatory and inhibitory neurons carried by the horizontal fiber network of the superficial cortical layers might affect the processing of future stimuli at distant points in visual cortex.

To investigate this possibility, a convenient paradigm is the apparent motion protocol: two individual stimuli are successively flashed at two neighboring visual locations (see Figure 11A). If the interval between the two stimuli and the distances in visual space are low enough, this give rise to the visual illusion of one moving object instead of two different flashed objects, hence the name: *apparent motion* stimulus.

Using voltage-sensitive dye imaging in the primary vi-

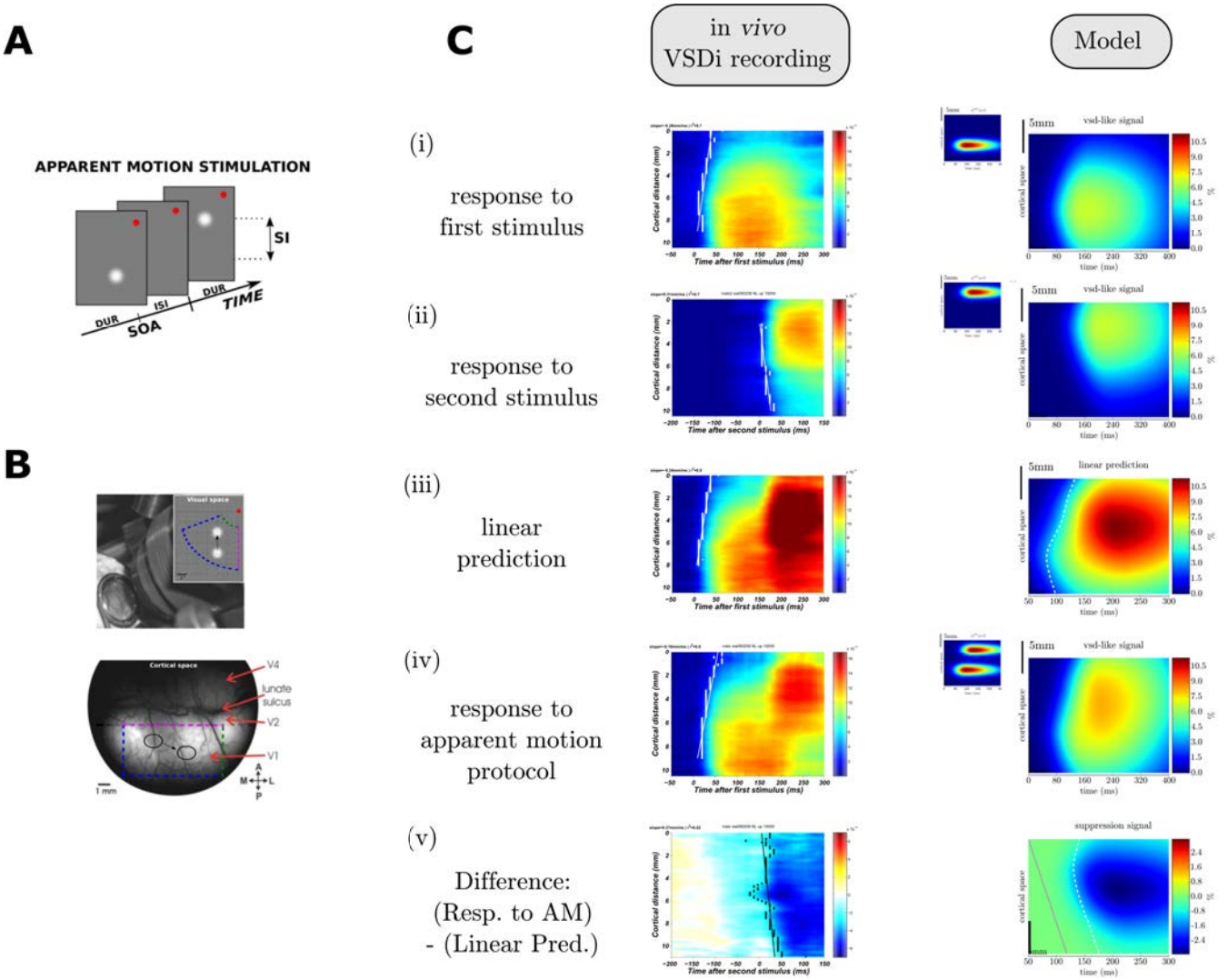

Figure 11: Deintricating the cortical operation underlying the response to an apparent motion (AM) stimulus: comparison between the model and VSDi recordings in fixating monkeys. (A) The apparent motion protocol. During a single trial, the monkey had to fixate on a central red dot for 1–2s. The animal's gaze was constrained in a window of $2^o \times 2^o$. Two Gaussian blob stimuli (each of 0.5^o spatial extent) at two different position were successively presented during fixation. **(B)** VSDi allows for a real-time visualization of large neuronal population in primary visual cortex of fixating monkeys. **(C)** To deintricate the cortical computation, both in the theoretical model and in fixating monkey *in vivo*, we show the VSDi signal of different quantities: (i) the response to the first stimulus alone (ii) the response to the second stimulus alone, (iii) the linear prediction of the signal resulting from the two stimuli alone, (iv) the response to the two stimuli (AM stimulus) and (v) the spatio-temporal profile of the suppression signal (the linear prediction minus the observed response to the AM stimulation). The dashed magenta line in the model plot represents the conduction velocity. Note that the spatial scale in the model is higher than in the recordings (i.e. the model shows an enlarged region).

sual cortex of awake monkey (see Figure 11B), Chemla & Chavane (unpublished observations) showed that two visual stimuli in different positions in space and time evoke two distinct propagating waves, which can collide, see Figure 11C(iv). To understand the computation performed during this *collision*, they recorded the response to the two simple stimuli alone, see Figure 11C(i,ii), and then computed the linear prediction of the expected spatio-temporal profile in the absence of cortical operations, see Figure 11C(iii).

Notably, they found that the interaction between the two waves always results in the propagation of a suppressive (sub-linear) wave at a speed compatible with horizontal propagation (0.1-0.6 m/s). The suppression affected the second stimulus first and then propagated toward the first stimulus location.

We therefore tried to explain those observations in the light of our theoretical model. As previously mentioned, we calibrated the afferent input (mimicking thalamic input) to obtain a spatio-temporal responses similar to those observed *in vivo* (i.e. the cortical distance between the two stimuli was estimated as 8.1mm for a 2^o separation in the visual space). We next investigated the prediction of the theoretical model in response to the apparent motion stimulus, see Figure 11C.

Similarly to what was observed experimentally, we found that the normalized membrane potential response ($\sim$ VSDi signal) to the two successive inputs *collided*, see Figure 11C(iv), and resulted in a strongly dampened signal with respect to the linear prediction, see Figure 11C(v). This suppression signal was also found to propagate from the second stimulus location toward the first stimulus location. To investigate quantitatively the properties of this propagation, we implemented the same *early response line* analysis than previously described (see previous section). We found that the propagation of the suppression was led by the conduction velocity (see comparison with the dotted magenta line in Figure 11C(v)). Importantly, it should be noted that in addition to this qualitative similarity, the quantitative prediction of the model seems to match those of the experimental recordings: the suppression peaks at $\sim$ 50 % of the response to a single stimulus both in the model and in the VSDi recordings (for the experimental recordings, response to first and second stimulus have a maximum of $\Delta F/F \sim 12$ ‰, suppression peaks at $\Delta F/F \sim 6$ ‰, in the model, the "VSDi-like" signal response to first and second stimulus have a maximum of $\delta V/V_0 \sim 6\%$, suppression peaks at $\delta V/V_0 \sim 3\%$) .

We conclude that the the horizontal fiber network combined with the strongly sublinear relation between membrane potential deflection and activity in the local network (see Figure 8) appears as a putative sufficient explanation for the observation found in VSDi recordings during an apparent motion stimulus in fixating monkeys.

Discussion

The present study has two main contributions.

In a first part, we investigated whether the Markovian formalism proposed in El Boustani and Destexhe (2009) is able to describe the temporal dynamics of artificial neural networks. Though this formalism was shown to be a relatively accurate description of the response simulated in numerical networks, we highlighted two example phenomena that were missed by our description. The relative complexity of the theoretical problem should be stressed, indeed no exact treatment of this situation could be achieved as this represents a really tough mathematical problem.

In a second part, by taking advantage of this theoretical work performed at the mesoscopic level ($\sim$ 10000 neurons) to analytically describe population dynamics in terms of few variables, we were able to design a tractable model of population dynamics in Layer II-III at the $\sim$ 30 millimeter scale of the neocortical sheet. We studied the properties of this model in the context of multi-input integration. In particular, we implemented a typical paradigm of visual processing: the apparent motion protocol. Similarly to what is observed *in vivo* we found a strong suppression signal originating in the second stimulus that propagated toward the first stimulus.

Unlike previous studies (Brunel, 2000; Vogels and Abbott, 2005; Kumar et al., 2008; El Boustani and Destexhe, 2009), we introduced asymmetric electrophysiological properties between excitatory and inhibitory cells. The reason was twofold: first it was an insightful step to demonstrate the relative accuracy of the markovian formalism (with the semi-analytical approach) in a situation including this increased complexity, but more importantly, this asymmetry in the excitabilities was the mechanism that led to a very strong suppression in the response to multiple inputs. When the external stimulation increases the local excitatory activity, inhibition is recruited via recurrent connections and because of its higher excitability this recruitment is stronger than for the excitatory population (see e.g. Figure 6B).This feature, combined with the interplay of driving forces, produced an inhibitory control of the mean membrane potential fluctuations.

Other suppressive mechanisms were present in this model: conductance shunting of the external input due to background activity (Hô and Destexhe, 2000; Chance et al., 2002) (where an increase in background activity is evoked by the first stimulus) as well spike-frequency adaptation currents (as least its stationary effect). The effect of those mechanisms has been investigated in absence of the electrophysiological asymmetry (i.e. by considering pure FS cells networks and pure RS cell network), they indeed produced a suppression with a similar spatio-temporal pattern such as the one observed in the experimental data. Nonetheless, when keeping their value to estimated physiological range, the amplitude of the suppression was at least one order of magnitude lower than that observed in experimental recordings (not shown, but the slight suppression for the firing activity in Figure 8B(ii) is the trace of this effect), thus suggesting that they weakly participate to the very strong suppression effect observed in VSDi recordings.

An important remark is that the strong suppressive mechanism had to be cortico-cortical to account for the experimental observations. Depression at the thalamo-cortical synapses can contribute to the suppression of

cortical responses (see Carandini et al. (2002) for cross-orientation suppression), but this seems unlikely to play here as the sensory stimuli are well separated in the visual space and are likely to also be well separated in the thalamus, thus ruling out the hypothesis of synaptic depression at the thalamo-cortical synapse.

We envision several future directions for the present model.

First, the theoretical descriptions of the local cortical network could be improved. For example the strong hyperpolarization of population activity after a transient rise (see Figure 6B) was shown to be missed by the formalism under this version. Indeed, this version does not have a memory of the previous activity levels and thus can not account for the effect of the long-lasting spike-frequency adaptation mechanism that has been strongly activated by the activity evoked by the stimulus. This is easily solvable within the Markovian framework, one can introduce a new variable: the "population adaptation current", that can directly be derived from the equation of the AdExp model (not shown). The simplicity and high tractability of this model in its current form would allow several inclusion without running into the drawback of a high computational cost.

Finally, we would like to test the model ability to explain other typical cortical properties. In particular, similar propagation of suppressive interactions have already been shown but using bipartite stationary stimuli (Reynaud et al., 2012), unveiling the cortical dynamics subtending the so-called surround suppression. What is the explanatory power of the model in the surround suppression framework ? As an additional example, the response to a stimulus depends on the level of ongoing activity (Arieli et al., 1996) dependency on the level of ongoing activity. When the the ongoing activity is modulated by the level of afferent activity is this model sufficient to describe the spatio-temporal variability in evoked response ? Answering those questions will be the focus of future work.

References

Amit DJ, Brunel N (1997) Model of global spontaneous activity and local structured activity during delay periods in the cerebral cortex. *Cerebral Cortex* 7:237–252.

Arieli a, Sterkin a, Grinvald a, Aertsen A, An JH (1996) Dynamics of ongoing activity: explanation of the large variability in evoked cortical responses. *Science (New York, N.Y.)* 273:1868–71.

Ascoli GAG, Alonso-Nanclares L, Anderson SA, Barrionuevo G, Benavides-Piccione R, Burkhalter A, Buzsáki G, Cauli B, Defelipe J, Fairén A, Others (2008) Petilla terminology: nomenclature of features of GABAergic interneurons of the cerebral cortex. *Nature Reviews ...* 9:557–568.

Berger T, Borgdorff A, Crochet S, Neubauer FB, Lefort S, Fauvet B, Ferezou I, Carleton A, Lüscher HR, Petersen CCH (2007) Combined voltage and calcium epifluorescence imaging in vitro and in vivo reveals subthreshold and suprathreshold dynamics of mouse barrel cortex. *Journal of neurophysiology* 97:3751–3762.

Brette R, Gerstner W (2005) Adaptive exponential integrate-and-fire model as an effective description of neuronal activity. *Journal of neurophysiology* pp. 3637–3642.

Brunel N (2000) Dynamics of sparsely connected networks of excitatory and inhibitory spiking neurons. *Journal of computational neuroscience* 8:183–208.

Brunel N, Hakim V (1999) Fast global oscillations in networks of integrate-and-fire neurons with low firing rates. *Neural computation* 11:1621–1671.

Brunel N, Wang XJ (2003) What determines the frequency of fast network oscillations with irregular neural discharges? I. Synaptic dynamics and excitation-inhibition balance. *Journal of neurophysiology* 90:415–430.

Buzás P, Kovács K, Ferecskó AS, Budd JML, Eysel UT, Kisvárday ZF (2006) Model-based analysis of excitatory lateral connections in the visual cortex. *The Journal of comparative neurology* 499:861–81.

Carandini M, Heeger DJ, Senn W (2002) A synaptic explanation of suppression in visual cortex. *The Journal of neuroscience : the official journal of the Society for Neuroscience* 22:10053–10065.

Chance FS, Abbott LF, Reyes AD (2002) Gain modulation from background synaptic input. *Neuron* 35:773–782.

Chemla S, Chavane F (2010) A biophysical cortical column model to study the multi-component origin of the VSDI signal. *NeuroImage* 53:420–438.

Civillico EF, Contreras D (2012) Spatiotemporal properties of sensory responses in vivo are strongly dependent on network context. *Frontiers in systems neuroscience* 6:25.

Contreras D, Llinas R (2001) Voltage-sensitive dye imaging of neocortical spatiotemporal dynamics to afferent activation frequency. *The Journal of neuroscience : the official journal of the Society for Neuroscience* 21:9403–9413.

Daley DJ, Vere-Jones D (2007) *An introduction to the theory of point processes: volume II: general theory and structure*, Vol. 2 Springer Science & Business Media.

Destexhe A, Rudolph M, Paré D (2003) The high-conductance state of neocortical neurons in vivo. *Nature Reviews Neuroscience* 4:739–751.

El Boustani S, Destexhe A (2009) A master equation formalism for macroscopic modeling of asynchronous irregular activity states. *Neural computation* 21:46–100.

Ferezou I, Bolea S, Petersen CCH (2006) Visualizing the Cortical Representation of Whisker Touch: Voltage-Sensitive Dye Imaging in Freely Moving Mice. *Neuron* 50:617–629.

Goodman DFM, Brette R (2009) The brian simulator. *Frontiers in Neuroscience* 3:192–197.

Hansel D, Sompolinsky H (1996) Chaos and synchrony in a model of a hypercolumn in visual cortex. *Journal of Computational Neuroscience* 3:7–34.

Hô N, Destexhe A (2000) Synaptic background activity enhances the responsiveness of neocortical pyramidal neurons. *Journal of neurophysiology* 84:1488–96.

Kuhn A, Aertsen A, Rotter S (2004) Neuronal integration of synaptic input in the fluctuation-driven regime. *The Journal of neuroscience : the official journal of the Society for Neuroscience* 24:2345–56.

Kumar A, Schrader S, Aertsen A, Rotter S (2008) The high-conductance state of cortical networks. *Neural Computation* 20:1–43.

99

Latham PE, Richmond BJ, Nelson PG, Nirenberg S (2000) Intrinsic Dynamics in Neuronal Networks. I. Theory. *J Neurophysiol* 83:808–827.

Ledoux E, Brunel N (2011) Dynamics of networks of excitatory and inhibitory neurons in response to time-dependent inputs. *Frontiers in computational neuroscience* 5:25.

Markram H, Muller E, Ramaswamy S, Reimann MW, Abdellah M, Sanchez CA, Ailamaki A, Alonso-Nanclares L, Antille N, Arsever S, Kahou GAA, Berger TK, Bilgili A, Buncic N, Chalimourda A, Chindemi G, Courcol JD, Delalondre F, Delattre V, Druckmann S, Dumusc R, Dynes J, Eilemann S, Gal E, Gevaert ME, Ghobril JP, Gidon A, Graham JW, Gupta A, Haenel V, Hay E, Heinis T, Hernando JB, Hines M, Kanari L, Keller D, Kenyon J, Khazen G, Kim Y, King JG, Kisvarday Z, Kumbhar P, Lasserre S, Le B?? JV, Magalh??es BRC, Merch??n-P??rez A, Meystre J, Morrice BR, Muller J, Mu??oz-C??spedes A, Muralidhar S, Muthurasa K, Nachbaur D, Newton TH, Nolte M, Ovcharenko A, Palacios J, Pastor L, Perin R, Ranjan R, Riachi I, Rodr??guez JR, Riquelme JL, R??ssert C, Sfyrakis K, Shi Y, Shillcock JC, Silberberg G, Silva R, Tauheed F, Telefont M, Toledo-Rodriguez M, Tr??nkler T, Van Geit W, D??az JV, Walker R, Wang Y, Zaninetta SM, Defelipe J, Hill SL, Segev I, Sch??rmann F (2015) Reconstruction and Simulation of Neocortical Microcircuitry. *Cell* 163:456–492.

Markram H, Toledo-Rodriguez M, Wang Y, Gupta A, Silberberg G, Wu C (2004) Interneurons of the neocortical inhibitory system. *Nature reviews. Neuroscience* 5:793–807.

McCormick DA, Connors BW, Lighthall JW, Prince Da (1985) Comparative electrophysiology of pyramidal and sparsely spiny stellate neurons of the neocortex. *Journal of neurophysiology* 54:782–806.

Muller L, Reynaud A, Chavane F, Destexhe A (2014) The stimulus-evoked population response in visual cortex of awake monkey is a propagating wave. *Nature communications* 5:3675.

Papoulis A (1991) *Probability, random variables and stochastic processes* McGraw-Hill.

Petersen CCH, Sakmann B (2001) Functionally Independent Columns of Rat Somatosensory Barrel Cortex Revealed with Voltage-Sensitive Dye Imaging. *The Journal of neuroscience : the official journal of the Society for Neuroscience* 21:8435–8446.

Peyrache A, Dehghani N, Eskandar EN, Madsen JR, Anderson WS, Donoghue Ja, Hochberg LR, Halgren E, Cash SS, Destexhe A (2012) Spatiotemporal dynamics of neocortical excitation and inhibition during human sleep. *Proceedings of the National Academy of Sciences of the United States of America* 109:1731–6.

Reinhold K, Lien AD, Scanziani M (2015) Distinct recurrent versus afferent dynamics in cortical visual processing. *Nature Neuroscience* 18.

Renart A, Brunel N, Wang XJ (2004) Mean-field theory of irregularly spiking neuronal populations and working memory in recurrent cortical networks. *Computational neuroscience: A comprehensive approach* pp. 431–490.

Reynaud A, Masson GS, Chavane F (2012) Dynamics of local input normalization result from balanced short- and long-range intracortical interactions in area V1. *The Journal of neuroscience : the official journal of the Society for Neuroscience* 32:12558–69.

Steriade M, Timofeev I, Grenier F (2001) Natural waking and sleep states: a view from inside neocortical neurons. *Journal of neurophysiology* 85:1969–1985.

van Vreeswijk C, Sompolinsky H (1996) Chaos in neuronal networks with balanced excitatory and inhibitory activity. *Science (New York, N.Y.)* 274:1724–6.

Vogels TP, Abbott LF (2005) Signal propagation and logic gating in networks of integrate-and-fire neurons. *The Journal of neuroscience* 25:10786–10795.

Zerlaut Y, Telenczuk B, Deleuze C, Bal T, Ouanounou G, Destexhe A (2016) Heterogeneous firing response of mice layer V pyramidal neurons in the fluctuation-driven regime. *in revision* .

Part III

Discussion

In this thesis, we aimed at understanding how the biophysical and circuit properties characterizing neocortical assemblies shape population dynamics in neural networks.

While investigating how layer V pyramidal cells respond to membrane potential fluctuations, we found a strong heterogeneity between cells in their firing response. Consequently, we developed an analytical framework including dendritic integration to investigate the putative functional consequences of this cell-to-cell variability. In parallel, we studied how recurent and lateral connectivity might influence neocortical processing. We now discuss those results.

Heterogeneity in neocortex

We found a strong heterogeneity in the firing response of neocortical neurons in the visual cortex of juvenile mice in **Work 1**. Many factors could underlie this variability, notably: 1) recording at different days (between P8 and P13), 2) recording over different animals (see e.g. Schulz et al. (2006)) or 3) there is indeed an intrinsic variability within the layer V neocortical network in juvenile mice. We could quantify the impact of hypothesis 1) and it was found relatively small, on the other hand hypothesis 2) is hard to quantify because of the low number of recorded cells per animal.

Even in the hypothesis of the intrinsic heterogeneity in juvenile mice cortex, a natural question is whether this feature disappears in more mature animals. This is hard to answer from the litterature as experimental characterization usually report results with respect to a *control* situation. Nonetheless, the heterogeneity seems much reduced in adult animals. Köndgen et al. (2008) studied the response of mature layer V neurons in somato-sensory cortex to modulated noisy input. The quantity that will shape this response is somehow similar to our "sensitivity to the speed of the fluctuations", and as visually estimated from the presented errorbars, the variability seems much reduced, although still present (and all inputs were adjusted to reproduce a baseline trend). On the other hand, at least $\sim$4mV standard deviation in action potential threshold levels seems to be routinely measured in adult mice cortex (Crochet et al., 2011; Okun et al., 2015; Yang et al., 2015).

An important remark is that we performed this study using the *perforated patch* technique and not the with widespread *whole cell* technique. A possibility is that, because of the *dialysis* of the intracellular medium, *whole*

cell recordings render the electrophysiological properties more homogenous. The *perforated patch* technique would thus reveal the *true* heterogeneity. On the opposite, maybe the *perforated patch* technique introduces cell-to-cell variability. A precise quantification of those possible effects appears as a necessary step for future studies.

Consequently, we believe that the main contribution of our work was only to 1) design a functionnally relevant space to scan neuronal responses and 2) evidence its ability to capture cell-to-cell variability in a relatively favorable system (because immature), but the evidence and extent of the intrinsic functional heterogeneity in neocortical networks remains a fairly open problem.

Putative functional impact of heterogeneity

In **Work 2**, we speculated that the biophysical heterogeneity that we reported could offer a *multiplexing* mode to cortical computation. Some neurons would preferentially respond to local network activity (proximally targetting activity), while some other neurons would respond either to long-range stimulation or an increased synchrony due to a change in stimulus statistics. The core of this mechanism would be that neurons possess various levels of sodium inactivation. Slow fluctuations due to distal or medium conductance input do not allow a neuron with strong inactivation to fire. On the other hand, the strong conductance (because localized) associated to proximal input produces very fast fluctuations and allows to deinactivate sodium channels and thus to elicit spikes. At this stage, this is a very speculative statement, it should be investigated whether neocortical dynamics *in vivo* and its associated modulations of the membrane potential fluctuations render those effects possible.

Previous theoretical work (Mejias and Longtin, 2012) in recurrent networks suggested that a given heterogeneity level in action potential threshold could optimize network information transmission for the rate coding strategy. This value was found to be around 4mV, quite close from the $\sim$ 5-6mV from our characterization of **Work 1**. Evidencing such a contribution *in vivo* would be extremely challenging, it would require to reduce or increase the excitability variations on a whole population and then study its ability to transmit/amplify a given sensory input.

On the other hand, because neural networks lie in a very high dimensional

space (including electrophysiological, synaptic, neuromodulatory and circuit properties), one can not exclude that this heterogeneity is not compensated by an other variability so that the effect on network dynamics cancels, see Prinz et al. (2004) for an example of such an effect (reviewed in Marder and Goaillard (2006)).

On the need of analytical descriptions of dendritic integration

In **Work 2**, we presented an analytical description of dendritic integration in the fluctuation-driven regime (whose weaknesses were also emphasized). We suggested that it could be of great use to theoretical analysis in systems neuroscience. We present here such an example.

It was proposed that the recurrent circuitry of neocortical networks could self-sustain activity (i.e. maintain activity in the absence of an external drive) (Kuhn et al., 2004; Vogels and Abbott, 2005; Kumar et al., 2008). It is thus an important question to evaluate whether cortical activity is self-sustained during asynchronous dynamics or whether it is driven by an asynchronous input (e.g. a thalamic drive) as those two scenarii will surely lead to different computations of afferent input.

The mechanism by which this self-sustained activity emerges is the following (see Kuhn et al. (2004) for details): we have a recurrent network globally dominated by excitation and the excitatory run-away is avoided by a very strong shunting conductance that reduces the post-synaptic potentials at high activity levels. Examining the plausibility of this mechanism can therefore be reduced to examining whether this shunting effect can happen in a physiological range. This hypothesis was formulated in the single-compartment approximation, thus rendering the comparison with neocortical cells difficult. On the other hand, we have a theoretical model that has an accurate surface area and a relatively accurate distribution of transfer resistances to the soma. We used physiologically-realistic synaptic and membrane parameters (identical to those of **Work 2**) and examined whether a strong enough shunting could appear in the physiological range. The criteria for this physiological range was that the somatic input conductance should be no more than four times the leak conductance (reviewed in Destexhe et al. (2003)). In this range, we found that the model predicted a too weak shunt-

ing to enable such an effect (not shown, but see the effects on σ_V and τ_V in Figure 4 of **Work 2**). This analysis predicts that cortical networks can not self-sustain activity. In accordance with this view, recent evidences accumulate to show that during asynchronous activity the cortex is driven by a thalamic drive (Poulet et al., 2012; Reinhold et al., 2015).

We believe that many other theoretical questions could benefit from the quantitative insight offered by this model.

Modulation of sensory responses by network state

In **Work 3**, we proposed a general mechanism, that might be an important principle for information processing in neural networks.

The amplitude of the response to a sensory stimulus result from the competition between:

- cellular gain modulation. Background activity and its associated conductance level has a *shunting* effect on post-synaptic responses (Hô and Destexhe, 2000; Chance et al., 2002; Altwegg-Boussac et al., 2014). This mechanism favors high responses in the quiescent-state.

- recruitment within the network. A given afferent stimulus will be amplified by the recurrent activity in the presence of ongoing activity. This mechanism is in favor of the active-state. Importantly, the potentiation exerted by the active state (with respect to the quiescent state) increases as a function of the number of networks when arranged in a feedforward manner (e.g. A1 -> A2 ->etc. . .)

This also tells us that interpreting measurements requires to take care about what is actually measured. Somatic intracellular do not predict the same effect as multi-unit activity. The predictions of this model is that in terms of multi-unit activity, the response should be systematically lower in the Down-state than in the Up-state. Note that this property was visible in the data of **Work 3**, in the spikes recorded during intracellular recordings (Reig, Vergara and Sanchez-Vives, private communication).

A notable exception would appear for very strong stimuli (Hô and Destexhe, 2000) (see also Figure 4 in **Work 3**), at very high levels the spiking probability is higher in the Down state, but this would presumably result in

a pathological state (e.e. epileptic seizure) as this effect appears when all neurons respond.

Rationale behind a *bottom-up* approach: models of high empirical content

In **Work 4**, we have built a large-scale model of the supra-granular network, the modeling procedure to build this model can be seen as a kind of *bottom-up* approach: starting from the cellular level we build-up the dynamical system describing the mesoscopic scale (the cortical column) via the *mean-field* approach, finally we embed this description into a spatial model to reach the macroscopic scale (the sensory area).

It is worth comparing the theoretical model resulting from our *bottom-up* approach to other models in the literature. Competing models for macroscopic population dynamics are phenomenological models, the most prominent example being the model of Rubin et al. (2013) for primary visual cortex computation. This model has only two variables: the excitatory and inhibitory population activities (comparable to our two population model). It has also very few parameters: the 3 parameters of their *power law* input-output function and the connectivity parameters. This very low number of parameters might be seen as a clear advantage because it will allow a parameter scan to investigate the robustness of the findings. The number of parameters is a lot larger in our model (30 parameters: ionic channel parameters, synaptic quantities, membrane quantities, morphology parameters, circuit properties, ...) and clearly prevents such a procedure. Nonetheless, we argue here that it has a notable advantage: it has a higher *empirical content* (Popper, 2005), i.e. because it generates predictions at all scales, it can be falsified (or confirmed) by several measurements at all scales (from intracellular recordings to large scale optical imaging). Those theoretical models thus offer a very convenient (because highly testable) framework to understand neocortical computation.

Bibliography

Altwegg-Boussac, T., Chavez, M., Mahon, S., and Charpier, S. (2014). Excitability and responsiveness of rat barrel cortex neurons in the presence and absence of spontaneous synaptic activity in vivo. *The Journal of physiology*, 592(Pt 16):3577–3595.

Amit, D. J. and Brunel, N. (1997). Model of global spontaneous activity and local structured activity during delay periods in the cerebral cortex. *Cerebral Cortex*, 7(3):237–252.

Arieli, a., Sterkin, a., Grinvald, a., Aertsen, A., and An, J. H. (1996). Dynamics of ongoing activity: explanation of the large variability in evoked cortical responses. *Science (New York, N.Y.)*, 273(5283):1868–71.

Baudot, P., Levy, M., Marre, O., Monier, C., Pananceau, M., and Frégnac, Y. (2013). Animation of natural scene by virtual eye-movements evokes high precision and low noise in V1 neurons. *Frontiers in neural circuits*, 7(December):206.

Brette, R. (2013). Sharpness of spike initiation in neurons explained by compartmentalization. *PLoS computational biology*, 9(12):e1003338.

Brette, R. (2015). Philosophy of the spike: rate-based vs. spike-based theories of the brain. *Frontiers in Systems Neuroscience*, 9(151):1–14.

Brunel, N. (2000). Dynamics of sparsely connected networks of excitatory and inhibitory spiking neurons. *Journal of computational neuroscience*, 8(3):183–208.

Brunel, N. and Hakim, V. (1999). Fast global oscillations in networks of integrate-and-fire neurons with low firing rates. *Neural computation*, 11(7):1621–1671.

Brunel, N. and Wang, X.-J. (2003). What determines the frequency of fast network oscillations with irregular neural discharges? I. Synaptic dynamics and excitation-inhibition balance. *Journal of neurophysiology*, 90(1):415–430.

Chance, F. S., Abbott, L. F., and Reyes, A. D. (2002). Gain modulation from background synaptic input. *Neuron*, 35:773–782.

Crochet, S., Poulet, J. F. A., Kremer, Y., and Petersen, C. C. H. (2011).

Synaptic mechanisms underlying sparse coding of active touch. *Neuron*, 69(6):1160–1175.
Destexhe, A., Rudolph, M., and Paré, D. (2003). The high-conductance state of neocortical neurons in vivo. *Nature Reviews Neuroscience*, 4(9):739–751.
Deweese, M. R. and Zador, A. M. (2004). Shared and private variability in the auditory cortex. *Journal of neurophysiology*, 92(3):1840–1855.
Ecker, A. S., Berens, P., Keliris, G. A., Bethge, M., Logothetis, N. K., and Tolias, A. S. (2010). Decorrelated neuronal firing in cortical microcircuits. *Science (New York, N.Y.)*, 327(5965):584–7.
El Boustani, S. and Destexhe, A. (2009). A master equation formalism for macroscopic modeling of asynchronous irregular activity states. *Neural computation*, 21(1):46–100.
El Boustani, S., Pospischil, M., Rudolph-Lilith, M., and Destexhe, A. (2007). Activated cortical states: experiments, analyses and models. *Journal of physiology, Paris*, 101(1-3):99–109.
Harris, K. D. (2013). Top-down control of cortical state. *Neuron*, 79(3):408–10.
Hô, N. and Destexhe, A. (2000). Synaptic background activity enhances the responsiveness of neocortical pyramidal neurons. *Journal of neurophysiology*, 84(3):1488–96.
Hodgkin, A. L. and Huxley, A. F. (1952). A quantitative description of membrane current and its application to conduction and excitation in nerve. *J. Physiol*, (117):500–544.
Ilin, V., Malyshev, A., Wolf, F., and Volgushev, M. (2013). Fast computations in cortical ensembles require rapid initiation of action potentials. *The Journal of neuroscience : the official journal of the Society for Neuroscience*, 33(6):2281–92.
Kole, M. H. P. and Stuart, G. J. (2008). Is action potential threshold lowest in the axon? *Nature neuroscience*, 11(11):1253–5.
Köndgen, H., Geisler, C., Fusi, S., Wang, X.-J. J., Lüscher, H.-R. R., and Giugliano, M. (2008). The dynamical response properties of neocortical neurons to temporally modulated noisy inputs in vitro. *Cerebral Cortex*, 18(9):2086–2097.
Kuhn, A., Aertsen, A., and Rotter, S. (2004). Neuronal integration of synaptic input in the fluctuation-driven regime. *The Journal of neuroscience : the official journal of the Society for Neuroscience*, 24(10):2345–56.
Kumar, A., Schrader, S., Aertsen, A., and Rotter, S. (2008). The high-conductance state of cortical networks. *Neural Computation*, 20(1):1–43.

Kwan, K. Y., Sestan, N., and Anton, E. S. (2012). Transcriptional co-regulation of neuronal migration and laminar identity in the neocortex. *Development*, 139(9):1535–1546.
Latham, P. E., Richmond, B. J., Nelson, P. G., and Nirenberg, S. (2000). Intrinsic Dynamics in Neuronal Networks. I. Theory. *J Neurophysiol*, 83(2):808–827.
Ledoux, E. and Brunel, N. (2011). Dynamics of networks of excitatory and inhibitory neurons in response to time-dependent inputs. *Frontiers in computational neuroscience*, 5(May):25.
Lin, I. C., Okun, M., Carandini, M., and Harris, K. D. (2015). The Nature of Shared Cortical Variability. *Neuron*, 87(3):645–657.
Marder, E. and Goaillard, J.-M. (2006). Variability, compensation and homeostasis in neuron and network function. *Nature Reviews*, 7(July):563–574.
McCormick, D. a., Shu, Y., and Yu, Y. (2007). Neurophysiology: Hodgkin and Huxley model–still standing? *Nature*, 445(7123):E1–2; discussion E2–3.
Mejias, J. F. and Longtin, A. (2012). Optimal heterogeneity for coding in spiking neural networks. *Physical Review Letters*, 108(22):228102.
Naundorf, B., Wolf, F., and Volgushev, M. (2006). Unique features of action potential initiation in cortical neurons. *Nature*, 440(7087):1060–3.
Naundorf, B., Wolf, F., and Volgushev, M. (2007). Naundorf et al. reply: Hodgkin and Huxley model–still standing? *Nature*, 445(7123):E1–2; discussion E2–3.
Okun, M., Steinmetz, N. a., Cossell, L., Iacaruso, M. F., Ko, H., Barthó, P., Moore, T., Hofer, S. B., Mrsic-Flogel, T. D., Carandini, M., and Harris, K. D. (2015). Diverse coupling of neurons to populations in sensory cortex. *Nature*, 521(7553):511–515.
Ostojic, S. (2014). Two types of asynchronous activity in networks of excitatory and inhibitory spiking neurons. *Nature neuroscience*, 17(4):594–600.
Popper, K. (2005). *The Logic of Scientific Discovery*, volume 2005.
Poulet, J. F. a., Fernandez, L. M. J., Crochet, S., and Petersen, C. C. H. (2012). Thalamic control of cortical states. *Nature neuroscience*, 15(3):370–2.
Prinz, A. A., Bucher, D., and Marder, E. (2004). Similar network activity from disparate circuit parameters. *Nature neuroscience*, 7(12):1345–52.
Purves D, Augustine GJ, Fitzpatrick D, et al., E. (2001). *Neuroscience*. Sunderland (MA): Sinauer Associates.
Rall, W. (1962). Electrophysiology of a dendritic neuron model. *Biophysical journal*, 2(2 Pt 2):145.
Rall, W. (1977). Core conductor theory and cable properties of neurons.

Comprehensive Physiology.
Reinhold, K., Lien, A. D., and Scanziani, M. (2015). Distinct recurrent versus afferent dynamics in cortical visual processing. *Nature Neuroscience*, 18(12).
Renart, A., Brunel, N., and Wang, X.-J. (2004). Mean-field theory of irregularly spiking neuronal populations and working memory in recurrent cortical networks. *Computational neuroscience: A comprehensive approach*, pages 431–490.
Renart, A., Rocha, J. D., Bartho, P., Hollender, L., Parga, N., Reyes, A., Harris, K. D., and de la Rocha, J. (2010). The asynchronous state in cortical circuits. *Science (New York, N.Y.)*, 327(5965):587–90.
Rossant, C., Leijon, S., Magnusson, a. K., and Brette, R. (2011). Sensitivity of Noisy Neurons to Coincident Inputs. *Journal of Neuroscience*, 31(47):17193–17206.
Rubin, D. B., VanHooser, S., Miller, K. D., Hooser, S. D. V., and Miller, K. D. (2013). The stabilized supralinear network : A unifying circuit motif underlying multi-input integration in sensory cortex. *Neuron*, 85(2):402–417.
Rudolph, M. and Destexhe, A. (2003). Tuning neocortical pyramidal neurons between integrators and coincidence detectors. *Journal of Computational Neuroscience*, 14(3):239–251.
Scholvinck, M. L., Saleem, A. B., Benucci, A., Harris, K. D., and Carandini, M. (2015). Cortical State Determines Global Variability and Correlations in Visual Cortex. *Journal of Neuroscience*, 35(1):170–178.
Schulz, D. J., Goaillard, J.-M., and Marder, E. (2006). Variable channel expression in identified single and electrically coupled neurons in different animals. *Nature neuroscience*, 9(3):356–362.
Shadlen, M. N. and Newsome, W. T. (1994). Noise, neural codes and cortical organization. *Current Opinion in Neurobiology*, 4(4):569–579.
Softky, W. R. and Koch, C. (1993). The highly irregular firing of cortical cells is inconsistent with temporal integration of random EPSPs. *The Journal of neuroscience : the official journal of the Society for Neuroscience*, 13(1):334–50.
Tsodyks, M. V. and Sejnowski, T. (1995). Rapid state switching in balanced cortical network models. *Network: Computation in Neural Systems*.
van Vreeswijk, C. and Sompolinsky, H. (1996). Chaos in neuronal networks with balanced excitatory and inhibitory activity. *Science*, 274(5293):1724–1726.
Vogels, T. P. and Abbott, L. F. (2005). Signal propagation and logic gating in networks of integrate-and-fire neurons. *The Journal of neuroscience*,

25(46):10786–10795.
Wehr, M. and Zador, A. M. (2003). Balanced inhibition underlies tuning and sharpens spike timing in auditory cortex. *Nature*, 426(6965):442–446.
Yang, H., Kwon, S. E., Severson, K. S., and O'Connor, D. H. (2015). Origins of choice-related activity in mouse somatosensory cortex. *Nature neuroscience*, 19(1):127–134.
Zagha, E., Casale, A. E., Sachdev, R. N. S., McGinley, M. J., and McCormick, D. a. (2013). Motor cortex feedback influences sensory processing by modulating network state. *Neuron*, 79(3):567–78.